Beyond the Speckles: New Horizons in High-Contrast Imaging for Exoplanet Science

by

Adam B. Johnson
B.Eng., University of Victoria, 2021

A Dissertation Submitted in Partial Fulfillment of the
Requirements for the Degree of

DOCTOR OF PHILOSOPHY

in the Department of Mechanical Engineering

© Adam B. Johnson, 2025
University of Victoria

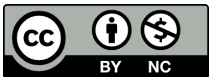

This work is licensed under a Creative Commons Attribution-NonCommercial 4.0 International License (CC BY–NC 4.0)

We acknowledge and respect the Lək̓ʷəŋən (Songhees and Xʷsepsəm/Esquimalt) Peoples on whose territory the university stands, and the Lək̓ʷəŋən and W̱SÁNEĆ Peoples whose historical relationships with the land continue to this day.

Beyond the Speckles: New Horizons in High-Contrast Imaging for Exoplanet Science

by

Adam B. Johnson
B.Eng., University of Victoria, 2021

Supervisory Committee

Dr. C. Bradley, Supervisor
(Department of Mechanical Engineering)

Dr. C. Marois, Co-Supervisor
(Department of Physics and Astronomy)

Dr. P. Wild, Committee Member
(Department of Mechanical Engineering)

Dr. S. Oya, Outside Member
(National Astronomical Observatory of Japan)

ABSTRACT

Direct imaging of exoplanets offers a uniquely powerful way of characterizing planetary atmospheres, surface conditions, and potential biological markers beyond our solar system. However, the extreme contrast and small angular separations involved present significant observational challenges that demand continual innovation in instrumentation and observing strategies. This dissertation addresses these challenges through a coordinated set of developments in instrumentation for focal plane wavefront sensing, post-processing, calibration systems, and atmospheric tomography.

The first contribution presents the design, implementation, and deployment of the SPIDERS instrument for the Subaru Telescope. This compact, modular platform integrates the fast atmospheric self-coherent camera technique (FAST), a Lyot-based low-order wavefront sensor (LLOWFS), and an imaging Fourier transform spectrometer (IFTS) to validate advanced wavefront control, spectral retrieval, and post-processing techniques. A custom ultra-low speed optical chopper (ULSOC) enables stable fringe modulation at subhertz frequencies, supporting focal plane wavefront sensing and coherent differential imaging (CDI). A dedicated motion control system further supports full-field broadband spectral acquisition through the IFTS.

The second major contribution focuses on the CAL 2.0 upgrade for the Gemini Planet Imager (GPI). The system incorporates adapted versions of the focal plane mask (FPM) wheel and polarization modulator (PolMod) from the original CAL architecture, along with a facility-class ULSOC, enabling real-time focal plane wavefront correction and enhanced post-processing. Informed by lessons from SPIDERS, these upgrades are expected to improve contrast by up to two orders of magnitude beyond current state-of-the-art systems for bright stars at small angular separations.

Finally, the dissertation introduces STARLITE, a mission concept for satellite-aided atmospheric tomography. STARLITE proposes a constellation of small satellites carrying laser beacons in highly elliptical orbits, periodically aligning with ground-based observatories to enable tomographic reconstruction of atmospheric turbulence. A feasibility study is presented, evaluating orbital mechanics, optical performance, and reconstruction fidelity, demonstrating STARLITE's potential to support diffraction-limited, high-contrast imaging for small separation targets.

Together, these contributions advance the capabilities of direct imaging systems and establish a technical foundation for future instruments to probe terrestrial exoplanets and explore their potential for life with unprecedented precision.

Contents

Supervisory Committee **ii**

Abstract **iii**

Table of Contents **iii**

List of Tables **vii**

List of Figures **ix**

Acknowledgements **xxvi**

Authorship **xxviii**

Dedication **xxix**

Glossary of Terms and Acronyms **xxix**

1 Introduction **1**

1.1 Motivation for Directly Imaging Exoplanets 4

1.1.1 Exoplanet Classification, Formation, and Evolution 4

1.1.2 The Habitable Zone Around a Star 7

1.1.3 Challenges and Strategies in Exoplanet Research 9

1.1.4 Methods of Exoplanet Detection and Characterization 10

1.1.5 Confirmed and Nearby Exoplanets 13

1.1.6 Identifying Biomarkers Through Spectroscopy 15

1.1.7 Current Innovations in Direct Imaging Technologies 16

1.2 Observational Foundations for Direct Imaging 18

1.2.1 Angular Separation and Limitations of a Telescope 18

1.2.2 Visible and Thermal Planet-to-Star Contrast 22

1.2.3 Stellar Magnitude, Luminosity, and Flux 26
1.2.4 Standard Photometric/Wavelength Bands 29
1.2.5 Spectroscopic Methods and Techniques 30
1.2.6 Photon Noise and the Signal-to-Noise Ratio 32
1.2.7 Limits and Confidence of Faint Detections 33
1.3 Principles of High-Contrast Direct Imaging 36
1.3.1 Propagation and Diffraction of Monochromatic Light 37
1.3.2 Using Fourier Transforms to Propagate Light 43
1.3.3 Optical Coherence and Broadband Propagation 44
1.3.4 Sources and Representations of Optical Aberrations 47
1.3.5 Impact of Aberrations on the Point Spread Function 53
1.3.6 Coronagraphic Techniques to Block Starlight 55
1.3.7 Speckle Evolution in the Focal Plane 59
1.3.8 Speckle Subtraction Techniques 61
1.3.9 Pupil Plane Wavefront Sensing 68
1.3.10 Focal Plane Wavefront Sensing 71
1.3.11 Deformable Mirrors for Wavefront Correction 74
1.3.12 Wavefront Error Budget and Strehl Expectations 79

2 SPIDERS: The Subaru Pathfinder Instrument for Detecting Exoplanets & Retrieving Spectra 82
2.1 Introduction 82
2.2 Mechanical Constraints and Design 86
2.2.1 Structural Frame and Electronics Housing 89
2.2.2 Thermal Management and Water Cooling 91
2.2.3 Lifting and Structural Safety 95
2.2.4 Hexapod Alignment System and Mechanical Safety 99
2.2.5 Hexapod Inverse Kinematics and Workspace 103
2.3 Blinking the fringes, initial development and results of the Ultra-Low Speed Optical Chopper for the Self-Coherent Camera 114
2.3.1 Introduction 114
2.3.2 Applications 114
2.3.3 Operational Principles 117
2.3.4 Technical Design 118
2.3.5 Preliminary Design and Results 121

2.3.6 Next Steps and What to Expect 122
2.3.7 Conclusions 124
2.4 Exoplanet Detection and Characterization: Development and Results of a New Generation Imaging Fourier Transform Spectrometer 125
2.4.1 Introduction 125
2.4.2 Operational Principles 126
2.4.3 Closed-Loop Velocity Control 127
2.4.4 Implementation, Performance, and Early Results 128
2.4.5 Conclusions and Future Work 132

3 GPI, CAL 2.0: The Gemini Planet Imager Calibration Unit 2.0 Upgrade 133
3.1 CAL 2.0: Introduction and System Overview 134
3.1.1 Focal Plane Mask Wheel 136
3.1.2 Polarization Modulator 140
3.1.3 Ultra-Low Speed Optical Chopper 143

4 STARLITE: Superluminous Tomographic Atmospheric Reconstruction with Laser-beacons for Imaging Terrestrial Exoplanets 147
4.1 A SmallSat Mission Study for STARLITE 147
4.1.1 Introduction 148
4.1.2 Concept Overview 149
4.1.3 Mission Profile 150
4.1.4 Science Overview 151
4.1.5 Instrument / Laser Payload 155
4.1.6 Trajectory 157
4.1.7 Propulsion and Launch 158
4.1.8 Attitude Dynamics and Control 159
4.1.9 Data Processing 160
4.1.10 Telemetry Tracking and Command 161
4.1.11 Power 162
4.1.12 Environmental Protection 163
4.1.13 Assembly and Structures 164
4.1.14 Integration and Testing 165
4.1.15 Cost Budget 167

4.1.16 Conclusion 167
4.1.17 Acknowledgments 168
4.2 An Optical Feasibility Study for STARLITE 170
4.2.1 Introduction 170
4.2.2 Optical System Overview 172
4.2.3 Designing an Atmospheric Turbulence Model 173
4.2.4 On-Axis Phase Residuals at the Focal Plane 175
4.2.5 Off-Axis Tomographic Reconstruction Phase Residuals 179
4.2.6 Conclusions 182
4.2.7 Future Work 183

5 Conclusions **184**

A Additional Information **188**
A.1 Detector Types, Readout Strategies, and the Photo-Electric Relationship 188
A.2 Simulating a Chromatic Wavefront 192
A.2.1 Simulating an Exoplanet Companion 200
A.3 Simulating Atmospheric Turbulence 205
A.3.1 Validating the Atmospheric Turbulence Model 209

Bibliography **212**

List of Tables

Table 1.1 Properties of main-sequence stars by spectral type, including approximate habitable zone distance, surface temperature, and stellar mass (in solar masses, $M_\odot$). 8
Table 1.2 Exoplanetary systems within the habitable zone, ordered by increasing distance from Earth. Multi-planet systems are grouped into single rows, with lowercase letters (b, c, d, etc.) identifying planets and comma separated parameters. Planets within the habitable zone are shown in green. 14
Table 1.3 Angular separation in milliarcseconds of a Jupiter- or Earth-like planet observed at various distances. 19
Table 1.4 Telescope diameter requirements for resolving Jupiter and Earth-like exoplanet-to-star separations at various distance. Existing telescopes are highlighted in green, while those not yet realized are shown in red. 20
Table 1.5 Telescope diameter requirements for resolving Jupiter and Earth-like exoplanet-to-star separations at various distance with a 3 λ/D coronagraphic inner working angle (IWA). Existing telescopes are highlighted in green, while those not yet realized are shown in red. 21
Table 1.6 Photometric bands, their effective wavelengths, and some corresponding Vega flux reference zero-point values reported by Colina 1996 [56]. 29

Table 1.7 Integration times for achieving specific SNRs at varying distances for a 10^{-6} contrast target around a 10th magnitude star in J-band using a 10 m telescope are calculated under the following parameters: 5% throughput, 0.1 e/s dark current, 2 e/s thermal background, 10 e/read read noise, 0.1 s frame rate, and an electron-to-photon ratio of 1. Assuming no stellar signal contamination, the required integration times to reach the target SNR are provided for distances of 1, 5, 10, and 20 parsecs. 35
Table 1.8 Example wavefront error (WFE) budget for a representative exoplanet imaging AO system, utilizing a Shack-Hartmann wavefront sensor (WFS) and 64×64 deformable mirror (DM) [99]. The total WFE is calculated as the quadrature sum (root-sum-square, RSS), assuming statistical independence of the error sources. . . 80

Table 2.1 Mechanical requirements and specifications for the SPIDERS optical bench support structure and platform interface. 86

Table 3.1 Mechanical and control constraints for the CAL 2.0 focal plane mask wheel. 137
Table 3.2 Mechanical and control constraints for the CAL 2.0 polarization modulator. 140
Table 3.3 Mechanical and control constraints for the CAL 2.0 optical chopper. 143

Table 4.1 The science traceability matrix for the STARLITE mission. . . . 153
Table 4.2 S-band communication link budget 161
Table 4.3 GPS communication link budget 162
Table 4.4 Power requirements of each CubeSat for each of the three modes: Science, Idle, and Eclipse. 163
Table 4.5 Cost estimate per STARLITE satellite and for a five-beacon constellation. 168

List of Figures

Figure 1.1 Planet mass versus orbital distance of current confirmed exoplanets sorted by detection method using data retrieved from the NASA Exoplanet Archive [34]. Only planets with a reported mass and semi-major axis are plotted, while all detections are counted in the legend categories and in total. 13

Figure 1.2 Transmission spectrum of an Earth-like atmosphere, showing absorption features from molecules such as ozone (O_3), water vapor (H_2O), carbon dioxide (CO_2), and methane (CH_4). Image credit: NASA, ESA, CSA, Leah Hustak (STScI) [35]. 15

Figure 1.3 Illustration of how distance from the observer to the target and the separation between the objects define the angular separation. 19

Figure 1.4 Two point sources of equal luminosity as observed through a diffraction-limited telescope at three angular separations: unresolved (left), just resolved (middle), and fully resolved (right). In the absence of other errors, this fundamental limit defines the smallest angular separation at which a telescope or imaging system can distinguish two closely spaced objects. 20

Figure 1.5 Blackbody spectra at various temperatures, with planet-to-star contrast ratios at peak spectral radiance (λ_p) for Jupiter (J) and Earth-sized (E) blackbodies orbiting a Sun-like blackbody. The Sun's blackbody curve is shown for reference. 26

Figure 1.6 Schematic of a basic adaptive optic (AO) system. A deformable mirror corrects wavefront distortions based on feedback from the wavefront sensor, and a beam splitter divides the incoming light between the sensor and the science camera, enabling concurrent feedback and image capture. 36

Figure 1.7 A side-viewed, on-axis simulation of a 500 nm plane wave diffracting through a circular pupil using the Rayleigh-Sommerfeld integral (top), illustrating the transition from Fresnel to Fraunhofer regimes (red dotted line). The bottom set of line plots show the normalized intensity of the wavefront at discrete distances for the Rayleigh-Sommerfeld integral (black solid), with Fresnel (blue dotted) and Fraunhofer (orange dotted) approximations overlaid in their respective near and far-fields for comparison. . 42

Figure 1.8 Fourier optics model of a flat, monochromatic wave propagating through a basic telescope, showing diffraction-limited intensity distributions at the pupil and focal planes. The pupil plane images are cropped to only show the aperture, and the focal plane image scaled for better visualization of the diffraction pattern. The transformations between these planes are governed by the forward and inverse two-dimensional Fourier transforms, $\mathcal{F}$ and $\mathcal{F}^{-1}$, respectively. 43

Figure 1.9 Focal plane intensity for monochromatic (left) and narrowband (right) light near the photometric V-band (500–600 nm). Monochromatic light produces a distinct Airy disk, while chromatic broadening blurs these features. Exponential scaling of the image was applied to increase the contrast globally without altering structure. 46

Figure 1.10 Illustration of a point source emitting a spherical wavefront, which becomes approximately planar at a sufficient distance. As the wavefront passes through the Earth's atmosphere, it accumulates amplitude and phase distortions due to turbulence and refractive index variations. The telescope's primary mirror focuses the light towards the focal plane, accumulating more errors as it passes through intermediate optics, beam splitters, filters, etc., before reaching the sensor/detector (e.g., a camera) to capture the intensity distribution of the wavefront. 47

Figure 1.11 Zernike polynomials up to the fifth radial order, arranged by increasing radial degree (n) and azimuthal frequency (m), with commonly used aberration names. Each polynomial is normalized over the unit circle and can be scaled to represent various wavefront distortions. 49

Figure 1.12 Kolmogorov power spectral density (PSD) function from Eq. 1.45 for various r_0 values, plotted on a logarithmic scale for positive f_x values and when $f_y = 0$ (left). The full-form 2D PSD is used with random coefficients to generate the spatial domain phase screen in radians using an $r_0 = 20$ cm (right). At 500 nm, the optical path difference in micrometers is also shown for scale. A 10 m telescope diameter is overlaid as a white circle to illustrate the grid and beam size used. 51

Figure 1.13 Theoretical Kolmogorov-Zernike residual phase error after removing the first three Zernike modes, $\sigma_{\phi,3}$ from Eq. 1.46, as a function of the Fried parameter r_0 for different wavelengths. . . 53

Figure 1.14 Point spread function (PSF) (bottom row) resulting from a monochromatic point source viewed through a pupil with varying amplitude (top row) and phase (middle row) aberrations. The intensity is uniformly scaled to enhance contrast while preserving structural features. 54

Figure 1.15 Simulation of an error-free wavefront passing through an amplitude mask and Lyot stop coronagraph, with intensity shown at key locations before and after the 4 λ/D radius FPM and 0.9 D Lyot stop mask. Contrast is shown relative to the peak intensity of the unmodified PSF through a circular pupil. 56

Figure 1.16 Simulation of a 4 λ/D vortex phase-mask coronagraphic system with resulting intensities at various planes. Contrast is shown relative to the peak intensity of the unmodified PSF passing through a circular pupil. 56

Figure 1.17 Simulation of an apodized pupil combined with a 4 λ/D vortex phase-mask coronagraph and Lyot stop. Contrast is shown relative to the peak intensity of the unmodified PSF through a circular pupil. 57

Figure 1.18 Simulated focal plane intensity without aberrations for $10^{-7} - 10^{-10}$ contrast planets in V-band, analogous to our solar system, observed from 10 parsecs with a 10 m telescope. LEFT: amplitude blocking FPM and Lyot stop coronagraph; MIDDLE: vortex phase FPM and Lyot stop coronagraph; RIGHT: apodized pupil with vortex phase FPM, amplitude blocking FPM, and Lyot stop. Contrast is quantified in each image by dividing the final intensity by the unocculted peak intensity of the star. Only four of the eight planets are visible in each plot, with the inner planets and lower contrasts obscured by bright residual diffraction patterns around the central star. 58

Figure 1.19 Animated simulation of monochromatic speckles evolving spatially and temporally in the focal plane (right) due to atmospheric turbulence using a three-layer Kolmogorov turbulence model at $r_0 = 20$ cm (left). The simulation sampling occurs over 2 s at 30 Hz and 120 ms at 500 Hz. The telescope size is overlaid on the wavefront phase (left), with a magnified aperture for visualization (middle). 59

Figure 1.20 Animation of quasi-static speckles induced by thermal and flexural drift. The model incorporates optics with ∼175 nm RMS figure error, radial polishing artifacts, and ∼85% transmission/reflectivity. Displayed are the wavefront phase errors (left), amplitude errors (middle), and their effect on the focal plane image (right). The evolution timescale is influenced by the optical configuration and environmental conditions, but could occur over minutes to hours. 60

Figure 1.21 Reference differential imaging (RDI) suppressing static speckles using a reference PSF with slight intensity variations and small random wavefront errors. Implemented with an apodized pupil Lyot stop coronagraphic system, RDI processing reveals four of the eight $10^{-4} - 10^{-7}$ companions, significantly improving planet contrast and reducing diffraction effects. However, small deviations between the reference and observation PSFs limit subtraction effectiveness, particularly for high-contrast targets near the host star. 62

Figure 1.22 Animation of angular differential imaging (ADI) removing static speckles for a 30-image sequence of eight $10^{-4} - 10^{-7}$ companions through an apodized pupil Lyot stop coronagraph system with low-power random phase fluctuations and drift. The final stacked median image on the right demonstrates the contrast improvement, revealing seven of the eight companions with the 30-image stack. 63

Figure 1.23 Animated schematic of the Self-Coherent Camera (SCC) optical path with fringed and unfringed focal plane images. Incoming starlight is tilted off-axis and defocused using a tilt-Gaussian phase focal plane mask (FPM), splitting into science and reference paths, passing through the Lyot stop/pinhole, then recombined to produce spatial fringes in the focal plane. The final focal plane intensity is rotated by 30° to better visualize the fringes and minimize fringe-aligned detector readout artifacts. ∼25 nm RMS phase errors with reduced low-order terms are used to simulate first stage adaptive optics (AO) residuals. 64

Figure 1.24 Low-pass filtering of the side lobe (top row) and main pupil (middle row) from the fringed SCC focal plane image at the end of the optical path in Figure 1.23. A subtraction of the fringed and unfringed images provides the pinhole PSF after masking and filtering (bottom row). 66

Figure 1.25 Animation of final CDI-subtracted intensity for 10^{-15} contrast companions (10^6 dimmer than Earth in the visible) and the subtracted intensity without companions, illustrating the average 10^{20} contrast gain from a noiseless simulation subtraction. The final plot is divided by the peak intensity of the unocculted star to provide numerical contrast values at each pixel. The image is in logarithmic scale to better visualize the contrast improvement across many orders of magnitude. 67

Figure 1.26 Schematic of the Shack-Hartmann Wavefront Sensor (SHWFS). A wavefront traveling through a lenslet array forms focal spots on a detector (left), with their shape and position a function of any present aberrations (middle). A flat wavefront produces centred and focused spots (right). 69

Figure 1.27 Schematic of the Pyramid Wavefront Sensor (PyWFS). The pyramidal prism is modulated in a circular motion (left), sequentially shifting the beam between quadrants on the detector (middle). The sensor exhibits a linear response for small wavefront distortions but transitions to a nonlinear regime near saturation or the noise floor (right). 70

Figure 1.28 Estimated wavefront amplitude (left) and phase (right) components from self-coherent camera (SCC) images containing ∼25 nm RMS phase errors, with reduced low-order terms to simulate first-stage adaptive optics (AO) residuals. The wrapped phase cannot be directly used for real-time wavefront correction, as deformable mirrors require a continuous surface for accurate wavefront shaping. 73

Figure 1.29 Animation of arbitrary sinusoidal phase modes (left column) applied to the wavefront in the pupil plane in a noiseless simulation. The resulting PSF pairs in the SCC image are shown in the middle column, and the fringed minus the optically chopped unfringed image in the right column. The top row illustrates the effect of lateral phase adjustments on the fringe phase, while the bottom row shows the influence of spatial frequency and orientation on speckle placement. 73

Figure 1.30 Animated example of three deformable mirrors (DMs) of varying actuator densities correcting an $r_0 = 20$ cm atmosphere on a 10 m telescope through iterative fitting and subtraction. The wavefront phase (first column), Gaussian-coupled actuator commands (second column), reconstructed DM surface via cubic spline interpolation (third column), residual phase error with RMS values (fourth column), and focal plane intensity, propagated through an apodized aperture and focal plane mask with (first frame) or without (second frame) a Lyot stop coronagraph, is presented with contrast scales to quantify improvement (fifth column). 77

Figure 1.31 Visualization of the Maréchal approximation for Strehl ratio as a function of wavefront error (WFE) at various wavelengths. For a given WFE, shorter wavelengths experience greater phase distortion, resulting in a more pronounced reduction in Strehl ratio. The approximation becomes less accurate for WFEs exceeding approximately $\lambda/9$, as highlighted by the shift in transparency around a Strehl ratio of 0.62. 81

Figure 2.1 The SPIDERS instrument installed on the Nasmyth platform of the 8.2 m Subaru Telescope on Maunakea, Hawaii. During observations, the Nasmyth platforms rotate azimuthally to maintain alignment with the telescope's optical path. A human figure is shown for scale. Telescope image courtesy of the National Astronomical Observatory of Japan (NAOJ) [104]. 83

Figure 2.2 SPIDERS optical layout provided by W. Thompson [105]. Four primary optical paths are shown: the deployable calibration source (green) simulates the Subaru AO3k input (blue), both feeding three downstream paths — the self-coherent camera (SCC, red), Lyot-based low-order wavefront sensor (LLOWFS, purple), and imaging Fourier transform spectrograph (IFTS, yellow). . . 84

Figure 2.3 Exploded view (left) and integrated view (right) of the SPIDERS assembly on the Subaru telescope's Nasmyth Platform. The exploded diagram highlights the five key subassemblies: (1) enclosure, (2) optical bench, (3) hexapod positioning system, (4) structural frame and electronics housing, and (5) booster-seat interface module. Light from AO3k is directed into SPIDERS via the beam switcher, which routes starlight to different instruments on the platform. 89

Figure 2.4 Design of the SPIDERS structural frame and electronics housing for the laboratory development phase, featuring lockable casters. Cables from controllers and hoses for water cooling exit through the sides of the frame. Extruded polystyrene insulation is applied to the top, ends, and one side of the base (translucent for clarity). Primary components, mechanical features, and dimensions are labeled. 90

Figure 2.5 Unpopulated frame and electronics racks during initial construction (left), and the fully assembled SPIDERS system (right). Image on right courtesy of Olivier Lardière. 91
Figure 2.6 Schematic of the SPIDERS water cooling system. The closed-loop design includes a liquid-to-liquid heat exchanger (HX) interface with Subaru's facility glycol system and a toggleable internal fan-cooled radiator. Temperature and pressure sensor locations are shown for real-time monitoring and validation. 92
Figure 2.7 Left: Assembled SPIDERS cooling system (dry configuration) showing the pump, reservoir, radiator assembly, Subaru-coupled heat exchanger (HX), and quick-disconnects and distribution blocks for the cameras. Right: System installed on a suspended shelf within the SPIDERS frame, providing vibration isolation and reserved space for final component integration. The HX and pressure sensor were not installed at the time of these images. . 93
Figure 2.8 Temperature profiles recorded over a 24-hour period in the development laboratory under 100 W and 200 W thermal loading conditions at various times throughout the day. Temperature data was collected using sensors mounted on the water lines and on the upper and lower surfaces of the optical bench. The system was intermittently cycled as part of ongoing software tuning and component validation. 94
Figure 2.9 SPIDERS lifting system design showing the full assembly. Safety factors (SFs) for the custom G10 plate interface and Working Load Limit Factors (WLLFs) for the commercial hardware are annotated based on the conservative two-arm loading scenario. SFs for the lifting arm assembly components are shown in Figure 2.10. 96
Figure 2.10 Detailed view of the SPIDERS lifting assembly evaluated under the conservative two-arm configuration, with two engaged bolts per interface. Safety factors (SF) are annotated at each interface below the corresponding limiting failure mode. The three lowest SFs are highlighted in bold text. 98

Figure 2.11 SPIDERS six-degree-of-freedom (6-DOF) hexapod alignment system. Left: Full instrument layout showing the adjustment location (SPIDERS focus) and resultant load distribution across each bipod under the maximum allowable bench load. Right: Close-up of a single bipod leg with labeled rod end and turnbuckle components. Note: The coordinate system shown is defined specifically for the hexapod system to align with standard conventions used in classical workspace analysis. 99
Figure 2.12 Component-level safety factor (SF) analysis for a single bipod under worst-case loading. Limiting failure modes are annotated at each interface. Evaluated leg length and angular ranges are indicated for reference. 101
Figure 2.13 Assembled bipod forming one of the three leg pairs in the SPIDERS hexapod, shown in the nominal home position. Custom parts were fabricated locally by HAA's Design and Fabrication Services (DFS) shop. 102
Figure 2.14 The Stewart–Gough (hexapod) platform layout, with the SPIDERS hexapod geometry shown for reference. The nominal input focus is defined as the global origin. A sample pose adjustment is illustrated as the target input for the inverse kinematics (IK) solution. 104
Figure 2.15 SPIDERS hexapod system showing the numbered legs, base and platform joint positions in their home positions, reference plane heights, and global origin. 106
Figure 2.16 Adapted inverse kinematics (IK) calculator for the SPIDERS 6-DOF hexapod platform. **Inputs** include zero-displacement configuration, pose adjustments, and workspace constraints. **Outputs** provide leg length solutions, angular adjustments, workspace analysis, and pose saving and export capabilities. 108
Figure 2.17 Inverse kinematics (IK) calculation output displaying absolute leg length changes and corresponding angular adjustments. . . . 109
Figure 2.18 User-defined search resolution and pose to analyze from with status feedback for workspace computation. Coarser resolutions solve faster but yield lower fidelity evaluations. 109

Figure 2.19 Animated view of the reachable workspace from the home pose with roll, pitch, and yaw set to zero. The hexagonal bipyramid shape reflects the system's symmetric geometry and actuator constraints. Faint dots are plotted periodically to show a found boundary point, while the closed surface uses all of the found points. Colour is mapped to the Z component for visualization only. 110
Figure 2.20 Animated view of the orientation workspace from the home pose with X, Y, Z fixed. The shape reflects asymmetric angular limits imposed by hexapod geometry and actuator constraints. 111
Figure 2.21 Animated visualization of the adjusted reachable workspace (left) and orientation workspace (right) from a representative pose $[11.935, 7.529, -5.381]$ mm, $[0.000, -0.252, 0.323]^\circ$. The pose is positioned near the boundary of one of the six leg's range, indicated by its proximity to the edges of each workspace. 112
Figure 2.22 PNG export interface for saving workspace visualizations. . . 112
Figure 2.23 Chopping an optical beam with a rotating segmented blade. The intensity is "chopped" into discrete pulses. 115
Figure 2.24 A portion of the optical layout for the SPIDERS instrument, from left to right: the Subaru entrance pupil mask; the apodizer for the Apodized Pupil Lyot Coronagraph (APLC) [118] system; The Tilt-Gaussian (TG) Focal Plane Mask (FPM) [102]; the reflective Lyot stop for LLOWFS [116]; and the resulting images on the detector plane [91]. The SPIDERS instrument is currently being assembled and will be tested on-sky in 2023 at the 8.2 m Subaru telescope. 116
Figure 2.25 The block diagram of a current controlled, closed-loop stepper motor system with a phase-locked loop. 117
Figure 2.26 The same block diagram of the chopper system from Figure 2.25 but simplified by the use of a smart motor. 118
Figure 2.27 The initial mechanical design of the ULSOC (top right), and the custom assembly for the SPIDERS instrument exploded (left) and isometric (bottom right) view. 119
Figure 2.28 The initial electrical design concept for the ULSOC for the SPIDERS instrument. 120

Figure 2.29 On the left, a rendering of the control box V2 concept. On the right, the manufactured chopper mechanism for SPIDERS. . . . 122
Figure 2.30 A comparison of fringed (left, unchopped), unfringed (centre, chopped), and differential (right) images, with the differential image containing the PSF of the pinhole for the self-coherent camera (SCC). The top and bottom rows represent the loop-open and loop-closed configurations, respectively. All images are colour-mapped for clarity. Detector saturation near the core, caused by excessive illumination, leads to missing fringe information and gaps in the differential image. 124
Figure 2.31 A scanning Michelson interferometer receives an image input and outputs an interferogram. A Fourier transform along each pixel yields the spectral data cube of the input image. A helium-neon (HeNe) laser provides positional feedback, while a white light source identifies the absolute centre. 126
Figure 2.32 A closed-loop velocity-current cascade controller to regulate the voice coil motor scan speed. 128
Figure 2.33 The custom IFTS controller system (left) and early experimental setup in the NEW EARTH lab (right). 129
Figure 2.34 The open and closed-loop response in position and velocity for a 0.36 mm/s continuous-scan. 129
Figure 2.35 The interferogram produced and recorded by the SPIDERS IFTS (left) and the processed broadband image (right). 130
Figure 2.36 The 2D interferogram (left) and wavelength spectrum (right) of a benchtop supercontinuum white light source. 131

Figure 3.1 Optical layout of CAL 2.0, illustrating the light shared between the integral field spectrograph (IFS) and the wavefront sensing arms. A legacy low-order wavefront sensor (LOWFS) is positioned behind the focal plane mask (FPM) wheel, providing fallback support for the original non-common path CAL architecture. 134
Figure 3.2 Section view of CAL 2.0 mechanical structure and labeled main subsystems, with isometric view in the top right. Figures courtesy of C. Marois [131]. 135

Figure 3.3 Exploded CAD view of the CAL 2.0 FPM Wheel assembly with labeled critical components (left). Isometric views are shown with the beam path (right) 138
Figure 3.4 Initial laboratory assembly of the CAL 2.0 focal plane mask wheel side (left) and front (right) view. 139
Figure 3.5 Exploded CAD view of the CAL 2.0 polarization modulator with labeled components (left). Front and rear isometric views illustrate the beam path through the mechanism (right). Component colours are for visualization purposes only. 141
Figure 3.6 Partial (left) and complete (middle and right) laboratory assembly of the CAL 2.0 polarization modulator with linear and rotational stages, wiring, and sensor harnessing installed. The polarization optic will be installed following system validation and prior to final CAL 2.0 integration. 142
Figure 3.7 Exploded CAD view of the CAL 2.0 chopper with critical components labeled (left), and isometric views with the main/reference beam path shown (right). 145
Figure 3.8 Laboratory assembly of the CAL 2.0 chopper, showing the partially assembled configuration (left), and the uncoated chopper blade installed in the fully assembled system mounted on a test bracket (middle and right). 146

Figure 4.1 STARLITE five-beacon constellation concept design with generalized MCAO ground station system. The constellation aligns with the target star at apogee during a highly-elliptical orbit, and the laser light is used to enhance the system's ability to correct the wavefront and acquire signal from any potential exoplanets. 149
Figure 4.2 STARLITE concept of operations (ConOps), from launch to end of life. 151
Figure 4.3 Planet mass (in Earth masses) versus orbital distance (in AU) of current confirmed exoplanets sorted by detection method. The plot was created using data retrieved from the NASA Exoplanet Archive [34]. 152

Figure 4.4 Candidate target stars, coloured by tier, dot size inversely proportional to distance from Earth, and translucent when farther than 10 *pc* away. Concentric circles denote declination and angular ticks denote right ascension. The number of targets in the potential orbit are identified in the legend above as *(-TIER- : -TOTAL TARGETS- , -WITHIN* 10 *pc-).* 154
Figure 4.5 The designed laser wavelength next to the blue side of the oxygen A-band (left). The apparent magnitude of various laser powers is plotted over the distance from the beacon to the telescope (right). 155
Figure 4.6 Conceptual optical layout for a single STARLITE CubeSat. . . 156
Figure 4.7 Conceptual trajectory of CubeSat constellation in isoplanatic field of view relative to Keck Telescope (left) and close-up view of observation window size relative to constellation positioning (right). 158
Figure 4.8 Conceptual representation of the satellite in orbit and the maneuvering window at perigee. 159
Figure 4.9 STARLITE orbit with RF (black) and GPS coverage (dashed red). 160
Figure 4.10 Rendering of the preliminary STARLITE CubeSat concept in launch (left) and deployed (right) configurations. 164
Figure 4.11 Exploded view of the STARLITE system with critical components and subsystems labeled. 165
Figure 4.12 The SMDS class of 2023 after the final Mission Concept Review (MCR) at Cornell University (left). The organizational chart including support instructors and teaching assistants (right). . . 169
Figure 4.13 STARLITE five-beacon constellation concept with generalized ground station system. The constellation aligns with a science target at apogee where onboard lasers generate superluminous guide stars for adaptive optics on the ground. 171
Figure 4.14 Simplified MCAO layout at apogee with the on-and off-axis beacons in front of the target to provide different lines of sight through the atmosphere to reconstruct the on-axis wavefront throughout the duration of the observation. 172
Figure 4.15 PSD model and result comparison (left) and RMS error validation (right). 174

Figure 4.16 PSF of $10m$ telescope with circular aperture without errors (left) and with errors from the atmosphere (right). Peak-valley and RMS error across the pupil includes piston, tip, and tilt - compared to the expected RMS in Figure 4.15. 175
Figure 4.17 RMS error and visual comparison of on-axis first, second, and third order polynomial predictors applied to 10, 1, and 0.1 kHz atmosphere model samples with the best predictor residual PSF shown (cubic, linear, and linear, respectively). 178
Figure 4.18 Comparison of on-axis PSD with time lag and first, second, and third order polynomial predictors applied to 10, 1, and 0.1 kHz atmosphere model samples. 178
Figure 4.19 Beacon fields of view (lines of sight) around on-axis target for reconstruction (white circles), with on-axis target and field of view (green circle and dot) for a targeted reconstruction altitude of 4 km above the 10 m telescope. 180
Figure 4.20 PSF of the residual phase error after reconstruction of 10", 1", and 0.1", with reconstructor type and RMS of each simulation above their plot. 180
Figure 4.21 On-axis average and reconstructor residual PSDs for 10", 1", and 0.1" constellation radii with bilinear, bicubic, and bicubic spline interpolation reconstruction. 181

Figure A.1 Simulated focal plane intensity for monochromatic (left), narrowband (centre), and broadband (right) light spanning the U to R photometric bands (300–800 nm), using $np = 2048$, $D = 10$ m, and $b_r = 0.1$, the λ/D rings (in blue) illustrate the grid relationship with the wavelength and telescope diameter. Monochromatic light produces a distinct Airy disk, while chromatic broadening blurs these features and increases the PSF size. Exponential scaling of the intensity enhances image contrast globally without altering structure. The plotted intensities are zoomed in from the full Nyquist limit range, where $f_{\max} = 10.24$ cycles/m. 196

Figure A.2 Simulated intensity for a narrowband (left) and broadband (right) focal plane image with multiple point sources, including phase and amplitude errors. Chromatic blurring is modeled via Fourier-domain zero-padding, with wavelength-dependent focal plane intensities scaled and incoherently summed. A 124x124-actuator deformable mirror partially corrects the speckles around the on-axis occulted star, while faint point source companions with contrasts between 10^{-2} and 10^{-5} are visible. The coronagraphic FPM at the centre becomes progressively less effective at longer wavelengths, with diffraction around the mask becoming more prominent. A contrast scale based on the unocculted peak intensity is shown for reference. 199

Figure A.3 Simulated colour-coded intensity for narrowband (left) and broadband (right) focal plane images containing multiple point sources. The simulations use the same environment and setup as Fig. A.2. Spectral channels are coloured by wavelength over the simulation range, with the scale shown for reference. 200

Figure A.4 The simulated diffraction-only focal plane intensity for monochromatic point sources at separations analogous to our solar system, as viewed from 10 parsecs away with a 10 m telescope at $10^7\times$ the contrasts in the visible (left). At visible wavelength contrasts, the planets are practically invisible compared to the overwhelmingly bright Sun (right). The contrast at each pixel is calculated by dividing each pixel of the final intensity image by the peak star intensity, the Sun in this case. 203

Figure A.5 The amplitude (top left, log-scale for visibility) and phase (bottom left) components of the random Fourier coefficients $\hat{\phi}(f_x, f_y)$. The resulting phase screen $\phi(x, y)$ (right) is shown with a $D = 10$ m aperture overlaid in white, using $np = 2048$, $b_r = 0.5$, $r_0 = 0.2$ m, and $\lambda = 500$ nm. 206

Figure A.6 Animation of a 1-second three-layer Kolmogorov atmosphere simulation over 20 frames at a sampling rate of $\Delta t = 0.05$ s (20 Hz), with arrows showing the direction and distance each layer moves between each sample k. The model is implemented using typical atmospheric conditions measured at the summit of Maunakea [73], such as $\mathrm{f}_{r_0} = [0.59, 0.21, 0.20]$, $v_{wind} = [5.67, 9.94, 14.87]$ m/s, and $\alpha_{wind} = [216.5, 312.8, 46.6] \cdot \frac{\pi}{180^\circ}$ radians. The other simulation parameters remain the same from the single phase screen generated in Figure A.5. 209

Figure A.7 Binned histogram of RMS phase error across a 10 m pupil for 10,000 randomly generated Kolmogorov phase screens with $r_0 = 20$ cm, after a least-squares fit subtraction of the first Zernike mode (piston). The theoretical RMS given by $\sigma_{\phi,1}$ in Equation 1.46 is nearly double the observed mean RMS, due to the remaining low-order contributions in the theoretical model, which occur infrequently. 210

Figure A.8 Binned histogram of RMS phase error across a 10 m pupil for 10,000 randomly generated Kolmogorov phase screens with $r_0 = 20$ cm, after a least-squares fit subtraction of piston, tip, and tilt Zernike modes. The theoretical RMS given by $\sigma_{\phi,3}$ in Equation 1.46 aligns more closely with the observed mean. . . . 211

ACKNOWLEDGEMENTS

I would like to express my deepest gratitude to the many individuals and organizations who supported me throughout this journey:

Dr. Christian Marois and Dr. Colin Bradley — for their exceptional mentorship, support, encouragement, and patience throughout my graduate studies.

Dr. William Thompson — for his mentorship and support in computer science and astronomy.

Dr. Olivier Lardière — for his guidance and expertise in optical design and optomechanical engineering.

Joeleff Fitzsimmons — for his mentorship and technical insight in mechanical engineering.

Dr. Krzysztof Caputa — for his mentorship and guidance in electrical engineering.

Darryl Gamroth — for his assistance and guidance in electrical and software engineering.

Dr. Kathryn Jackson, Dr. Jean-Pierre Véran, Dr. Maaike van Kooten, and Glen Herriot — for sharing their expertise in adaptive optics, tomography, and control theory.

Dr. Frédéric Grandmont — for his mentorship and supervision during my internship at ABB, and continued support for SPIDERS work.

Dr. Chris Mann — for insightful discussions on coherent differential imaging that helped solidify my understanding.

Dr. Garima Singh — for her valuable advice and mentorship in wavefront sensing and adaptive optics.

Dylan Kerr and Angus Bews — for their co-op work term contributions to the development of the SPIDERS lifting system and temperature monitoring setup, respectively.

National Research Council Canada — for the resources, professional opportunities, and collaborative environment that significantly supported this work.

The New Technologies for Canadian Observatories (NTCO) NSERC CREATE Program — for funding my graduate studies, supporting travel to conferences and workshops, and enabling a valuable industrial internship experience.

I am especially grateful to my partner in life, **Becky Brooks**, for her unwavering love, strength, and belief in me throughout this journey, and to our three feline

companions, **Banff**, **Jasper**, and **Zorro**, for their occasionally selective affection and consistently overwhelming cuteness.

This work would not have been possible without the lifelong love, support, and encouragement of my grandmother, **Ruby Johnson**, and my late grandfather, **Carl Johnson**; my sisters, **Paula Miller** and **Christie Miller**; and my close friend and mentor, **Keith Mandel**. I am also deeply appreciative of my extended family, family friends, and close friends for their enduring support.

I respectfully acknowledge the cultural, historical, and spiritual significance of Maunakea to the Native Hawaiian community. I recognize the privilege of conducting research on this sacred mountain and remain mindful of its importance to the Indigenous peoples of Hawai'i.

AUTHORSHIP

This dissertation includes material presented in conferences, publications, and collaborative research projects. Specific contributions to individual chapters are noted where relevant. The following individuals and groups also provided intellectual, technical, or collaborative support to the overall development of this dissertation:

- **Dr. Christian Marois** and **Dr. Colin Bradley** provided ongoing mentorship and guidance throughout my graduate studies, including critical feedback during the writing and revision of this dissertation.
- **Dr. Peter Wild**, a member of the supervisory committee, provided technical guidance on Chapters 2 and 3.
- **Dr. William Thompson** contributed to the design and validation of SPIDERS control systems, particularly integrating the ULSOC and IFTS subsystems, and assisted with instrument operation during data collection for Chapter 2.
- **Dr. Olivier Lardière** and **Joeleff Fitzsimmons** provided technical mentorship in optical and mechanical design across both SPIDERS and CAL 2.0 systems, presented in Chapters 2 and 3.
- **Dr. Krzysztof Caputa** and **Darryl Gamroth** contributed technical advice in electrical and control system design supporting the same SPIDERS and CAL 2.0 instrumentation platforms, presented in Chapters 2 and 3.
- **Dr. Kathryn Jackson** assisted with simulations and mathematical derivations for the STARLITE feasibility study presented in Chapter 4.2.
- **Dr. Chris Mann** supported the development of coherent differential imaging for SPIDERS, offering valuable discussions and insights relevant to Chapters 1.3, A.2, and A.3.
- **Collaborators from Cornell University and international institutions** contributed to mission planning and feasibility analysis for STARLITE, as presented in Chapter 4.1.
- **The National Research Council of Canada** and **the NEW EARTH Laboratory** supported the development of the SPIDERS and CAL 2.0 instrumentation. Results from these collaborations are shown in Chapters 2 and 3.

DEDICATION

In memory of my mom, Tammy Lynn Miller, and grandpa, Carl Burton Johnson.

Glossary of Terms and Acronyms

λ/D Diffraction angular scale set by wavelength λ and entrance pupil diameter D; sets resolution limit and focal plane scaling.

ADI (angular differential imaging)
Differential imaging technique using field rotation to separate static speckles from real companions.

Airy disk
Diffraction-limited focal plane pattern of a circular pupil with central bright core and surrounding rings of decreasing intensity.

AO (adaptive optics)
Real-time correction of atmospheric or instrumental aberrations using a wavefront sensor, reconstructor, and deformable mirror.

AO3k (Subaru adaptive optics system)
Subaru AO system feeding SPIDERS on the Subaru Nasmyth platform.

APLC (apodized pupil Lyot coronagraph)
Coronagraph combining pupil apodization with focal plane and Lyot stop masks.

AU (astronomical unit)
The mean Earth-to-Sun distance ($\sim$149,600,000 km).

CAL 2.0 (Calibration Unit 2.0)
A common-path focal plane wavefront sensor downstream of GPI's AO system that also enables post-processing capabilities using an SCC architecture.

CDI (coherent differential imaging)
Post-processing technique exploiting optical coherence to calibrate and subtract speckles.

coronagraph

Optical system that suppresses on-axis starlight while preserving off-axis signals.

dark hole

Region of a coronagraphic image where residual starlight (speckles) is actively reduced by wavefront control to reveal faint sources.

DM (deformable mirror)

Mirror whose optical surface is reshaped in real-time by a 2D actuator array, either a continuous face sheet or a segmented surface; commanded strokes impose controlled wavefront phase/amplitude for AO correction and calibration.

DOF (degree of freedom)

Independent coordinate describing a system's configuration or motion; an unconstrained rigid body in 3D has six (three translational, three rotational).

FAST (fast atmospheric self-coherent camera technique)

An SCC-based method enabling real-time sensing and suppression of residual speckles in the focal plane.

FOV (field of view)

Angular extent of the scene or instrument coverage.

FPM (focal plane mask)

Coronagraphic mask placed at a focal plane to suppress on-axis starlight.

Fried parameter r_0

Atmospheric coherence length over which the RMS phase error is 1 rad; scales as $r_0(\lambda) = r_{0,500\,\mathrm{nm}}(\lambda/500\,\mathrm{nm})^{6/5}$.

GPI (Gemini Planet Imager)

Facility instrument for high-contrast imaging; context for CAL 2.0 upgrade.

HWO (Habitable Worlds Observatory)

Planned NASA space telescope concept for future high-contrast imaging.

IFS (integral field spectrograph)

Instrument that acquires spatially resolved spectra to form a spectral data cube.

IFTS (imaging Fourier transform spectrometer)

Scanning Michelson interferometer producing an interferogram per pixel; Fourier transform along each pixel yields a spectral cube.

IK (inverse kinematics)

Maps a desired end-effector pose (position and orientation) to joint angles or actuator lengths.

IWA (inner working angle)

Smallest angular separation at which a coronagraph provides a usable off-axis signal; typically expressed in λ/D.

JWST (James Webb Space Telescope)

NASA/ESA/CSA infrared space telescope referenced for context.

Kolmogorov turbulence

Statistical model of atmospheric refractive-index fluctuations; phase differences scale with separation to the 5/3 power.

LLOWFS (Lyot-based LOWFS)

Wavefront sensor using the Lyot stop plane to sense low-order aberrations (tip, tilt, focus, etc.).

LOWFS (low-order WFS)

Wavefront sensor optimized for sensing low-order aberrations (tip, tilt, focus, etc.).

Lyot stop

Pupil plane mask that blocks diffracted light after the focal plane mask to enhance stellar suppression.

mas (milliarcsecond)

10^{-3} arcsecond; where 1 arcsecond is equal to 1/206265 radians.

NCPA (non-common path aberrations)

Aberrations differing between science image and WFS paths; require calibration or post-processing.

OAE/OAP (off-axis ellipsoidal/parabolic mirror)

Reflective mirrors formed as off-axis sections of an ellipsoid or paraboloid; used as achromatic relays in high-contrast instruments like SPIDERS and CAL 2.0.

OPD (optical path difference)

Difference in optical path length between two beams in an interferometer; sets fringe phase.

pc (parsec)

The distance at which 1 AU subtends 1 arcsecond ($1\,\mathrm{pc} \approx 206265\,\mathrm{AU}$).

PDI (polarization differential imaging)

Differential imaging technique using polarization states to suppress unpolarized light and reveal polarized signals.

planet-to-star contrast

Flux (or intensity) ratio $C = F_{planet}(\lambda)/F_{star}(\lambda)$; wavelength-dependent (reflected visible light or thermal infrared emission).

PolMod (polarization modulator)

Mechanism within CAL 2.0 providing precise positioning and angular control of a polarization optic for calibration and science observations.

PSD (power spectral density)

Distribution of power versus spatial or temporal frequency (e.g., turbulence or surface error models).

PSF (point-spread function)

Optical system's spatial response to a point source; determines image core and surrounding structure, and is modified by aberrations.

PyWFS (pyramid WFS)

Pyramidal prism splits a converging beam into four pupils; quadrant intensity differences encode local slopes.

Rayleigh criterion

Classical resolution limit; first minimum of Airy disk intensity at $\theta \approx 1.22\,\lambda/D$.

RDI (reference differential imaging)
Differential imaging technique using reference-star images to model and subtract starlight.

RMS (root-mean-square)
Quadratic mean of deviations quantifying variation amplitude (e.g., phase RMS).

RSS (root-sum-square)
Quadrature combination of uncorrelated error terms (e.g., WFE budget).

RTC (real-time computer)
Low-latency control computer for the AO system; applies calibrations, performs wavefront reconstruction, and commands the DM with deterministic timing.

SCC (self-coherent camera)
A focal plane wavefront sensing technique using a pinhole reference in the Lyot plane to fringe speckles for coherent calibration in real-time and post-processing.

SCExAO (Subaru Coronagraphic Extreme Adaptive Optics)
High-contrast imaging platform at Subaru referenced as an AO instrument.

SDI (spectral differential imaging)
Differential imaging technique using wavelength diversity (e.g., spectral data cube from IFS or IFTS) to disentangle speckles from companions.

SF (safety factor)
Dimensionless margin against mechanical failure; ratio of allowable (e.g., yield) stress to the maximum applied stress: $\mathrm{SF} = \sigma_{\mathrm{allow}}/\sigma_{\mathrm{applied}}$.

SHWFS (Shack–Hartmann WFS)
Lenslet array that forms a spot pattern; local slopes from spot displacements enable pupil plane phase reconstruction.

SNR (signal-to-noise ratio)
Ratio of signal to noise; quantifies measurement quality.

speckles
Residual starlight structures in the focal plane from phase/amplitude aberrations and diffraction; $\sim \lambda/D$ scale, time and wavelength-dependent, and can mimic point sources.

SPHERE (Spectro-Polarimetric High-contrast Exoplanet REsearch)
An instrument on the Very Large Telescope (VLT), designed for direct imaging and characterization of exoplanets.

SPIDERS (Subaru Pathfinder Instrument for Detecting Exoplanets & Retrieving Spectra)
Prototype instrument combining IFTS with focal plane wavefront sensing and correction for exoplanet imaging and characterization.

SR (Strehl ratio)
Ratio of aberrated to ideal PSF peak; for small aberrations $S \approx \exp(-(2\pi\,\mathrm{WFE}/\lambda)^2)$.

STARLITE (Superluminous Tomographic Atmospheric Reconstruction with Laser Beacons for Imaging Terrestrial Exoplanets)
Mission concept using satellite laser beacons to enable atmospheric tomography for high-contrast ground-based imaging.

ULSOC (ultra-low speed optical chopper)
Ultra-low speed optical chopper providing stable fringe modulation for the SCC and CDI post-processing.

WFE (wavefront error)
Departure of an optical wavefront from an ideal reference wavefront.

WFS (wavefront sensor)
Sensor that measures local wavefront slopes or phase/amplitude (e.g., Shack–Hartmann, pyramid, SCC) for AO correction.

Zernike polynomials
Orthogonal basis on the unit disk used to represent wavefront aberrations (low- to high-order modes).

ZPD (zero optical path difference)
The position in an interferometer where the optical path lengths of the two arms are equal, corresponding to the interferogram centre burst.

Chapter 1

Introduction

Studying Jupiter-like and Earth-like planets around nearby Sun-like stars offers a unique opportunity to understand our cosmic origins and anticipate our future trajectory in the universe. Analyzing the absorbed, emitted, and reflected light from a broad range of exoplanets, from large Jovian giants to small terrestrial worlds, enables the characterization of their atmospheric chemistry and the search for biological markers that may indicate habitability or signs of life [1]. Direct imaging and spectral characterization of these planets help address fundamental questions in astronomy, including how planetary systems form and evolve, the conditions required for life, and the uniqueness of Earth. These investigations are essential for understanding planetary evolution and guiding the ongoing search for life beyond our solar system.

Despite the immense scientific potential of directly imaging exoplanets, several major observational challenges persist. The apparent brightness of a stellar system decreases with the square of the distance (flux $\propto$ distance^{-2}), reducing the total signal available for detection. Independently, the brightness contrast between an exoplanet and its host star at visible wavelengths is extreme, often on the order of $F_{\text{Earth}}/F_{\text{Sun}} \sim 10^{-10}$ [2], making it difficult to isolate the planetary signal. Additionally, the angular separation between a planet and its star, as observed from Earth, is typically very small and often falls below the diffraction limit of even the largest 10 meter telescopes. These difficulties are further compounded by Earth's atmosphere, which absorbs, distorts, and scatters incoming light. Combined, these factors make the direct detection of Jupiter-like and Earth-like exoplanets using conventional imaging techniques exceptionally difficult.

To overcome these limitations, significant advancements in optical science have emerged across both astronomy and engineering. These innovations have led to the

discovery of thousands of exoplanets in recent decades through a combination of indirect and direct detection methods. Indirect techniques, such as monitoring the dimming of a star during a planetary transit or measuring the gravitational influence of a planet on its host star, have proven highly effective at detecting a wide range of exoplanets, from small terrestrial bodies to large Jovian giants. Direct imaging techniques, on the other hand, provide spatially resolved observations of planetary systems, allowing for simultaneous detection and atmospheric characterization. While direct imaging has successfully captured dozens of young Jupiter-like exoplanets at wide separations, imaging mature Jupiter-like and Earth-like planets in the habitable zones of nearby Sun-like stars remains beyond current observational capabilities.

Although space-based imaging holds tremendous promise, implementing advanced technologies in space requires substantial resources and human capital. As a result, the development of the next generation of extremely large telescopes continues to favor ground-based solutions. Even with state-of-the-art systems on the world's most powerful telescopes, astronomers remain fundamentally limited by light availability and the telescope's diffraction limit [3]. Achieving diffraction-limited imaging for high-contrast, small-separation targets requires not only real-time correction of wavefront errors during observations, but also the use of advanced post-processing techniques to suppress residual starlight and extract faint planetary signals from the surrounding noise [2].

In this dissertation, I examine the challenges of direct exoplanet imaging and present my contributions to the development and optimization of advanced astronomical instrumentation. By exploring both current and next-generation direct imaging technologies, this work aims to advance the frontiers of observational astronomy and move closer to the first direct detection of mature Jupiter-like and Earth-like exoplanets in nearby stellar systems.

Agenda

The contents of this dissertation are organized as follows:

Chapter 1 establishes the scientific motivation for direct exoplanet imaging and introduces the foundational principles of observational astronomy, wavefront sensing, and high-contrast imaging. Together, these elements provide the theoretical basis for the instrumentation and methods explored in the following chapters.

Chapter 2 describes the design and development of the SPIDERS instrument, a modular and compact testbed deployed on the Subaru Telescope. The chapter details its system architecture, which includes the structural frame, hexapod alignment mechanism, ultra-low speed optical chopper, and imaging Fourier transform spectrometer, with a focus on how these components support the validation of focal plane wavefront sensing and spectral retrieval techniques.

Chapter 3 outlines the CAL 2.0 upgrade to the Gemini Planet Imager, a facility-class instrument developed through international collaboration. It focuses on the on-going implementation of upgraded optomechanical subsystems that combine proven components with newly developed hardware, particularly the focal plane mask wheel, polarization modulator, and ultra-low speed optical chopper.

Chapter 4 introduces STARLITE, a conceptual satellite constellation for atmospheric tomography. It presents feasibility studies encompassing constellation design and space mission architecture, as well as ground-based reconstruction simulations used to assess the optical performance for future applications in exoplanet imaging.

Chapter 5 concludes the dissertation by summarizing the key contributions and outlining potential directions for future research in high-contrast imaging, system integration, and instrumentation for adaptive optics.

1.1 Motivation for Directly Imaging Exoplanets

The study of exoplanetary systems addresses fundamental questions about the nature of the universe, such as: Are we alone in the cosmos? What conditions are necessary for life to develop? By directly imaging exoplanets, astronomers seek to uncover insights into the formation, composition, and potential habitability of planets beyond our solar system. This method of observation allows for the detailed characterization of exoplanetary atmospheres, surfaces, and potential biological markers, which could provide crucial evidence for the existence of life beyond Earth.

1.1.1 Exoplanet Classification, Formation, and Evolution

An **exoplanet**, or extrasolar planet, is traditionally defined as *a celestial body that orbits a star other than the Sun, residing within stellar systems outside our own* [4, 5]. For an object to be classified as an exoplanet, it must meet the following criteria:

- **Upper Mass Limit:** The object must not possess sufficient mass to sustain deuterium fusion, which defines an upper mass limit of approximately 13 Jupiter masses (M_J). Objects exceeding this mass threshold can be classified as brown dwarfs, if they are capable of undergoing limited nuclear fusion.
- **Lower Mass/Size Limit:** The object must have enough mass for self-gravity to maintain hydrostatic equilibrium in an orbit around its host star and to clear the neighborhood around the object's orbit. No limit is usually put on this, but examples from our own solar system can provide a reference - e.g. Mercury is 0.055 Earth masses ($M_\oplus$).

The observed diversity in exoplanet mass, composition, and orbital characteristics within these limits provides valuable insights into planetary formation, evolution, and the potential for habitable environments. This variation also underscores the complexity of planetary systems, prompting the identification of distinct categories that aid in classifying exoplanets. These categories help focus our understanding of the broad variety of planetary systems across the universe.

Categories of Exoplanets

Exoplanets are categorized based on a combination of their physical properties and orbital characteristics, informed by both observational data and theoretical models. The primary categories include:

- **Gas Giants:** Large planets predominantly composed of hydrogen and helium, similar to Jupiter or Saturn. These planets are commonly found both at significant orbital separations from their host stars and in close-in configurations, such as "hot Jupiters".
- **Ice Giants:** Planets of intermediate mass, containing substantial amounts of water, ammonia, and/or methane, similar to Neptune or Uranus.
- **Super-Earths:** Planets with masses greater than Earth but smaller than Neptune, exhibiting a range of compositions, from rocky to gaseous, and possibly possessing atmospheres capable of supporting life.
- **Terrestrial Planets:** Smaller, rocky planets such as Earth and Mars, typically located within or near the habitable zone of their parent stars, where conditions may allow for liquid water to exist on their surfaces (see §1.1.2).
- **Emerging Subcategories:** New classifications, such as mini-Neptunes and Earth analogs, are emerging to refine exoplanet categorization based on observed properties like atmospheric composition, density, and temperature.

This classification is essential for understanding exoplanetary diversity and enabling more precise identification of planets with potential habitability. By leveraging these categories, we can refine the search for Earth-like planets and assess their capacity to support life, a key aspect of advancing exoplanet exploration and the broader study of planetary systems.

Modes of Formation

Exoplanet formation occurs within the dynamic environment of protoplanetary disks surrounding young stars [6]. These disks form from the gas and dust left over after star formation, eventually settling into a flat, rotating structure. Two primary mechanisms are recognized as the dominant pathways for planet formation, each driven by distinct physical processes and conditions:

- **Core Accretion (Cold Start):** Core accretion is the dominant theory for the formation of rocky planets and gas giants in relatively close orbits. This process begins with the slow coagulation of dust and ice grains within the protoplanetary disk, forming solid planetesimals that collide and grow into planetary cores. Once these cores reach a critical mass, they gravitationally attract and accrete

gas from the surrounding disk, forming a dense atmosphere. Core accretion is most efficient in regions of the disk with high solid material density, and it explains the formation of both terrestrial planets and gas giants.

- **Gravitational Instability (Hot Start):** Gravitational instability operates in the outer regions of massive protoplanetary disks, where local instabilities cause rapid collapse under their own gravity. This mechanism bypasses the slow process of core growth and directly forms massive, gas-rich planets. Gravitational instability is critical for explaining the formation of distant gas giants and some brown dwarfs.

The mechanisms of core accretion and gravitational instability are considered leading scenarios for planet formation, with core accretion thought to dominate in closer orbits and gravitational instability potentially contributing to the formation of distant gas giants. Continued study of these processes remains essential for developing a deeper understanding of planetary system evolution.

Planetary Formation and Evolution

The formation and evolution of planets, encompassing both the core accretion and gravitational instability models, progress over characteristic timescales, transitioning from dynamic, high-temperature environments over millions of years (Myr) to more stable conditions that may eventually support life over billions of years (Gyr). Each stage is characterized by specific durations and temperature regimes [7, 8, 9, 10]:

- **Protoplanetary Disk ($<$ 1 Myr):** This initial phase involves the cooling of the circumstellar disk, dust coagulation, and the formation of planetesimals. Inner disk temperatures range from 1000 to 2500 K, while the outer disk remains significantly cooler ($<$1000 K), depending on the distance from the host star.

- **Planetesimal and Core Formation (0.1–10 Myr):** Dust grains collide and grow into planetesimals, which then accrete material to build planetary cores. Temperatures during this phase vary with location in the disk, typically ranging from 300 to 2500 K.

- **Gas Accretion (0.1–10 Myr):** Once formed, cores begin slowly accreting gas, with growth limited by cooling efficiency. If the core mass remains below a critical threshold (typically $\lesssim$100 $M_\oplus$), accretion stays gradual, forming small

to intermediate-mass planets. Above this threshold, runaway gas accretion can occur, rapidly forming gas giants with massive H-He envelopes. Disk location and accretion rate determine local temperatures, which can range from 300 to 2000 K.

- **Planetary Cooling (10 Myr–1 Gyr):** Following formation, planetary interiors and atmospheres gradually cool and stabilize. This phase is characterized by a decline in temperature from several hundred kelvin down to as low as 50 K, with typical atmospheric temperatures in the range of 50 to 1200 K.
- **Stabilized Environment ($>$ 1 Gyr):** Over time, planetary environments reach equilibrium. For planets within the habitable zone (see §1.1.2), surface temperatures typically stabilize between 200 and 300 K, which can support liquid water and potentially life. Outside this zone, temperatures may range from 50 to 500 K, depending on orbital distance and atmospheric composition. This stage reflects the development of a stable and mature planetary system.

This progression offers valuable insights into the diversity of exoplanetary systems and the factors that may influence their potential to support life. Understanding these stages is also important for focusing direct imaging efforts (discussed in §1.2.1) and for assessing planetary habitability under varying conditions.

1.1.2 The Habitable Zone Around a Star

Liquid water is widely considered essential for supporting life, making its presence a fundamental criterion in defining planetary habitability. The region around a star where such conditions may exist is referred to as the habitable zone (HZ). This region generally corresponds to orbital distances where a planet can maintain surface temperatures between 0 and 100°C [4]. The extent of the habitable zone depends on stellar luminosity, atmospheric composition and pressure, and surface albedo, all of which affect energy balance and temperature regulation. To remain habitable, a planet must achieve equilibrium between incoming radiation from the star and outgoing thermal emission.

Variation in the habitable zone across stellar systems is determined largely by stellar type. Stars are generally classified by spectral type in the sequence O, B, A, F, G, K, and M, representing a progression from hot, massive stars to cool, low-mass stars. O and B stars are extremely luminous with short lifespans. A-type stars are

also hot and bright but live slightly longer. F and G stars, including the Sun, have moderate temperatures and lifetimes suitable for long-term planetary development. K and M stars are cooler and smaller but live significantly longer, making them especially relevant to planetary habitability studies. Most stars fall within the main sequence, where hydrogen fusion occurs in a stable phase.

Differences in luminosity across these types directly affect the location of the habitable zone. Hotter stars have their habitable zones located farther out, while cooler stars host much closer zones. Table 1.1 summarizes representative HZ distance, temperature, and mass for main-sequence A through M-type stars, based on published models [11, 12, 13, 14, 15, 16] and the scaling relation $d_{HZ} \propto \sqrt{L/L_{\odot}}$ [17], where L is stellar luminosity, $L_{\odot}$ is the solar luminosity, and d_{HZ} is the distance in astronomical units (AU, where 1 AU is the average distance from Earth to the Sun, ∼149,600,000 km).

Table 1.1: Properties of main-sequence stars by spectral type, including approximate habitable zone distance, surface temperature, and stellar mass (in solar masses, $M_{\odot}$).

Star Type	d_{HZ} **(AU)**	**Temperature (K)**	**Mass** ($M_{\odot}$)
A	$2.9 \sim 10.4$	$7{,}500 \sim 10{,}000$	$1.65 \sim 2.8$
F	$1.5 \sim 2.4$	$6{,}000 \sim 7{,}500$	$1.15 \sim 1.65$
G	$0.95 \sim 1.7$	$5{,}300 \sim 6{,}000$	$0.95 \sim 1.15$
K	$0.5 \sim 1.1$	$3{,}900 \sim 5{,}300$	$0.55 \sim 0.95$
M	$0.08 \sim 0.3$	$2{,}500 \sim 3{,}900$	$0.16 \sim 0.55$

While the habitable zone serves as a useful guideline for identifying potentially life-supporting planets, it remains a simplified model. Greenhouse effects, cloud cover, and other atmospheric properties can shift the effective boundaries. Moreover, stars such as O, B, and A types, despite having wide habitable zones, are typically not considered viable hosts for life. Their high ultraviolet and X-ray radiation levels, combined with short lifespans, limit the potential for stable planetary environments. By comparison, M-dwarfs, although long-lived and common, pose significant challenges for habitability due to the close proximity of their habitable zones, which exposes orbiting planets to intense stellar flares, high levels of ultraviolet and X-ray radiation, and increases the likelihood of tidal locking.

1.1.3 Challenges and Strategies in Exoplanet Research

Despite major advances in exoplanet discovery, key challenges continue to hinder the detection and detailed characterization of these distant worlds. Addressing these obstacles is essential for advancing direct imaging and depends on continuous innovation in instrumentation and observational techniques.

- **Brightness Contrast:** The overwhelming brightness of host stars compared to their planets remains one of the most significant hurdles. In visible wavelengths, stellar light can outshine planetary signals by factors up to 10^{10} [4, 18]. Overcoming this contrast requires advanced high-contrast imaging methods, such as coronagraphy and wavefront control, supported by post-processing algorithms that isolate faint planetary light from stellar glare.

- **Angular Separation:** Exoplanets typically appear very close to their host stars in the sky, with angular separations often measured in milliarcseconds. Resolving such fine separations requires large-aperture telescopes along with high-precision optical systems capable of maintaining near-diffraction-limited performance.

- **Atmospheric Turbulence:** Ground-based observatories face distortion from atmospheric turbulence, which induces phase variations that blur and scatter incoming light. Adaptive optics systems correct these wavefront errors in real-time, improving image sharpness and approaching diffraction-limited performance.

- **Technological and Logistical Constraints:** Both ground-based and space-based observatories demand highly specialized, high-precision optics developed over many years with considerable technical and human investment. Space-based platforms such as HST [19] and JWST [20] bypass atmospheric effects but pose their own challenges: extremely high development costs, decades-long design cycles, stringent engineering requirements, and finite mission lifespans, making these missions inherently resource-intensive.

- **Data Complexity and Processing:** Modern imaging systems generate vast data volumes that require real-time control and extensive computational post-processing. Extracting weak exoplanet signals embedded in stellar noise relies on advanced algorithms and high-performance computing architectures.

- **Engineering Complexity and Precision:** Mechanical and thermal stability are crucial for astronomical instruments. Telescopes operate on meter scales yet require optical alignment accuracy in the micron to nanometer range. Achieving this level of precision while managing vibration, structural flexure, and thermal expansion under variable conditions presents significant engineering challenges.

Overcoming these barriers requires a multidisciplinary approach integrating optical engineering, computational science, and observational expertise. Key strategies for mitigating these obstacles include:

- **Coronagraphy:** Coronagraphs suppress starlight to enhance the visibility of nearby planets. Innovations such as phase-induced amplitude apodization (PIAA) and vortex designs improve suppression through advanced phase and amplitude mask configurations [21, 22], as detailed in §1.3.6.

- **Post-processing Techniques:** Techniques like angular differential imaging (ADI) and reference differential imaging (RDI) remove residual speckles and enhance contrast by combining and subtracting multiple observations [23, 24]. These methods are covered further in §1.3.8.

- **Adaptive Optics:** Real-time wavefront correction mitigates atmospheric distortion, enabling sharper imaging. Continuous improvements in adaptive optics have made it possible to directly image gas giants and brown dwarfs, and will be key to the success of next-generation ground-based telescopes [25], discussed in §1.3.

Continued advancement in these areas is essential to push the limits of exoplanet detection and work toward imaging Earth-like planets in the habitable zones of nearby stars.

1.1.4 Methods of Exoplanet Detection and Characterization

In response to the challenges posed by vast distances, faint signals, and complex environments, a range of techniques have been developed to detect and characterize exoplanets. These methods fall into two broad categories: indirect methods, which infer the presence of exoplanets through their gravitational or radiative effects on their host stars or surroundings; and direct methods, which aim to capture and analyze

light emitted or reflected by the planets themselves. Additionally, advanced techniques such as spectroscopy and polarimetry enable detailed studies of atmospheric and physical properties, providing insights on composition, structure, and potential habitability [4].

Indirect Methods

Indirect detection relies on observing the effects of exoplanets on their host stars or surrounding environments. Key methods include:

- **Radial Velocity:** This technique detects the gravitational pull of a planet on its host star, resulting in periodic Doppler shifts in the star's spectral lines. It is particularly effective for determining a planet's minimum mass and orbital parameters. This method enabled the landmark discovery of 51 Pegasi b, the first Jupiter-mass exoplanet orbiting a Sun-like star [26].

- **Transit Photometry:** By measuring periodic dips in stellar brightness caused by a planet passing in front of its star, this technique yields the planet's size, orbital period, and, in favorable cases, atmospheric composition. Transmission spectroscopy during transits can detect molecular signatures such as water, methane, or carbon dioxide. The first detailed atmospheric characterization via transit observations was achieved for HD 209458 b [27].

- **Astrometry:** This method involves measuring slight positional shifts in a star due to the gravitational influence of one or multiple orbiting planets. It provides accurate measurements of orbital inclinations and true planet masses. Gaia Data Release 3 applied high-precision astrometry to detect the orbital motion of giant exoplanets, including HD 81040 b, enabling robust mass and inclination estimates [28, 29].

- **Gravitational Microlensing:** This technique identifies temporary brightening of background stars caused by the gravitational field of a star-planet system. It is especially effective for detecting distant or free-floating planets. OGLE-2005-BLG-390Lb, a cold, low-mass planet, was discovered this way, highlighting the method's sensitivity to distant Earth-like worlds [30].

- **Other Methods:** Additional approaches, including disk kinematics, transit/eclipse timing variations, and orbital brightness modulation, capture subtle

changes in stellar motion, light curves, or timing to infer planetary presence. For example, transit timing variations confirmed the Kepler-9 system, revealing gravitational interactions in a multi-planet configuration [31].

Direct Methods

Direct methods aim to isolate and analyze the light from exoplanets themselves. These include:

- **Direct Imaging:** This approach captures light directly from an exoplanet, enabling measurements of brightness and atmospheric properties. High-contrast techniques such as adaptive optics, coronagraphy, and post-processing are crucial to overcoming the brightness contrast between stars and planets. Infrared imaging is particularly effective for detecting young or hot planets. The first direct image of multiple exoplanets was obtained around HR 8799 [25].

- **Polarimetry:** By measuring the polarization of light scattered by a planet's atmosphere or surface, polarimetry reveals atmospheric composition, cloud structures, and potential surface features such as oceans or ice. Since starlight is largely unpolarized, the polarized component from a planet stands out. Combined with imaging, polarimetry can enhance sensitivity by suppressing residual starlight. Polarimetric imaging constrained Beta Pictoris b's orbit and revealed a misaligned inner debris disk [32].

- **Spectroscopy:** High-resolution spectroscopy of directly imaged or transiting planets reveals molecular absorption features such as water, methane, oxygen, and carbon dioxide — critical for assessing habitability, temperature, and atmospheric dynamics. Spectroscopy can also uncover rotation rates and cloud structures via Doppler broadening. JWST's detection of water vapor and other molecules in WASP-39b's atmosphere demonstrated the power of transmission spectroscopy for atmospheric characterization [33].

These complementary methods provide a comprehensive framework for studying exoplanetary systems. Indirect techniques yield statistical insights into planetary populations and orbital architectures, while direct methods allow for in-depth studies of individual planets. Follow-up observations using spectroscopy and polarimetry further refine our understanding by revealing atmospheric and surface characteristics. Together, these tools form a robust foundation for exploring planet formation, evolu-

tion, and habitability.

1.1.5 Confirmed and Nearby Exoplanets

The continuous refinement of indirect and direct detection methods has resulted in a rapidly expanding catalog of confirmed exoplanets. Figure 1.1 illustrates the distribution of confirmed exoplanets categorized by the detection method. This broad view underscores the contributions of various techniques to the growing understanding of planetary systems. Direct imaging, while limited in scope, has primarily identified massive gas giants at wide orbital separations, highlighting both its successes and constraints. Despite capturing less than 2% of all confirmed exoplanets, direct imaging has been instrumental in revealing the atmospheres, compositions, and orbital dynamics of these distant worlds.

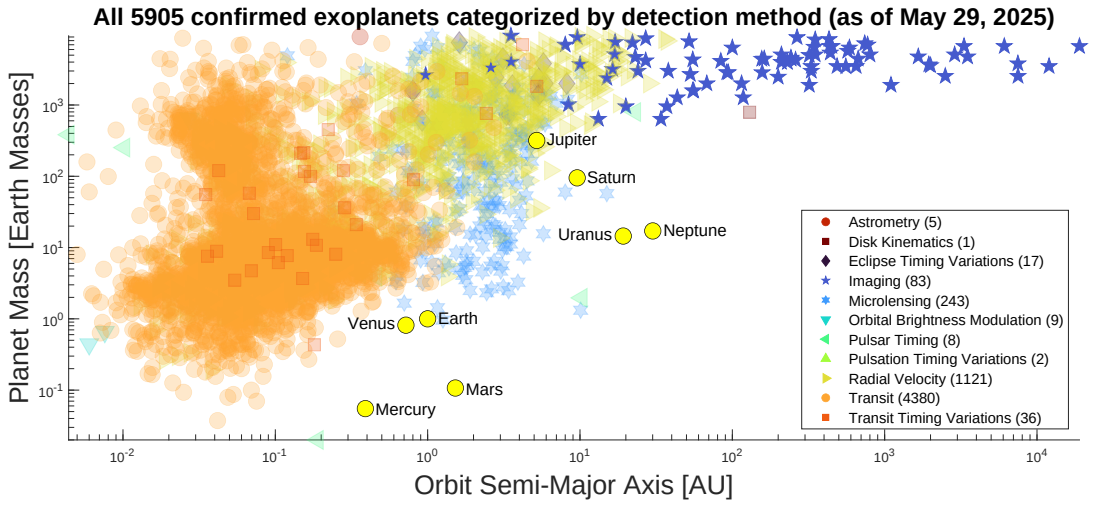

Figure 1.1: Planet mass versus orbital distance of current confirmed exoplanets sorted by detection method using data retrieved from the NASA Exoplanet Archive [34]. Only planets with a reported mass and semi-major axis are plotted, while all detections are counted in the legend categories and in total.

Although recent advances in both detection and characterization have significantly expanded the exoplanet catalog, many challenges remain. The majority of confirmed planets have been identified using indirect methods, which provide robust population statistics but offer limited spatial and spectral resolution. While direct imaging delivers high-fidelity data on individual planets and their atmospheres, it is currently restricted to detecting massive gas giants in wide orbits. To achieve direct imaging

of Earth-like planets in their stars' habitable zones, considerable advancements in adaptive optics, coronagraphy, and post-processing algorithms are required.

Nearby and Potentially Habitable Exoplanets

From the rapidly expanding catalog of known exoplanets, a subset of nearby worlds emerges as promising candidates for future direct imaging. These planets, typically discovered through indirect methods, span Earth- to Jupiter-like masses and radii that reside within the habitable zones of their host stars. While several M-type stars host such planets, their close orbital separations increase the likelihood of tidal locking and exposure to intense stellar activity, which may limit long-term habitability, as discussed in §1.1.2. Accordingly, the list presented here emphasizes F, G, and K-type stars, which offer more stable and extended habitable environments. Table 1.2 presents nearby systems ordered by increasing distance from Earth in parsecs (where 1 parsec = 206,265 AU ≈ 3.26 light years), each containing at least one planet within habitable zone boundaries (defined in Table 1.1).

Table 1.2: Exoplanetary systems within the habitable zone, ordered by increasing distance from Earth. Multi-planet systems are grouped into single rows, with lowercase letters (b, c, d, etc.) identifying planets and comma separated parameters. Planets within the habitable zone are shown in green.

Planet Name	Distance (parsecs)	Planet Mass ($M_\oplus$)	Planet Radius ($R_\oplus$)	Semi-Major Axis (AU)	Host Star Spectral Type
GJ 887 b, c	3.29	4.20, 7.60	1.88, 2.67	0.07, 0.12	M1 V
tau Ceti e, f, g, h	3.60	3.93, 3.93, 1.75, 1.83	1.81, 1.81, 1.18, 1.19	0.54, 1.33, 0.13, 0.24	G8.5 V
Wolf 1061 b, c, d	4.31	1.91, 3.41, 7.70	1.21, 1.66, 2.69	0.04, 0.09, 0.47	M3.5
HD 20794 b, d, e, f	6.00	2.70, 4.80, 4.77, 5.82	1.45, 2.04, 2.03, 2.28	0.13, 0.36, 0.51, 1.35	G6 V
HD 69830 b, c, d	12.56	10.20, 11.80, 18.10	3.17, 3.46, 4.45	0.08, 0.19, 0.63	K0 V
HD 147513 b	12.90	385.00	13.70	1.32	G5 V
HD 40307 b, c, d, f, g	12.94	4.00, 6.60, 9.50, 5.20, 7.10	1.83, 2.46, 3.04, 2.13, 2.56	0.05, 0.08, 0.13, 0.25, 0.60	K2.5 V
HD 128311 b, c	16.33	562.24, 1204.26	13.50, 13.00	1.08, 1.74	K0
HD 10647 b	17.34	298.75	13.80	2.02	F9 V
HD 216520 b, c	19.55	10.26, 9.44	3.18, 3.03	0.20, 0.53	K2
16 Cygni B b	21.14	565.74	13.50	1.66	G3 V
HD 210277 b	21.30	410.00	13.60	1.13	G0 V
HIP 57274 b, c, d	25.86	6.36, 130.00, 167.40	2.40, 14.20, 14.20	0.07, 0.18, 1.01	K4 V
HD 60532 b, c	25.97	336.90, 797.75	13.80, 13.30	0.77, 1.60	F6 IV
HD 128356 b	26.15	282.87	13.90	0.87	K3 V

As direct imaging capabilities advance, the nearby systems highlighted here represent compelling targets for observing planets in habitable zones across a range of evolutionary stages. They offer strong potential for detecting atmospheric biomarkers and deepening our understanding of planetary formation, evolution, and long-term habitability beyond the solar system.

1.1.6 Identifying Biomarkers Through Spectroscopy

Spectroscopy is a cornerstone of modern astronomy, offering a detailed analysis of light emitted, absorbed, or reflected by celestial bodies. By dispersing light into its component wavelengths, critical information about an object's composition, temperature, density, and motion can be revealed. In the context of exoplanet research, spectroscopy enables the study of planetary atmospheres, facilitating the detection of molecular signatures, temperature profiles, and potential biological markers (biomarkers) that may suggest the presence of life.

Biomarkers such as oxygen (O_2), ozone (O_3), methane (CH_4), water (H_2O), and carbon dioxide (CO_2) are among the key indicators used to evaluate a planet's potential habitability. Figure 1.2 shows a transmission spectrum of an Earth-like atmosphere, highlighting key molecular features relevant to evaluating exoplanet habitability.

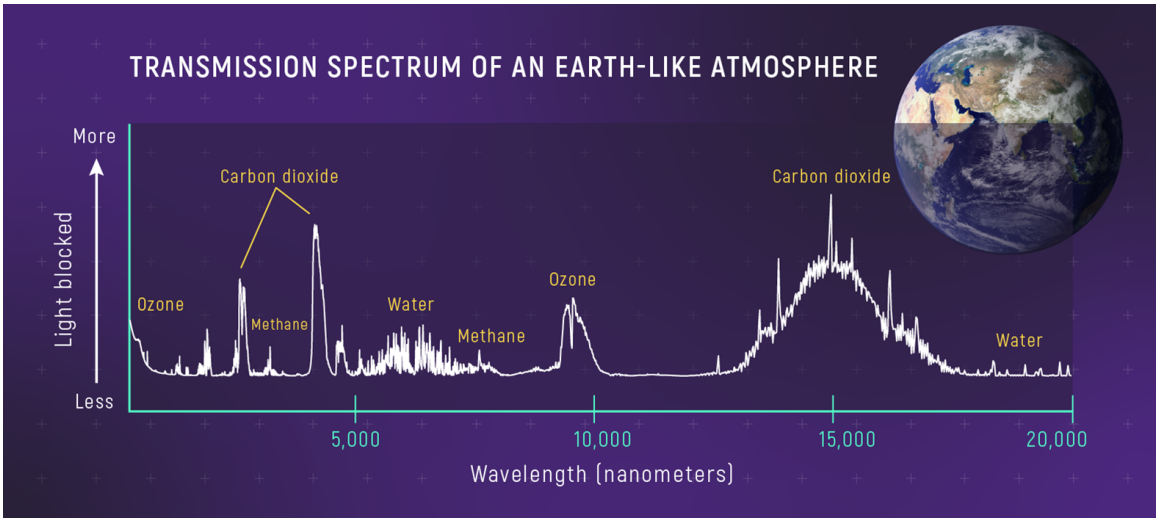

Figure 1.2: Transmission spectrum of an Earth-like atmosphere, showing absorption features from molecules such as ozone (O_3), water vapor (H_2O), carbon dioxide (CO_2), and methane (CH_4). Image credit: NASA, ESA, CSA, Leah Hustak (STScI) [35].

Atmospheric characterization for exoplanet research relies on two primary spectroscopic techniques:

- **Transmission Spectroscopy:** This technique analyzes starlight filtered through a planet's upper atmosphere during transit, revealing its composition at high altitudes. Near-surface conditions are often obscured by absorption, scattering, and cloud opacity.

- **Emission Spectroscopy:** This method examines the thermal radiation emitted by the planet, revealing insights into its surface temperature, atmospheric conditions, and weather patterns.

Spectroscopy remains a vital technique in exoplanet research, providing essential insights into the atmospheric composition of distant worlds. Through methods like transmission and emission spectroscopy, biomarkers indicative of potential habitability such as water vapor, methane, and oxygen can be identified. As spectroscopic technology progresses, our ability to characterize exoplanet atmospheres and assess their potential for supporting life will continue to improve, furthering our understanding of planets beyond our solar system.

1.1.7 Current Innovations in Direct Imaging Technologies

Recent advancements in technology have significantly enhanced the capabilities of direct imaging, pushing the boundaries of our ability to study exoplanets in unprecedented detail. These innovations have expanded the range of observable exoplanets by utilizing advanced techniques such as adaptive optics, coronagraphy, and post-processing. Below, some key imaging systems currently deployed are reviewed, highlighting their technical capabilities, achievements, and contributions to the ongoing efforts in exoplanetary science.

Hubble Space Telescope (HST)

Although limited by its smaller 2.4 m aperture, the Hubble Space Telescope (HST) remains pivotal in exoplanet imaging, particularly in the ultraviolet, visible, and near-infrared (0.2 to 1.7 μm). Operating in orbit at 520 km above Earth, Hubble achieves contrast levels down to 10^{-6}. Its primary advantage is operating above the atmosphere, avoiding turbulence and enabling stable, high-precision imaging. Since its 1990 launch, Hubble's development and operation have totaled approximately $16 billion USD [19, 36].

Gemini Planet Imager (GPI)

The Gemini Planet Imager (GPI), located at the 8.1 m Gemini South Observatory in Chile (until 2020, see §3), employs high-contrast imaging techniques, adaptive optics, and coronagraphy to directly image exoplanets in the near-infrared spectrum. With additional polarimetric and spectroscopic capabilities, GPI allows for the detailed

study of exoplanets, their atmospheres, and circumstellar debris disks. Operating between 0.9 and 2.4 μm, GPI achieves contrast ratios as low as 10^{-6}. The system has made significant discoveries, such as the direct imaging of 51 Eri b, enhancing our understanding of exoplanetary atmospheres and debris disks. The estimated cost for commissioning GPI was approximately $24 million USD [25, 37, 38].

SPHERE (Spectro-Polarimetric High-contrast Exoplanet REsearch)
SPHERE, located at the 8.2 m Very Large Telescope (VLT) in Chile, is an advanced adaptive optics system with a coronagraph designed for high-contrast direct imaging. Operating in the wavelength range from 0.5 to 2.3 μm, SPHERE provides contrast capabilities down to 10^{-6}, conducting high-resolution polarimetric and spectroscopic observations of exoplanet atmospheres and debris disks. The estimated cost of SPHERE is over $100 million USD [39, 40].

James Webb Space Telescope (JWST)
Launched in 2021, the 6.5 m James Webb Space Telescope (JWST) is a joint NASA /ESA/CSA mission designed for infrared observations spanning 0.6 to 28 μm. Operating from space, it avoids atmospheric turbulence and thermal background noise, providing the image stability and sensitivity needed for high-contrast exoplanet studies with contrast levels down to 10^{-6}, without real-time correction. JWST combines coronagraphy and slitless spectroscopy to directly image and analyze exoplanets, enabling detection of key atmospheric molecules such as water vapor. The mission launched at a cost exceeding $10 billion USD [20].

Direct imaging systems such as Hubble, GPI, SPHERE, and JWST have significantly advanced exoplanet science by enabling the detection of atmospheric features and characterizing circumstellar environments. These instruments have played a central role in identifying key molecular signatures, including oxygen, methane, and water vapor, essential for assessing habitability. Continued progress in adaptive optics, coronagraphy, and image processing is expanding observational reach. However, directly imaging Jupiter and Earth-like exoplanets in reflected visible light remains a major challenge, with contrast requirements of $\sim 10^{-10}$ exceeding current capabilities and driving the development of future imaging technologies.

1.2 Observational Foundations for Direct Imaging

In observational astronomy, directly detecting and characterizing exoplanets is a major challenge due to the significant brightness disparity between the planet and its host star, their small angular separations, and the limitations of current technology. This section explores the key principles and methodologies for measuring important parameters, such as angular separation, the physical limits of telescopes, planet-to-star contrast ratios, stellar flux, and luminosity. It also examines how detector characteristics and spectroscopic strategies influence detection performance. Finally, concepts like integration time and signal-to-noise ratio are addressed in the context of planning and interpreting high-contrast observations.

1.2.1 Angular Separation and Limitations of a Telescope

The ability of a telescope to resolve distant celestial objects is fundamentally limited by diffraction, which sets a bound on the angular separation between distinguishable sources. This diffraction limit is determined by the telescope's aperture size and the wavelength of light, and it governs the resolution of features in astronomical observations. In addition, the concept of the inner working angle defines the smallest angular separation at which a telescope can detect faint objects, such as exoplanets, near a bright central star. Understanding these limits is crucial for optimizing observational strategies and designing high-resolution astronomical instruments capable of exploring the universe in detail.

Angular Separation

The angular separation formed by two celestial objects as observed from a given point can be described using trigonometry, and for large distances, this can be simplified using the small-angle approximation. When $a \ll d$, where a represents the separation between the objects, and d denotes the distance to the observer in the same units as a, the angular separation θ in radians is given by:

$$\theta = \tan^{-1}\left(\frac{a}{d}\right) \simeq \frac{a}{d} \tag{1.1}$$

This simplified relationship is illustrated below in Figure 1.3.

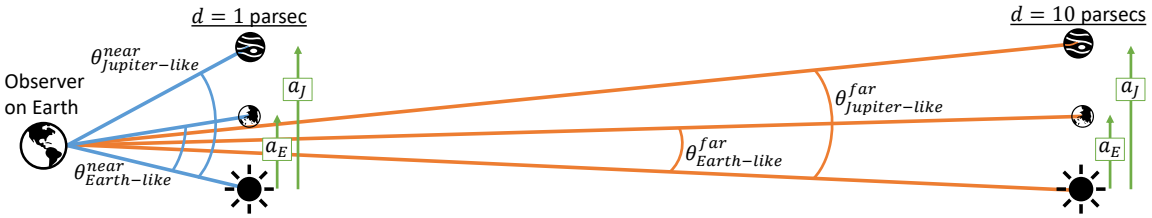

Figure 1.3: Illustration of how distance from the observer to the target and the separation between the objects define the angular separation.

Using the distances between the Earth and Sun (1 AU = 1/206265 parsecs) and Jupiter and the Sun (5.2 AU = 5.2/206265 parsecs), the angular separation can be determined from various distances (Table 1.3). These very small angles are typically expressed in milliarcseconds (mas), where 206,265 arcseconds equal one radian.

Table 1.3: Angular separation in milliarcseconds of a Jupiter- or Earth-like planet observed at various distances.

Distance [parsecs]		1	10	100	1000
Angular Separation θ [mas]	Jupiter-like	5060	506	51	5
	Earth-like	1000	100	10	1

As the distance between the two objects and the observer increases, the angular separation between them decreases, making them more difficult to distinguish. Achieving clear differentiation at these small scales requires an observer (or telescope) with sufficient angular resolution.

Diffraction Limit of the Telescope

The angular separation between an exoplanet and its host star can establish a baseline for a telescope's resolution requirements. This limitation arises from diffraction, where light traveling through an aperture limits clarity based on aperture size and wavelength [41]. The Rayleigh criterion quantifies this, defining the minimum angular separation in radians to distinguish two objects. The minimum diameter D of the telescope's primary mirror (aperture) is determined by rearranging this relationship into the following equation:

$$D \simeq 1.22\frac{\lambda}{\theta} \tag{1.2}$$

where λ is the wavelength and θ is the angular separation of two point sources. This relationship shows that two points are distinguishable if they have an angular separation of at least 1.22 λ/D between each other, entirely a function of the telescope size and observing wavelength. A visual representation of this effect is shown in Figure 1.4 below.

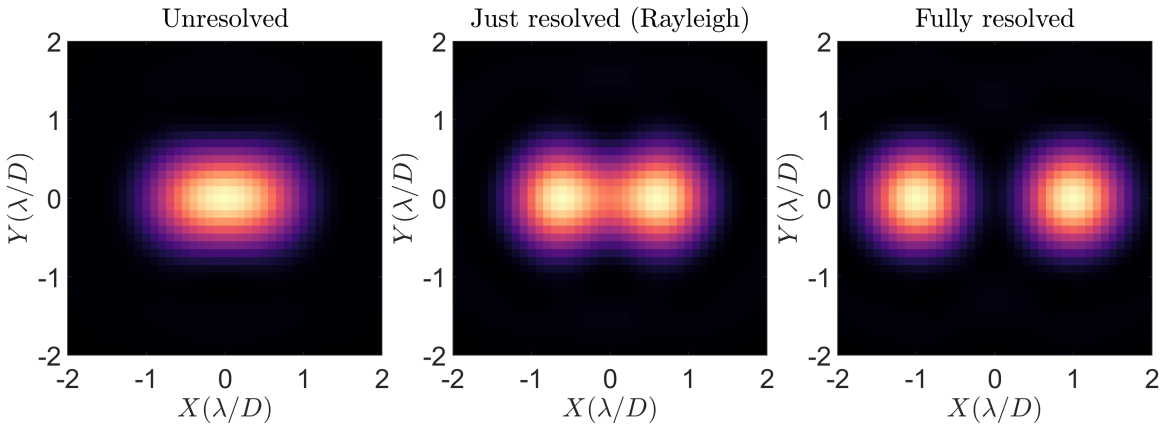

Figure 1.4: Two point sources of equal luminosity as observed through a diffraction-limited telescope at three angular separations: unresolved (left), just resolved (middle), and fully resolved (right). In the absence of other errors, this fundamental limit defines the smallest angular separation at which a telescope or imaging system can distinguish two closely spaced objects.

Using the angular separations defined in Table 1.3, the minimum telescope diameter required to resolve a nearby Jupiter or Earth-like exoplanet at 0.8 μm and 1.6 μm in a diffraction-limited imaging regime is determined in Table 1.4 below:

Table 1.4: Telescope diameter requirements for resolving Jupiter and Earth-like exoplanet-to-star separations at various distance. Existing telescopes are highlighted in green, while those not yet realized are shown in red.

Distance [parsecs]		1	10	30	100
Diameter req'd at 0.80 μm, D [m]	Jupiter-like	0.04	0.40	1.19	3.98
	Earth-like	0.20	2.01	6.04	20.13
Diameter req'd at 1.60 μm, D [m]	Jupiter-like	0.08	0.80	2.39	7.96
	Earth-like	0.40	4.03	12.08	40.26

While the theoretical limit for resolving two objects is defined for an idealized system, practical applications often restrict us from achieving this regime.

Inner Working Angle

A coronagraph is typically employed in exoplanet imaging systems as an optical instrument that effectively blocks the bright light of a star, allowing the detection of faint light emitted by nearby exoplanets, discussed in §1.1.3. Due to atmospheric turbulence and mechanical vibrations, the apparent position of the star can shift during an observation, leading to potential leakage of starlight around the coronagraph. To address this issue, coronagraphs are typically designed with a slightly larger coverage area, creating an inner working angle (IWA) that ensures the star's light remains effectively blocked even if its position fluctuates slightly between observations due to tracking/centring errors. Implementing and simulating a coronagraph system is discussed later in §1.3.6.

Using a reasonably sized coronagraph with an IWA of 3 λ/D, similar to those used on JWST [42], the angular separation of Jupiter and Earth-like exoplanets (from Table 1.3) with an inner limit imposed by the coronograph that is centred on a target host start is tabulated below in Table 1.5. This comparison reveals that with a 10-meter telescope (the largest currently available), a standard coronagraph restricts us to observing Earth-like exoplanets around Sun-like stars within approximately 10 parsecs and Jupiter-like exoplanets within 100 parsecs, for visible to near-infrared wavelengths.

Table 1.5: Telescope diameter requirements for resolving Jupiter and Earth-like exoplanet-to-star separations at various distance with a 3 λ/D coronagraphic inner working angle (IWA). Existing telescopes are highlighted in green, while those not yet realized are shown in red.

Distance [parsecs]		1	10	30	100
Diameter req'd at 0.80 μm, D [m]	Jupiter-like	0.10	0.98	2.94	9.78
	Earth-like	0.50	4.95	14.85	49.50
Diameter req'd at 1.60 μm, D [m]	Jupiter-like	0.20	1.96	5.87	19.57
	Earth-like	0.99	9.90	29.70	99.01

These limits underscore the necessity for larger telescope apertures, not only to achieve adequate resolution in the observing wavelength but also to account for the practical challenges posed by coronagraphic designs. Examples of coronagraphic designs and their impact on the image quality are presented later in §1.3.6.

1.2.2 Visible and Thermal Planet-to-Star Contrast

Telescope aperture and coronagraph design limitations emphasize the need to effectively address the immense brightness difference between stars and their orbiting exoplanets. A critical parameter in this effort is the planet-to-star contrast ratio, which quantifies the difference in light intensity between two objects. When a telescope has sufficient resolution to distinguish an object or exoplanet from its host star, this contrast ratio becomes an essential metric for the detection and study of planets within the star's glow. In this context, contrast can be expressed as the ratio of the planet's flux to the flux of its host star:

$$C_{planet-star} = \frac{F_{planet}(\lambda)}{F_{star}(\lambda)}\,, \tag{1.3}$$

where the contrast between the planet and star is a function of the wavelength, λ. Because the contrast is wavelength dependent, it is important to consider the source and range of wavelengths being emitted by the object. The light observed from an exoplanet combines reflected starlight (visible) and thermal emission from its own heat (infrared) — a continuum shaped by the planet's atmospheric composition, temperature, and gravity. While the star's brightness dominates in visible wavelengths as a very hot, near-black-body emitter, exoplanetary light persists as a mix of reflected light and thermal emission, gradually cooling over hundreds of millions of years.

Reflected Visible Light

The planet-to-star contrast in the visible is mostly a reflected emission spectrum of their star as they orbit, with the intensity a function of wavelength and absorption lines related to the planet's atmospheric characteristics. Between around 300 to 800 nm, the contrast ratio for a planet in reflected visible light can be approximated as

$$C_{visible} \simeq A_g(\lambda)\phi(\lambda,\alpha)\left(\frac{r_P}{a_P}\right)^2\,, \tag{1.4}$$

where A_g is the visible geometric albedo spectrum (a function of wavelength, λ) [43],

ϕ is the phase function (a function of wavelength, and the phase angle α, the angle between the star, planet, and observer), r_P is the planet radius, and a_P is the physical distance between the planet and star. Both A_g and ϕ are related to the planet's atmospheric composition and characteristics. A high-albedo atmosphere reflects a significant portion of the light from its star, whereas a low-albedo atmosphere absorbs more light, reflecting less. A simplified (visible only, wavelength independent) phase function for a sphere reflecting and scattering light from a nearby source at some angle is approximated by the Lambertian sphere, described by:

$$\phi(\alpha) \simeq \frac{sin(\alpha) + (\pi - \alpha)cos(\alpha)}{\pi}, \tag{1.5}$$

where $\phi(\alpha = 0) = 1$ at superior conjunction, $\phi(\alpha = \pi/2) = 1/\pi$ at maximum elongation, and $\phi(\alpha = \pi) = 0$ at inferior conjunction, when observing a system edge-on. This scattering approximation works well for high-albedo planets like Venus, but not as well for rocky planets like Earth with absorptive and anisotropic surface features that are less reflective than a Lambertian sphere. Other useful phase functions like isotropic, asymmetric, and Rayleigh scattering can be used for a more representative Jupiter or Earth-like atmosphere [44], but with added complexity and uncertainty.

Applying Equation 1.4 for exoplanets similar to Earth and Jupiter reflecting visible light through ideal Lambertian scattering at maximum elongation ($\alpha = \pi/2$), the visible contrast ratio can be calculated. With geometric albedos of 0.434 and 0.538 in V-band ($461 - 639$ nm) [45], planetary radii of $4.264 * 10^{-5}$ AU and $4.673 * 10^{-4}$ AU, and distance from the their star of 1 AU and 5.2 AU, for Earth and Jupiter respectively [46], the approximate visible light contrasts are:

$$C_{visible,Earth} \simeq 2.51 * 10^{-10} \tag{1.6}$$

and

$$C_{visible,Jupiter} \simeq 1.45 * 10^{-9} \tag{1.7}$$

These contrast levels establish the baseline performance required of imaging systems to detect exoplanets near luminous host stars in reflected light at visible wavelengths. Optical imperfections, atmospheric distortion, and diffraction introduce scattered light (speckles, discussed in §1.3.7) surrounding the star, thereby obscuring faint exoplanets. Current state-of-the-art instruments achieve on-sky contrasts of 10^{-6} (see §1.1.7), demonstrating that these requirements remain beyond current capabilities.

Thermal Emission

Compared to the reflected visible light, the thermal emission from an exoplanet that is hot from recent formation is bright in infrared (IR) wavelengths and subsequently can have a higher contrast in IR, above $\sim 0.8\,\mu m$. At younger planet ages of $1-10$ Myr, luminosity evolution models for $1-10\,M_J$ exoplanets (Jupiter masses) predict temperatures between $500-2500$ K and radii up to $r_p \simeq 1.1-2.3\,R_J$ (Jupiter radii) [47, 7, 48, 8]. After ~ 1 Gyr, the planets are predicted to cool to < 500 K and contract to Jupiter-like radii, $r_p \simeq 1-1.2\,R_J$. These models tell us that the thermal emission from the youngest Jovian exoplanets peak at near-to-mid IR wavelengths, but move into the mid-IR as they age. For these wavelengths, the planet-to-star thermal emission contrast ratio can be approximated using the thermal flux and squared radius of the planet and star.

$$C_{IR} \simeq \frac{F_P(T_P, X, \lambda) r_P^2}{F_S(T_S, \lambda) r_S^2} \simeq \frac{B_{\nu,P}(T_P, \lambda) r_P^2}{B_{\nu,S}(T_S, \lambda) r_S^2}\,, \tag{1.8}$$

where F_P and F_S are the thermal fluxes from the planet and star, respectively, as functions of T (effective temperature), X (the planet's atmospheric composition and the presence of clouds) [49], and λ (wavelength). Assuming both bodies behave as uniformly luminous blackbodies, the contrast depends only on the spectral radiance B_ν and the radii r, rather than the planet's phase, as in the visible case. The spectral radiance for a blackbody emitter is given by Planck's Law:

$$B_\nu(T, \lambda) = \frac{2hc^2}{\lambda^5 (e^{\frac{hc}{\lambda k T}} - 1)}\,, \tag{1.9}$$

where h is Planck's constant, c is the speed of light, k is Boltzmann's constant, λ is the wavelength, and T is the temperature in Kelvin. Using the known radii and effective temperatures of Earth, Jupiter, and the Sun ($4.264 * 10^{-5}$ AU, $4.673 * 10^{-4}$ AU, $4.65 * 10^{-3}$ AU, 288 K, 125 K, and 5772 K, respectively), the contrast at a specific wavelength can be calculated. Although Jupiter is known to have bright features around 5 μm, where hotter core gasses can be seen through cold outer layers with great detail, the cooler effective temperature (considered the average blackbody temperature when observed as a distant gas giant) will be used here.

Applying Equation 1.8 to a near-IR wavelength of $1.6\,\mu m$ for Earth and Jupiter, the contrasts are very low due to the Sun's peak blackbody emission being around

0.5 μm, which is much shorter than the main emission wavelengths of the older and cooler planets found in our solar system.

$$C_{IR(1.6\,\mu m),Earth(288\,K)} \simeq 8.68 * 10^{-18} \tag{1.10}$$

and

$$C_{IR(1.6\,\mu m),Jupiter(125\,K)} \simeq 2.17 * 10^{-33} \tag{1.11}$$

It is clear from these contrasts that current technology would likely not be able to detect planets at these wavelengths, especially for small-separation exoplanets within the habitable zone.

Using Wein's displacement law, where $\lambda_{\text{peak}} = b/T_{eff}$, the effective temperature T_{eff} and the Wein constant b can be used to determine the peak emission wavelength λ_{peak} for blackbody radiation [50]. For Earth, this peak emission occurs around 10 μm, while for a cooler Jupiter it is around 23 μm. Thus, the peak thermal emission contrast in the infrared is:

$$C_{IR(10\,\mu m),Earth(288\,K)} \simeq 1.62 * 10^{-7} \tag{1.12}$$

and

$$C_{IR(23\,\mu m),Jupiter(125\,K)} \simeq 7.81 * 10^{-6} \tag{1.13}$$

While planet–star contrast is generally more favorable in the infrared, imaging at these wavelengths presents significant challenges. As wavelength increases, resolving close-in companions requires larger telescopes, and the coronagraph IWA becomes more limiting (discussed in §1.2.1). In addition, thermal background noise from both the instrument and the sky can be high in the infrared, making small-separation objects especially difficult or even infeasible to detect. For hotter, newly formed exoplanets of Earth and Jupiter size, the peak emission will be at shorter wavelengths and have greater luminosity, reducing resolution and contrast requirements. While the contrast increases for these observations, dense debris disks and protoplanetary dust are likely to still surround the system and obscure these planets. During formation, within the first few Myr, if a planet's mass becomes sufficiently large ($\gtrsim$ 100 $M_\oplus$), the onset of runaway gas accretion may trigger a brief phase of rapid gas inflow accompanied by elevated thermal luminosity (discussed in §1.1.1). This transient brightening, tied to delayed accretion energy release and envelope contraction, can temporarily enhance observational contrast before the planet cools and dims [10].

Evaluating Equations 1.8 and 1.9 for Jupiter and Earth-like exoplanets across

temperatures ranging from 150 and 2500 K, Figure 1.5 illustrates the resulting blackbody spectra, with peak spectral radiance occurring in the near-IR for hot, newly formed planets and shifting to the mid-IR for cooler, mature planets.

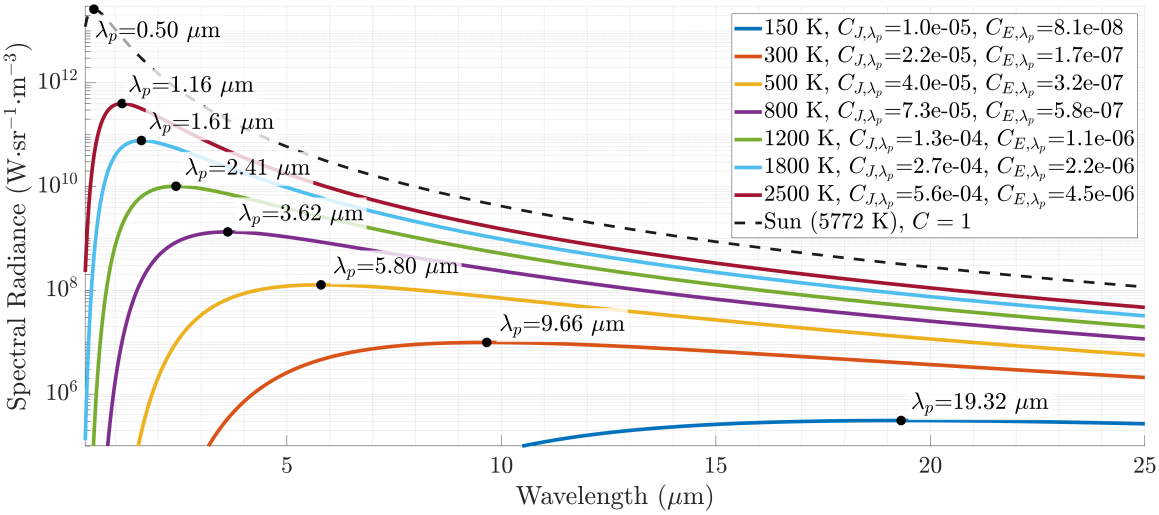

Figure 1.5: Blackbody spectra at various temperatures, with planet-to-star contrast ratios at peak spectral radiance (λ_p) for Jupiter (J) and Earth-sized (E) blackbodies orbiting a Sun-like blackbody. The Sun's blackbody curve is shown for reference.

The infrared contrasts discussed in this section, relative to those in the visible, reveal important advantages and limitations for imaging Jupiter and Earth-like exoplanets around Sun-like stars. The effectiveness of such imaging depends on a combination of factors, including telescope diameter, coronagraph IWA, the planet's luminosity, and the luminosity of the host star, all of which are strongly wavelength-dependent. As these parameters interact, selecting an optimal observing wavelength becomes essential to maximize detectability and contrast. Together, these considerations define the practical limits of current and future imaging efforts and play a central role in shaping observational strategies and instrument design.

1.2.3 Stellar Magnitude, Luminosity, and Flux

Brightness is a fundamental property that characterizes the light emitted by a star and its companions, quantified through both intrinsic luminosity and observed flux. Standard systems for brightness classification include apparent, absolute, and bolometric magnitudes, which together allow for meaningful comparisons between stellar objects, independent of their distance or observational limitations [51].

Apparent Magnitude

The apparent magnitude (m) quantifies how bright a star appears to an observer, typically on Earth. It is defined by the flux ratio to a reference star, traditionally Vega, such that:

$$m = -2.5 \log_{10} \left(\frac{F_{\text{star}}(\lambda)}{F_{\text{ref}}(\lambda)} \right), \tag{1.14}$$

where F_{star} is the flux received from the star, and F_{ref} is the flux of the reference star in the same wavelength band. It is defined on a logarithmic scale, where a difference of 5 magnitudes corresponds to a factor of 100 in brightness. For example, the apparent magnitude m of the Sun, the Moon, and a nearby M-type star (Proxima Centauri) in visible wavelengths (V-band) are -26.7, -12.7, and 11.0, respectively [52, 53, 54].

Absolute Magnitude

The absolute magnitude (M) describes the intrinsic brightness of a star, that is, how bright the star would appear if placed at a standard distance of 10 parsecs from the observer. This distance is chosen because it provides a standard reference for comparing stars' luminosities. The relationship between apparent and absolute magnitudes is given by the following equation:

$$M = m - 5 \log_{10} \left(\frac{d}{10} \right), \tag{1.15}$$

where d is the distance to the star in parsecs. This equation accounts for the effect of distance on the apparent brightness of the star, allowing astronomers to compare the intrinsic luminosities of stars at different distances. For example, the Sun has an absolute magnitude M of 4.84.

Bolometric Magnitude

The bolometric magnitude (M_{bol}) is a measure of the total energy output of a star across its entire electromagnetic radiation spectrum. Unlike apparent and absolute magnitudes, which are based on specific wavelength bands (e.g., visible light), the bolometric magnitude encompasses all wavelengths.

To relate the bolometric magnitude to the absolute magnitude in a specific photometric band (such as the visual band), the bolometric correction (BC) can be used. The bolometric correction is a function of the star's temperature and spectral type, and accounts for the portion of the star's energy emitted outside the observed

wavelength range. The bolometric magnitude is related to the absolute magnitude by:

$$M_{\text{bol}} = M + BC, \tag{1.16}$$

where BC is the bolometric correction, which varies depending on the star's characteristics. To complete the example, the Sun's bolometric magnitude $M_{\odot,\text{bol}}$ is approximately 4.74 [55], similar to the absolute magnitude in V-band because of its peak emission within that band. The bolometric correction helps ensure that the brightness measured in a specific band (e.g., visible light) can be converted to the star's total brightness, which can be important for stars emitting significant energy outside the optical range (such as cooler stars emitting more in the infrared or hotter stars in the ultra-violet).

Stellar Luminosity and Flux

The luminosity (L) of a star is the total energy radiated per unit time, typically expressed in Watts (Joules per second), and often compared to the Sun's luminosity, $L_\odot = 3.828 \times 10^{26}\,\text{W}$ [52]. Luminosity is related to the bolometric magnitude (M_{bol}) through the following equation:

$$L = L_\odot \cdot 10^{0.4(M_{\odot,\text{bol}} - M_{\text{bol}})}, \tag{1.17}$$

where $M_{\odot,\text{bol}}$ ($= 4.74$) is the Sun's bolometric magnitude. Using this relationship, the total energy output of a star can be compared to that of other celestial objects.

To relate a star's flux to its luminosity and the distance to the star (d), the energy per unit area (flux, F) received by an observer can be used through the following inverse-square law:

$$F = \frac{L}{4\pi d^2}. \tag{1.18}$$

This relationship emphasizes that the observed flux decreases with the square of the distance from the star, while the intrinsic luminosity remains constant. Combining definitions of apparent magnitude, absolute magnitude, and luminosity enables the calculation and comparison of a star's observed brightness and its intrinsic energy output across different wavelengths and distances.

Discussed in §1.2.2, the spectral radiance (or specific intensity) of any thermally emitting celestial body can be approximated using the Planck function, as given in Equation 1.9. The units of the Planck function are expressed in $erg/(s \cdot cm^2 \cdot \text{Å} \cdot sr)$,

which must be converted to photon units for the purposes of signal processing, such as signal-to-noise calculations. This conversion can be achieved by using the energy of a photon, $E_n = hc/\lambda$, and the relationship between photon flux density and spectral radiance, $\dot{n} = B_\nu \lambda / hc$. The specific intensity in photons per second, unit area, wavelength, and solid angle is then given by:

$$\dot{n}_\lambda(T) = \frac{2c}{\lambda^4 (e^{\frac{hc}{\lambda kT}} - 1)} \,. \tag{1.19}$$

To determine the total photon flux received by a distant observer per unit area, we use the solid angle $\Omega = \pi \, (r/d)^2$ steradians (sr) for an object at a distance d with radius r. The total photon flux, $\dot{N}_\lambda(T)$, can thus be expressed as:

$$\dot{N}_\lambda(T) = \dot{n}_\lambda(T)\Omega \,, \tag{1.20}$$

where the units are $photons/(s \cdot cm^2 \cdot \text{Å})$. This expression is important for signal and noise analysis, and photometric calibration of a camera within an imaging system.

1.2.4 Standard Photometric/Wavelength Bands

Focusing an observation on a specific narrow wavelength band has many advantages, including improved contrast, less chromatic blurring, and the ability to detect biomarkers (discussed throughout §1.1 and 1.2). Standardized photometric systems have been developed to define these specific wavelength bands, which are essential for calibration and measurements across various instruments and observational conditions [51, 56]. Each photometric band is associated with a letter designation corresponding to a central effective wavelength (λ_{eff}). The flux of Vega, when its apparent magnitude is zero, provides a reference zero-point for flux calibration in each band. The effective wavelength for each band and the corresponding Vega flux reference for the Johnson-Cousins UBVRI system are summarized in Table 1.6 below.

Table 1.6: Photometric bands, their effective wavelengths, and some corresponding Vega flux reference zero-point values reported by Colina 1996 [56].

Band	**Effective wavelength** λ_{eff}	**Flux zero-point** F_{ref} (erg s^{-1} cm^{-2} Å^{-1})
U	365 nm (ultraviolet)	4.34×10^{-9}

B	445 nm (visible blue)	6.40×10^{-9}
V	551 nm (visible green)	3.67×10^{-9}
R	658 nm (visible red)	1.92×10^{-9}
I	806 nm (infrared)	9.39×10^{-10}
J	1,250 nm (near-infrared)	3.06×10^{-10}
H	1,650 nm (near-infrared)	1.24×10^{-10}
K	2,200 nm (near-infrared)	3.92×10^{-11}
L	3,400 nm (mid-infrared)	—
M	5,000 nm (mid-infrared)	—
N	10,200 nm (far-infrared)	—
Q	21,000 nm (far-infrared)	—

These effective wavelengths provide a standardized basis for comparing the magnitudes of different stars or for combining observations from various instruments. Vega's spectrum serves as the calibration reference for these bands, with its flux at λ_{eff} set as the zero-point for magnitude systems. Once the reference flux is established, the apparent magnitude of a star in any given band is calculated by comparing the star's flux to Vega's reference flux in that band using Equation 1.14. This approach allows for the brightness of a star across different bands to be quantified by comparing the energy output throughout the spectrum.

1.2.5 Spectroscopic Methods and Techniques

Spectroscopy is a cornerstone of observational astronomy, enabling the compositional analysis of celestial objects by dispersing their light into constituent wavelengths. In exoplanet science, spectroscopy plays a critical role in the analysis of atmospheric compositions, thermal properties, and chemical processes. Several methods are employed, each tailored to specific scientific objectives and observational challenges, including:

- **Narrowband filtering:** This method isolates specific wavelength bands using optical filters. It is particularly effective for identifying spectral features associated with molecules such as water (H_2O) and methane (CH_4). While straightforward to implement, its limited spectral resolution and throughput restrict its utility to targeted surveys or preliminary detections of exoplanets.

- **Dispersion-based spectroscopy:** This technique employs prisms or diffraction gratings to spatially separate a point source of light, typically delivered via a fiber or slit, into its wavelength components. It enables precise measurements of fine spectral features and is widely used in both ground- and space-based instruments.

- **Integral field spectroscopy (IFS):** IFS combines spatial and spectral data by dispersing light from multiple field locations, typically using a microlens array, image slicer, or fiber bundle. The resulting spectra are projected onto a detector array, allowing measurement of discrete wavelength intensities.

- **Wavefront energy characterization:** This technique provides spatially resolved spectral data by precisely measuring the photon energy at each location in the field of view on a detector pixel. Like IFS, wavefront energy characterization offers wide-field spectroscopic analysis, but with the advantage of direct measurement, which reduces throughput loss and minimizes noise.

- **Fourier transform spectroscopy (FTS):** FTS reconstructs spectra from interference patterns produced by a modulated optical path difference, providing high throughput and broad spectral coverage. It enables atmospheric characterization, debris disk studies, and simultaneous imaging and spectroscopy across the full field of view. Although not yet applied in exoplanet research, it will be used for the first time on SPIDERS, as discussed in §2.

These spectroscopic techniques form the foundation of modern exoplanetary science, enabling the detection and characterization of planets beyond our solar system. Narrowband filtering and dispersion-based spectroscopy excel in measuring molecular features with high precision, and are utilized by instruments such as JWST's NIRSpec (near-infrared spectrograph), HIRES (high-resolution echelle spectrometer) at Keck, SPHERE, and GPI to study exoplanetary atmospheres and surface compositions [57, 58, 40, 37]. Fourier transform spectroscopy facilitates broader spectral and spatial analyses, implemented in instruments like SITELLE (Spectromètre Imageur à Transformée de Fourier pour l'Etude en Long et en Large de raies d'Emission) and SPIDERS (Subaru pathfinder instrument for detecting exoplanets & retrieving spectra) where an imaging FTS provides adjustable spectral resolution and the ability to cover a large field of view, making it suitable for the simultaneous spectroscopic

analysis of multiple objects [59, 60] (discussed in §2.4). While wavefront energy characterization techniques show promising potential for spectroscopy, the first instruments like the MEC (MKID Exoplanet Camera) on SCExAO (Subaru coronagraphic extreme adaptive optics) are still being optimized for on-sky use [61]. Supported by advances in instrumentation and data processing, these methods continue to expand our understanding of planetary systems and their properties. A presentation and discussion of typical detector types for astronomical imaging and spectroscopy, readout strategies, and the photon-to-electron relationship are outlined in §A.1.

1.2.6 Photon Noise and the Signal-to-Noise Ratio

In any imaging system, photon noise, also referred to as shot noise, is a fundamental limitation. It arises from the random arrival times of photons at a detector and is governed statistically by a Poisson process [62, 63, 64]. This inherent uncertainty plays a critical role in determining the precision of wavefront sensing and the overall performance of adaptive optics (AO) systems. For large photon counts, photon noise can be approximated as a Gaussian process, where its variance depends solely on the number of detected photons. The relationship between the signal, noise, and photon count is given by:

$$\text{Signal}_{\text{photon}} = F_\lambda \cdot \Delta t \ , \qquad \sigma_{\text{photon}} = \sqrt{F_\lambda \cdot \Delta t}, \tag{1.21}$$

where F_λ represents the photon flux (photons per second), and Δt is the integration (or exposure) time in seconds. The photon noise σ_{photon} scales with the square root of the total signal, emphasizing the diminishing returns of increasing photon flux for noise reduction. The signal-to-noise ratio (SNR) quantifies the reliability of the signal compared to the noise involved in the measurement [65]. The SNR is formally defined as:

$$\text{SNR} = \frac{S}{N}, \tag{1.22}$$

where S represents the signal strength, typically the detected photon flux, and N is the total noise. The total noise in an astronomical observation is typically a combination of photon noise, thermal background noise, and detector noise. The SNR in photon-limited conditions, accounting for these sources, is:

$$\text{SNR} = \frac{\eta F_\lambda \Delta t}{\sqrt{\eta F_\lambda \Delta t \ + \ N_{\text{thermal}} \Delta t \ + \ N_{\text{dark}} \Delta t \ + \ N_{\text{read}}^2 \Delta t \text{ fps} \ + \ \sigma_{other}}}, \tag{1.23}$$

where:

- F_λ is the photon flux, in units of photons per second per unit area.
- η is the detector efficiency or system throughput, representing the fraction of incident photons converted into detectable electrons.
- Δt is the integration time over which photons are collected, in seconds.
- N_{thermal} is the thermal background noise rate, in electrons per second.
- N_{dark} is the dark current, in electrons per second.
- N_{read} is the readout noise, in electrons per frame.
- fps is the readout rate, in frames per second.
- σ_{other} represents any additional noise sources not included in the aforementioned categories, such as speckle noise that can affect high-contrast imaging systems.

To correctly apply this equation, detector noise contributions must be converted from electrons to photons using a detector-specific conversion factor, similar to Equation A.1. Achieving high SNR is critical for accurate wavefront sensing, which directly impacts the ability to correct aberrations and detect faint planetary signals with confidence. However, optimizing SNR involves balancing factors such as target brightness, integration time, and detector characteristics. For instance, longer integration improves signal strength under low-light conditions but also increases susceptibility to atmospheric scattering and distortions. Advances in detector technology, including higher quantum efficiency and lower readout and dark current noise, have significantly enhanced SNR performance. Nonetheless, under the demanding conditions of high-contrast imaging, careful optimization of these parameters remains essential during both system design and operation.

1.2.7 Limits and Confidence of Faint Detections

In the direct imaging of exoplanets, the ability to confidently detect faint planetary signals is influenced by several factors, including the telescope's sensitivity (§1.2.1), the contrast between the exoplanet and its host star (§1.2.2), the duration of the observation, and the various noise sources affecting the measurement (§1.2.6). The sensitivity of an imaging system determines its ability to detect faint signals, often

represented by the limiting apparent magnitude, a parameter that characterizes the faintest detectable source. Detection confidence quantifies the probability of a true detection for an imaged object, considering all the noise contributions.

Limiting Magnitude for an Observation

A celestial object (or exoplanet) is considered detected if its observed signal exceeds a specified signal-to-noise ratio (SNR) threshold, $\mathrm{SNR}_{\mathrm{thresh}}$, relative to the total noise. The limiting flux F_{lim} required for detection can be expressed as:

$$F_{\mathrm{lim}} = \frac{\mathrm{SNR}_{\mathrm{thresh}} \cdot \sigma_{\mathrm{total}}}{\eta A \Delta t}, \tag{1.24}$$

where A is the telescope's collecting area, η is the total system efficiency, Δt is the integration time, and σ_{total} represents all of the noise contributions. Using this flux, the corresponding limiting magnitude m_{lim} is given by:

$$m_{\mathrm{lim}} = -2.5 \log_{10} \left(\frac{F_{\mathrm{lim}}}{F_{\mathrm{ref}}} \right), \tag{1.25}$$

where F_{ref} is the reference flux for the chosen photometric band, as outlined in Table 1.6. This equation provides the sensitivity limit of an observation by incorporating both the instrumental characteristics and observational parameters. Understanding the limiting magnitude is essential for determining the faintest stellar or exoplanet sources that can be reliably detected.

Detection Confidence

Detection confidence in exoplanet imaging is directly related to the SNR and the Gaussian nature of the noise, where detection is confirmed when the planetary signal surpasses the noise floor with sufficient confidence. A Gaussian model is used to quantify the detection confidence, with the probability of detection, $P(\mathrm{detection})$, expressed as:

$$P(\mathrm{detection}) = 1 - \frac{1}{2} \mathrm{erfc} \left(\frac{\mathrm{SNR}}{\sqrt{2}} \right). \tag{1.26}$$

Here, $\mathrm{erfc}(x)$ is the complementary error function, and the subtraction and scaling $1 - \frac{1}{2}$ accounts for the symmetry of the normal distribution, isolating the likelihood of the signal being above the threshold and normalizing the result to a confidence value between 0 and 1. Detection thresholds are commonly set at 3σ (corresponding

to a 99.7% confidence level) or 5σ (corresponding to a 99.99994% confidence level) for robust detections. The relationship between SNR and detection confidence is grounded in the statistical properties of Gaussian noise, where the SNR corresponds to the number of standard deviations (σ) above the noise mean. For example, an SNR of 3 corresponds to a detection at the 3σ level, meaning the signal is three times the noise, with a 99.7% confidence in that the signal is not just noise.

To illustrate how these relationships can be applied, an example using the relevant parameters to iteratively solve for the integration time needed to reach a desired SNR for a detection at various distances is computed in Table 1.7.

Table 1.7: Integration times for achieving specific SNRs at varying distances for a 10^{-6} contrast target around a 10th magnitude star in J-band using a 10 m telescope are calculated under the following parameters: 5% throughput, 0.1 e/s dark current, 2 e/s thermal background, 10 e/read read noise, 0.1 s frame rate, and an electron-to-photon ratio of 1. Assuming no stellar signal contamination, the required integration times to reach the target SNR are provided for distances of 1, 5, 10, and 20 parsecs.

SNR	1 parsec	5 parsecs	10 parsecs	20 parsecs
1	0.1 sec	41.1 sec	10.60 min	2.80 hr
3	1.2 sec	6.17 min	1.59 hr	25.23 hr
5	3.4 sec	17.13 min	4.42 hr	70.08 hr

Although this example primarily reflects throughput limitations and photon noise, additional complications such as bright stellar speckles around the host star from atmospheric turbulence or imperfect optics will significantly reduce the ability to detect nearby exoplanets. These speckles introduce further noise into the measurement, which, in turn, increases the required observation time to achieve a highly confident detection.

In summary, the concepts of limiting magnitude and detection confidence are crucial for understanding the constraints in exoplanet imaging. These parameters define the balance between the planet's signal, the host star's flux, the instrumental noise, and the required confidence level for detection. A comprehensive understanding of these factors is essential for evaluating the capabilities of direct imaging systems and for developing observational strategies that maximize the likelihood of successful exoplanet detection.

1.3 Principles of High-Contrast Direct Imaging

Adaptive optic (AO) systems are essential for mitigating the effects of atmospheric turbulence and reducing the impact of optical imperfections. These systems actively correct wavefront distortions, which would otherwise prevent telescopes from achieving diffraction-limited performance, significantly enhancing the resolution and clarity of astronomical observations [65]. AO has been extensively deployed on large ground-based telescopes for many years, including instruments such as GPI, SPHERE, and SCExAO [37, 40, 66]. Although space-based AO remains an emerging technology, with initial deployments planned for the upcoming Roman Space Telescope [67], ground-based systems offer greater performance benefits relative to their cost and implementation complexity. A basic AO system is shown in Figure 1.6, though modern implementations often incorporate more sophisticated architectures designed to meet specific observational requirements and sensing approaches.

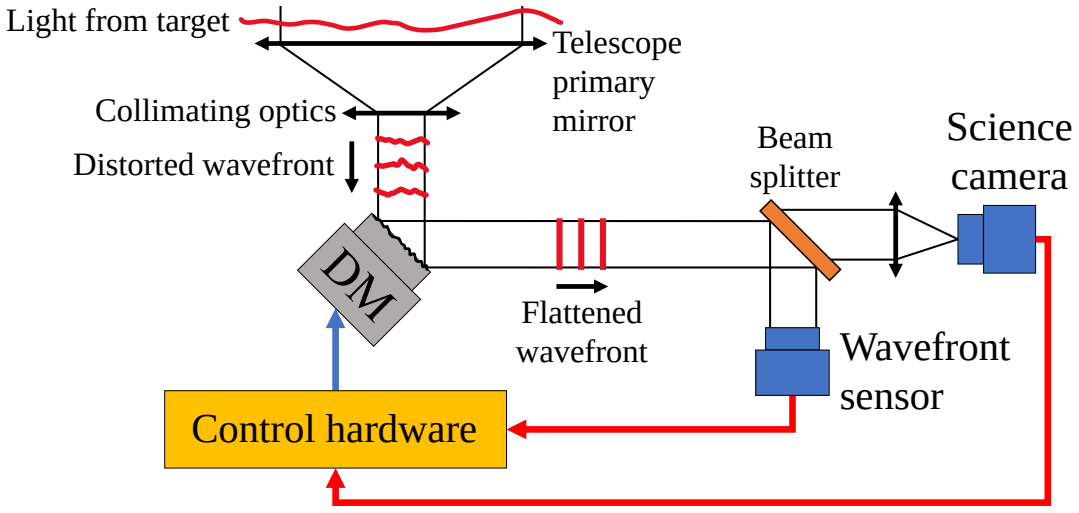

Figure 1.6: Schematic of a basic adaptive optic (AO) system. A deformable mirror corrects wavefront distortions based on feedback from the wavefront sensor, and a beam splitter divides the incoming light between the sensor and the science camera, enabling concurrent feedback and image capture.

The typical AO architecture features a wavefront sensor that quantifies distortions in incoming light by comparing the wavefront phase to an ideal flat profile. This data is processed by a real-time control system, which calculates the necessary corrections. A deformable mirror (DM) then applies these corrections by dynamically adjusting its surface to counteract the measured distortions. In this configuration, a beam splitter

shares the corrected light with both the wavefront sensor for feedback and the science camera for imaging, allowing for real-time wavefront correction while simultaneously capturing high-resolution, sharp images.

In this section, the fundamental principles of AO systems are presented, beginning with the propagation of light through space, sources and representations of optical aberrations, and the cumulative impact on the image quality. The discussion continues with an examination of coronagraphic techniques to improve contrast, stellar speckle evolution in the focal plane, speckle subtraction techniques with post-processing, and real-time wavefront sensing and correction utilizing deformable mirrors. The chapter concludes with the development of a wavefront error budget to plan and estimate the overall performance of an AO system.

1.3.1 Propagation and Diffraction of Monochromatic Light

An understanding of how light propagates through space, the atmosphere, and through an imaging system is crucial in designing, simulating, and implementing optical systems. When a photon from a distant celestial object (considered both as a particle or a wave) travels through the vacuum of space, it remains relatively unaffected. However, as it traverses Earth's atmosphere, turbulent air that mixes layers of varying density and refractive index induces phase and amplitude errors (deviations or aberrations) on the wavefront, distorting the image. These aberrations change in real-time, are wavelength-dependent, and can occur at low to high spatial frequencies, resulting in significant distortions.

Light as a Wave

To understand how light propagates through any medium (vacuum or air), it can be modeled as an electromagnetic wave, with its electric field traveling through space [68, 69]. In a homogeneous medium with a constant refractive index, the scalar electromagnetic field in the pupil (or aperture) plane can be represented in the spatial domain as:

$$E_{pp}(t, x', y', \lambda) = A(t, x', y', \lambda)e^{i\phi(t,x',y',\lambda)} \tag{1.27}$$

where $A(t, x', y', \lambda)$ is the amplitude, representing the wave's envelope or the aperture shape, and $\phi(t, x', y', \lambda)$ is the phase, describing deviations from a flat wavefront with zero phase. Both the amplitude and phase depend on spatial coordinates x' and y', wavelength λ, and possibly time t if the wavefront is evolving (e.g. due to

atmospheric turbulence or mechanical vibration). In the context of simulation, time can be treated as constant for a single wavefront if only modeling how it evolves from one plane to another, rather than considering its temporal evolution. For clarity, the t term will be dropped for derivations in this section.

The Rayleigh-Sommerfeld Diffraction Integral

When the electromagnetic field passes through the pupil of an imaging system (or the primary mirror of a telescope), diffraction occurs depending on the wavelength relative to the pupil size. For monochromatic light, the field can be described by its 2D Fourier transform, which characterizes how the wavefront is modified by diffraction or, equivalently, how it convolves with the point-spread function (PSF), the optical system's response to a point source.

$$\mathcal{F}[E_{pp}](k_x, k_y, \lambda) = \int_{-\infty}^{\infty}\int_{-\infty}^{\infty} A(x', y', \lambda) e^{i\phi(x', y', \lambda)} e^{-2\pi i(k_x x + k_y y)} \cos(\theta)\, dx\, dy \quad (1.28)$$

where k_x and k_y are the transverse spatial frequency components of the wave vector $\mathbf{k}$ (which has magnitude $k = 2\pi/\lambda$), λ is the wavelength of the incident light, x' and y' are the spatial coordinates in the aperture plane, and $\mathcal{F}[\cdot]$ represents the 2D Fourier transform. The term $\cos(\theta)$ accounts for the angular dependence of the wave propagation. For this derivation, the $\cos(\theta)$ term will be set to 1 to consider the simplified on-axis case. When propagating the electromagnetic field forward, the free-space transfer function $e^{ik_z z}$ is multiplied with the Fourier-transformed field, and an inverse Fourier transform then applied to recover the field at distance z:

$$E^+(x, y, z, \lambda) = \mathcal{F}^{-1}\left[\mathcal{F}[E_{pp}] e^{ik_z z}\right] = \frac{1}{4\pi^2}\int_{-\infty}^{\infty}\int_{-\infty}^{\infty} \mathcal{F}[E_{pp}] e^{ik_z z} e^{i(k_x x + k_y y)}\, dk_x\, dk_y \ . \quad (1.29)$$

The transition to the Rayleigh-Sommerfeld diffraction integral begins by interpreting the inverse Fourier transform in real space. The $e^{ik_z z}$ transfer function accounts for the propagation of each Fourier component along the z-axis, with $k_z = \sqrt{k^2 - k_x^2 - k_y^2}$. Applying the Huygens-Fresnel principle, the aperture is treated as a source of secondary wavelets, whose superposition determines the propagated field. The distance between an aperture point (x', y') and observation point (x, y, z) can be defined as:

$$r = \sqrt{(x - x')^2 + (y - y')^2 + z^2} \ . \quad (1.30)$$

The Rayleigh-Sommerfeld diffraction integral can then formally be derived as:

$$E^{+}(x,y,z,\lambda) = \frac{1}{i\lambda}\int\int_{\text{aperture}} E_{pp}(x',y',\lambda)\frac{e^{ikr}}{r}\,dx'\,dy' \ . \tag{1.31}$$

In this form, the Rayleigh-Sommerfeld integral is often too complex for practical and efficient calculations. To simplify this integral, either the Fresnel (near-field) or the Fraunhofer (far-field) approximation is typically applied. These approximations are based on the distance from the aperture to the observation plane, which defines the diffraction behavior of the wavefront.

The Near-Field (Fresnel) Approximation

The Fresnel approximation is applicable when the observation plane is relatively close but not at the aperture, such that the diffraction pattern changes noticeably with distance. In this regime, the exponential phase factor in Eq. 1.31 can be simplified using the paraxial approximation (a first-order Taylor series expansion), which assumes small angles of diffraction. For the Fresnel approximation, the distance r in Eq. 1.30 can be approximated as:

$$r \approx z + \frac{(x-x')^2 + (y-y')^2}{2z} \qquad \text{for} \quad z > 0 \ . \tag{1.32}$$

Substituting this approximation into Eq. 1.31 leads to the Fresnel diffraction integral:

$$E^{+}(x,y,z,\lambda) \approx \frac{e^{ikz}}{i\lambda z}\int\int_{\text{aperture}} E_{pp}(x',y',\lambda)e^{ik\frac{(x-x')^2+(y-y')^2}{2z}}\,dx'\,dy' \ . \tag{1.33}$$

In this expression, the term $e^{ik\frac{(x-x')^2+(y-y')^2}{2z}}$ represents the quadratic phase factor, which governs the curvature of the wavefront in the near-field regime. While the Fresnel approximation is a simplification of Eq. 1.31, the form is still computationally expensive and complex to implement.

The Far-Field (Fraunhofer) Approximation

In the far-field (Fraunhofer) regime, it is assumed that the observation distance z is much greater than the lateral distances in the aperture or observation plane. Under these conditions, the diffraction pattern retains its structural features while only its overall scale changes with distance. In this approximation, the phase factor from the

Rayleigh-Sommerfeld integral can be further simplified using small-angle approximations. The distance r from the Fresnel approximation in Eq. 1.32 can be expanded to isolate the first order observation plane variables:

$$r \approx z + \frac{x^2+y^2}{2z} + \frac{xx'}{z} + \frac{yy'}{z} \approx z \qquad \text{for} \quad z \gg \sqrt{x^2+y^2}\ . \tag{1.34}$$

Using the Fraunhofer approximation, the quadratic phase factors simplify to linear factors, reducing the general form of the electric field in the observation plane to:

$$E^+(x,y,z,\lambda) \approx \frac{e^{ikz}e^{ik\frac{(x^2+y^2)}{2z}}}{i\lambda z}\int\int E_{pp}(x',y',\lambda)e^{ik\frac{xx'}{z}}e^{ik\frac{yy'}{z}}\,dx'\,dy' \tag{1.35}$$

where $e^{ik\frac{x'x}{z}}e^{ik\frac{y'y}{z}}$ are the linear phase factors corresponding to the far-field approximation, and the remaining factors become independent of the integral. Using these simplifications, the electric field in the observation plane can be expressed as the 2D Fourier transform of the aperture field:

$$E^+(x,y,z,\lambda) \approx \frac{e^{ikz}e^{ik\frac{(x^2+y^2)}{2z}}}{i\lambda z}\mathcal{F}[A(x',y',\lambda)e^{i\phi(x',y',\lambda)})] \approx \mathcal{F}[E_{pp}(x',y',\lambda)]\ . \tag{1.36}$$

When interested in only the relative electric field at the focal plane of an imaging system (i.e. the diffraction pattern or formed image), the scaling terms $e^{ikz}e^{ik\frac{(x^2+y^2)}{2z}}/i\lambda z$ are often dropped for simplicity. This final Eq. 1.36 represents the far-field approximation, where the diffraction pattern can be determined directly by the Fourier transform of the aperture field. It is computationally efficient and can make use of the Cooley-Tukey fast-Fourier transform (FFT) algorithm [70, 71] for simulating diffraction patterns, discussed and applied later in §1.3.2.

The Fresnel Number

The Fresnel number, F, is a fundamental parameter that characterizes the diffraction regime, distinguishing between near-field and far-field propagation. It is defined as:

$$F = \frac{a^2}{d\lambda}, \tag{1.37}$$

where a is the aperture radius, d is the distance to the observation plane, and λ is the wavelength.

Near-field regime ($F \geq 1$):
In this regime, diffraction effects vary significantly with distance, and the Fresnel approximation is applicable. However, its accuracy diminishes as F becomes $\gg 100$. For shorter propagation distances, the Rayleigh-Sommerfeld integral may be required to achieve higher accuracy.

Far-field regime ($F < 1$):
In the far-field, the diffraction pattern becomes effectively independent of distance, and the Fraunhofer approximation holds. This approximation is generally valid for $F \ll 1$, while its accuracy decreases as F approaches 1. When $F \sim 1$, using the near-field approximation may be necessary, particularly for high-precision simulations.

Intensity of the Wavefront
In an imaging system, the intensity of the wavefront observed on a detector or at the focal plane is given by the square modulus of the electric field. For any of the Rayleigh-Sommerfeld, Fresnel, or Fraunhofer integrals, the intensity I of the wavefront at a point in the observation plane is given by:

$$I(x, y, z, \lambda) = |E^{+}(x, y, z, \lambda)|^2 \ . \tag{1.38}$$

This expression provides the electric field intensity, which can be used to visualize a simulated diffraction pattern or correlate the measurable intensity on a detector with the propagated wavefront. Figure 1.7 illustrates the transition from the near-field to far-field diffraction regimes by evaluating the intensity of the Rayleigh-Sommerfeld integral (Eq. 1.31) for a flat, monochromatic wave propagated along the z-axis through a circular aperture. Below the image, the intensity plots of the Fresnel and Fraunhofer approximations are overlaid on the Rayleigh-Sommerfeld intensity at discrete propagation distances for comparison.

The Problem with Reconstructing the Wavefront from the Intensity
To reconstruct the wavefront from the detected intensity, the amplitude A can be directly retrieved from the square root of the measured intensity I:

$$A(x, y, z, \lambda) = \sqrt{I(x, y, z, \lambda)}, \tag{1.39}$$

while the phase information ϕ is fundamentally lost in the detection process. This limitation arises when using a standard detector that measures only the total intensity of the incident wavefront, rather than its complex components. As a result, phase retrieval or reconstruction necessitates additional methodologies beyond direct intensity conversion, like the pupil plane wavefront sensing presented in Figure 1.6 or other approaches, discussed later in §1.3.9 and 1.3.10.

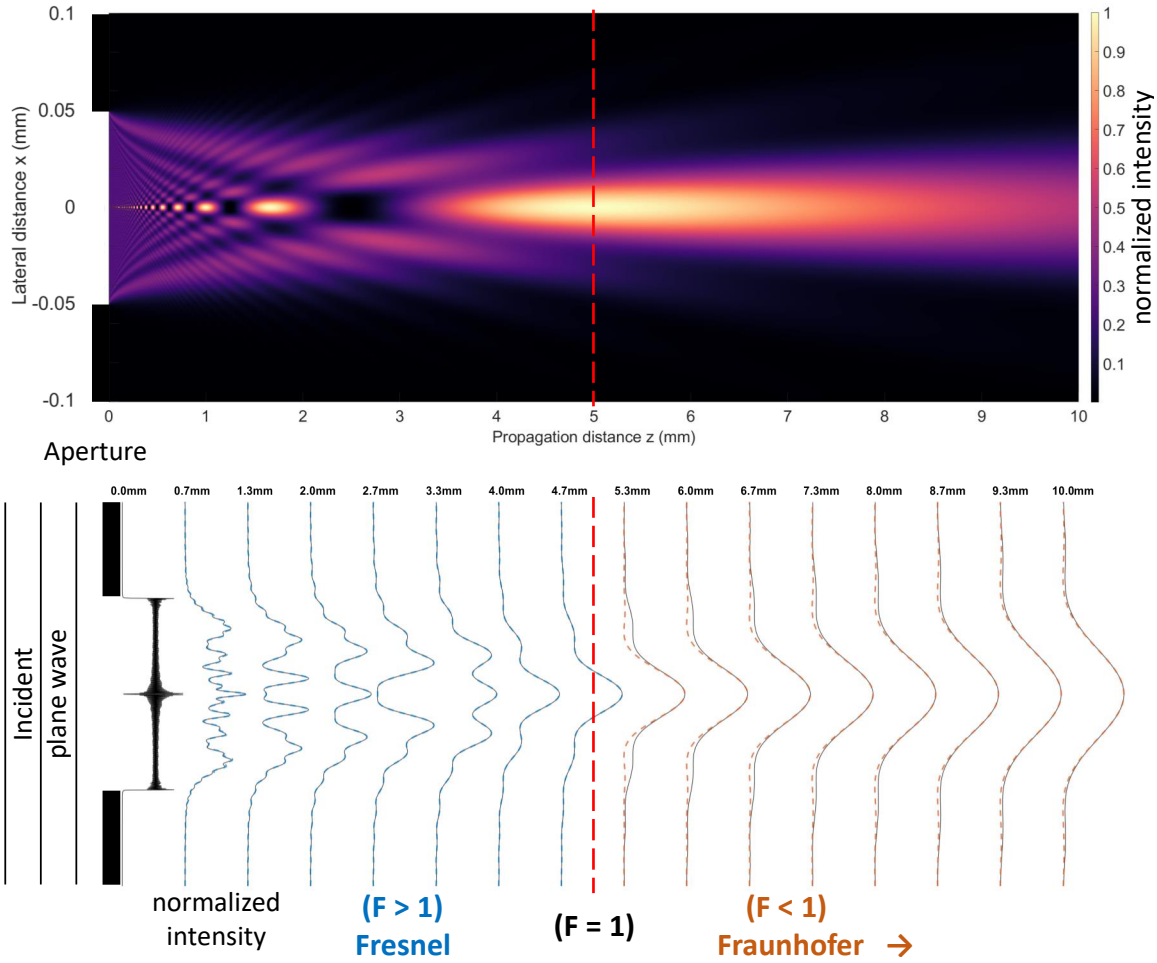

Figure 1.7: A side-viewed, on-axis simulation of a 500 nm plane wave diffracting through a circular pupil using the Rayleigh-Sommerfeld integral (top), illustrating the transition from Fresnel to Fraunhofer regimes (red dotted line). The bottom set of line plots show the normalized intensity of the wavefront at discrete distances for the Rayleigh-Sommerfeld integral (black solid), with Fresnel (blue dotted) and Fraunhofer (orange dotted) approximations overlaid in their respective near and far-fields for comparison.

1.3.2 Using Fourier Transforms to Propagate Light

Fourier optics extends the Fraunhofer approximation, providing a powerful framework for modeling and analyzing optical systems. The Fourier transform (FT) is a specific instance of this approximation, derived in §1.3.1, where the observation plane coincides with the focal plane of a focused optical system. This approximation holds regardless of the focal length, as the FT describes both light focusing and image formation by lenses or mirrors [18, 68]. Thus, Fourier optics leverages the Fraunhofer approximation to elegantly describe wavefront propagation and image formation.

As light passes through an ideal focusing lens, the wavefront undergoes a transformation that converts spatial variations in the input field into angular variations in the output field. This process maps the spatial domain representation of the electric field to its frequency domain counterpart, with each point corresponding to a specific spatial frequency component of the original wavefront. In this way, the lens serves as a physical implementation of the two-dimensional (2D) Fourier transform, directly connecting physical optics with Fourier transform theory. Figure 1.8 illustrates this process within an imaging system, showing intensity distributions at both the pupil and focal planes.

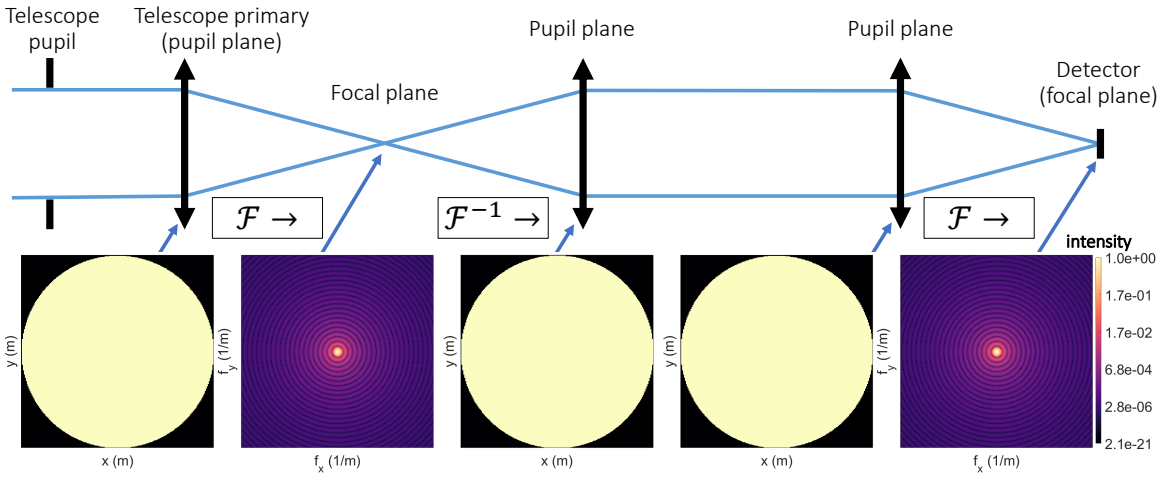

Figure 1.8: Fourier optics model of a flat, monochromatic wave propagating through a basic telescope, showing diffraction-limited intensity distributions at the pupil and focal planes. The pupil plane images are cropped to only show the aperture, and the focal plane image scaled for better visualization of the diffraction pattern. The transformations between these planes are governed by the forward and inverse two-dimensional Fourier transforms, $\mathcal{F}$ and $\mathcal{F}^{-1}$, respectively.

By facilitating the transition between the spatial and frequency domains, the FT

allows for the detailed analysis of frequency components, essential for simulating optical phenomena such as diffraction, interference, filtering, and masking. For accurate simulations, the discretized wavefront must be constructed carefully to represent the relevant spatial frequencies. Adherence to the Nyquist criterion for proper sampling is crucial to avoid aliasing and ensure the fidelity of the optical system model. Additionally, numerical noise, especially at high frequencies, can arise due to discretization and may be amplified through repeated domain transformations. By addressing these challenges, Fourier optics plays a pivotal role in the design and analysis of high-performance optical instruments, enabling precise simulations of wavefront behavior across the pupil and focal planes. A more detailed discussion on the application of Fourier optics in simulating an optical system for a chromatic wavefront is provided in §A.2 and §A.2.1.

1.3.3 Optical Coherence and Broadband Propagation

Optical coherence governs how light interferes with itself, playing a crucial role in astronomical imaging, including the observation and analysis of exoplanets. It describes the phase correlation of an optical wavefront over space and time, fundamentally determining the structure of the image formed in an optical system. Astrophysical sources such as stars and planets typically exhibit low or partial coherence due to their large distances and intrinsic emission properties [4, 18]. In such systems, the star and exoplanet are mutually incoherent, regardless of whether the planetary light is thermally emitted or reflected. This incoherence affects how different wavelengths contribute to the intensity distribution at an observation plane, influencing image contrast and signal extraction techniques. A comprehensive understanding of both spatial and temporal coherence is essential for modeling wavefront evolution, optimizing coronagraphic suppression, and interpreting interferometric data in exoplanet imaging.

- **Spatial coherence:** Quantifies the phase correlation of an electromagnetic wavefront at different points in space, determining the ability to produce stable diffraction/interference patterns. A highly coherent source, such as a monochromatic laser, maintains a uniform phase structure, enabling precise focusing and minimal beam divergence. Low spatial coherence, as seen in starlight, results in phase variations across the wavefront, leading to a more diffuse intensity distribution and increased beam spread.

- **Temporal coherence:** Refers to the correlation of the phase of an electromagnetic wavefront over time. It is determined by the spectral bandwidth of the source, where narrowband light, with a limited range of wavelengths, maintains a stable phase relationship over time. Broadband light, with a wider range of wavelengths, experiences greater phase fluctuations over time, leading to reduced temporal coherence. This affects the ability to form stable interference patterns and is important for interferometric measurements and high-contrast imaging.

The coherence properties of light dictate how intensities from different sources combine, impacting the effectiveness of coronagraphs and other wavefront control techniques in exoplanet observations.

The Intensity of Incoherent Light

Incoherent light, such as that emitted by stars and exoplanets, consists of electromagnetic waves that lack a fixed phase relationship. As a result, the intensity distribution in the focal plane is obtained by summing the intensities of the individual waves, with each wavelength contributing independently. This model is appropriate for most astronomical sources, which typically emit broadband, incoherent light. Mathematically, the total intensity of incoherent light at an observation plane is the sum of the individual intensities of each wavelength:

$$I_{\text{total}} = \sum_i I_i = \sum_i |E_i|^2 \tag{1.40}$$

where E_i represents the electromagnetic field corresponding to the i-th wavelength. This approach assumes that the waves do not interfere with one another, making it suitable for the broadband light sources.

The Intensity of Coherent Light

Conversely, coherent light, such as that from lasers or monochromatic sources with a fixed phase relationship, requires a different treatment. In this case, the electromagnetic field contributions from each wavelength must be summed before computing the intensity, as the waves can interfere constructively or destructively. The total

intensity for coherent light at an observation plane is given by:

$$I_{\text{total}} = \left| \sum_i E_i \right|^2 \tag{1.41}$$

This formula accounts for the phase relationships between the electromagnetic fields of different wavelengths, resulting in interference effects that can modify the intensity distribution. An example of monochromatic and narrowband intensity at the focal plane are shown in Figure 1.9, illustrating the incoherent addition of different wavelength intensities that blur the diffraction pattern. Regardless of the parameter space in this simulation, the Airy disk pattern for monochromatic light has its first minima defined at the Rayleigh criterion (§1.2.1), providing a means to relate the PSF on the computational grid to a physical wavelength and aperture size. The simulation of chromatic wavefront propagation is formally discussed in §A.2.

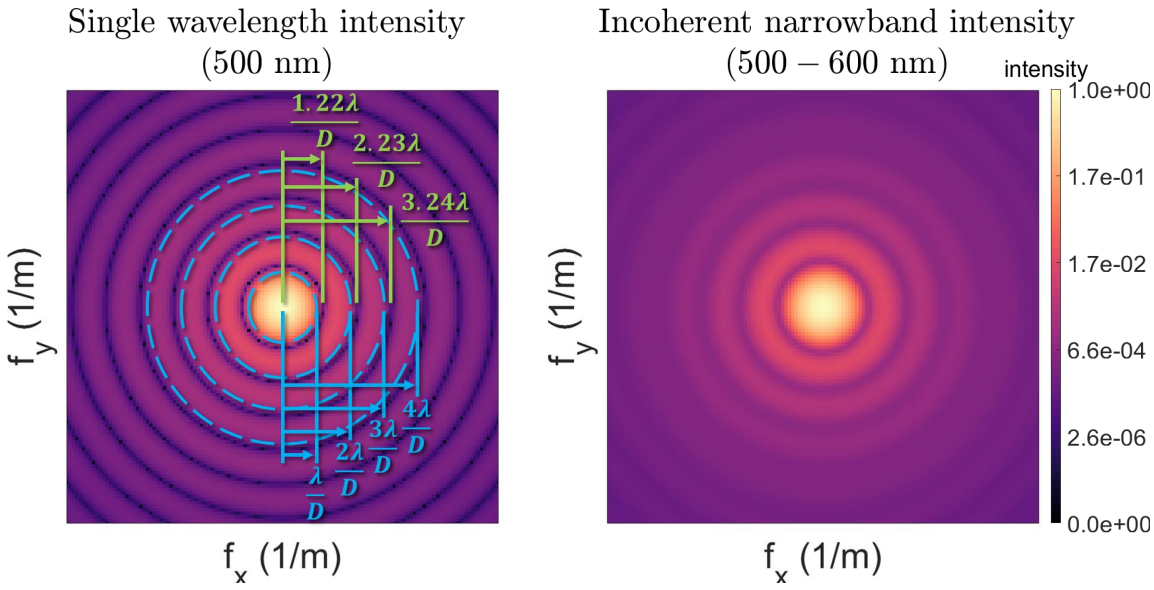

Figure 1.9: Focal plane intensity for monochromatic (left) and narrowband (right) light near the photometric V-band (500–600 nm). Monochromatic light produces a distinct Airy disk, while chromatic broadening blurs these features. Exponential scaling of the image was applied to increase the contrast globally without altering structure.

While coherent light is uncommon in direct astronomical observations, it is often encountered in laser-based systems, narrowband filtering, or by interfering the wavefront with itself. The fringing patterns generated by interference can be analyzed to

recover information about the source and the wavefront. Coherence for high-contrast imaging plays a critical role in current exoplanet imaging techniques, and is discussed later in §1.3.8 and §1.3.10. A detailed discussion on simulating a chromatic wavefront and the intensity at the focal plane are presented in §A.2 and §A.2.1.

1.3.4 Sources and Representations of Optical Aberrations

Aberrations in optical systems result from various factors that distort the wavefront of incoming light by altering its amplitude and phase, degrading image quality and preventing the system from achieving diffraction-limited performance [18]. The sources of aberrations can be broadly categorized into external and internal factors. External sources primarily involve atmospheric disturbances and inhomogeneity, while internal factors arise from imperfections in optical components or misalignments within the system. Aberrations can also be classified based on their spatiotemporal characteristics, either as dynamic or quasi-static, providing insight into their evolution over time and space. These aberrations impact the light between its point of emission and the optical system's detectors, as illustrated in Figure 1.10.

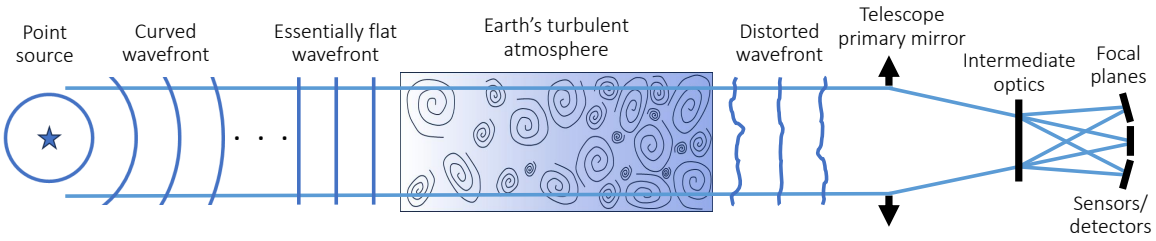

Figure 1.10: Illustration of a point source emitting a spherical wavefront, which becomes approximately planar at a sufficient distance. As the wavefront passes through the Earth's atmosphere, it accumulates amplitude and phase distortions due to turbulence and refractive index variations. The telescope's primary mirror focuses the light towards the focal plane, accumulating more errors as it passes through intermediate optics, beam splitters, filters, etc., before reaching the sensor/detector (e.g., a camera) to capture the intensity distribution of the wavefront.

Atmospheric Aberrations

Electromagnetic waves from distant point sources, such as stars and exoplanets, traverse the Earth's atmosphere, encountering refractive index variations caused by thermal gradients, compositional differences, and turbulent mixing. These variations distort the wavefront, affecting both its amplitude and phase, resulting in image distortion and scintillation. The instantaneous atmospheric mass responsible for these

distortions can be represented as a single or multi-layer phase screen model, which represents the integrated optical effect of the atmosphere. While the turbulence evolves randomly in space and time, it adheres to underlying thermodynamic principles, which are discussed in greater detail later in this section.

Optical System Aberrations

In addition to atmospheric distortions, imperfections within the optical system itself contribute to aberrations. These include defects or misalignments in components such as lenses and mirrors, as well as external factors like vibrations, thermal expansions, and structural instabilities. Such imperfections can give rise to both dynamic and quasi-static errors. Dynamic aberrations are time-varying, typically caused by mechanical vibrations or thermal fluctuations, which alter the optical path in real-time. Quasi-static aberrations, while appearing stable over minutes to hours, evolve over longer timescales due to gradual misalignments or long-term structural deformations. These errors accumulate between the optical elements and the final detection plane, potentially introducing non-common path aberrations (NCPAs) that degrade calibration, sensing, and correction efforts, further compromising image quality.

Zernike Polynomials

Phase distortions over a circular pupil can be efficiently represented using Zernike polynomials, which form an orthogonal basis for describing wavefront aberrations. Their widespread use in optical systems arises from their ability to decompose complex distortions into a sum of orthogonal terms, providing a compact and mathematically rigorous characterization [18, 72]. Defined over the unit disk, the polynomials are parameterized by two integers: the radial degree n, a non-negative integer; and the azimuthal frequency m, an integer such that $|m| \leq n$ and $n - |m|$ is even. This ensures that the polynomials are orthogonal over the unit disk. In practical applications, the Zernike polynomials are often used in their real-valued form, decomposing the azimuthal dependence into cosine and sine components, depending on the sign of m. The general form of a Zernike polynomial is:

$$Z_n^m(r,\theta) = \begin{cases} \cos(m\theta) \cdot R_n^m(r), & \text{for } m \geq 0, \\ \sin(|m|\theta) \cdot R_n^{|m|}(r), & \text{for } m < 0, \end{cases} \tag{1.42}$$

where r is the normalized radial coordinate, θ is the azimuthal angle, and $R_n^m(r)$ is

the corresponding radial polynomial:

$$R_n^m(r) = \sum_{k=0}^{\frac{n-|m|}{2}} (-1)^k \frac{(n-k)!}{k!(\frac{n+|m|}{2}-k)!(\frac{n-|m|}{2}-k)!} r^{n-2k}. \tag{1.43}$$

This decomposition ensures that all physically measurable aberrations are expressed as real-valued functions. The orthogonality of Zernike polynomials over the unit disk enables efficient least-squares fitting of complex wavefront distortions, decomposing them into individual modal contributions. Figure 1.11 illustrates the first five radial orders of these polynomials, organized by increasing radial degree (n) and azimuthal frequency (m).

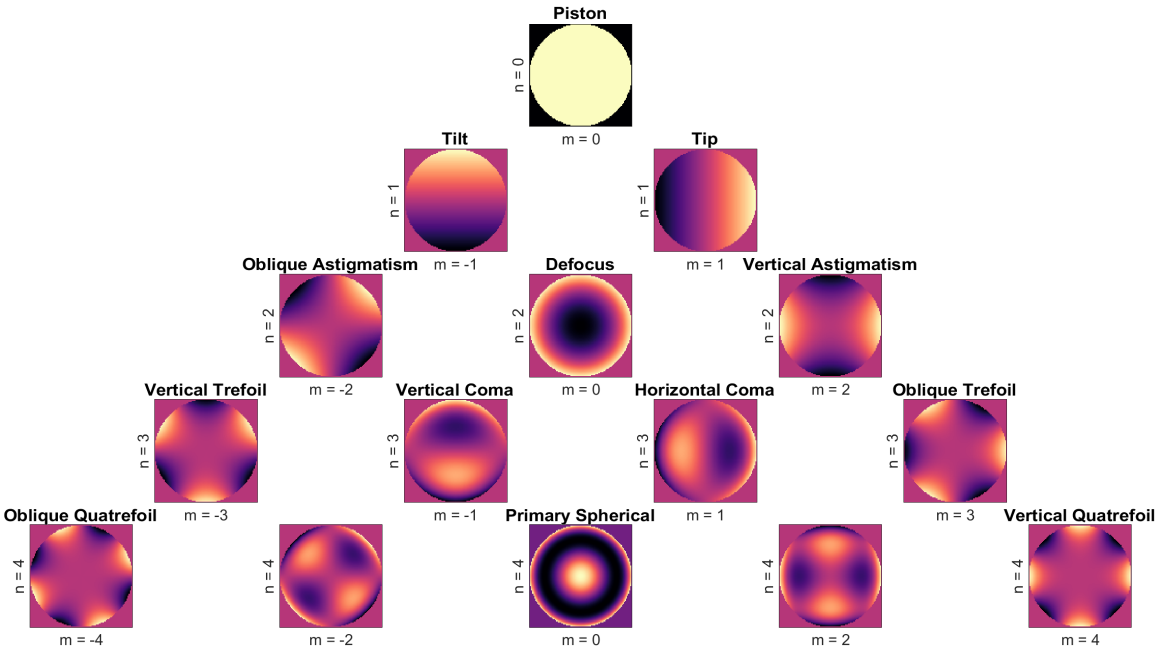

Figure 1.11: Zernike polynomials up to the fifth radial order, arranged by increasing radial degree (n) and azimuthal frequency (m), with commonly used aberration names. Each polynomial is normalized over the unit circle and can be scaled to represent various wavefront distortions.

Due to their orthogonality and systematic structure, Zernike polynomials are widely used in wavefront sensing and adaptive optics as a natural basis for describing optical systems. Misalignments in such systems are typically represented by low-order modes, such as defocus, astigmatism, and coma. Decomposing a measured wavefront into Zernike terms enables the characterization of both low- and high-order aber-

rations, thereby supporting various correction strategies in high-precision imaging systems.

Fried Parameter (r_0)

The Fried parameter, r_0, is a critical measure of atmospheric turbulence's impact on optical wavefronts. It defines the spatial coherence length over which phase distortions cause a root-mean-square (RMS) wavefront error of 1 radian [18]. A smaller r_0 corresponds to stronger turbulence and degraded optical performance. This parameter is essential for assessing atmospheric seeing conditions and is formally given by the equation:

$$r_0 = \left[0.423\, k^2 \sec(\theta) \int_0^\infty C_n^2(h)\, dh\right]^{-3/5}, \tag{1.44}$$

where $k = 2\pi/\lambda$ is the wavenumber, λ is the wavelength of light, $C_n^2(h)$ represents the refractive index structure as a function of altitude h, and θ is the zenith angle. The factor $\sec(\theta)$ accounts for the greater atmospheric thickness at higher zenith angles, amplifying turbulence effects. The value of $C_n^2(h)$ varies with altitude, time of day, and atmospheric conditions, making it a dynamic parameter that significantly influences optical system performance, though its real-time measurement is challenging. Over short time spans (minutes to hours), the value of r_0 is often treated as approximately constant and given in units of centimeters. Typical values of r_0 at sea-level can be between 1 and 10 cm, while good conditions at high-altitude observatory sites like Maunakea can be as 20 cm or more [73].

Kolmogorov Turbulence

Atmospheric turbulence is commonly modeled using Kolmogorov's theory, which assumes that energy cascades from larger to smaller eddies in a statistically homogeneous and isotropic manner [18]. This theory provides a model for the power spectral density (PSD) of turbulence-induced refractive index variations, forming the foundation for simulating its impact on optical wavefronts. In the context of simulating atmospheric turbulence's effect on optical wavefronts, the Kolmogorov PSD can be used to generate a two-dimensional turbulent phase screen that captures the phase distortions caused by turbulence. The PSD of the phase screen Φ_ϕ in $\mathrm{rad}^2/\mathrm{m}^2$, is given by:

$$\Phi_\phi(f_x, f_y) = 0.023\, r_0^{-5/3} \left(f_x^2 + f_y^2\right)^{-11/6}, \tag{1.45}$$

where f_x and f_y are the spatial frequencies in the x- and y-directions, and r_0 is the Fried parameter. This equation exhibits the $-11/3$-power law scaling for Kolmogorov turbulence in the spatial frequency domain, with higher frequencies corresponding to smaller eddies that dominate the turbulent phase distortions. A 1-dimensional representation of the PSD is shown in 1.12, while the full-form use of the PSD is discussed in §A.3.

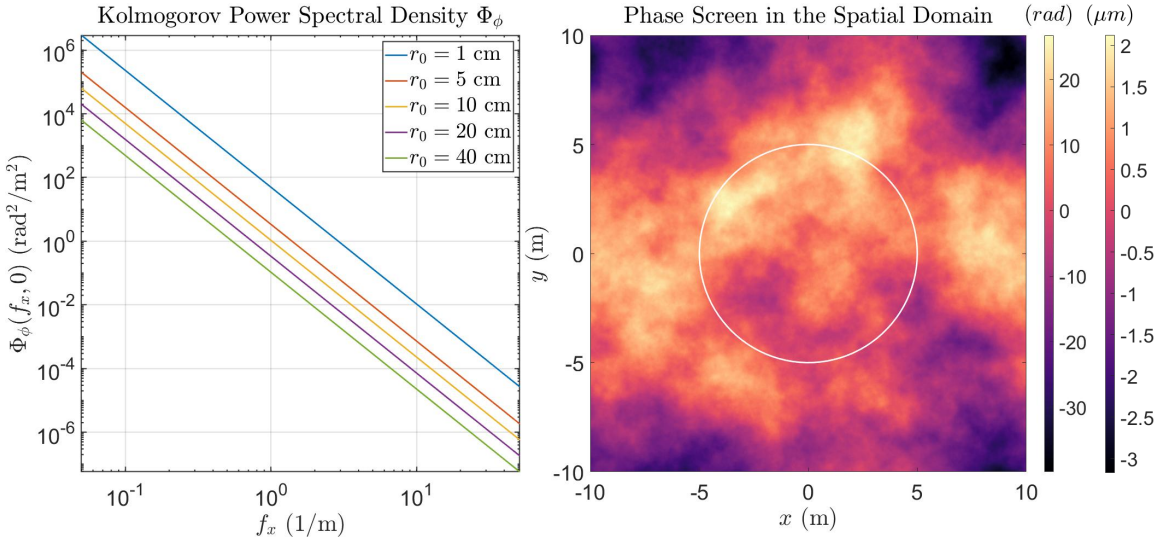

Figure 1.12: Kolmogorov power spectral density (PSD) function from Eq. 1.45 for various r_0 values, plotted on a logarithmic scale for positive f_x values and when $f_y = 0$ (left). The full-form 2D PSD is used with random coefficients to generate the spatial domain phase screen in radians using an $r_0 = 20$ cm (right). At 500 nm, the optical path difference in micrometers is also shown for scale. A 10 m telescope diameter is overlaid as a white circle to illustrate the grid and beam size used.

The effect of this phase distortion on the wavefront can significantly degrade optical performance, especially for high-contrast imaging observations. As the atmosphere moves and mixes, this phase distortion evolves spatially and temporally. To approximate the temporal evolution of atmospheric turbulence, Taylor's frozen flow hypothesis is often applied in conjunction with the Kolmogorov model. This assumption treats the turbulence as a static phase screen advected across the telescope aperture by a uniform wind vector, such that $\phi(x, y, t) \approx \phi(x - v_x t, y - v_y t, 0)$ [74]. This simplifies the generation of time-dependent phase screens from a spatially defined PSD by shifting the screen over time, enabling computationally efficient simulations. While effective under steady wind and slowly evolving conditions, the approximation becomes less accurate in highly dynamic or multi-layer turbulence.

The effect of this evolution in the final image is discussed in §1.3.5 and §1.3.7. A detailed discussion on simulating a representative atmospheric model to generate phase screens is presented in §A.3 and §A.3.1.

Cumulative Effect of Turbulence and the Expected Residual Error

The influence of atmospheric turbulence on the phase of a wavefront can be quantified through the statistical variance of phase fluctuations. A widely adopted metric for this is the Zernike-Kolmogorov residual phase variance, which characterizes the phase distortion remaining after correction up to a given Zernike mode (see Figure 1.11 for the first 15 Zernike modes). This provides critical insight into optical performance under turbulent conditions. As derived by Noll (1976) [72], the theoretical residual phase variance after removing the first few Zernike modes is given by:

$$\sigma^2_{\phi,1} = 1.0299 \left(\frac{D}{r_0}\right)^{5/3}, \quad \sigma^2_{\phi,2} = 0.582 \left(\frac{D}{r_0}\right)^{5/3}, \quad \sigma^2_{\phi,3} = 0.134 \left(\frac{D}{r_0}\right)^{5/3}, \ldots \quad (1.46)$$

where D is the aperture diameter and r_0 is the Fried parameter. This relationship demonstrates the dependence of phase variance on turbulence strength and pupil size. The residual variance for any number of corrected modes follows from a coefficient table provided in Noll's work [72], though only the first three terms are explicitly shown in Equation 1.46.

Scaling the Fried Parameter r_0

The phase variance σ^2_ϕ is inherently wavelength-dependent, requiring the Fried parameter r_0 to be adjusted accordingly based on the observational conditions. Conventionally, r_0 is reported at a reference wavelength of 500 nm [18] and can be scaled for other wavelengths based on the Zernike-Kolmogorov relationship $\sigma^2_\phi \propto \left(\frac{D}{r_0}\right)^{5/3}$ from Eq. 1.46. Applying this dependence, the wavelength-scaled r_0 is given by:

$$r_0 = r_{0,500\,\mathrm{nm}} \left(\frac{\lambda}{500\,\mathrm{nm}}\right)^{6/5}. \quad (1.47)$$

This expression indicates that at shorter wavelengths, the effective r_0 decreases, leading to increased wavefront distortion due to reduced spatial coherence lengths. Conversely, at longer wavelengths, turbulence effects are less pronounced, resulting in a larger r_0 and reduced phase distortion. To illustrate this dependence, the theoretical

Zernike-Kolmogorov RMS residual error is plotted as a function of r_0 for different wavelengths in Figure 1.13.

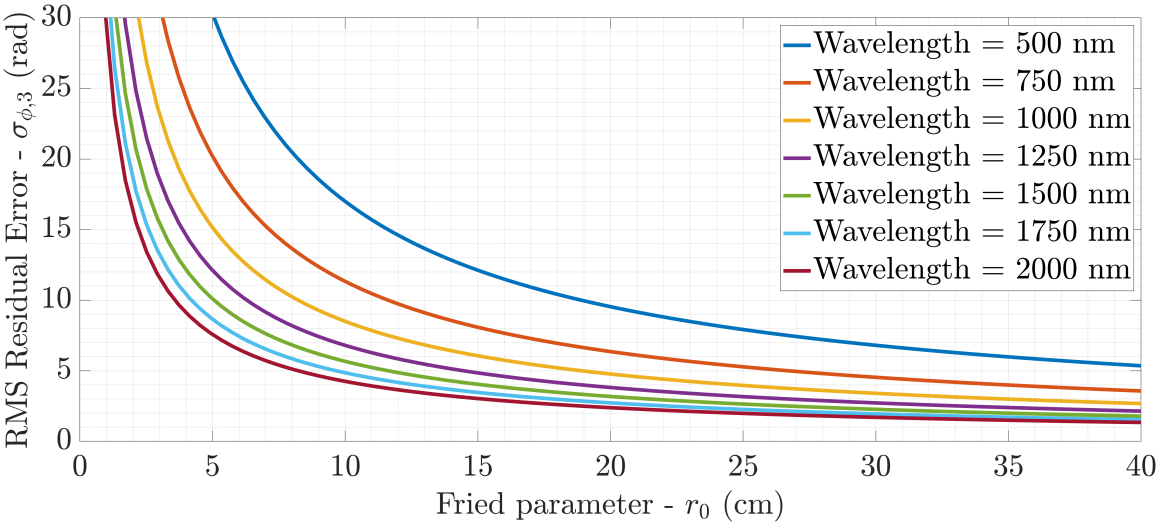

Figure 1.13: Theoretical Kolmogorov-Zernike residual phase error after removing the first three Zernike modes, $\sigma_{\phi,3}$ from Eq. 1.46, as a function of the Fried parameter r_0 for different wavelengths.

Amplitude Aberrations

Although wavefront control primarily target phase, amplitude aberrations also contribute significantly to contrast degradation and reduced image fidelity in high-precision optical systems. These errors can arise from Fresnel diffraction, partial transmission, reflectivity variations, coating defects, polarization-dependent effects, and scattering due to surface roughness or particulate contamination [75, 76]. Although amplitude is directly measurable from focal plane intensity, these measurements do not distinguish between aberrated and ideal pupil plane distributions without access to the corresponding phase. Furthermore, amplitude and phase components become coupled during propagation, complicating their isolation and correction. Since conventional wavefront sensors are largely insensitive to amplitude variations, accurate compensation typically relies on focal plane wavefront estimation techniques capable of reconstructing the full complex electric field, discussed in §1.3.10.

1.3.5 Impact of Aberrations on the Point Spread Function

Wavefront aberrations, arising from phase or amplitude distortions, modify the point-spread function (PSF) of an optical system, which represents its spatial response to a

point source. Consequently, even small deviations from an ideal (flat) wavefront can degrade image quality. Such aberrations may result from atmospheric turbulence, optical surface imperfections, or misalignments in the optical path, as discussed in §1.3.4. Because they are wavelength-dependent, they also produce chromatic blurring, particularly in broadband imaging. This effect is especially detrimental in high-contrast observations, where residual aberrations impose fundamental limits on performance, since a single deformable mirror can provide only one phase correction across all wavelengths (discussed in §1.3.11).

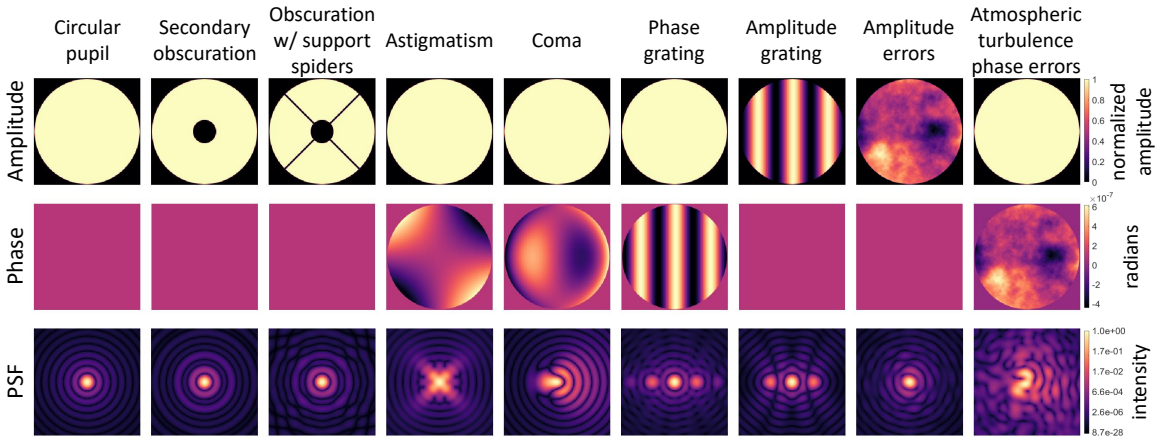

Figure 1.14: Point spread function (PSF) (bottom row) resulting from a monochromatic point source viewed through a pupil with varying amplitude (top row) and phase (middle row) aberrations. The intensity is uniformly scaled to enhance contrast while preserving structural features.

Ideal PSF

In the absence of aberrations, a circular aperture illuminated by a monochromatic plane wave produces an Airy disk pattern at the focal plane. This diffraction-limited PSF consists of a central bright core surrounded by concentric rings of decreasing intensity, a result of far-field (Fraunhofer) diffraction, as described in §1.3.1 and 1.3.2. The first three columns in Figure 1.14 represent the diffraction-limited cases for three common telescope pupil shapes.

Aberrated PSF

When the wavefront deviates from ideal, energy within the PSF is redistributed, distorting its structure and degrading image quality. Phase aberrations, such as those caused by atmospheric turbulence, introduce time-varying speckle patterns,

while amplitude aberrations from Fresnel diffraction or optical surface defects alter the symmetry of the PSF and suppress intensity in specific regions. The spatial distribution of these distortions depends on the scale and magnitude of the aberrations: lower-order aberrations shift energy away from the core, while higher-order aberrations introduce fine-scale speckles. Columns four through nine in Figure 1.14 illustrate the PSF of a circular aperture with varying phase and amplitude distortions.

Correcting the Aberrated PSF

Aberration mitigation combines optimized optical design, real-time correction via AO, and computational post-processing. Precision fabrication and alignment reduce static aberrations from optical surfaces and misalignments, while AO corrects both static and dynamic wavefront errors to restore the PSF and approach diffraction-limited performance [18]. Post-processing techniques, including deconvolution and differential imaging, further suppress residual aberrations in the recorded data, enhancing contrast beyond the limits of hardware alone [24]. These complementary strategies are essential for high-contrast imaging, where residual errors and speckle noise fundamentally constrain the detectability of faint companions and nearby structures.

1.3.6 Coronagraphic Techniques to Block Starlight

Coronagraphy is a key technique in high-contrast imaging, enabling the detection of faint exoplanets by suppressing diffracted and scattered starlight (§1.1.3). This suppression is achieved using specialized optical elements that reduce on-axis stellar light while preserving off-axis planetary signals. A variety of coronagraph architectures have been deployed in the field (e.g., on Hubble, GPI, and SPHERE [36, 37, 40]), each designed to optimize wavefront control, contrast performance, and meet specific observational constraints. The following provides an overview of some widely used coronagraph designs in exoplanet imaging:

1. **Amplitude Mask Coronagraph**: This foundational design employs an amplitude focal plane mask (FPM) to block core starlight, along with a Lyot stop in the pupil plane to eliminate diffracted light, effectively suppressing stellar light and enhancing contrast. The simple design shown in Figure 1.15 achieves a contrast improvement (or suppression factor) of 10^4, where signals as weak as 10^{-4} of the star's intensity are now the most prominent features in the image.

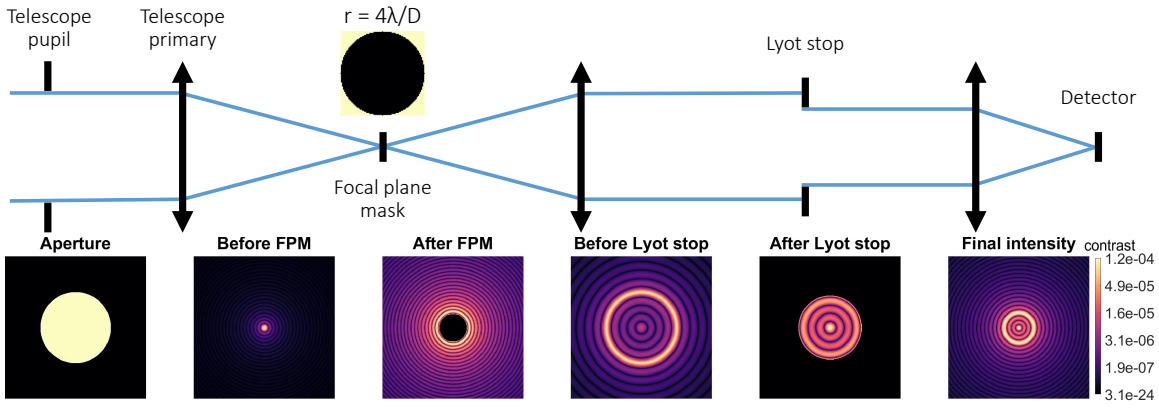

Figure 1.15: Simulation of an error-free wavefront passing through an amplitude mask and Lyot stop coronagraph, with intensity shown at key locations before and after the 4 λ/D radius FPM and 0.9 D Lyot stop mask. Contrast is shown relative to the peak intensity of the unmodified PSF through a circular pupil.

2. **Phase Mask Coronagraph**: This design uses a phase mask in the focal plane to introduce a phase shift that causes destructive interference with starlight. Examples include the Four-Quadrant (4 Q) phase mask and the vortex coronagraph, which creates a phase vortex that nullifies starlight at the centre while preserving off-axis light. The vortex FPM in Figure 1.16 achieves a suppression factor of approximately 10^4 while providing regions of higher suppression along paths around the star.

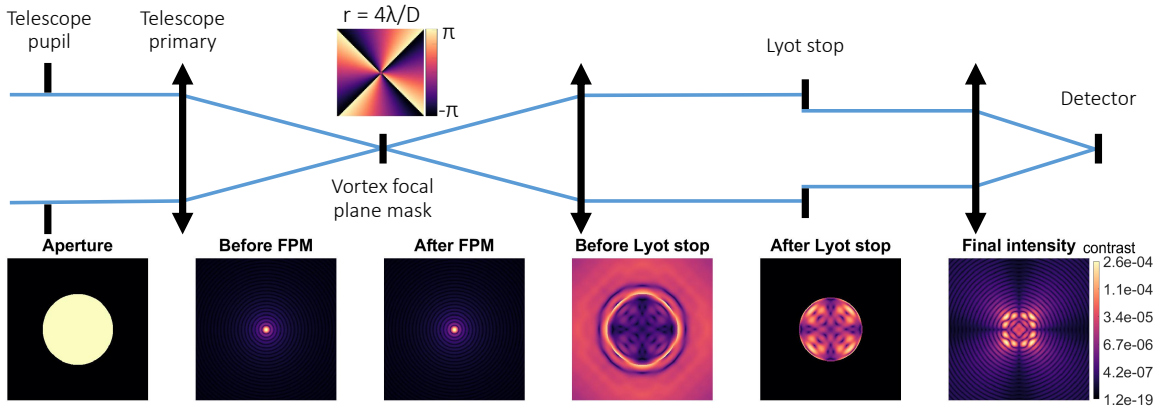

Figure 1.16: Simulation of a 4 λ/D vortex phase-mask coronagraphic system with resulting intensities at various planes. Contrast is shown relative to the peak intensity of the unmodified PSF passing through a circular pupil.

3. **Apodized Pupil Coronagraph**: Apodization mitigates diffraction by smoothing the sharp edges of the telescope aperture, thereby suppressing high-spatial-frequency content that contributes to bright diffraction rings at moderate to wide angular separations in the focal plane. While the simplest conceptual implementation involves a Gaussian transmission profile, practical systems employ optimized apodizers using binary amplitude masks or coatings tailored to specific optical configurations. In the example shown in Figure 1.16, the combination of an apodized pupil and a vortex focal plane mask improves contrast by approximately three orders of magnitude. Achieving optimal performance, however, requires joint optimization of the apodizer and coronagraph to match system parameters and observational constraints.

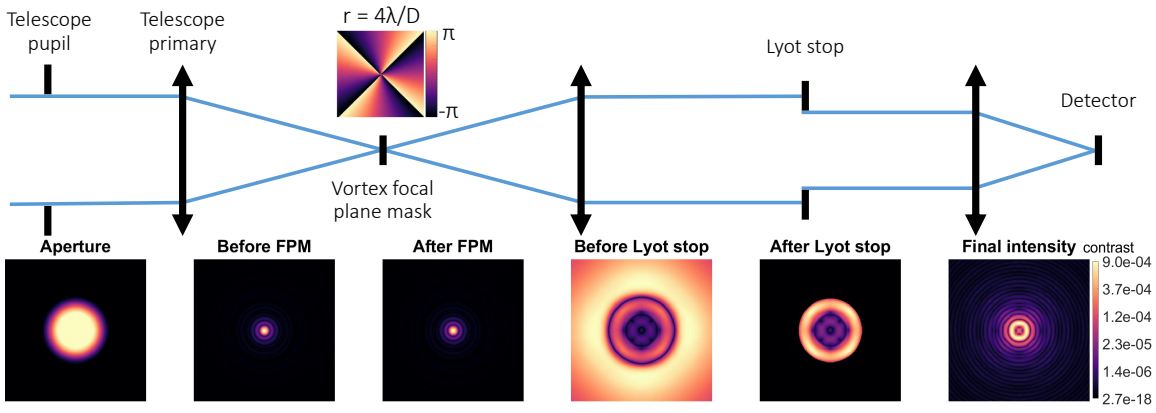

Figure 1.17: Simulation of an apodized pupil combined with a 4 λ/D vortex phase-mask coronagraph and Lyot stop. Contrast is shown relative to the peak intensity of the unmodified PSF through a circular pupil.

4. **Other Techniques**: Additional coronagraph designs include:

   - *Occulter/Starshade Coronagraphs*: These external shades, positioned far from the telescope, block starlight before it enters the optical system. Although no full-scale system has been deployed yet, the concept has been extensively studied [77].
   - *Phase-Induced Amplitude Apodization Coronagraphs (PIAA)*: These coronagraphs improve contrast by redistributing the light across the pupil using specially shaped optics that modify both phase and amplitude [21]. This process leverages Fresnel propagation to convert phase changes into an

apodized amplitude profile, allowing efficient starlight suppression with minimal loss of throughput and strong off-axis performance.

Each coronagraphic design offers unique advantages and challenges, with selection based on specific mission requirements such as contrast, inner working angle, chromaticity, and robustness to optical aberrations. Combining these techniques often enhances performance by optimizing trade-offs between competing design factors, although it may require additional optical elements that reduce overall system throughput. Using the tools described in §A.2 and §A.2.1, three coronagraphic designs are simulated in Figure 1.18 to assess their contrast improvements in detecting faint companion exoplanets at visible-light contrasts.

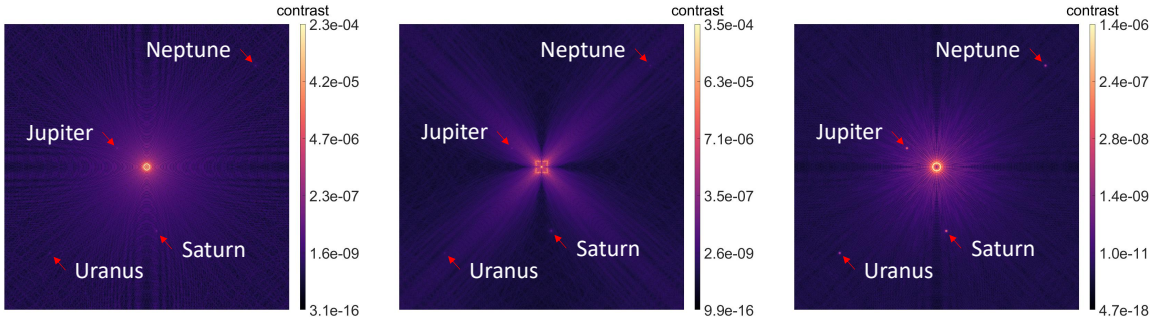

Figure 1.18: Simulated focal plane intensity without aberrations for $10^{-7} - 10^{-10}$ contrast planets in V-band, analogous to our solar system, observed from 10 parsecs with a 10 m telescope. LEFT: amplitude blocking FPM and Lyot stop coronagraph; MIDDLE: vortex phase FPM and Lyot stop coronagraph; RIGHT: apodized pupil with vortex phase FPM, amplitude blocking FPM, and Lyot stop. Contrast is quantified in each image by dividing the final intensity by the unocculted peak intensity of the star. Only four of the eight planets are visible in each plot, with the inner planets and lower contrasts obscured by bright residual diffraction patterns around the central star.

Although optimized coronagraph designs have significantly improved starlight suppression and enabled the detection of faint exoplanets, especially those with Earth-like characteristics, challenges remain. Detecting inner planets is still difficult due to their proximity to the star and the bright residual diffraction patterns around the central star. Advanced coronagraph designs, including tailored apodization patterns and specialized focal plane masks, offer promising solutions for further starlight suppression. However, such designs require intricate optimization and precise manufacturing to achieve their full potential. Continued development of coronagraph technologies,

combined with techniques like post-processing and adaptive optics, is crucial for overcoming the limitations of current systems.

1.3.7 Speckle Evolution in the Focal Plane

Speckles in the focal plane image arise from phase and amplitude wavefront errors that mimic exoplanet signals, limiting the ability to detect faint companions near their host stars [22, 78]. As discussed in §1.3.4, these errors originate from a combination of atmospheric turbulence, optical imperfections, misalignments, and thermal or mechanical instabilities. Understanding speckle behavior and developing mitigation strategies is essential for advancing high-contrast exoplanet detection.

Dynamic Speckles

Dynamic speckles arise primarily from atmospheric turbulence, which introduces rapidly varying phase aberrations on the wavefront. These fluctuations occur on timescales ranging from microseconds to milliseconds, dictated by the turbulence's coherence time and characterized by metrics such as the Fried parameter r_0 and wind speed (as discussed in §1.3.4 and §A.3). Mechanical vibrations from components like cooling fans, pumps, or telescope movements can further contribute, causing rapid oscillations in low-order modes (e.g., tip, tilt, defocus).

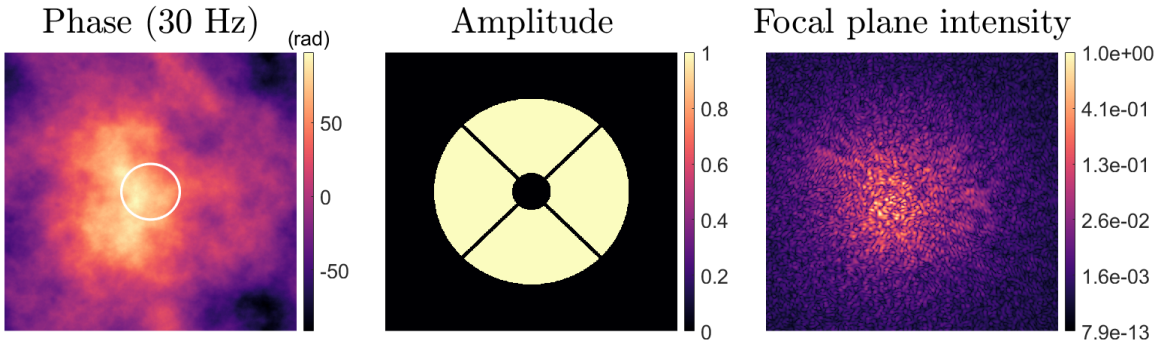

Figure 1.19: Animated simulation of monochromatic speckles evolving spatially and temporally in the focal plane (right) due to atmospheric turbulence using a three-layer Kolmogorov turbulence model at $r_0 = 20$ cm (left). The simulation sampling occurs over 2 s at 30 Hz and 120 ms at 500 Hz. The telescope size is overlaid on the wavefront phase (left), with a magnified aperture for visualization (middle).

While dynamic speckles appear to change rapidly (first half of Figure 1.19 animation), low-order aberrations evolving over longer timescales can cause some speckles

to persist when the sampling rate is sufficiently high. In high-speed cases, these dynamic speckles can become quasi-static, maintaining their size and position across multiple frames, complicating the distinction between planetary and stellar light (as illustrated in the latter half of the Figure 1.19 animation).

Static/Quasi-Static Speckles

Static speckles arise from imperfections in optical components, such as polishing defects and coating irregularities. Quasi-static speckles emerge when these fixed aberrations shift or deform over time due to structural flexure or thermal drift, leading to gradual changes in their position and intensity. Over both short and long timescales, variations in air temperature around the telescope can further alter seeing conditions. Unlike dynamic speckles, quasi-static speckles typically form repeatable spatial patterns linked to the telescope and instrument configuration. Their persistence and slow evolution complicate suppression, necessitating long-term system stability and specialized post-processing techniques. Figure 1.20 illustrates how static speckles appear as localized intensity fluctuations in the focal plane that may closely resemble exoplanet signals, but change gradually as optical alignments drift.

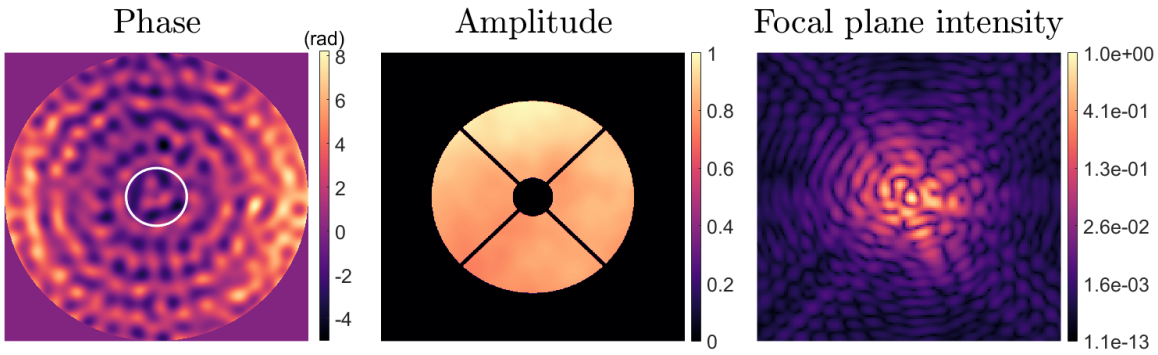

Figure 1.20: Animation of quasi-static speckles induced by thermal and flexural drift. The model incorporates optics with ∼175 nm RMS figure error, radial polishing artifacts, and ∼85% transmission/reflectivity. Displayed are the wavefront phase errors (left), amplitude errors (middle), and their effect on the focal plane image (right). The evolution timescale is influenced by the optical configuration and environmental conditions, but could occur over minutes to hours.

Spectral Evolution

In addition to their temporal evolution, speckles exhibit wavelength-dependent behavior due to chromatic phase and amplitude wavefront errors, leading to variations in their size, position, and intensity in the focal plane. This chromatic dependence

leads to spatial-spectral cross-talk, which degrades spatial coherence and complicates mitigation strategies, especially in broadband observations critical for exoplanet atmosphere studies [25]. Managing spectral evolution requires careful optical design to minimize chromatic aberrations, along with advanced post-processing techniques such as spectral differential imaging (SDI) [22, 79], which exploit the wavelength dependence of speckles to separate them from astrophysical signals.

Combined Impact

The combined effects of dynamic, quasi-static, and spectral speckle evolution significantly impact the final image and detection of faint exoplanets. These speckles introduce both short-term and long-term noise, complicating the separation of exoplanet signals from stellar light, and necessitating an optimized coronagraphic design, wavefront control, and advanced post-processing techniques for effective suppression, discussed next in §1.3.8.

1.3.8 Speckle Subtraction Techniques

Speckle noise caused by dynamic atmospheric turbulence and optical imperfections poses a fundamental challenge in high-contrast imaging, limiting the ability to detect faint exoplanets near bright host stars. To address this, differential imaging methods have been developed as a class of post-processing strategies. Key techniques include Reference Differential Imaging (RDI), Angular Differential Imaging (ADI), Coherent Differential Imaging (CDI), Spectral Differential Imaging (SDI), and Polarization Differential Imaging (PDI) [23, 80, 22, 79, 24]. Each approach leverages distinct astrophysical or instrumental properties to suppress speckle noise and improve contrast. The effectiveness of these methods depends on factors such as system stability, observing conditions, and target characteristics.

Reference Differential Imaging (RDI)

RDI suppresses static speckle noise by leveraging a reference observation of a well-matched calibration target to approximate the optical system's point spread function (PSF). The technique is most effective when the reference star closely resembles the science target in spectral type and brightness and is observed under nearly identical atmospheric and instrumental conditions. However, even minor variations in the observing conditions between the reference and science observations introduce residual

speckle noise, limiting the subtraction's effectiveness [22, 24]. For this reason, RDI is primarily used with data from space-based platforms such as HST and JWST, where the instrumental PSF remains highly stable.

The RDI algorithm consists of acquiring a reference image, aligning it with the science image, and performing a pixel-wise subtraction to remove static speckles originating from the host star. When the reference PSF closely matches the science PSF, the residual structure primarily consists of astrophysical sources, such as exoplanets and circumstellar disks. However, any mismatch in wavefront errors, optical aberrations, or temporal variations in the instrument optics degrades speckle suppression effectiveness and limits the achievable contrast. An example of the RDI process is shown in Figure 1.21.

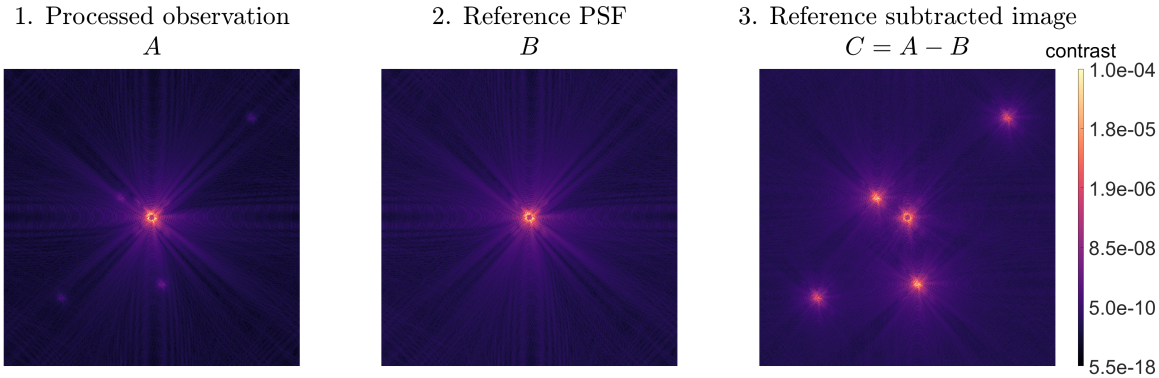

Figure 1.21: Reference differential imaging (RDI) suppressing static speckles using a reference PSF with slight intensity variations and small random wavefront errors. Implemented with an apodized pupil Lyot stop coronagraphic system, RDI processing reveals four of the eight $10^{-4} - 10^{-7}$ companions, significantly improving planet contrast and reducing diffraction effects. However, small deviations between the reference and observation PSFs limit subtraction effectiveness, particularly for high-contrast targets near the host star.

Angular Differential Imaging (ADI)

ADI exploits field rotation inherent to alt-azimuth telescopes, where the sky rotates relative to the fixed orientation of the instrument. In this configuration, static speckles remain stationary in the image plane, while astrophysical sources rotate around the host star due to Earth's rotation, provided the instrument is aligned with the telescope pupil. By constructing a model PSF from the target itself and subtracting it from each frame, ADI enhances contrast and isolates faint companions. The technique is most effective when the observation spans a sufficient parallactic angle to distinguish real

signals from residual speckle noise; otherwise, self-subtraction can degrade sensitivity, especially for sources near the star [23, 24].

The ADI algorithm involves aligning each image to a common reference frame, modeling the speckle noise PSF either by stacking the observation images or using advanced reduction pipelines, and subtracting this model before rotating and stacking the observations to enhance planetary signals. An example of ADI's process and effectiveness is illustrated in Figure 1.22.

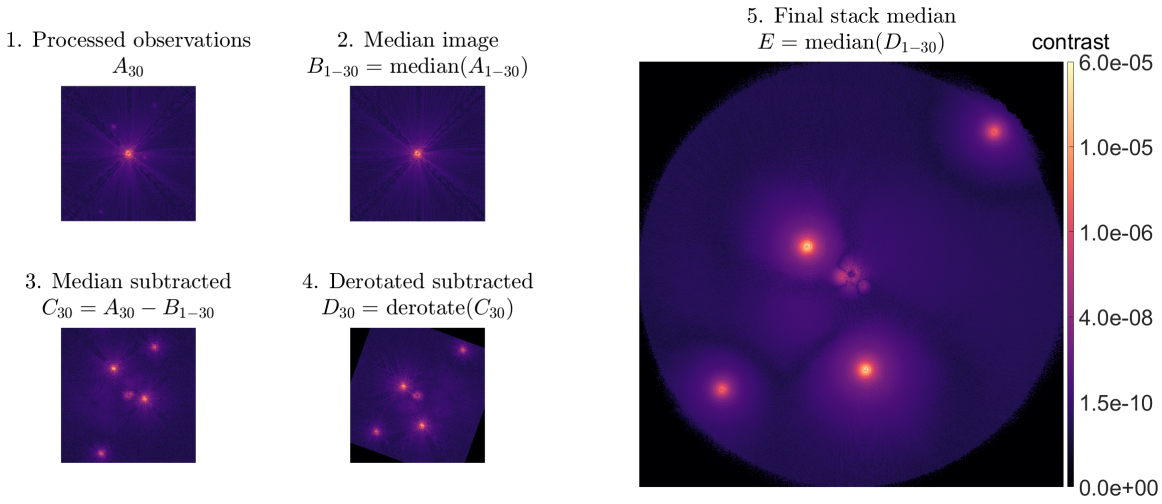

Figure 1.22: Animation of angular differential imaging (ADI) removing static speckles for a 30-image sequence of eight $10^{-4} - 10^{-7}$ companions through an apodized pupil Lyot stop coronagraph system with low-power random phase fluctuations and drift. The final stacked median image on the right demonstrates the contrast improvement, revealing seven of the eight companions with the 30-image stack.

Coherent Differential Imaging (CDI)

CDI utilizes techniques such as the Self-Coherent Camera (SCC), Electric Field Conjugation (EFC), or speckle nulling to exploit the coherent nature of starlight speckles in the focal plane, effectively distinguishing between incoherent planetary light and coherent stellar light [81, 82, 83, 84]. This method requires precise intensity measurements, making it sensitive to errors and noise [22, 24]. The CDI algorithm measures the wavefront's self-interference in real-time to capture image-specific speckle characteristics, which are then used to subtract a coherent speckle model from the science image. The success of this algorithm critically depends on the accuracy of these focal plane wavefront measurements, as errors can degrade the subtraction quality and leave residual speckle noise.

Among CDI approaches, the SCC offers a particularly effective implementation by

encoding speckle phase and amplitude information directly in the focal plane through optical interference. Its optical configuration begins with a coronagraph that redirects on-axis starlight, leaving off-axis planetary signals and residual speckles. A portion of the redirected starlight passes through a pinhole in the Lyot stop, forming a reference beam with a broad diffraction pattern. This beam is recombined with the speckle field in the focal plane, producing spatially modulated fringes that encode the phase of the starlight. The fringe spatial frequency is set by the pinhole's displacement from the main pupil, analogous to Young's double-slit experiment. An optical chopper modulates the reference beam, allowing recovery of a key component of the wavefront through direct subtraction. This design preserves planetary signals, which remain unmodulated, while enabling high-fidelity wavefront reconstruction. An illustration of the SCC and resulting fringe pattern is shown in Figure 1.23.

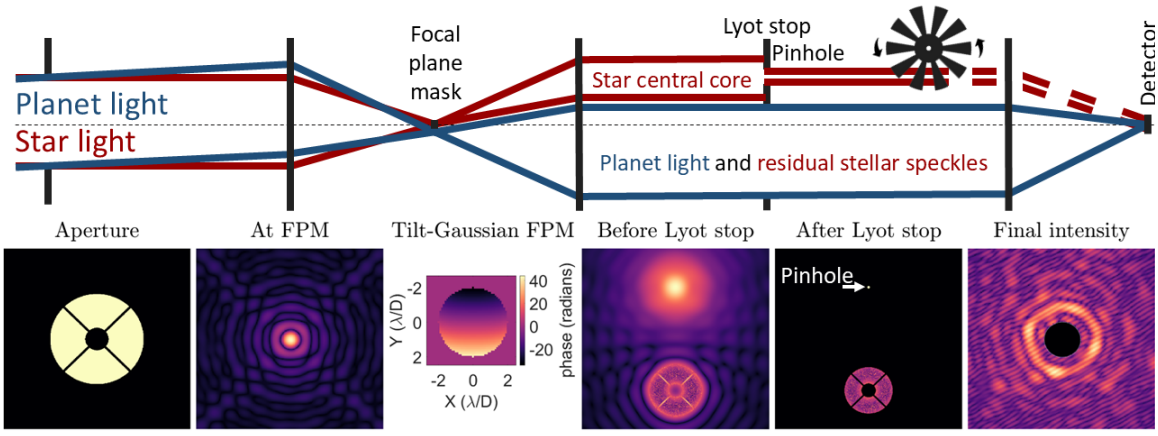

Figure 1.23: Animated schematic of the Self-Coherent Camera (SCC) optical path with fringed and unfringed focal plane images. Incoming starlight is tilted off-axis and defocused using a tilt-Gaussian phase focal plane mask (FPM), splitting into science and reference paths, passing through the Lyot stop/pinhole, then recombined to produce spatial fringes in the focal plane. The final focal plane intensity is rotated by 30° to better visualize the fringes and minimize fringe-aligned detector readout artifacts. ∼25 nm RMS phase errors with reduced low-order terms are used to simulate first stage adaptive optics (AO) residuals.

Mathematically, the focal plane intensity in the presence of the reference beam is expressed as:

$$I(\alpha) = |A_{\text{star}}|^2 + |A_{\text{ref}}|^2 + |A_{\text{planet}}|^2 + A_{\text{star}} A_{\text{ref}}^* e^{\frac{2\pi i\, \alpha\, \xi_0}{\lambda}} + A_{\text{star}}^* A_{\text{ref}}\, e^{\frac{-2\pi i\, \alpha\, \xi_0}{\lambda}}, \quad (1.48)$$

where α is the angular coordinate in the science image, and A_{star}, A_{planet}, and A_{ref}

represent the complex amplitudes of the starlight, planetary signal, and reference beam, respectively. Here, I_i denotes the intensity $|A_i|^2$, A_i^* is the complex conjugate of A_i, and ξ_0 is the spatial separation between the main beam and the reference pinhole in the pupil plane. Utilizing the relationship between the wavefront amplitude and measured intensity, as discussed in §1.3.2, Equation 1.48 can be rewritten as:

$$I_{\mathrm{SCC}} = I_{\mathrm{star}} + I_{\mathrm{planet}} + I_{\mathrm{ref}} + 2M\sqrt{I_{\mathrm{star}} I_{\mathrm{ref}}}, \tag{1.49}$$

where M is the modulation factor (or the 'fringe function', varying between 0 and 1) introduced by the interference, carrying the phase information of the starlight, and the factor of 2 accounts for the complex conjugate pair within this fringed pattern. Since the reference beam is derived from the starlight and shares the same optical prorogation length, it remains coherent with the stellar speckles, enabling an interferometric measurement of the phase aberrations.

To extract the planetary intensity, Fourier-based filtering and analyses are employed. The spatial modulation introduced by the off-axis reference creates shifted sub-Nyquist peaks in the Fourier transform of $I(\alpha)$ (the optical transfer function, OTF), referred to as side lobes. By isolating only one of the specific side lobes in the OTF, both the factor of 2 in the fringe term and the modulated component M in Eq. 1.49 are removed, allowing separation of the different spatial frequency components. This is achieved by using a binary mask to isolate the side lobe, and then shifting it to the centre of the Fourier plane, which alters only the phase of the focal plane intensity, not its amplitude. The high-frequency side lobe can be represented as:

$$|I_-| = \sqrt{I_{\mathrm{star}} I_{\mathrm{ref}}} = \left| \mathcal{F}^{-1}\Big(\mathrm{shift}\Big(\mathcal{F}(I_{\mathrm{SCC}}) \cdot \mathrm{mask}_1\Big)\Big) \right|, \tag{1.50}$$

while the main lobe of the image, already centred in the frequency plane and Nyquist sampled, contains the incoherent sum of focal plane intensities:

$$I_{\mathrm{incoherent}} = I_{\mathrm{star}} + I_{\mathrm{planet}} + I_{\mathrm{ref}} = \left| \mathcal{F}^{-1}\Big(\mathcal{F}(I_{\mathrm{SCC}}) \cdot \mathrm{mask}_2\Big) \right|. \tag{1.51}$$

The pinhole point spread function (PSF) can be directly obtained from the differential image using the optical chopper:

$$I_{\mathrm{ref}} = \left| \mathcal{F}^{-1}\Big(\mathcal{F}(I_{\mathrm{SCC,\ fringed}} - I_{\mathrm{unfringed}}) \cdot \mathrm{mask}_3\Big) \right|. \tag{1.52}$$

If the pinhole PSF I_{ref} is perfectly recovered (without considering noise), a reconstruction of I_{star} can be achieved by the following:

$$I_{\text{star}} = \frac{|I_-|^2}{I_{\text{ref}}}. \tag{1.53}$$

This process recovers the terms corresponding to the starlight, the reference beam, and the interference term, as illustrated in Figure 1.24.

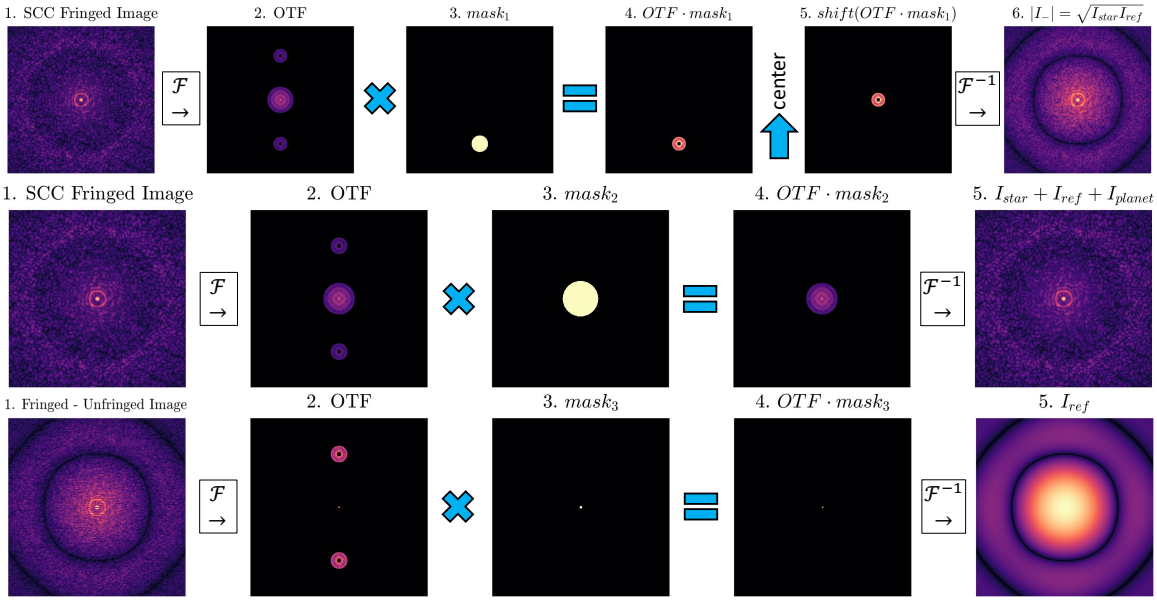

Figure 1.24: Low-pass filtering of the side lobe (top row) and main pupil (middle row) from the fringed SCC focal plane image at the end of the optical path in Figure 1.23. A subtraction of the fringed and unfringed images provides the pinhole PSF after masking and filtering (bottom row).

Thus, a full subtraction of all terms in Equation 1.49, except for I_{planet}, is achievable. Assuming the pinhole PSF is noiseless, the subtracted image I_{CDI} is given by:

$$I_{\text{CDI}} = (I_{\text{star}} + I_{\text{planet}} + I_{\text{ref}}) - \left(\frac{|I_-|^2}{I_{\text{ref}}} + I_{\text{ref}}\right) = I_{\text{planet}} + \left(I_{\text{star}} - \frac{|I_-|^2}{I_{\text{ref}}}\right). \tag{1.54}$$

As shown in Equation 1.54, if the star and reference PSF are perfectly reconstructed, the term $\left(I_{\text{star}} - \frac{|I_-|^2}{I_{\text{ref}}}\right)$ becomes zero, leaving only the planetary intensity. Although numerical noise from floating-point arithmetic, round-off, and discretization is inevitable, the CDI algorithm can still achieve extreme contrast gains when the measured and filtered images are sufficiently accurate. Figure 1.25 illustrates a noiseless

simulation of the CDI subtraction for both the case with and without extremely dim companions. CDI using the SCC can offer significant advantages for high-contrast

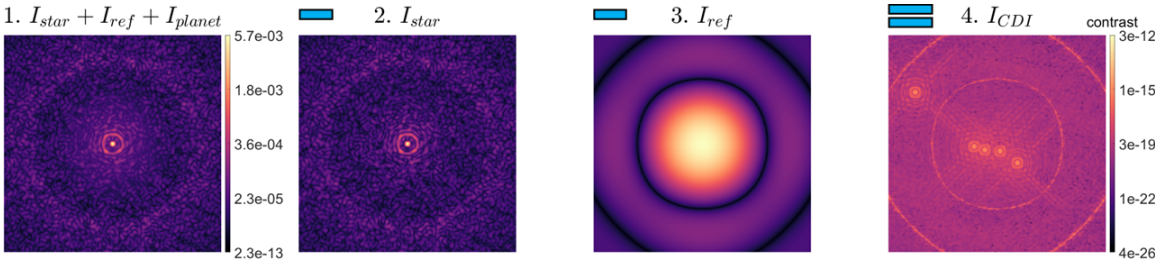

Figure 1.25: Animation of final CDI-subtracted intensity for 10^{-15} contrast companions (10^6 dimmer than Earth in the visible) and the subtracted intensity without companions, illustrating the average 10^{20} contrast gain from a noiseless simulation subtraction. The final plot is divided by the peak intensity of the unocculted star to provide numerical contrast values at each pixel. The image is in logarithmic scale to better visualize the contrast improvement across many orders of magnitude.

imaging. By utilizing a reference beam that propagates through the same optical path as the science beam, non-common-path aberrations are inherently minimized. The use of focal plane interferometry enhances sensitivity to low and high-order aberrations, which can be challenging to measure with conventional wavefront sensors. Furthermore, because the planet's signal remains unmodulated, the SCC facilitates simultaneous wavefront sensing and scientific observation, making it an efficient and powerful tool for direct exoplanet imaging.

Spectral Differential Imaging (SDI)

While the previously discussed differential techniques (RDI, ADI, CDI) suffer from chromatic spreading of the PSF and are optimal in monochromatic or narrowband cases, SDI leverages the chromatic dependence of speckle patterns and uses images at multiple wavelengths to better isolate the planet signal. Since speckles scale predictably with wavelength, exoplanets may exhibit strong spectral features at certain wavelengths only. Therefor, subtracting images at different wavelengths can enhance planetary signals [23, 24, 80].

The SDI algorithm registers images from multiple spectral channels using image magnification, speckle alignment, and pixel modulation transfer function (MTF) correction to construct a speckle noise model with minimal distortion. This model is then subtracted from the observational data to suppress speckle noise. SDI is particularly effective for detecting methane-rich exoplanets but can be limited by chromatic

aberrations and low spectral contrast between the star and planet.

Polarization Differential Imaging (PDI)

Further looking at other properties of light, PDI exploits the differing polarization properties of stellar and planetary light. Starlight is typically minimally polarized, whereas scattered light from circumstellar disks or planetary atmospheres often exhibits polarization. By measuring polarization states, PDI can suppresses unpolarized speckle noise while preserving astrophysical signals [24].

The PDI algorithm utilizes acquires images at different polarization angles, then constructs and subtracts an unpolarized speckle noise model. This isolates polarized features, enhancing the visibility of disks and planetary signals. High polarimetric sensitivity and calibration are crucial due to the typically low polarization fraction of exoplanet light.

Combined Approach

Each of the aforementioned differential imaging techniques plays a crucial role in high-contrast imaging, and their effectiveness is often enhanced when combined. Depending on the observational conditions and goals, the combined impact of speckle subtraction techniques can significantly improve the contrast of companions around a host star. Continued advancements in instrument calibration, stability, and post-processing algorithms will further improve speckle suppression, pushing the limits of exoplanet imaging and characterization.

1.3.9 Pupil Plane Wavefront Sensing

Wavefront sensing is a key component of adaptive optics (AO) systems, enabling the measurement of wavefront distortions caused by atmospheric turbulence or aberrations within the optical system. Atmospheric turbulence primarily introduces phase errors, although amplitude variations through scintillation can also occur. Since aberrations are wavelength-dependent, wavefront measurements are typically performed within a small spectral band (within tens to hundreds of nanometers) to reduce chromatic effects and ensure accurate reconstructions [18].

Pupil plane wavefront sensing techniques operate by directly sampling the wavefront at the pupil plane. The most widely used techniques include the Shack-Hartmann Wavefront Sensor (SHWFS) and the emerging Pyramid Wavefront Sensor (PyWFS).

Shack-Hartmann Wavefront Sensor (SHWFS)

The SHWFS is one of the most widely used methods for wavefront sensing in AO, due to its simplicity, robustness, and effective performance. The SHWFS utilizes a lenslet array to divide the incoming wavefront into multiple sub-apertures, each of which produces a focal spot on the detector plane. By measuring the displacement of these focal spots from their nominal positions, the local slopes of the wavefront can be determined [85], illustrated in Figure 1.26.

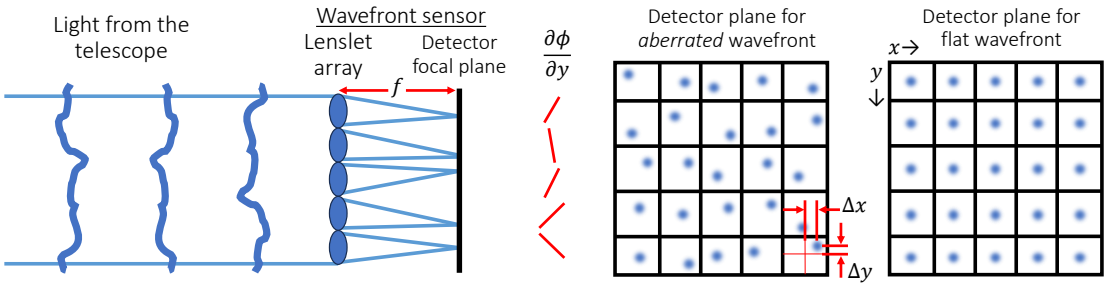

Figure 1.26: Schematic of the Shack-Hartmann Wavefront Sensor (SHWFS). A wavefront traveling through a lenslet array forms focal spots on a detector (left), with their shape and position a function of any present aberrations (middle). A flat wavefront produces centred and focused spots (right).

The wavefront slope provides direct information about the gradient of the phase. For a given grid point (i, j) in the Shack-Hartmann array, the local wavefront slopes along the x- and y-axes are given by:

$$\left.\frac{\partial \phi}{\partial x}\right|_{i,j} = \frac{\Delta x_{i,j}}{f}, \qquad \left.\frac{\partial \phi}{\partial y}\right|_{i,j} = \frac{\Delta y_{i,j}}{f}, \tag{1.55}$$

where $\Delta x_{i,j}$ and $\Delta y_{i,j}$ represent the displacement of a focal spot from its nominal position along the x- and y-axes, respectively, and f is the focal length of the lenslet array. These equations form the basis for wavefront reconstruction using the SHWFS, providing a method for recovering the wavefront phase across the pupil plane from local slope measurements. Centroiding algorithms are used to determine the centre of each spot created by the lenslet array. By recovering these centroids, the wavefront measurements can be directly converted to deformable mirror corrections, which flatten the wavefront phase, as discussed in subsequent section 1.3.11. Smaller lenslet sizes can be used to improve spatial resolution, but they demand higher de-

tector resolution, increased computational resources, and more illumination or longer integration times due to reduced light throughput. Furthermore, if the incoming distortions are too large, the focal spots may not stay in their local regions, contaminating other slope measurements and reducing the local slope measurement accuracy.

Pyramid Wavefront Sensor (PyWFS)

The Pyramid Wavefront Sensor (PyWFS) is a highly sensitive wavefront sensing technique, capable of detecting both low- and high-order aberrations in AO systems. It utilizes a pyramidal prism to split an incoming focused wavefront into four beams, which are subsequently directed onto a detector. The resulting intensity distribution encodes local wavefront slopes, enabling wavefront sensing in the pupil plane [86, 87, 88]. By analyzing intensity variations across the four quadrants, the wavefront can be reconstructed, provided the sensor operates within its linear response regime. The focused beam may be centred on the pyramid tip, maximizing sensitivity at the expense of a reduced linear range, or modulated around the tip to extend the sensor's dynamic range. This modulation improves robustness to larger aberrations by distributing intensity more evenly across the quadrants. A schematic representation of the PyWFS is shown in Figure 1.27.

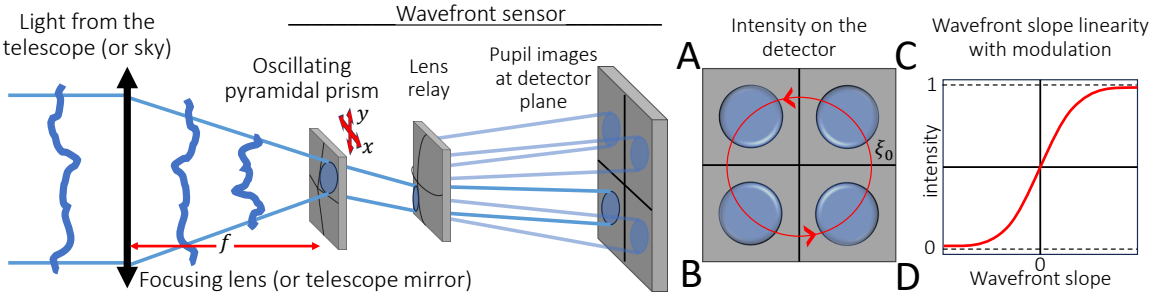

Figure 1.27: Schematic of the Pyramid Wavefront Sensor (PyWFS). The pyramidal prism is modulated in a circular motion (left), sequentially shifting the beam between quadrants on the detector (middle). The sensor exhibits a linear response for small wavefront distortions but transitions to a nonlinear regime near saturation or the noise floor (right).

The local wavefront slopes along the x- and y-axes are extracted from the intensity differences measured in the four detector quadrants. These slopes are proportional to

the normalized intensity gradients, given by:

$$\frac{\partial \phi}{\partial x} \approx \frac{\pi \xi_0}{2f} \frac{(I_\mathrm{B} + I_\mathrm{D}) - (I_\mathrm{A} + I_\mathrm{C})}{I_\mathrm{A} + I_\mathrm{B} + I_\mathrm{C} + I_\mathrm{D}}, \quad \frac{\partial \phi}{\partial y} \approx \frac{\pi \xi_0}{2f} \frac{(I_\mathrm{A} + I_\mathrm{B}) - (I_\mathrm{C} + I_\mathrm{D})}{I_\mathrm{A} + I_\mathrm{B} + I_\mathrm{C} + I_\mathrm{D}}. \tag{1.56}$$

Here, $\frac{\partial \phi}{\partial x}$ and $\frac{\partial \phi}{\partial y}$ represent the local wavefront slopes in the respective directions, while $I_\mathrm{A}, I_\mathrm{B}, I_\mathrm{C}$, and I_D correspond to the measured intensities in each quadrant. The parameter ξ_0 scales the intensity measurements to the wavefront phase gradient and depends on the modulation amplitude. The focal length f influences the sensor's sensitivity, with longer focal lengths increasing angular separation and enhancing spatial resolution. The numerator in each expression represents the differential intensity between opposing quadrants, encoding the local wavefront gradient. The denominator normalizes these values to maintain robustness against variations in total intensity, ensuring stable performance under fluctuating flux conditions.

Appropriate modulation of the pyramid tip enables a predominantly linear response, facilitating accurate wavefront reconstruction. This linearity is critical in high-order AO systems where precision and sensitivity are essential. Compared to the SHWFS, the PyWFS provides superior spatial resolution by directly sampling phase information across the entire detector grid, enabling finer detail recovery and improved correction of high-order aberrations. However, outside the linear regime or under significant aberrations, advanced reconstruction techniques are usually required [89, 90]. In extreme cases, saturation or null intensities can disrupt slope calculations, potentially destabilizing the control loop and degrading system performance.

1.3.10 Focal Plane Wavefront Sensing

Focal plane wavefront sensing (FPWFS) enables direct estimation of optical aberrations from the science image, facilitating real-time correction while mitigating non-common-path aberrations (NCPAs). Unlike pupil plane sensors, which measure the wavefront before any focal plane modifications, FPWFS operates within the same optical path as the science camera, capturing aberrations introduced along the way.

The Self-Coherent Camera (SCC), introduced in §1.3.8 and illustrated in Figure 1.23, leverages the coherence of starlight to retrieve the full complex electric field (amplitude and phase) of residual stellar speckles [81, 82, 83, 84]. By analyzing interference fringes in the focal plane, the SCC provides a way to directly estimate the wavefront. The interference terms in Equation 1.48 encode the aberrated wavefront,

appearing as lateral side lobes in Fourier space, shifted by $\pm\xi_0/\lambda$. Spatial filtering isolates one of these peaks, defining Equation 1.50. The estimated complex wavefront field in the pupil plane is then given by:

$$\Psi_{\text{est}}(\epsilon) = \mathcal{F}^{-1}\left[\frac{I_-(\alpha)}{A_{\text{R}}^*(\alpha)\, M(\alpha)}\right] \cdot L(\epsilon), \tag{1.57}$$

where ϵ and α denote pupil and focal plane coordinates, respectively. The pupil function $L(\epsilon)$ represents the Lyot stop transmission, where $L(\epsilon) = 1$ inside the stop and $L(\epsilon) = 0$ elsewhere. The coronagraphic mask function $M(\alpha)$ is defined as $M(\alpha) = e^{i\phi_{\text{FPM}}(\alpha)}$, where $\phi_{\text{FPM}}(\alpha)$ represents the focal plane mask phase shift. The term $A_{\text{R}}^*(\alpha)$ is the conjugate reference field amplitude, which can be estimated as the ratio between the isolated reference PSF and root of the stellar PSF ($I_-/\sqrt{I_{\text{star}}}$). Equation 1.57 provides a direct reconstruction of the complex wavefront field associated with upstream aberrations. The recovered wavefront $\Psi_{\text{est}}(\epsilon)$ can then be expressed in amplitude and phase components:

$$\Psi_{\text{est}}(\epsilon) = A_{\text{est}}(\epsilon)\, e^{i\phi_{\text{est}}(\epsilon)}, \tag{1.58}$$

where:

$$A_{\text{est}}(\epsilon) = \left|\Psi_{\text{est}}(\epsilon)\right|, \quad \phi_{\text{est}}(\epsilon) = \arg\left(\Psi_{\text{est}}(\epsilon)\right). \tag{1.59}$$

Figure 1.28 illustrates the reconstructed wavefront amplitude and phase components within the valid sensing region behind the Lyot stop, corresponding to the spatial domain where a deformable mirror (DM) can effectively apply corrections.

Although the wavefront is effectively reconstructed, direct phase extraction from the wrapped phase ($\phi_{\text{est}}(\epsilon)$) is not feasible due to noise and artifacts introduced by phase unwrapping. Therefore, model-based iterative phase retrieval techniques are required to produce a continuous and accurate phase estimate [84, 91]. These algorithms minimize discrepancies between the observed and modeled SCC intensities by fitting a forward model to the data. A calibration procedure generates an orthogonal set of phase modes corresponding to speckles at distinct locations in the focal plane. When applied to a DM, these modes allow controlled suppression of stellar speckles while preserving planetary signals. Proper calibration is crucial to prevent overfitting and artifacts in the PSF. Figure 1.29 illustrates how a sine wave applied to the wavefront phase creates off-axis fringed point sources and speckle patterns in the SCC image, which are determined by the phase direction, frequency, and magnitude.

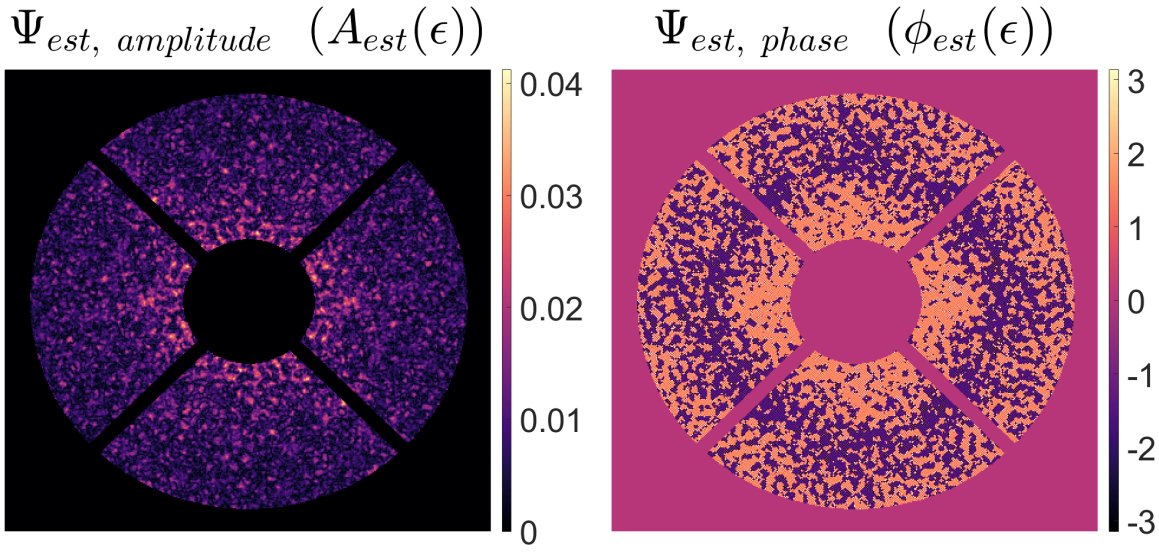

Figure 1.28: Estimated wavefront amplitude (left) and phase (right) components from self-coherent camera (SCC) images containing ∼25 nm RMS phase errors, with reduced low-order terms to simulate first-stage adaptive optics (AO) residuals. The wrapped phase cannot be directly used for real-time wavefront correction, as deformable mirrors require a continuous surface for accurate wavefront shaping.

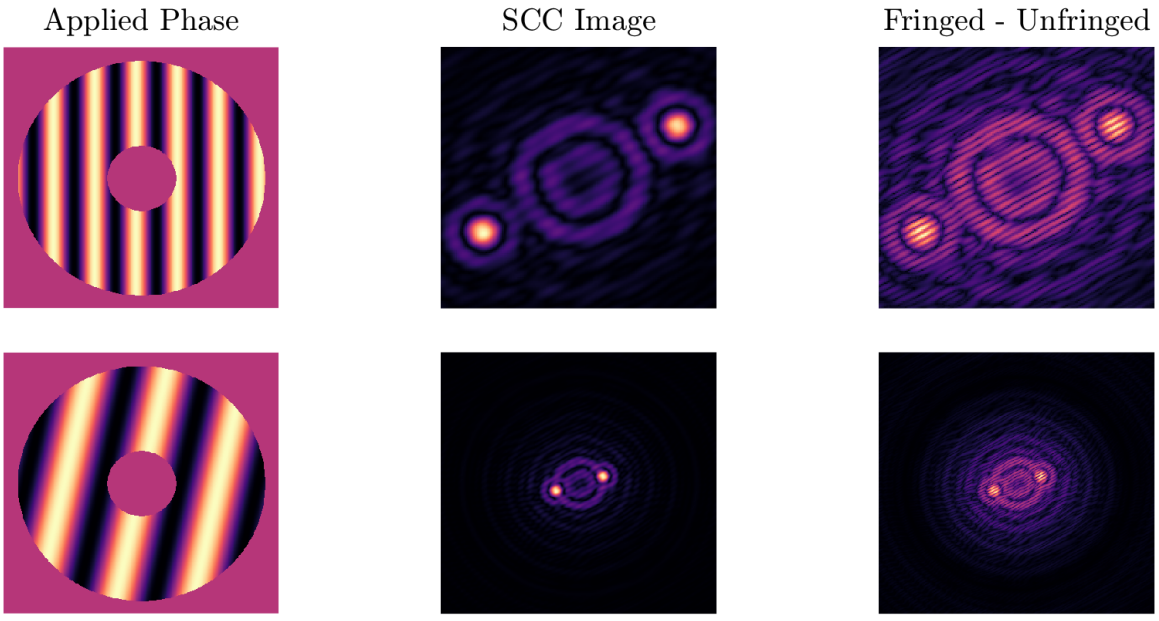

Figure 1.29: Animation of arbitrary sinusoidal phase modes (left column) applied to the wavefront in the pupil plane in a noiseless simulation. The resulting PSF pairs in the SCC image are shown in the middle column, and the fringed minus the optically chopped unfringed image in the right column. The top row illustrates the effect of lateral phase adjustments on the fringe phase, while the bottom row shows the influence of spatial frequency and orientation on speckle placement.

FPWFS using the SCC provides a powerful solution for real-time stellar speckle nulling. With precise calibration, this method enables accurate wavefront reconstruction, providing the DM with high-fidelity phase commands for real-time corrections, enhancing planetary signal contrast while effectively managing residual speckles.

1.3.11 Deformable Mirrors for Wavefront Correction

Deformable mirrors (DMs) are essential components in adaptive optics (AO) systems, designed to correct wavefront distortions in real-time. Early DM technologies utilized segmented mirrors, where each segment can be independently actuated to modify the piston, tip, or tilt at discrete locations. A widely adopted early approach involves a single thin-walled continuous mirror, actuated by a grid of actuators behind it, enabling uniform and continuous surface deformations. Advances in materials and actuator technologies, such as piezoelectric actuators and microelectromechanical systems (MEMS), have significantly improved the dynamic range, precision, and speed of continuous surface DMs. These advancements have made such DM architectures indispensable for high-resolution astronomical imaging, enabling precise correction of atmospheric turbulence and instrumental aberrations, thereby significantly improving the contrast and resolution of astronomical observations [18, 92].

In typical AO systems, the DM is placed in a plane conjugate to the telescope's entrance pupil and located upstream of the wavefront sensor (WFS), as shown in Figure 1.6. This configuration enables the DM to correct phase aberrations across the pupil while allowing the WFS to measure the corrected wavefront. Although alternative setups exist, such as open-loop systems with the DM placed after the WFS [93] or in focal plane wavefront sensing regimes (§1.3.10), the DM is generally conjugated to the entrance pupil and operates on the same principles. It corrects aberrations by deforming its reflective surface using an array of actuators that adjust the optical path length at specific pupil locations. These corrections are computed from WFS measurements, as discussed in §1.3.9 and §1.3.10.

Limitations: Speed, Fitting Error, and Stability Constraints

While DMs are indispensable for high-precision wavefront correction, they have inherent limitations that can influence their performance. These limitations must be carefully considered to optimize the effectiveness of DMs in practical applications. The following factors are essential in determining their capabilities and constraints:

- **Temporal Response:** The ability of a DM to correct dynamic aberrations, such as those induced by atmospheric turbulence, depends on its temporal response. Since turbulence evolves on millisecond timescales, high-speed actuators and a low-inertia system are necessary to minimize residual wavefront errors that degrade image quality.

- **Fitting Error and Spatial Frequency Limitations:** The spatial resolution of a deformable mirror (DM) is primarily determined by the actuator density. The smallest spatial scale that a DM can correct, known as the fitting error (Λ), is governed by the actuator spacing and is given by:

$$\Lambda \sim d_{\text{act}}, \tag{1.60}$$

  where d_{act} is the spacing between actuators in meters. This represents the smallest feature size of an aberration that can be corrected. Additionally, the maximum spatial frequency the DM can correct is limited by the number of actuators and the pupil diameter, and is given by:

$$f_{\max} = \frac{N_{\text{act}}}{2D}, \tag{1.61}$$

  where N_{act} is the number of actuators across the pupil diameter D in meters. This sets the highest spatial frequency the DM can correct, measured in cycles per pupil. At this limit, only one quadrature component of the aberration can be corrected, either the sine or cosine term, but not both. Increasing the actuator count expands the *correction region* in the coronagraphic image, enabling deeper contrast in the focal plane around the star. Insufficient actuator density leaves higher-order aberrations uncorrected.

- **Mechanical and Thermal Stability:** External disturbances, such as vibrations, ambient sound, and thermal fluctuations, can degrade DM performance by introducing unwanted aberrations. Effective environmental control is crucial for maintaining the accuracy of wavefront correction.

- **Actuator Hysteresis and Calibration:** Some DMs exhibit hysteresis, where the actuator response is influenced by prior commands. This introduces nonlinearity into the system, requiring precise pre-characterization and calibration to mitigate its impact on the correction process.

- **Implementation Challenges:** Practical limitations include actuator crosstalk, print-through, scalloping, dead or drifting actuators, influence function coupling, and nonuniform actuator gain. These effects can degrade correction fidelity, particularly at high spatial frequencies, and often require calibration or hardware-level mitigation.

Addressing these limitations is essential for optimizing DM performance in wavefront correction, thereby enhancing its ability to correct aberrations and improving both imaging quality and observational resolution.

Fitting a Deformable Mirror to a Phase Measurement

In AO systems, shaping a DM to correct a derived phase measurement is a critical task. A DM generally consists of a discrete array of actuators, each contributing locally to the overall mirror surface deformation. The resulting shape is the cumulative effect of all actuator contributions. Each actuator's influence is commonly modeled as a Gaussian function centred at its position. However, more accurate representations can be obtained by directly measuring the influence function of a specific DM, as it may vary between systems [94]. For simplicity, the DM surface, $\phi_{\mathrm{DM}}(x, y)$, can be closely approximated using a Gaussian influence function, expressed as:

$$\begin{aligned} \phi_{\mathrm{DM}}(x, y) &= \sum_{p,q} \mathbf{a}_{p,q} \exp\left(-\frac{(x - x_p)^2 + (y - y_q)^2}{2\sigma_{\mathrm{act}}^2}\right) \\ &= \sum_{p,q} \mathbf{a}_{p,q}\, \mathbf{G}(x - x_p, y - y_q), \end{aligned} \tag{1.62}$$

where σ_{act} is the characteristic width of the actuator influence, and $\mathbf{G}$ is the influence function applied to the actuator commands $a_{p,q}$ across the actuator grid indexed by p, q. This formulation ensures that the resulting surface is smooth and continuous, effectively accounting for inter-actuator coupling.

The goal of DM fitting is to compute the actuator commands that best reconstruct the target phase screen. This can be formulated as a least-squares problem, though in practice it is often more efficient to apply an iterative approach. The iterative method updates the actuator commands based on the residual between the current DM surface and the target phase. The update rule is given by:

$$\mathbf{a}_{\mathrm{new}} = \mathbf{a}_{\mathrm{old}} + \left(\phi_{\mathrm{target}} - \mathbf{G} * \mathbf{a}_{\mathrm{old}}\right), \tag{1.63}$$

where **G** is the convolution kernel describing the actuator influence function, and ϕ_{target} is the phase screen to be fitted. This update is applied iteratively until the residual between the fitted surface and the target falls below a specified convergence threshold. Once converged, the DM surface is resampled onto the high-resolution simulation grid using cubic spline interpolation. The quality of the fit can be assessed by computing the root-mean-square (RMS) residual error, ϵ_{fit}, defined as:

$$\epsilon_{\text{fit}} = \sqrt{\frac{1}{N_{\text{pix}}} \sum_{i,j} \left(\phi_{\text{target}}[i,j] - \phi_{\text{DM}}[i,j]\right)^2}, \tag{1.64}$$

where N_{pix} is the total number of pixels in the phase grid. This metric quantifies the

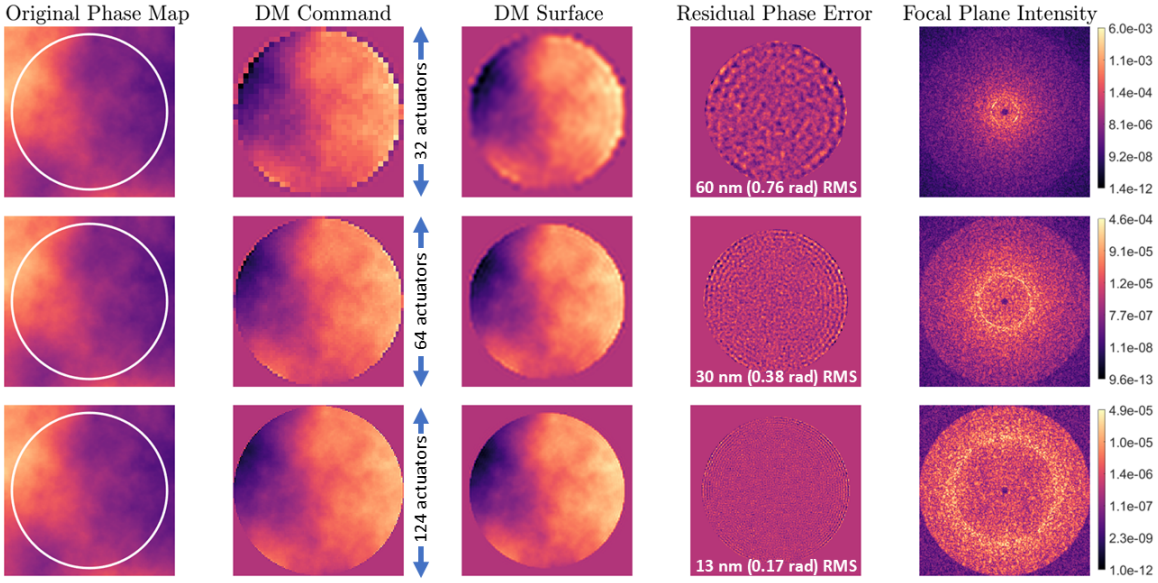

Figure 1.30: Animated example of three deformable mirrors (DMs) of varying actuator densities correcting an $r_0 = 20$ cm atmosphere on a 10 m telescope through iterative fitting and subtraction. The wavefront phase (first column), Gaussian-coupled actuator commands (second column), reconstructed DM surface via cubic spline interpolation (third column), residual phase error with RMS values (fourth column), and focal plane intensity, propagated through an apodized aperture and focal plane mask with (first frame) or without (second frame) a Lyot stop coronagraph, is presented with contrast scales to quantify improvement (fifth column).

residual phase structure that remains uncorrected due to the finite spatial resolution of the DM. As the actuator density increases, the residual error decreases, enabling more accurate reproduction of the target wavefront and improved overall performance of the AO system. An example illustrating the impact of actuator density on phase

fitting and the resulting coronagraphic image quality is shown in Figure 1.30.

Cost of Implementation

The cost of implementing a DM scales with the number of actuators, which directly impacts the quality of wavefront correction and the achievable image contrast. Entry-level devices, such as 12×12 actuator arrays (120 active actuators), are available from manufacturers like Thorlabs for approximately $20,000 USD [95]. However, high-contrast imaging applications typically require substantially higher actuator counts to adequately correct fine wavefront features (as illustrated in Fig. 1.30). Systems with up to 64 actuators across the pupil (approximately 3200 active actuators) are available from vendors such as Boston Micromachines [96] and ALPAO [97], though these can exceed $500,000 USD and often involve long lead times. To meet the demand for larger and more precise corrective capabilities, ALPAO has begun developing DMs with more than 10,000 active actuators, targeting further reductions in residual wavefront error. Despite these advancements, on-sky implementations such as Subaru's AO3K system, with a 3224-actuator DM [98], highlight the practical limitations in cost, scalability, and system complexity. These trends underscore the trade-offs between performance and affordability, reinforcing the need for continued innovation in DM technology and AO system design.

Paths to Optimization

Continued advancement in DM technology is essential for enabling the next generation of high-performance AO systems. Several key areas require ongoing development to improve system capability, robustness, and scientific return:

- **Increased actuator density:** Finer spatial control of the wavefront enables improved correction and higher contrast. However, increasing actuator count also expands the control space, necessitating more advanced wavefront reconstruction algorithms. Multi-DM architectures, where separate DMs address low and high-order aberrations, offer an approach to improved correction across a broad spatial frequency range, implemented on GPI and SPHERE [37, 40].

- **High-speed control loops:** To maintain correction accuracy under rapidly changing conditions, control loops must run at kilohertz rates, requiring low-latency wavefront sensing, fast reconstruction algorithms, and real-time computing hardware suited to dynamic observing environments.

- **Suppression of environmental disturbances:** Mechanical vibrations, optical bench flexure, and thermal drift can degrade AO performance over time. Mitigating these disturbances through a combination of active control and passive isolation strategies is essential for ensuring long-term system stability and calibration accuracy.
- **Integration of predictive control and machine learning:** Emerging techniques in predictive control and data-driven modeling offer substantial improvements in real-time wavefront estimation. These methods can anticipate atmospheric evolution, reduce latency-induced errors, and adaptively optimize system performance under variable observing conditions.

Together, these developments represent critical steps toward achieving deeper contrast at smaller angular separations, directly supporting the detection and characterization of exoplanets and other faint astronomical targets.

1.3.12 Wavefront Error Budget and Strehl Expectations

In high-contrast exoplanet imaging, accurately estimating the wavefront error (WFE) budget is critical for optimizing the performance of adaptive optics (AO) systems. The WFE budget quantifies the key sources of residual error, helping to guide the design trade-offs that maintain high image quality [99]. The principal contributors to WFE generally include:

- **Algorithmic Error**: This arises from limitations in the wavefront reconstruction and control algorithms, particularly due to discretization and numerical approximations.
- **Temporal Error**: Introduced by the latency in the AO control loop, leading to a phase lag in wavefront correction.
- **Wavefront Sensor (WFS) Detection Noise**: Includes contributions from photon noise, read noise, and bit depth limitations, which all degrade the fidelity of the wavefront measurement.
- **Deformable Mirror (DM) Fitting Error**: Due to the finite number of actuators on the DM, some high spatial frequency aberrations remain uncorrected beyond the DM's control bandwidth.

- **Non-Common Path Aberrations (NCPA)**: These static aberrations arise from differences in the optical paths between the science and wavefront sensing paths, requiring calibration and post-processing to be corrected.
- **Environmental Disturbances**: Vibrations, thermal drifts, and mechanical flexure can introduce dynamic wavefront errors that are not fully compensated by the AO system.

An example WFE budget for a typical exoplanet imaging AO system is shown in Table 1.8. The root-mean-square (RMS) values listed are indicative and should be refined for a specific system based on its architecture and performance goals.

Table 1.8: Example wavefront error (WFE) budget for a representative exoplanet imaging AO system, utilizing a Shack-Hartmann wavefront sensor (WFS) and 64×64 deformable mirror (DM) [99]. The total WFE is calculated as the quadrature sum (root-sum-square, RSS), assuming statistical independence of the error sources.

Error Source	**RMS WFE (nm)**
Algorithmic Error	15
Temporal Error	8
WFS Detection Noise (Photon, Read, Bit Depth)	50
DM Fitting Error	30
Non-Common Path Aberrations (NCPA)	10
Environmental Disturbances	20
Quadrature Sum (RSS)	**65**

The total WFE is derived using the root-sum-square (RSS) method, which assumes that the error sources are statistically uncorrelated. Effectively managing these contributions is crucial, as overcorrecting one error term at the expense of others may not improve overall performance. A well-optimized WFE budget ensures robust AO performance, which is necessary to achieve the high contrast levels needed for exoplanet detection.

Strehl Ratio and the Maréchal Approximation

The Strehl ratio (SR) serves as a helpful metric for optical image quality. It is defined as the ratio of the peak intensity of an aberrated point spread function (PSF) to that of a diffraction-limited, aberration-free PSF [18]. Consequently, the SR is directly

related to the residual WFE, which represents the RMS deviation from a perfect wavefront [100]. To account for potential lateral shifts in the peak of the aberrated PSF due to tip and tilt errors, the SR is typically computed using the maximum intensity value from each PSF rather than a fixed on-axis peak. For systems exhibiting small, approximately Gaussian-distributed aberrations, the Maréchal approximation provides a widely used estimate for the SR:

$$S = \frac{\max(I_{\text{aberrated}})}{\max(I_{\text{perfect}})} \approx \exp\left(-\left(\frac{2\pi \text{WFE}}{\lambda}\right)^2\right), \tag{1.65}$$

where λ is the wavelength of observation and WFE is the residual wavefront error in nanometers or meters. As the WFE decreases, the Strehl ratio increases, indicating improved optical quality and a more concentrated PSF. The approximation is most accurate for WFEs less than approximately $\lambda/9$, beyond which its accuracy declines [101]. Figure 1.31 illustrates the Maréchal approximation of the Strehl ratio as a function of WFE from 0 to 200 nm RMS for different wavelength cases.

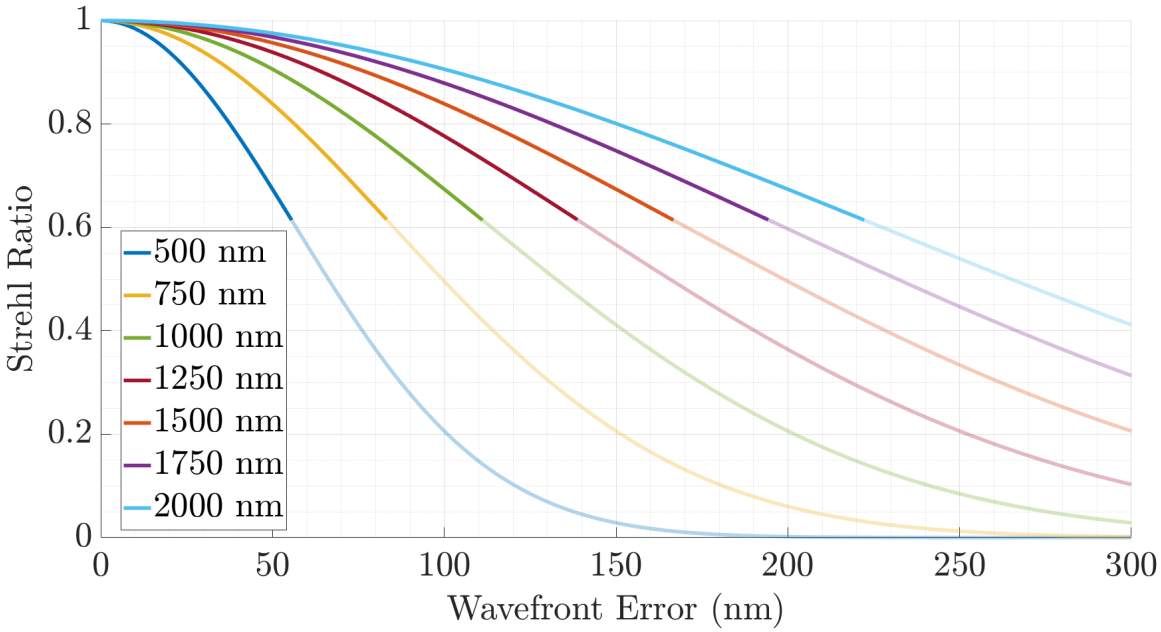

Figure 1.31: Visualization of the Maréchal approximation for Strehl ratio as a function of wavefront error (WFE) at various wavelengths. For a given WFE, shorter wavelengths experience greater phase distortion, resulting in a more pronounced reduction in Strehl ratio. The approximation becomes less accurate for WFEs exceeding approximately $\lambda/9$, as highlighted by the shift in transparency around a Strehl ratio of 0.62.

Chapter 2

SPIDERS: The Subaru Pathfinder Instrument for Detecting Exoplanets & Retrieving Spectra

The Subaru Pathfinder Instrument for Detecting Exoplanets and Recovering Spectra (SPIDERS) is a state-of-the-art instrument primarily developed by students, with substantial contributions from professionals at the National Research Council Canada (NRC) Herzberg Astronomy and Astrophysics Research Centre (HAA) and international collaborators. *This chapter examines the primary optical and mechanical design of SPIDERS, focusing on my contributions to the instrument, including the mechanical interfacing and alignment with the telescope, as well as the design and integration of both the system's optical chopper and the imaging Fourier transform spectrometer (IFTS). The success of the project has been made possible through collaborations with Principal Investigator C. Marois, Optical Engineer O. Lardière, Astronomer W. Thompson, and support from J. Fitzsimmons, T. Hardy, D. Gamroth, K. Caputa, F. Grandmont, A. Bews, and D. Kerr.*

2.1 Introduction

SPIDERS is a next-generation high-contrast imaging instrument developed to demonstrate the fast atmospheric self-coherent camera technique (FAST) on-sky for the first time [102, 103]. This method uses a common-path interferometer — the self-coherent camera (SCC; Fig. 1.23) — to enable real-time sensing and suppression of resid-

ual speckles directly in the focal plane across a ∼5 arcsecond field. The corrected beam is relayed to an imaging Fourier transform spectrometer (IFTS) with tunable spectral resolution and scan speed, enabling full-field, second-stage adaptive optics (AO)-corrected spectral data cubes. Initial laboratory tests using SPIDERS' internal source and a rotating phase screen, designed to emulate post-AO residual turbulence but currently run at a reduced speed during system development, achieved raw contrast levels down to 10^{-6} within the corrected dark hole, prior to post-processing.

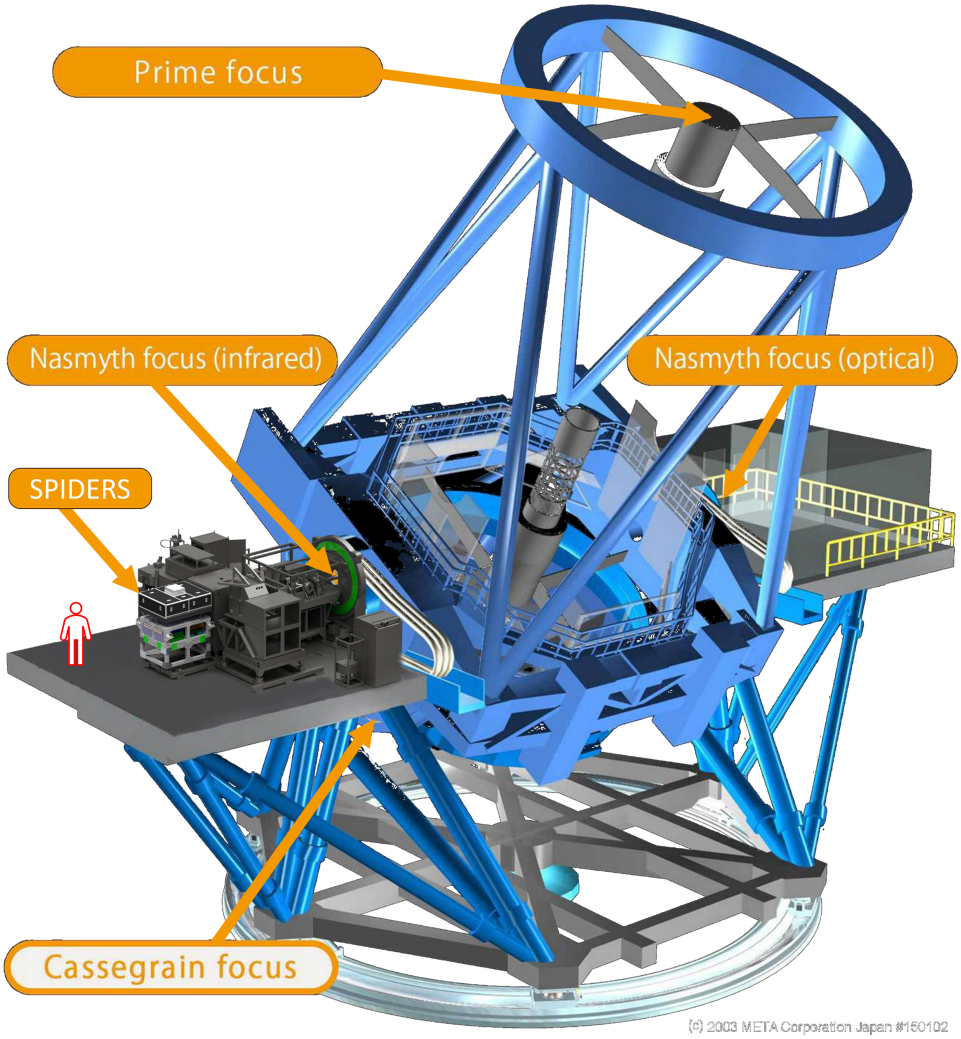

Figure 2.1: The SPIDERS instrument installed on the Nasmyth platform of the 8.2 m Subaru Telescope on Maunakea, Hawaii. During observations, the Nasmyth platforms rotate azimuthally to maintain alignment with the telescope's optical path. A human figure is shown for scale. Telescope image courtesy of the National Astronomical Observatory of Japan (NAOJ) [104].

Building on this performance, SPIDERS further combines angular, spectral, and coherent differential imaging (ADI, SDI, and CDI, respectively; see §1.3.8) to improve contrast sensitivity by up to two orders of magnitude in post-processing. This enables detection and characterization of faint astrophysical signals such as young giant exoplanets and debris disks, potentially surpassing the capabilities of previous instruments like the Gemini Planet Imager (GPI) [37]. Commissioning is scheduled for 2025–2026 on the infrared Nasmyth platform of the Subaru Telescope on Maunakea, Hawaii (Figure 2.1), where SPIDERS will operate behind Subaru's new AO3k system [98], using its partially corrected wavefront as input to SPIDERS' second-stage correction and science paths.

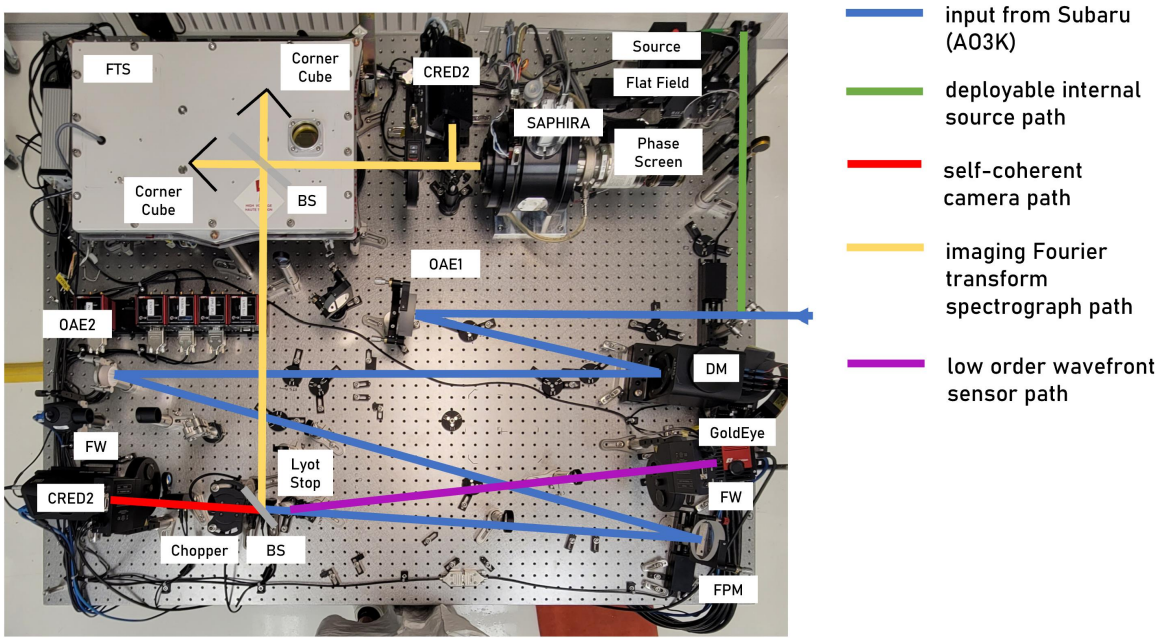

Figure 2.2: SPIDERS optical layout provided by W. Thompson [105]. Four primary optical paths are shown: the deployable calibration source (green) simulates the Subaru AO3k input (blue), both feeding three downstream paths — the self-coherent camera (SCC, red), Lyot-based low-order wavefront sensor (LLOWFS, purple), and imaging Fourier transform spectrograph (IFTS, yellow).

The optical design of SPIDERS, developed by Olivier Lardière et al. [106], integrates advanced wavefront control, interferometric sensing, and high-resolution spectroscopy within a compact optical system. To minimize chromatic aberrations and reduce the number of transmissive surfaces, SPIDERS uses off-axis ellipsoidal (OAE) mirrors to relay broadband infrared light between intermediate focal planes. As shown

in Fig. 2.2, four major optical paths pass through the same OAE mirrors, deformable mirror (DM), and masks:

- **Common Input Path:** Light from either the internal calibration source or AO-corrected starlight from Subaru's AO3k system is relayed through a shared optical path. This ensures both beams traverse identical downstream optics, maintaining alignment and calibration consistency.
  - **Calibration Source Input:** A deployable, internally calibrated light source used during integration, alignment, and commissioning to validate system performance and wavefront correction. A rotating phase screen simulates atmospheric residuals post-AO3k correction.
  - **Starlight Input from Subaru AO3k:** On-sky science and engineering observations use light corrected by AO3k, containing both residual wavefront errors and the astrophysical signal. This beam is relayed into SPIDERS for high-contrast imaging and spectroscopy.
- **LLOWFS Path (Lyot stop Low-Order Wavefront Sensor):** This path detects and corrects low-order aberrations (tip, tilt, vibration, flexure, thermal drift) that displace the stellar PSF, allowing light to bypass the coronagraph. Light blocked by the focal plane mask (FPM) is redirected at the Lyot stop to a *GoldEye* pupil plane wavefront sensor (§1.3.9), providing real-time feedback to the DM [107]. The LLOWFS works in tandem with focal plane-based high-order wavefront sensing strategies (§1.3.10) [91].
- **SCC Path (Self-Coherent Camera):** SPIDERS implements the SCC using the FAST method, which uses interference between residual speckles and a coherent reference beam at the focal plane (Fig. 1.23). An optical chopper modulates the interference pattern, allowing for real-time estimation and correction of quasi-static aberrations. This process generates a high-contrast "dark hole" around the star [79], significantly enhancing contrast. Additionally, the SCC enables CDI, further improving sensitivity to faint companions and circumstellar structures (Fig. 1.25).
- **IFTS Path (Imaging Fourier-Transform Spectrometer):** After correction by the LLOWFS and SCC, the beam enters the IFTS, which provides broadband imaging to R 20,000 spectral resolution over a 3.3 arcsecond field

of view at OPD scan speeds between 0.18 and 1.2 mm/s (§2.4). By acquiring interferograms across the focal plane, the IFTS reconstructs spectral data cubes during post-processing, enabling high-contrast, spatially resolved spectroscopy of exoplanet atmospheres and circumstellar material. The IFTS also facilitates SDI (§1.3.8), further enhancing sensitivity to faint astrophysical signals while providing precise spectroscopic characterization of exoplanet atmospheres, with superior throughput and flexible resolution compared to traditional spectroscopic methods (discussed in §1.2.5).

These complementary subsystems operate synergistically to achieve SPIDERS' core objectives: demonstrating FAST, CDI, and SDI on-sky using an IFTS, while paving the way for high-contrast imaging and spectroscopy of faint companions and circumstellar environments with unprecedented sensitivity.

2.2 Mechanical Constraints and Design

The SPIDERS system must satisfy a demanding set of mechanical requirements to ensure reliable operation within the spatial and environmental constraints of the Subaru telescope. These requirements include structural rigidity, thermal, electrical, and vibrational stability, as well as precise alignment throughout integration and on-sky operation. The mechanical assembly must support the full optical bench, maintain strict positional relationships relative to the AO3k focus, and conform to the geometric and load-bearing limits of the Nasmyth platform interface. It must also accommodate thermal management hardware, enable fine alignment, and integrate robust mechanical and electrical interfaces within a compact, serviceable footprint. Table 2.1 summarizes the core mechanical requirements and corresponding specifications for the SPIDERS supporting structure and platform interface.

Table 2.1: Mechanical requirements and specifications for the SPIDERS optical bench support structure and platform interface.

Requirement	**Specification**
Maximum supported mass of the 1200 × 1500 mm optical bench assembly (including all mounted components and enclosure), with safety factor ≥ 2	400 kg

Maximum final assembly mass for craning, with structural safety factor ≥ 5 and commercial rigging hardware working load limit factor ≥ 1.5	900 kg
Comfortable working height of optical bench for lab assembly and development	900 - 1000 mm (floor to benchtop, parallel)
Lockable caster feet for lab maneuverability	Rated for $\geq$ lab weight
Nominal position and orientation of SPIDERS focus relative to AO3k focus	$\Delta X = 9.687$ mm (horizontal) $\Delta Y = 200.0$ mm (vertical) $\Delta Z = 1954.3$ mm (depth) Yaw = 0.178° (clockwise, looking down) Roll, Pitch = 0° (parallel to floor)
SPIDERS focus position and orientation tolerance (relative to nominal focus)	±78 µm in X and Y ±386 µm in Z (focus) ±0.36 mrad in pitch and yaw (No roll requirement)
Focus position and orientation adjustability for optical alignment during integration	Translation: ±10 mm range, with 50 µm resolution in X, Y, and Z Rotation: ±5 mrad range, with 0.2 mrad resolution in pitch, yaw, and roll
Nasmyth platform interface defined by 4× ATT Metrology Solutions 1.5-TM kinematic mounts (1.5 in sphere receivers centred 200.25 mm above platform floor) located at any four locations within the optical bench footprint.	±0.5 mm in X and Z relative to nominal location for each mount
Clean-space enclosure over optical bench with HEPA-filtered airflow	Fits on 1.2 × 1.5 m optical bench Height $\leq$ 550 mm Opaque, removable panels for bench access Meets ISO 14644-1 Class 5 or better ($\leq$100,000 particles/m^3 $\geq$0.1 µm)
Rack space for electronics and support hardware	4× standard 8U racks with shelving
Water cooling capacity for science cameras	$\leq$ 400 W thermal load Water temperature $\leq$ 10 °C above ambient
Electrical isolation from Nasmyth platform	Electrically insulating barrier somewhere between frame and interface

These constraints reflect the complexity of integrating SPIDERS into a compact,

high-performance astronomical environment. Core mechanical challenges include achieving sub-micron alignment with limited adjustability, controlling thermal loads effectively and mass without compromising stiffness, and maintaining positional stability under gravitational and vibrational loading. The adoption of kinematic mounts enables precise and repeatable instrument placement, but imposes strict positional tolerances that in turn drive the system's mechanical design and integration strategy.

To meet the specifications outlined in Table 2.1, the SPIDERS mechanical system is divided into five subassemblies. Together, these components span the meter-scale infrastructure of the telescope while enabling micron-level stability and alignment:

1. **Enclosure:** A clean-space shell enclosing the optical bench to limit particulate contamination and air movement. A HEPA-filtered air source maintains ISO Class 5 cleanliness when SPIDERS is in non-cleanroom environments. Opaque panels block ambient light and particulates while allowing full access to the instrument during integration and maintenance. The enclosure was both designed and assembled by O. Lardière.

2. **Optical Bench:** The primary mechanical reference surface that supports all science optics, cameras, and instrumentation. It defines the alignment datum for the instrument and provides a rigid, stable platform for optical mounting (see Fig. 2.2). The optical bench was designed, aligned, and assembled by O. Lardière.

3. **Hexapod Assembly:** A six-degree-of-freedom (6-DOF) passive adjustment mechanism for optical alignment. Turnbuckles actuate bipod legs to precisely adjust the position and orientation of the optical bench, enabling alignment of SPIDERS relative to the AO3k beam.

4. **Structural Frame and Electronics Housing:** A rigid structural assembly that houses control electronics, provides lifting interfaces for craning, and isolates the system electrically via G10 composite plates. Integrated fans, a water cooling system, and thermal insulation reduce convective currents caused by heat near the science path, supporting thermal stability on the bench and around the SPIDERS focus.

5. **Interface Subassembly ("Booster Seat"):** A structural adapter that elevates SPIDERS to the nominal focus height and provides a mechanically re-

peatable interface to the Nasmyth platform through four kinematic mount receivers. G10 composite plates are positioned between the frame and the adapter, mechanically fastening the two while electrically isolating SPIDERS from the platform. Designed by Opto-Mécanique de Précision Inc. (OMP) in Québec City, this module is installed only during final commissioning when elevation is required.

Figure 2.3 shows an exploded and integrated view of the SPIDERS mechanical architecture on the Nasmyth platform, in the context of other telescope systems. Subsequent sections provide additional detail on the structural frame, thermal management, lifting system, and alignment mechanism.

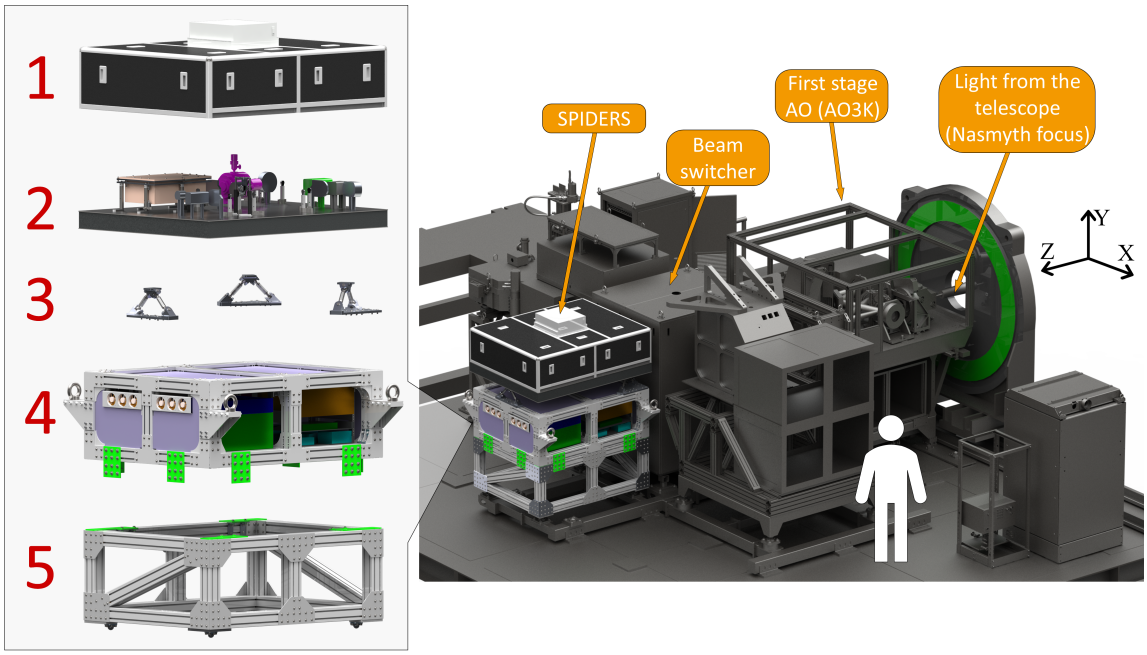

Figure 2.3: Exploded view (left) and integrated view (right) of the SPIDERS assembly on the Subaru telescope's Nasmyth Platform. The exploded diagram highlights the five key subassemblies: (1) enclosure, (2) optical bench, (3) hexapod positioning system, (4) structural frame and electronics housing, and (5) booster-seat interface module. Light from AO3k is directed into SPIDERS via the beam switcher, which routes starlight to different instruments on the platform.

2.2.1 Structural Frame and Electronics Housing

The structural frame of SPIDERS plays a critical role in supporting both real-time wavefront control and the acquisition of science data. It houses essential subsystems,

including the main real-time computer (RTC), deformable mirror electronics (DME), camera controllers, power supplies, and various auxiliary electronics required for optical bench operations. Standardized server rack units are utilized to mount electronic components securely at the front, while integrated vented shelves offer organized storage for loose hardware and water-cooling elements.

To minimize dynamic speckle formation in the focal plane image due to mechanical vibrations on the optical bench, silicone dampers are strategically employed to isolate the frame from disturbances originating in hardware components, frame-mounted fans, and the fans and pump of the water-cooling system. Additionally, the frame is insulated with thin extruded polystyrene panels on the top, ends, and one side of the base. This insulation prevents localized heat accumulation beneath the optical bench, channels airflow effectively, and ensures efficient thermal regulation by the cooling system, as detailed in §2.2.2.

Figure 2.4 presents the structural frame and electronics housing design during the laboratory development phase. Key components, mechanical features, and physical dimensions are annotated for clarity.

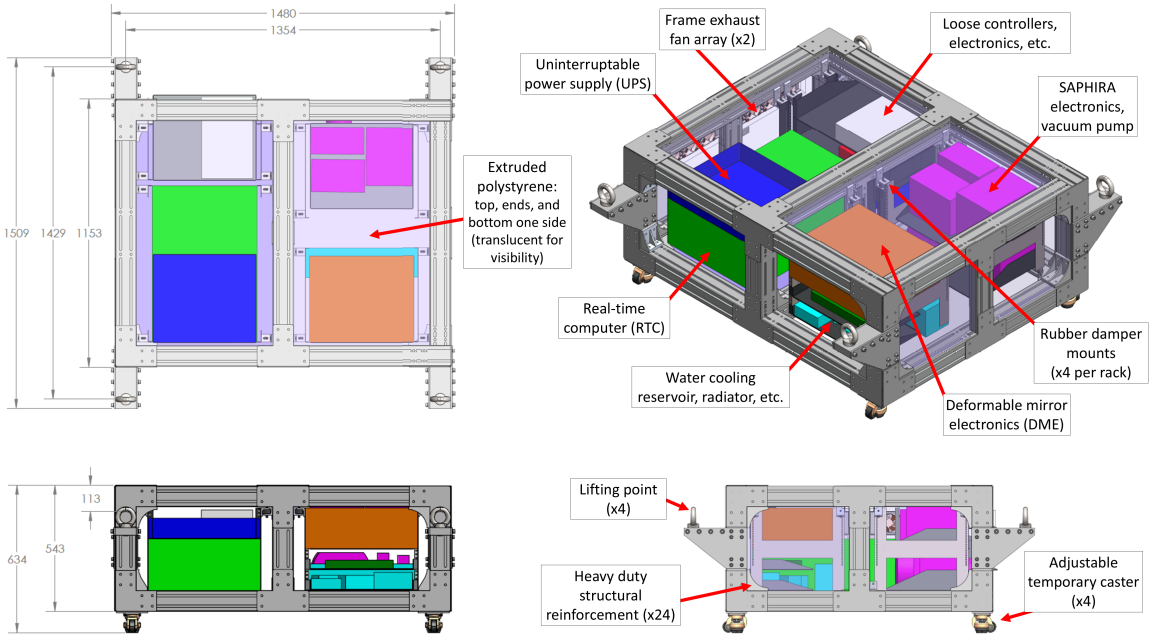

Figure 2.4: Design of the SPIDERS structural frame and electronics housing for the laboratory development phase, featuring lockable casters. Cables from controllers and hoses for water cooling exit through the sides of the frame. Extruded polystyrene insulation is applied to the top, ends, and one side of the base (translucent for clarity). Primary components, mechanical features, and dimensions are labeled.

The fully assembled SPIDERS system, shown in Figure 2.5, is currently located in the clean room of the NRC HAA Integration Facility in Victoria, BC. Final assembly stages are underway, including the installation of lifting hardware and integration of remaining components. A comprehensive analysis of the system's structural integrity for lifting and crane operations is provided in §2.2.3.

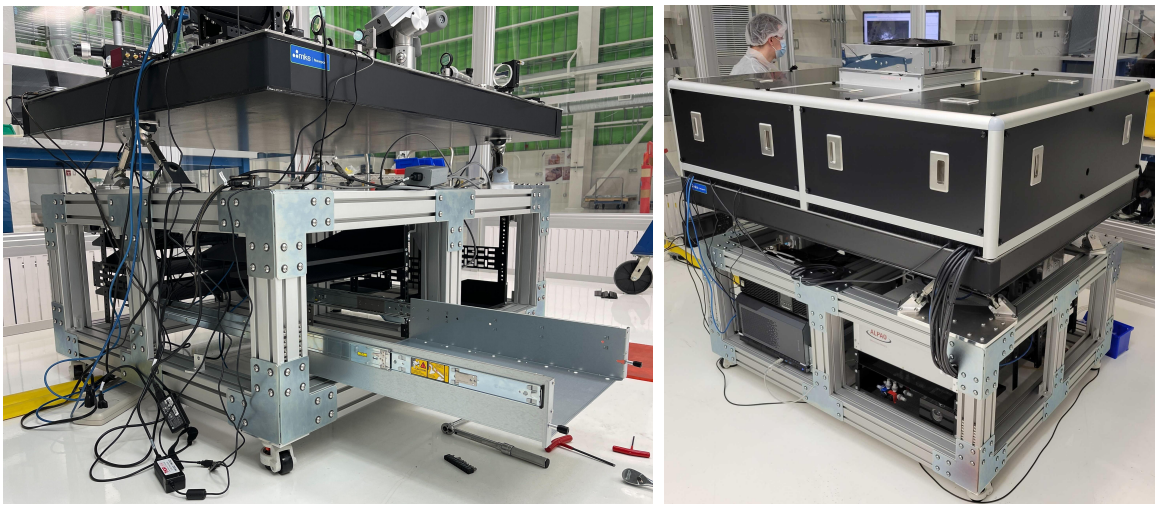

Figure 2.5: Unpopulated frame and electronics racks during initial construction (left), and the fully assembled SPIDERS system (right). Image on right courtesy of Olivier Lardière.

2.2.2 Thermal Management and Water Cooling

Thermal regulation is critical to the optical, mechanical, and electronic performance of the SPIDERS instrument. Sustained temperature gradients can drive buoyancy-induced convective currents within and around the enclosure, introducing local turbulence that degrades image quality and system stability. Fluctuating or elevated temperatures increase thermal background noise in detectors and impose stress on sensitive electronics, accelerating degradation mechanisms such as component fatigue and calibration drift. Furthermore, differential heating across the optical bench, particularly between its upper and lower surfaces, can result in non-uniform expansion, leading to structural warping and optical misalignment.

To mitigate these effects, a combination of closed-loop water cooling and passive thermal controls were implemented to maintain stable temperatures across the optical bench, supporting frame, and the ambient environment surrounding the enclosure. The system provides direct heat removal from the cameras and supports regulation

of air temperature within the frame through circulation driven by the internal fans and guided by extruded polystyrene insulation. The design includes a liquid-to-liquid heat exchanger (HX) for seamless integration with Subaru's facility glycol loop. This interface enables high-capacity cooling using near-ambient temperature fluid while maintaining full hydraulic isolation between the instrument and facility systems. The overall cooling architecture is illustrated in Figure 2.6.

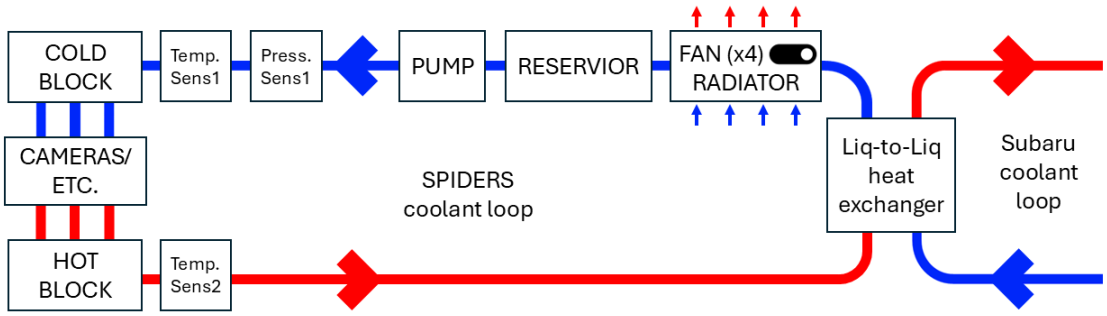

Figure 2.6: Schematic of the SPIDERS water cooling system. The closed-loop design includes a liquid-to-liquid heat exchanger (HX) interface with Subaru's facility glycol system and a toggleable internal fan-cooled radiator. Temperature and pressure sensor locations are shown for real-time monitoring and validation.

During laboratory integration at HAA, thermal regulation was provided by an internal fan-cooled radiator in the absence of Subaru facility coolant. For on-site operation, the radiator fans can be disabled to eliminate vibrational input, as the Subaru coolant loop offers sufficient thermal capacity to manage the full system load. The water circuit includes modular hot and cold distribution manifolds with quick-disconnect fittings for streamlined integration. Temperature sensors positioned at key inlet and outlet points enable real-time thermal monitoring across both the internal radiator and facility-coupled HX.

System integrity is verified through pressure monitoring using a transducer located downstream of the circulation pump. For pre-shipment validation, the SPIDERS cooling loop undergoes a 24-hour pressure hold at 1.3 times its nominal operating pressure. Separately, the Subaru-side HX loop is pressure tested at 100 psi to meet facility requirements. Because the HX is non-mixing, the two loops remain hydraulically isolated and can be tested independently. The physical configuration of the integrated system is shown in Figure 2.7.

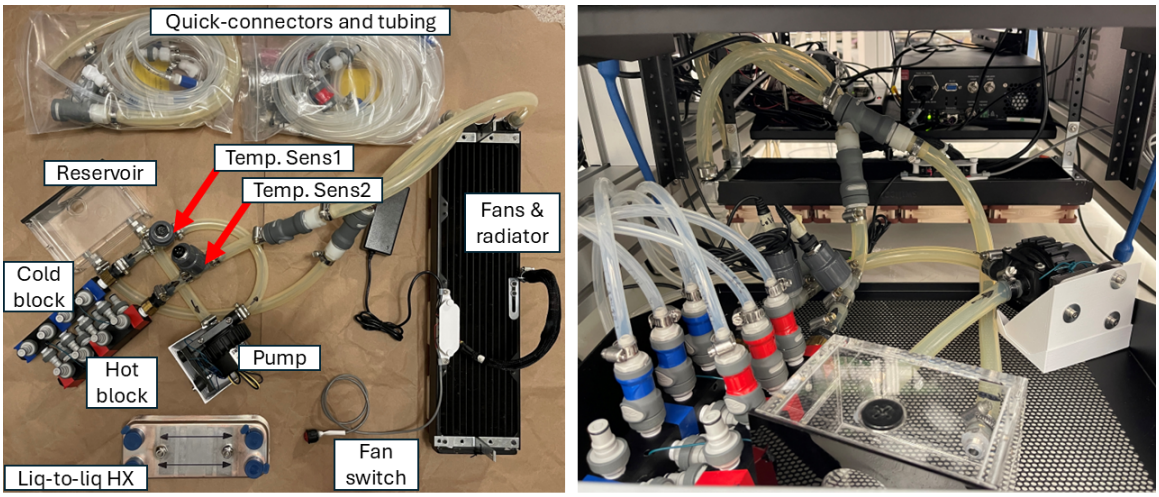

Figure 2.7: Left: Assembled SPIDERS cooling system (dry configuration) showing the pump, reservoir, radiator assembly, Subaru-coupled heat exchanger (HX), and quick-disconnects and distribution blocks for the cameras. Right: System installed on a suspended shelf within the SPIDERS frame, providing vibration isolation and reserved space for final component integration. The HX and pressure sensor were not installed at the time of these images.

At the time of testing, only two of the three science cameras had been installed due to ongoing procurement and development constraints. Nevertheless, a representative thermal performance test was conducted during a typical system development cycle. The configuration included two CRED2 cameras contributing thermal load to the water cooling loop, with all other subsystems on the optical bench and within the frame fully powered, approximating the operational thermal conditions expected during routine observation runs.

To simulate thermally suboptimal conditions, the extruded polystyrene insulation was removed from the frame. This allowed warm air generated by electronics in the lower enclosure to rise and increase the thermal load on the underside of the optical bench. The water cooling system was sequentially loaded with 100 W (one camera) and 200 W (two cameras), corresponding to 25 and 50 percent of the design thermal budget listed in Table 2.1. These values do not include additional internal heat sources such as the real-time computer (RTC), deformable mirror electronics (DME), power distribution unit (PDU), SAPHIRA electronics, and other components mounted both within the frame and directly on the bench. Temperature readings were collected using sensors on the water lines and adhesive thermistors on the upper and lower bench surfaces. The results are shown in Figure 2.8.

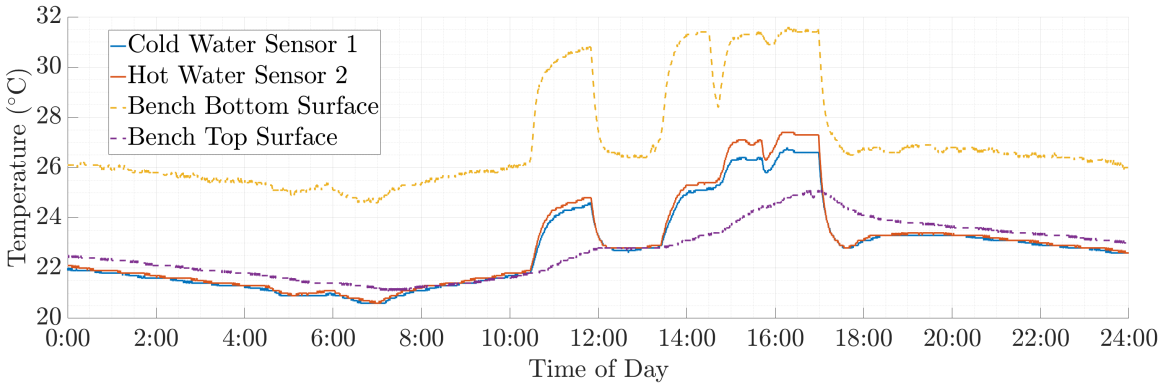

Figure 2.8: Temperature profiles recorded over a 24-hour period in the development laboratory under 100 W and 200 W thermal loading conditions at various times throughout the day. Temperature data was collected using sensors mounted on the water lines and on the upper and lower surfaces of the optical bench. The system was intermittently cycled as part of ongoing software tuning and component validation.

Under an applied thermal load of 200 W, the internal water cooling circuit stabilized at approximately 5 °C above ambient, aided by fan-assisted convection. This remains within the specified operational limit of 10 °C. Although the full design load of 300 W was not tested directly, performance extrapolation indicates continued compliance under full system operation.

While the cooling circuit effectively regulates the temperature of key components, it does not control the air temperature. Several uncooled, heat-generating devices on the bench and in the lower electronics frame contribute to convective warming above and beneath the optical bench. Testing showed a localized air temperature increase of up to 10 °C below the bench and a 3 °C rise at the bench surface, without reaching steady state above the bench. The absence of polystyrene insulation during testing contributed to the vertical thermal gradient. Reinstallation of this insulation is expected to improve thermal uniformity and minimize distortion by limiting upward heat transfer. Frame-mounted fans further assist with air circulation and help manage internal gradients.

During deployment, the system will use Subaru's facility coolant, supplied at approximately 2 °C above ambient with higher flow capacity than the laboratory setup. Final integration activities, including installation of the third science camera, thermal validation, and pressure qualification, are planned for early summer. Temperature data will be recorded using 1-Wire digital sensors at one minute intervals, with storage extending to 48 months for long term monitoring and diagnostics.

2.2.3 Lifting and Structural Safety

The SPIDERS lifting system is designed to support safe, repeatable handling during transport, integration, and deployment within the confined environment of the Subaru Telescope's Nasmyth platform (Figure 2.1). The system prioritizes personnel safety, equipment protection, and strict compliance with applicable mechanical and occupational safety standards.

The design methodology adheres to WorkSafeBC Occupational Health and Safety Regulation (OHSR) [108] and ASME B30.26 [109], from which the required safety margins are derived and summarized in Table 2.1. For certified commercial hardware, compliance is evaluated using the *Working Load Limit Factor* (WLLF):

$$\text{WLLF} = \frac{\text{WLL}}{\text{Load}} \tag{2.1}$$

A minimum WLLF of 1.5 is required for non-personnel lifts, limiting applied loads to 67% of the manufacturer's rated Working Load Limit (WLL). All commercial lifting components in SPIDERS must meet or exceed this requirement and be ASME-certified.

For custom-fabricated components, structural adequacy is verified through classical stress analysis, focusing on tensile and shear failures in regions of stress concentration [110]. Safety margins are quantified using the conventional safety factor (SF):

$$\text{SF} = \frac{\text{Material Yield Strength}}{\text{Applied Stress}} \tag{2.2}$$

A minimum SF of 5.0 is required per WorkSafeBC guidelines. All analyses were performed under conservatively estimated loading conditions to ensure compliance.

Design Assumptions and Load Conditions

The structural analysis was based on a conservative two-arm lifting scenario in which only half of the lifting arms are assumed to carry the full system load. This accounts for potential rigging asymmetries such as cable slack, uneven positioning, or misalignment. Including a 45 kg contingency margin, the total system mass is estimated at 850 kg, resulting in a static vertical load of 4,169 N per arm. The lifting system layout and design is depicted in Figures 2.9 and 2.10.

Due to rigging constraints from the Subaru-supplied H-beam, cables are oriented at 11.3° from vertical, introducing a horizontal force component and increasing the

resultant load per arm to approximately 4,252 N. The horizontal component is 833 N per arm under the two-arm assumption and approximately 416 N with a four-arm lift. To maintain a conservative and simplified model, the analysis evaluates each arm under vertical loading only. Using this simplification, load transfer is assumed to occur entirely through shear in bolted joints, excluding bending and out-of-plane moments to reduce model complexity and emphasize direct, robust load paths.

The booster seat interface was assessed using the same methodology, with its 165 kg load assumed to be carried by only three of eight G10 support plates. Each plate transfers 540 N through two M8 bolts entirely in shear. The resulting WLLFs for commercial hardware and the SF for the G10 plate is shown in Figure 2.9.

Further analysis of the frame was deemed unnecessary due to its high redundancy. The number of fasteners and structural joints in the frame corners exceeds those in the lifting arms by a factor of four, providing greater stiffness and reserve capacity. The lifting arms were therefore identified as the limiting structural elements.

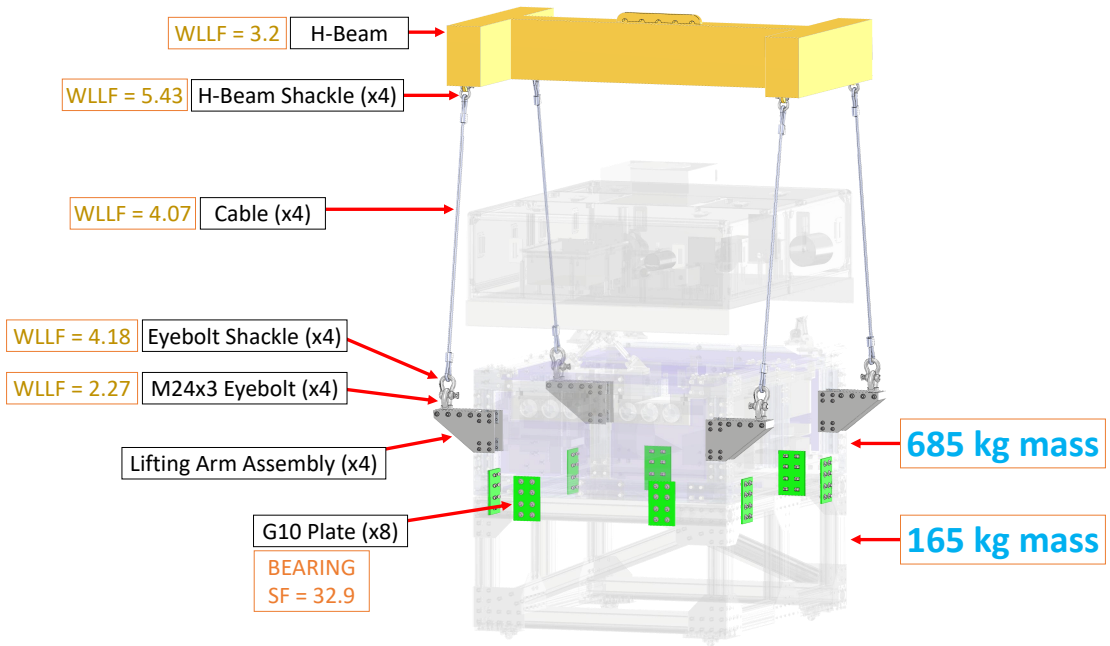

Figure 2.9: SPIDERS lifting system design showing the full assembly. Safety factors (SFs) for the custom G10 plate interface and Working Load Limit Factors (WLLFs) for the commercial hardware are annotated based on the conservative two-arm loading scenario. SFs for the lifting arm assembly components are shown in Figure 2.10.

Component-Level Lifting Arm Structural Analysis

The lifting arms are constructed primarily from machined 6061-T6 aluminum plates

fastened with high-strength Class 12.9 metric bolts. All joints are configured to promote shear-dominant load paths and minimize reliance on lower-strength threaded aluminum components. Four critical structural interfaces were identified and evaluated under the two-arm assumption:

- *Booster Seat to Frame (G10 Plate Interface):* This connection uses G10 composite plates to transfer vertical load from the 165 kg booster seat into the frame. Only three of eight plates are assumed to be active, each loaded via two M8 bolts at each connection. The limiting failure mode is bearing stress in the G10 at the bolt interface, with a calculated SF of 32.9.

- *Eyebolt to Top Plate Interface:* The central lifting point consists of an M24 stainless steel eyebolt mounted with a Class 12.9 nut into a counterbored aluminum plate. Threadlocker prevents loosening while allowing rotational movement. As per ASME B30.26, a 45% WLL reduction is applied for angular loading between 5° and 15°. The limiting condition is axial loading of the eyebolt, corresponding to a SF of 17.8 and a WLLF of 2.27.

- *Top Plate to Side Plate Interface:* Two of four M10 bolts connect the top and side plates. This interface was evaluated for bolt shear, bearing, tear-out, and plate rupture. The limiting mode is edge rupture in the side plate near the outermost M10 bolt, with a SF of 7.8.

- *Side Plate to Frame Interface:* Load transfer is facilitated through two of the eight M8 shoulder bolts interfacing with extrusion nuts. The deliberate selection of shoulder bolts was intended to maximize the bearing stress area on the side plates. The analysis encompassed bolt shear, tear-out, bearing stress, and frictional slip under both vertical load and induced moments. Frictional resistance was calculated based on an 18 Nm preload. The critical failure mode was identified as bearing stress in the side plate due to the M8 bolt shoulders, resulting in a safety factor of 5.04.

The detailed component-level design is illustrated in Figure 2.10, which includes safety factors for each interface based on the identified limiting failure modes.

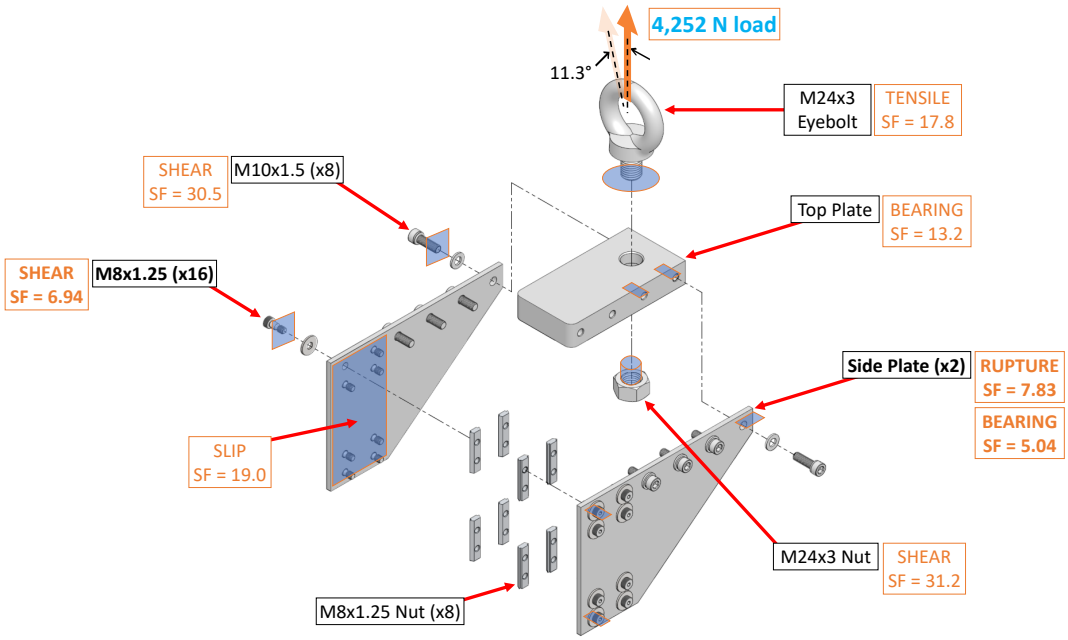

Figure 2.10: Detailed view of the SPIDERS lifting assembly evaluated under the conservative two-arm configuration, with two engaged bolts per interface. Safety factors (SF) are annotated at each interface below the corresponding limiting failure mode. The three lowest SFs are highlighted in bold text.

Summary and Compliance Verification

The structural evaluation confirms compliance with the safety requirements defined by WorkSafeBC OHSR, ASME B30.26, and the minimum thresholds listed in Table 2.1. The analysis was conducted using a conservative two arm lifting model with partial bolt engagement, assuming two of eight M8 bolts at the side plate to frame interface and two of four M10 bolts at the side plate to top plate interface. All critical interfaces and joints were evaluated for failure under these conditions.

The lowest verified WLLF was 2.27 for the M24 eyebolt under 11.3° angular loading. For custom-fabricated components, the minimum SFs were 5.04 for bearing stress in side plates from the M8 bolts, 6.98 for shear in the same bolts, and 7.83 for edge rupture in the side plates near the M10 bolts. All values exceed the minimum design requirements of 1.5 (WLLF) and 5.0 (SF), confirming sufficient margin across the lifting system.

Although the analysis was intentionally conservative, actual operation will use all four lifting arms, with most or all bolts fully engaged at each interface. This improves load distribution, increases redundancy, and reduces localized stress. The simplified vertical-only loading model is further justified by the expected engagement of the

full bolt patterns, which provides additional restraint not captured in the analysis. These conditions confirm that the SPIDERS lifting system is structurally sound, mechanically reliable, and well suited for repeated use during integration, transport, and deployment.

2.2.4 Hexapod Alignment System and Mechanical Safety

Precise six-degree-of-freedom (6-DOF) alignment of the SPIDERS instrument relative to a fixed focal point on the Nasmyth platform is critical to ensure accurate optical integration with the telescope. This alignment is achieved using a passive hexapod system that serves as the mechanical interface between the meter scale instrument structure and the micron level positioning accuracy required at the optical focal plane. Hexapod architectures are widely used in applications that require high precision and large scale spatial control, including optical alignment systems, motion simulators, and robotic platforms. Their compact geometry, structural rigidity, and ability to support fine adjustment across all translational and rotational axes make them particularly well suited for these purposes [111].

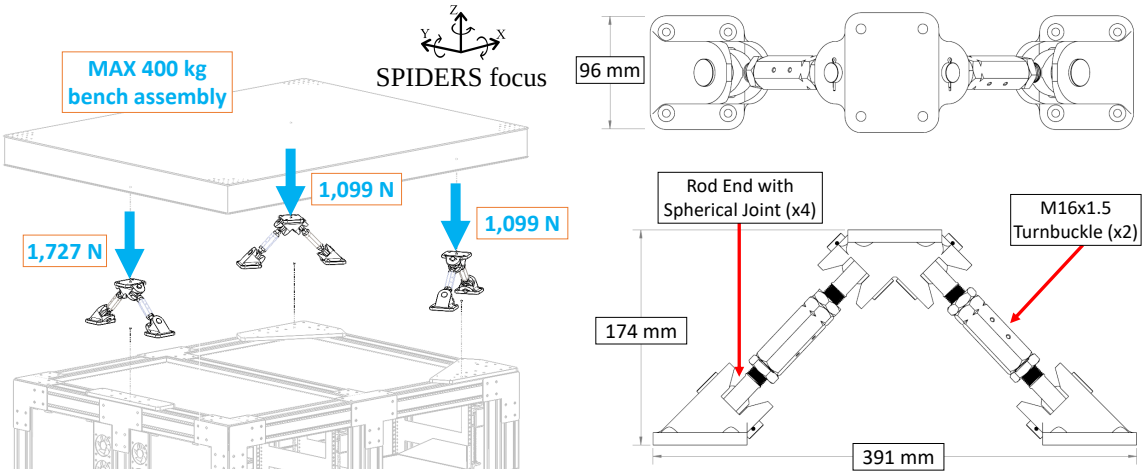

Figure 2.11: SPIDERS six-degree-of-freedom (6-DOF) hexapod alignment system. Left: Full instrument layout showing the adjustment location (SPIDERS focus) and resultant load distribution across each bipod under the maximum allowable bench load. Right: Close-up of a single bipod leg with labeled rod end and turnbuckle components. Note: The coordinate system shown is defined specifically for the hexapod system to align with standard conventions used in classical workspace analysis.

The hexapod system consists of six manually adjustable legs arranged in bipod assemblies, each incorporating a threaded turnbuckle and spherical rod end joints to

enable precise 6-DOF positioning. Adjustment is performed during initial commissioning and remains fixed in place during normal operation, secured via locking jam nuts. Each bipod is mounted to the optical bench and support frame using M6 × 1.0 316 stainless steel fasteners. The mechanical layout is shown in Figures 2.11 and 2.12, with further details on the alignment methodology and workspace validation provided in § 2.2.5.

To accommodate the required translational and angular adjustment ranges summarized in Table 2.1, large-format, high-precision rod ends (M16 and above) were selected, as smaller sizes did not provide sufficient shank length for the expected extension range. Each bipod leg supports uniaxial translation through its turnbuckle, while the spherical rod ends constrain the load path to pure axial tension or compression, thereby eliminating bending moments at the mounting interfaces. With the mechanical configuration established, structural analysis was conducted to verify strength and reliability under worst-case loading.

Design Assumptions and Load Conditions

The structural evaluation follows the same conservative methodology applied to the lifting components in §2.2.3, using classical failure theory to assess tensile, shear, and bearing loads at critical interfaces [110]. A worst-case supported mass of 400 kg is assumed, accounting for the 250 kg optical bench assembly, enclosure, and allowances for personnel contact and contingency.

Due to geometric asymmetry in the hexapod layout, loading from the optical bench is distributed unevenly along the X axis, as shown in Figure 2.11. Consequently, the most heavily loaded bipod pair experiences a total vertical force of 1,727 N at the top mounting surface. This load is assumed to be equally distributed between the two legs and aligned with the axis defined by the spherical joints, resulting in pure axial loading without moment transfer.

The analysis is performed in the YZ plane, as out of plane positions are limited to approximately 10° at full extension. Leg lengths ranging from 154 ± 20 mm were evaluated, corresponding to angular variations from 38.4° to 52.9°. This range reflects the full mechanical limits of the turnbuckle and rod end connections, including a 2 mm margin to account for potential over-extension. The resulting axial loads through each leg at minimum and maximum extension were calculated as 1,393 N and 1,084 N, respectively.

The M6 fasteners at the bipod bottom mounts are subjected to a horizontal force

component along the Y axis due to the leg angle. At the minimum leg angle, this results in a peak horizontal shear load of 1,093 N per mount. Under the conservative loading scenario, only two of the four bolts are assumed to carry the full shear load. At the top mounts, horizontal forces from opposing legs are assumed to cancel due to symmetrical geometry and loading. As a result, only the bottom mount in the two bolt configuration is considered for shear analysis.

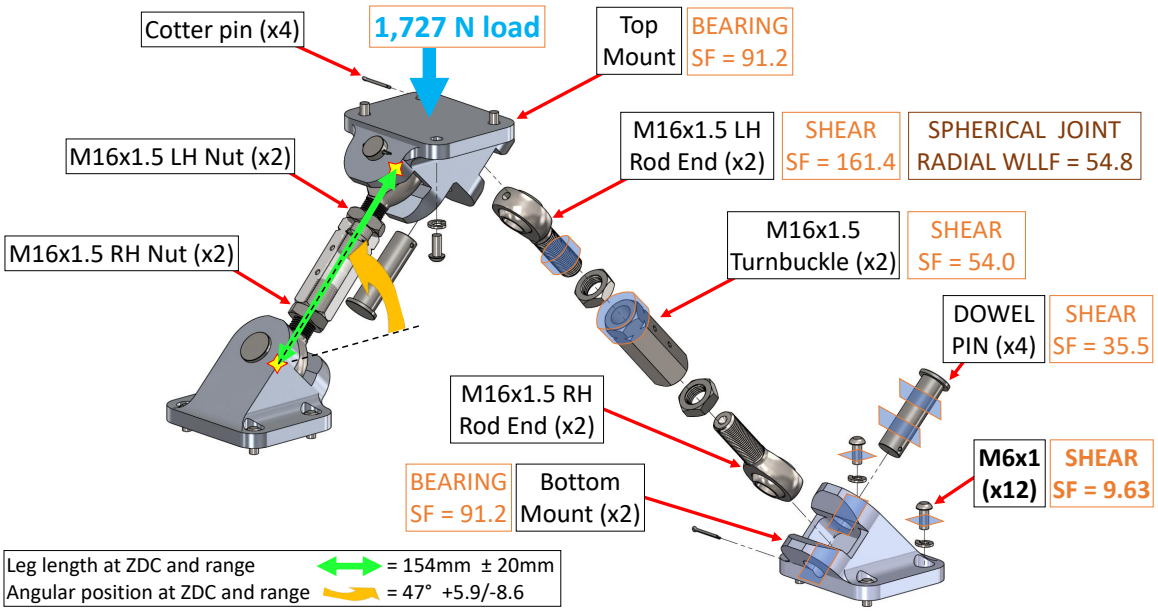

Figure 2.12: Component-level safety factor (SF) analysis for a single bipod under worst-case loading. Limiting failure modes are annotated at each interface. Evaluated leg length and angular ranges are indicated for reference.

Component-Level Analysis and Failure Modes

All structurally critical interfaces were evaluated to identify their governing failure modes under the defined loading conditions. Safety factor (SF), as defined in Equation 2.2, was used to assess the margin between material yield strength and applied stress in each limiting case. The following interfaces were identified as critical:

- *Lower mounting interface (M6 bolts to frame):* Shear stress was evaluated assuming load transfer through only two engaged M6 bolts, based on the horizontal force component induced by the leg angle. This condition resulted in a calculated SF of 9.63.

- *Upper and lower dowel pin interfaces:* Evaluated failure modes included dowel pin shear, bearing stress in the dowel holes, and axial loading of the rod end

joints. Rod ends were assessed using manufacturer-rated working load limits and the Working Load Limit Factor (WLLF) defined in Equation 2.1. Although not certified for lifting, the WLLF provides a consistent benchmark for comparison. The limiting failure mode was dowel pin shear at the minimum leg length and angle, with a resulting SF of 35.5.

- *Rod end to turnbuckle connection:* Internal and external thread shear were analyzed, with the critical case occurring at maximum leg extension and a minimum thread engagement depth of 10 mm. This condition resulted in an SF of 54. No additional failure modes were identified due to the symmetric and uniaxial nature of the applied loading.

Figure 2.12 summarizes the calculated SFs and corresponding limiting failure modes for each interface. A fully assembled bipod, representative of one of the three assemblies supporting the system, is shown in Figure 2.13.



Figure 2.13: Assembled bipod forming one of the three leg pairs in the SPIDERS hexapod, shown in the nominal home position. Custom parts were fabricated locally by HAA's Design and Fabrication Services (DFS) shop.

Summary and Compliance Verification

The SPIDERS hexapod system provides precise, stable, and mechanically robust six-degree-of-freedom alignment of the optical bench. As a passive mechanism, it is

designed for a one-time adjustment during initial commissioning at the Subaru Telescope and remains fixed thereafter. Structural analysis confirms that all components meet or exceed the SF requirement of 2 defined in Table 2.1, with the lowest calculated value being 9.63, governed by the bottom mount M6 bolts under the two bolt shear condition.

These results demonstrate that the hexapod system is mechanically reliable under worst-case loading and does not require additional handling precautions during development, transport, or integration.

2.2.5 Hexapod Inverse Kinematics and Workspace

Building on the design and structural validation presented in §2.2.4, this section addresses the functional implementation of the SPIDERS hexapod for precision optical alignment during system integration. This alignment directly affects the location and quality of the image formed on the science detectors and is essential to meeting the instrument's performance and calibration requirements.

To enable this alignment capability, the hexapod mechanism consists of six independently adjustable bipod legs, each functioning as a prismatic actuator between spherical joints mounted to the base (electronics frame) and platform (optical bench). This configuration forms a generalized Stewart–Gough platform, also known as a 6-6 parallel manipulator and commonly referred to as a hexapod [111].

Achieving the alignment adjustability and resolution requirements specified in Table 2.1 necessitates full six-degree-of-freedom (6-DOF) control from the hexapod. This includes a translational range of $\pm 10\,\mathrm{mm}$ with $50\,\mu\mathrm{m}$ resolution in X, Y, and Z, and a rotational range of $\pm 5\,\mathrm{mrad}$ ($0.286°$) with $0.2\,\mathrm{mrad}$ ($0.011°$) resolution in pitch, yaw, and roll. The corresponding positional tolerances are $\pm 78\,\mu\mathrm{m}$ in X and Y, $\pm 386\,\mu\mathrm{m}$ in Z (focus), and $\pm 0.36\,\mathrm{mrad}$ ($0.021°$) in pitch and yaw, with no specific requirement defined for roll.

Determining the leg configurations required to achieve a specific optical bench position is accomplished through an inverse kinematics (IK) formulation. The IK model computes the necessary leg lengths for a specified platform *pose* using a closed form geometric approach that yields a unique solution for each actuator [112, 113]. The associated forward kinematics (FK) problem, which determines the platform pose from a given set of leg lengths, is significantly more complex and results in multiple valid solutions. Because the system requires only commanded pose inputs during

alignment, the IK approach is sufficient and computationally efficient for practical use.

To support the IK formulation, the spatial configuration of the hexapod must be clearly defined, including its joint locations and coordinate reference frames. Figure 2.14 presents the complete spatial configuration, including the base and platform coordinate frames, spherical joint positions, and an example of a displaced platform pose. These parameters define the geometric framework for describing motion and computing the corresponding leg lengths needed to adjust SPIDERS' pose.

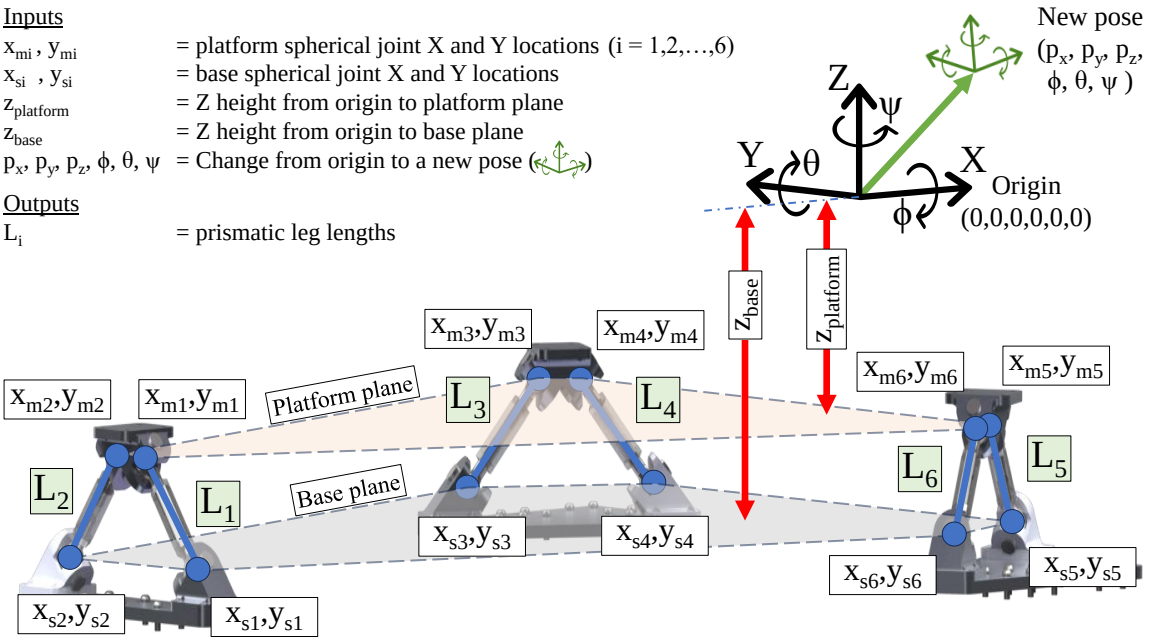

Figure 2.14: The Stewart–Gough (hexapod) platform layout, with the SPIDERS hexapod geometry shown for reference. The nominal input focus is defined as the global origin. A sample pose adjustment is illustrated as the target input for the inverse kinematics (IK) solution.

Inverse Kinematics Formulation

Given the defined geometry of the SPIDERS hexapod, the inverse kinematics (IK) model is used to compute the actuator lengths required to achieve a platform pose relative to the **home** configuration, defined as the pose in which the SPIDERS input focus is located at the global origin. Deviations from this pose are described by a translation in X, Y, Z and a rotation specified using ZYX Euler angles: roll (ϕ), pitch (θ), and yaw (ψ). With the positions of the base joints $\mathbf{a}_i$ and platform joints $\mathbf{b}_i$ known in their respective frames, the required leg lengths L_i are determined by transforming

the platform joint coordinates into the global frame.

The base and platform joint positions are defined in homogeneous coordinates as:

$$\mathbf{a}_i = \begin{bmatrix} x_{si} \\ y_{si} \\ z_{base} \\ 1 \end{bmatrix}, \quad \mathbf{b}_i = \begin{bmatrix} x_{mi} \\ y_{mi} \\ z_{platform} \\ 1 \end{bmatrix}, \quad \text{for } i = 1, 2, \ldots, 6 \tag{2.3}$$

where x_{si}, y_{si} and x_{mi}, y_{mi} denote the planar coordinates of the base and platform joints, respectively, and $z_{base}, z_{platform}$ specify their vertical offsets from the origin.

The translational displacement from the home configuration is represented by the vector:

$$\mathbf{p} = [p_x, p_y, p_z]^T \tag{2.4}$$

The platform orientation is described by a ZYX Euler angle sequence, comprising three sequential rotations: a yaw rotation (ψ) about the global z-axis, followed by a pitch rotation (θ) about the intermediate y-axis, and a roll rotation (ϕ) about the local x-axis. The resulting rotation matrix R is given by:

$$R = \begin{bmatrix} c_\theta c_\psi & -c_\theta s_\psi & s_\theta \\ c_\phi s_\psi + s_\phi s_\theta c_\psi & c_\phi c_\psi - s_\phi s_\theta s_\psi & -s_\phi c_\theta \\ s_\phi s_\psi - c_\phi s_\theta c_\psi & s_\phi c_\psi + c_\phi s_\theta s_\psi & c_\phi c_\theta \end{bmatrix} \tag{2.5}$$

where c and s denote the cosine and sine of the respective angles θ, ϕ, ψ.

The complete pose of the platform is captured by the homogeneous transformation matrix T:

$$T = \begin{bmatrix} R & \mathbf{p} \\ 0 & 1 \end{bmatrix} = \begin{bmatrix} c_\theta c_\psi & -c_\theta s_\psi & s_\theta & p_x \\ c_\phi s_\psi + s_\phi s_\theta c_\psi & c_\phi c_\psi - s_\phi s_\theta s_\psi & -s_\phi c_\theta & p_y \\ s_\phi s_\psi - c_\phi s_\theta c_\psi & s_\phi c_\psi + c_\phi s_\theta s_\psi & c_\phi c_\theta & p_z \\ 0 & 0 & 0 & 1 \end{bmatrix} \tag{2.6}$$

Applying this transformation to the platform joint coordinates yields their positions in the global frame, corresponding to the platform's new pose, denoted $\mathbf{b}'_i$:

$$\mathbf{b}'_i = T \cdot \mathbf{b}_i, \quad \text{for } i = 1, 2, \ldots, 6 \tag{2.7}$$

Finally, the actuator length L_i for each leg is computed as the Euclidean distance

between the transformed platform joint $\mathbf{b}'_i$ and the corresponding base joint $\mathbf{a}_i$:

$$L_i = \|\mathbf{a}_i - \mathbf{b}'_i\| = \sqrt{(a_{ix} - b'_{ix})^2 + (a_{iy} - b'_{iy})^2 + (a_{iz} - b'_{iz})^2} \tag{2.8}$$

The complete set of leg lengths $\{L_1, \ldots, L_6\}$ defines the IK solution for a specified hexapod pose. These lengths can be stored to serve as a reference for calculating relative adjustments to new pose parameters $\mathbf{p}, \phi, \theta, \psi$.

In the absence of real-time sensor feedback, platform alignment is performed manually by iteratively adjusting individual actuator lengths. Convergence toward the target pose is assessed using visual feedback from the cameras mounted on the SPIDERS bench. This process assumes initialization from a known reference configuration, defined for SPIDERS as a nominal home pose with equal leg lengths and parallel base and platform planes. The corresponding joint coordinates and pose parameters are derived from the system's CAD model and used as inputs to Equations 2.3 through 2.8. The associated geometric definitions are shown in Figure 2.15.

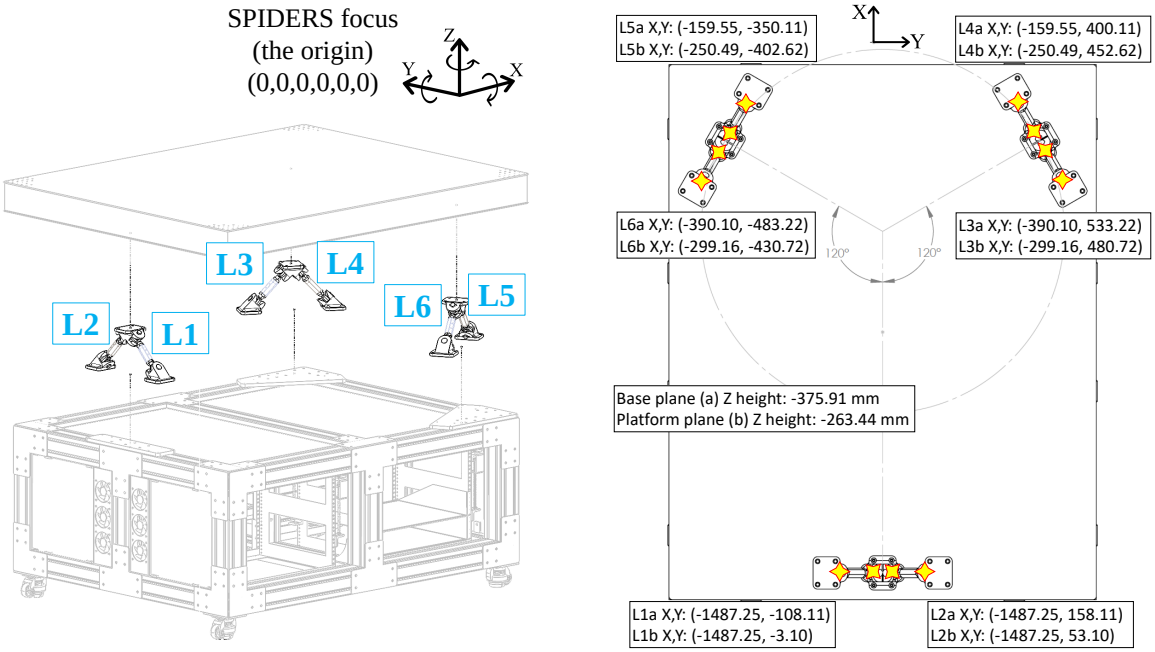

Figure 2.15: SPIDERS hexapod system showing the numbered legs, base and platform joint positions in their home positions, reference plane heights, and global origin.

Tracking the Pose and Evaluating the Workspace

To enable the application of the IK model and support manual adjustment of the SPIDERS hexapod, a MATLAB-based calculator was adapted from a forward/inverse

kinematics solver originally developed by Tae-Young et al. [112]. Significant modifications were made to tailor the tool to SPIDERS' needs, including enhanced visualization of actuator adjustments, structured storage of joint and reference plane coordinates, persistent configuration saving, and additional features to evaluate and export the platform's reachable and orientation workspaces. These enhancements provide critical insight into the system's operational limits and enable safe and precise alignment of SPIDERS' focus.

The software interface is organized into four primary sections, separated under **Inputs** and **Outputs** as described below:

- **User INPUTS**
  - **Zero-Displacement Configuration [mm]**: Joint and reference plane coordinates to define the home pose. The calculated focus-to-benchtop height is displayed for verification. Inputs can be locked to prevent accidental edits.
  - **Workspace Search Limits and Constraints**: Specifies allowable ranges for pose inputs and resulting leg lengths. '*abs. delta*' outputs exceeding these limits are highlighted in red; valid values appear in green. These constraints also define the bounds for workspace analysis.
  - **Change to Input Focus Pose**: Defines the commanded offset in X, Y, Z, roll, pitch, and yaw relative to the previously saved pose. Both the prior and updated absolute poses are displayed after solving the IK.
- **Calculator OUTPUTS**
  - **Leg Lengths [mm] and Angular Adjustment [°]**: Leg lengths are calculated using Equation 2.8. Both absolute and relative changes are shown, with angular equivalents derived from the specified actuator lead for manual adjustment.
  - **System Illustration**: The hexapod model is visualized using the current geometry and pose. Legs are colour-coded and the global origin is marked for reference.
  - **Saving to File**: Stores the active pose, configuration, and constraints in a '.txt' file for automatic loading and external access.

– **Draw Reachable/Orientation Workspace**: Solves and plots the reachable or orientation workspace. Results are saved as '.mat' files for reuse.

– **Export to PNG**: Generates PNG exports of computed workspaces plotted from current or saved '.mat' files, with support for multi-angle views.

Figure 2.16 shows the calculator interface using SPIDERS' home pose configuration.

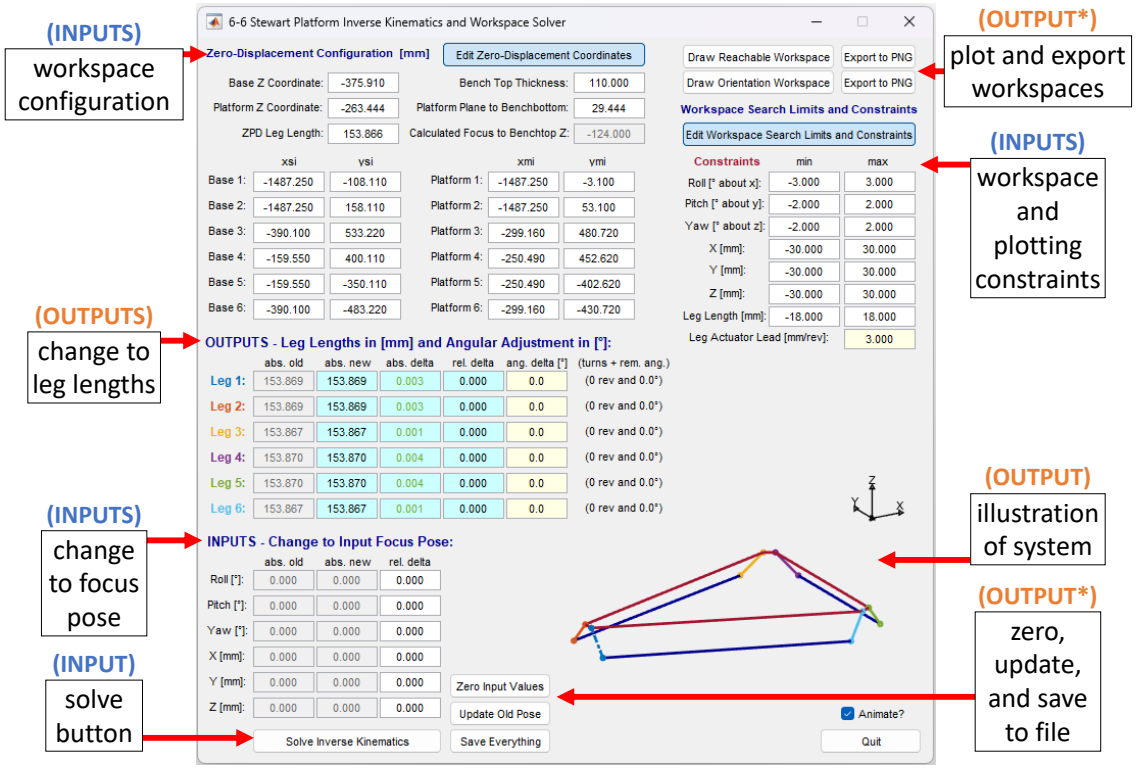

Figure 2.16: Adapted inverse kinematics (IK) calculator for the SPIDERS 6-DOF hexapod platform. **Inputs** include zero-displacement configuration, pose adjustments, and workspace constraints. **Outputs** provide leg length solutions, angular adjustments, workspace analysis, and pose saving and export capabilities.

The calculated *new* pose and associated leg lengths are shown in Figure 2.17 after solving the IK model. The *abs. delta* column in the output table indicates the absolute change in leg length from the home pose in millimeters and is colour-coded based on validity. Angular outputs are converted to actuator revolutions and residual angles in degrees using the specified actuator lead, aiding in manual adjustments for larger pose changes.

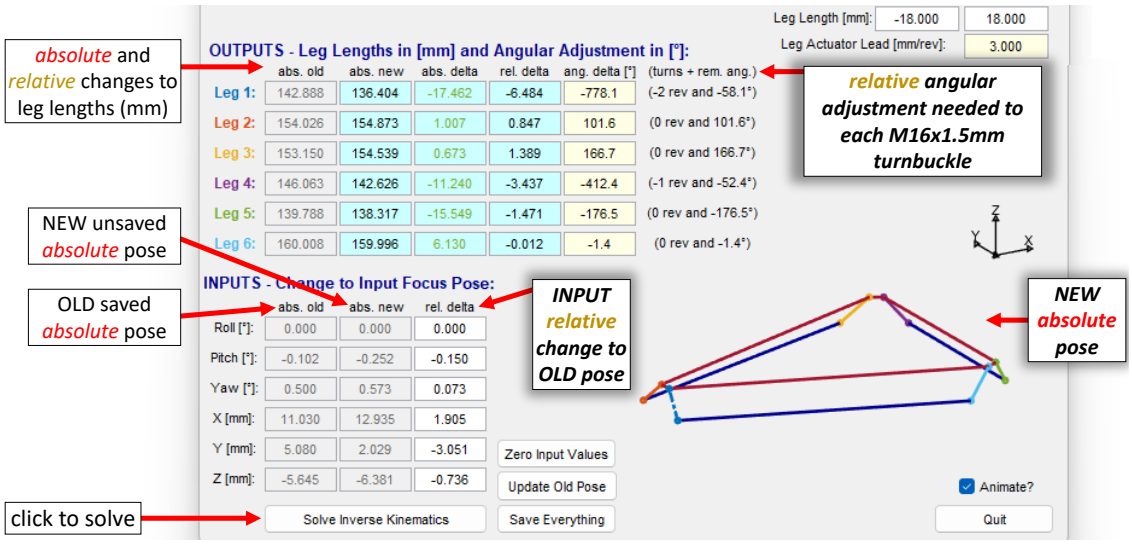

Figure 2.17: Inverse kinematics (IK) calculation output displaying absolute leg length changes and corresponding angular adjustments.

Reachable and Orientation Workspace Analysis

Utilizing the established IK framework, the calculator assesses both translational (**reachable**) and rotational (**orientation**) workspaces, providing a comprehensive kinematic evaluation.

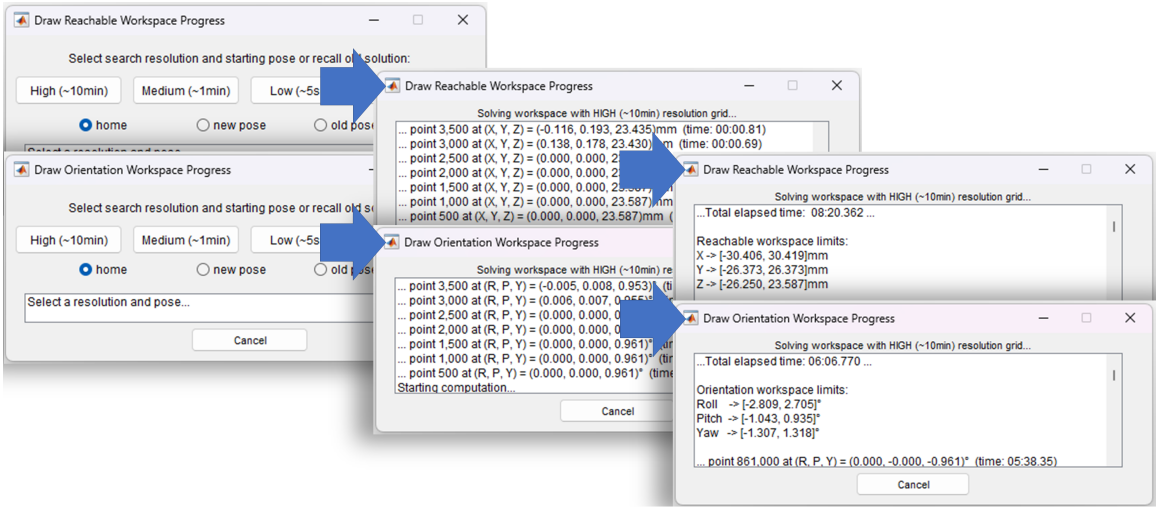

Figure 2.18: User-defined search resolution and pose to analyze from with status feedback for workspace computation. Coarser resolutions solve faster but yield lower fidelity evaluations.

The **reachable workspace** defines the platform's set of attainable translation positions in X, Y, Z coordinates at a fixed orientation, while the **orientation workspace**

specifies achievable roll, pitch, and yaw at a fixed position. In both cases, IK calculates actuator lengths to establish workspace boundaries based on the actuator stroke (leg length) limits.

To accurately identify these boundaries, the algorithm implements a radial-bisection search over a spherical grid. Starting from the specified pose, the bisection search iteratively refines boundary locations along each radial direction, achieving precise detection with computational efficiency. Before initiating the search, a preliminary check verifies that the evaluation can be done within the user-defined constraints, preventing incompatible configurations.

Search parameters and actuator constraints are defined in the **Workspace Search Limits and Constraints** panel, with resolution, execution, and visualization accessed via the **Draw Reachable/Orientation Workspace** button, as shown in Figure 2.18. The evaluation can be performed at the home, **new**, or **old** pose, with results plotted alongside the corresponding dimensional limits.

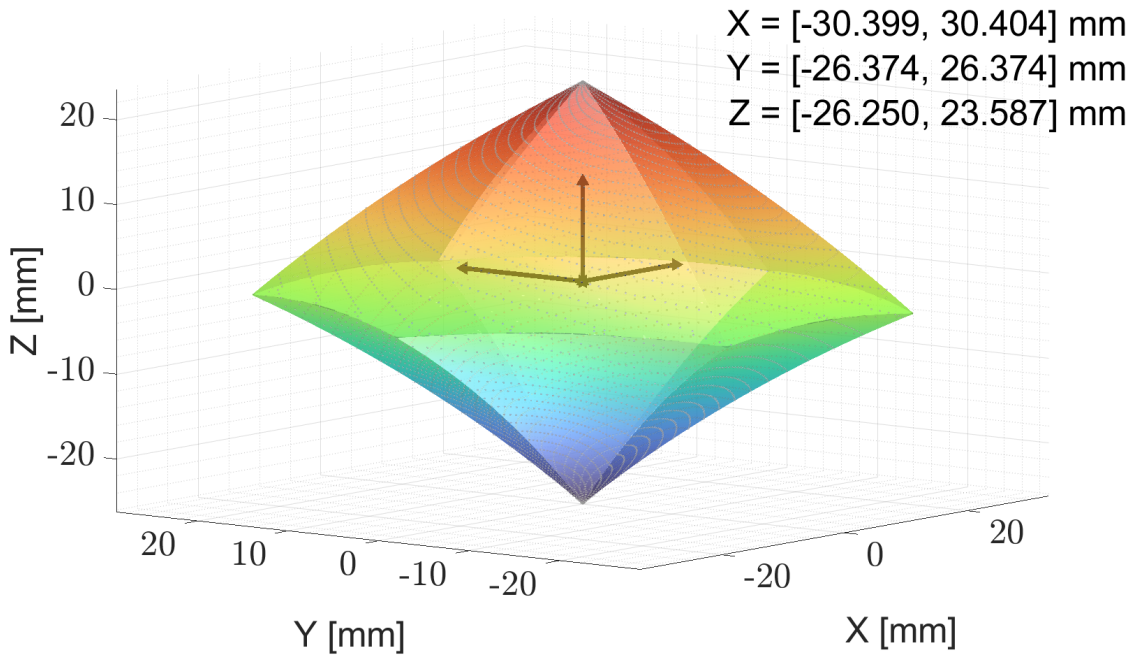

Figure 2.19: Animated view of the reachable workspace from the home pose with roll, pitch, and yaw set to zero. The hexagonal bipyramid shape reflects the system's symmetric geometry and actuator constraints. Faint dots are plotted periodically to show a found boundary point, while the closed surface uses all of the found points. Colour is mapped to the Z component for visualization only.

In symmetric hexapod designs like SPIDERS, the actuator configuration in the home position produces a distinct hexagonal pattern in the XY plane of the reachable workspace, reflecting uniform actuator constraints. The interaction between translation and rotation affects the translational range, varying with platform orientation. Figure 2.19 illustrates the X, Y, and Z boundaries of the reachable workspace from the home position, emphasizing a characteristic hexagonal bipyramid shape.

The orientation workspace, shaped by actuator limits and translation coupling, forms an asymmetric, dome-like volume centred at the home orientation. Figure 2.20 illustrates the roll, pitch, and yaw limits from the home position, highlighting the system's distinctive asymmetric shape.

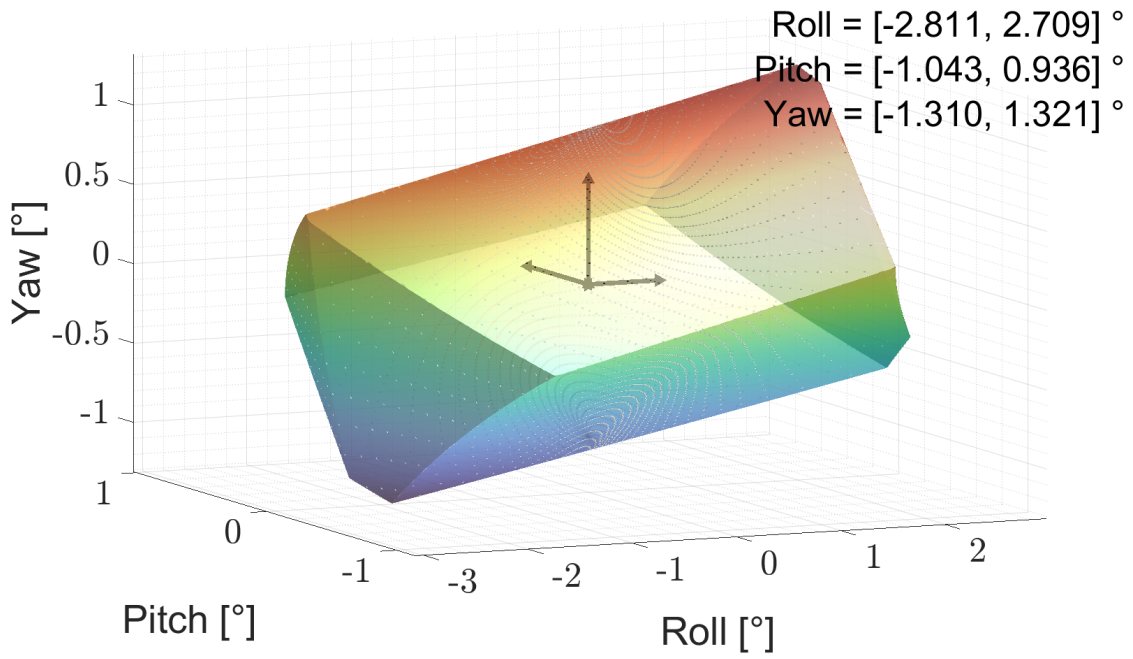

Figure 2.20: Animated view of the orientation workspace from the home pose with X, Y, Z fixed. The shape reflects asymmetric angular limits imposed by hexapod geometry and actuator constraints.

Following a pose adjustment, as depicted in Figure 2.17, the reachable and orientation workspaces can be re-evaluated to assess the impact on reachability. The resulting changes in workspace boundaries are illustrated in Figure 2.21, highlighting the effects of workspace interaction due to the pose modification.

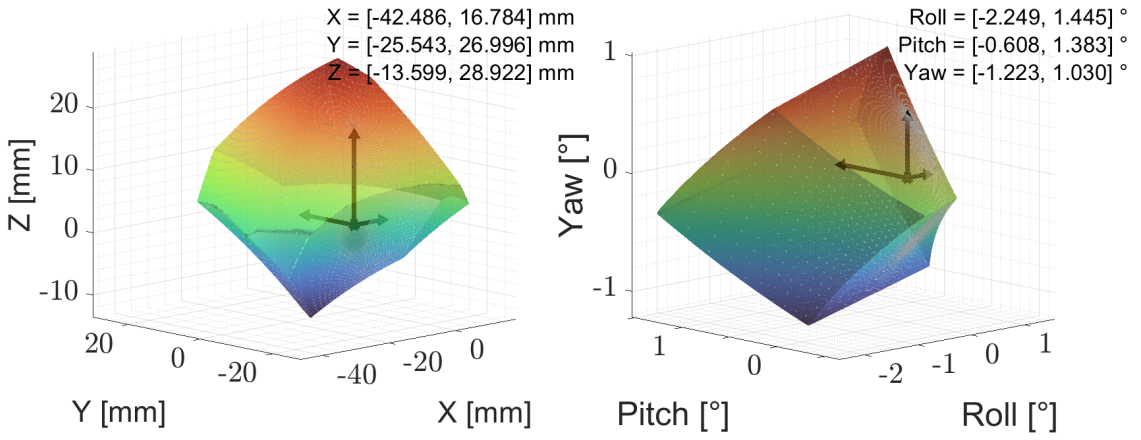

Figure 2.21: Animated visualization of the adjusted reachable workspace (left) and orientation workspace (right) from a representative pose $[11.935, 7.529, -5.381]$ mm, $[0.000, -0.252, 0.323]°$. The pose is positioned near the boundary of one of the six leg's range, indicated by its proximity to the edges of each workspace.

To support documentation of the visualizations, the program provides an export function that saves workspace plots in PNG format. Figure 2.22 illustrates the export interface for workspace visualizations.

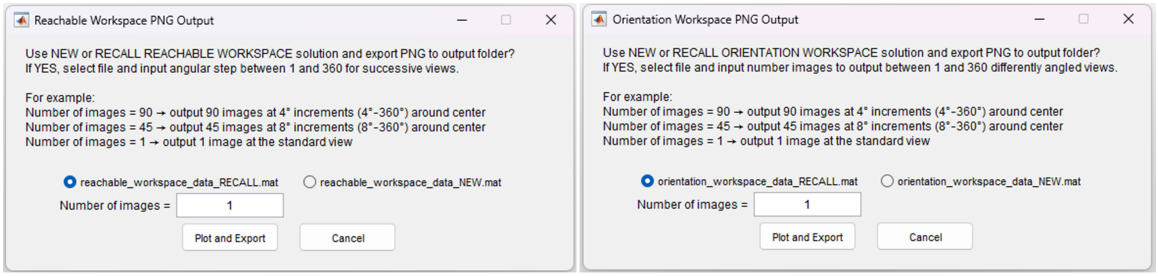

Figure 2.22: PNG export interface for saving workspace visualizations.

Summary and Compliance Verification

The SPIDERS hexapod calculator provides a precise method for determining the leg length adjustments required to achieve specified pose changes using M16x1.5 turnbuckles. To meet the minimum translational resolution of 50 µm in X, Y, Z and an angular resolution of 0.011° in roll, pitch, and yaw, the smallest necessary adjustments were identified as 2° and 1.5°, respectively. These values represent the limiting angular changes needed to satisfy alignment criteria, while other legs may require additional adjustment to reach the target pose. Accurate implementation of these adjustments can be achieved using basic measurement tools such as a mountable pro-

tractor and long wrench arms, ensuring precise control throughout the adjustment process.

Workspace analysis confirms that the system meets or exceeds the adjustability range specifications outlined in Table 2.1. With the home configuration and a ± 18 mm leg stroke range, the reachable workspace extends to boundary limits of $X = \pm 30.4$ mm, $Y = \pm 26.4$ mm, and $Z = [-26.3, 23.6]$ mm, exceeding the specified ± 10 mm range in all axes. Analytical verification of the Z range, based on leg length variations from 154 $\pm$ 18 mm and corresponding in-plane angular ranges of 39.5° to 52.4°, confirms the calculated $Z = [-26.3, 23.6]$ mm adjustment, further substantiating the workspace boundaries. The orientation workspace reaches roll, pitch, and yaw limits of $\pm 2.7°$, $\pm 0.9°$, and $\pm 1.3°$, respectively, exceeding the $\pm 0.286°$ requirement. While combined translation and rotation reduce the effective range of each degree of freedom, the calculator ensures that all commanded poses can be first simulated to ensure the system remains within defined operating limits.

In summary, the SPIDERS hexapod calculator leverages geometric modeling, IK, and visual feedback to deliver a comprehensive tool for precise and reproducible manual alignment. By integrating pose adjustment, workspace analysis, configuration management, and visualization export, the calculator ensures accurate implementation of alignment adjustments while maintaining adherence to specified translational and angular resolution limits. This approach not only facilitates effective pose control but also verifies workspace boundaries to prevent exceeding actuator limits, ultimately enhancing system reliability and operational safety.

2.3 Blinking the fringes, initial development and results of the Ultra-Low Speed Optical Chopper for the Self-Coherent Camera

This section is based on material published in the proceedings of the SPIE Volume 12185, Adaptive Optics Systems VIII in 2022 (10.1117/12.2630406). Authors: Adam B. Johnson, Christian Marois, Darryl Gamroth, Joeleff Fitzsimmons, Olivier Lardière, William Thompson, Garima Singh, Colin Bradley. *My contribution to this work was as the lead author, encompassing the mechanical design, initial software development, and testing. C. Marois served as the Principal Investigator for the NEW EARTH Lab, providing access to laboratory facilities. D. Gamroth was contracted to develop the software and electronics as a prototype demonstrator for a facility-class version intended for CAL 2.0. J. Fitzsimmons provided mechanical engineering support throughout the design process and reviewed the final drawing package. O. Lardière was responsible for designing and constructing the optics for the NEW EARTH Lab. W. Thompson integrated the chopper into the SPIDERS control loops, ensuring bench compatibility with the instrument. G. Singh contributed to the low-order wavefront sensor loops on SPIDERS. C. Bradley facilitated institutional support from the university.*

2.3.1 Introduction

Optical systems use devices known as optical choppers for a variety of reasons. Although the system it is being used in can differ greatly, the primary purpose of an optical chopper is simply to block and unblock a beam of light, in a consistent and periodic manner. By rotating a blade with identical and evenly distributed gaps, light traveling through the gap will blink on and off. Figure 2.23 below illustrates an incoming beam with some constant intensity as a function of time. As the beam passes through the spinning blade, the intensity as a function of time is divided into discrete and evenly distributed intensity pulses.

2.3.2 Applications

The primary motivation for the Ultra-Low Speed Optical Chopper (ULSOC) is its use in high-contrast imaging systems. When attempting to observe highly-contrasted

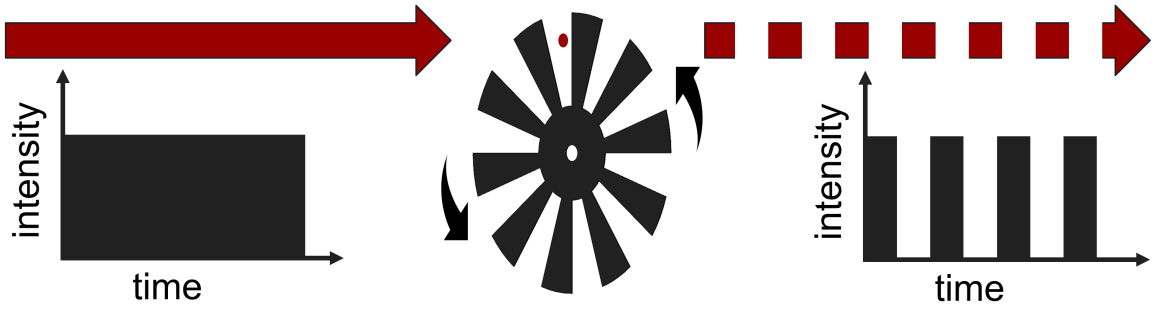

Figure 2.23: Chopping an optical beam with a rotating segmented blade. The intensity is "chopped" into discrete pulses.

objects such as a dim exoplanet next to a bright star, much of the star light pollutes and saturates the image being obtained. Many methods must be used to reduce the flux coming from the star in the image, such as the use of a coronagraph to obstruct the main star light, a wavefront sensing technique and deformable mirror to flatten the wavefront, and differential imaging methods to subtract out static and quasi-static stellar speckles. The Fast Atmospheric Self-coherent camera Technique (FAST) [22] incorporates optical chopping in these systems to provide real-time blinking from constructive interference of coherent starlight at the focal plane of the Self-Coherent Camera (SCC), presented and discussed in §1.3.8 and §1.3.10. Acquiring these paired images at tens to hundreds of Hertz is shown to "freeze" the local turbulence evolution and provide a simple means of avoiding static and quasi-static detector noise.

When the observed star is dim, a longer exposure of the camera is needed to collect more photons and a slower chopping frequency is required. The exact relationship between chopping frequency and star magnitude is unknown at this time and will be determined experimentally on-sky. The chopping frequency will need to be adjusted based on the number of photons hitting the detector and could require speeds down to 0.1 Hz for very dim stars and up to 100 Hz for very bright stars. Off-the-shelf chopper systems today are only designed for frequencies above 4 Hz [114, 115] where a shutter can be used for lower frequencies. The need for accurate chopping both below and above this barrier is what drives the need for the ULSOC system.

The SPIDERS Instrument for the Subaru Telescope

The Subaru Pathfinder Instrument for Detecting Exoplanets & Retrieving Spectra (SPIDERS) is a high-contrast extreme adaptive optics exoplanet imager that employs

many new technologies and techniques [106, 60]. The system takes advantage of the FAST technique [22], Lyot Low-Order Wavefront Sensing (LLOWFS) [116, 107], and the implementation of multiple differential imaging techniques [91, 117] on the bench in the NEW EARTH Lab at the National Research Council Canada, Herzberg Astronomy and Astrophysics Research Centre (NRC, HAA). The chopper will be placed in the optical path as shown in Figure 2.24 below, and blink the off-axis stellar core light on its way to the detector. The blinking light is spread across the detector plane, interfering with planet light and any residual stellar speckles. The resulting fringe pattern is related to the Point-Spread-Function (PSF) of the pinhole and is used in the wavefront correction calculations. This optical system configuration is known as a self-coherent camera (SCC), also presented in Figure 1.23)).

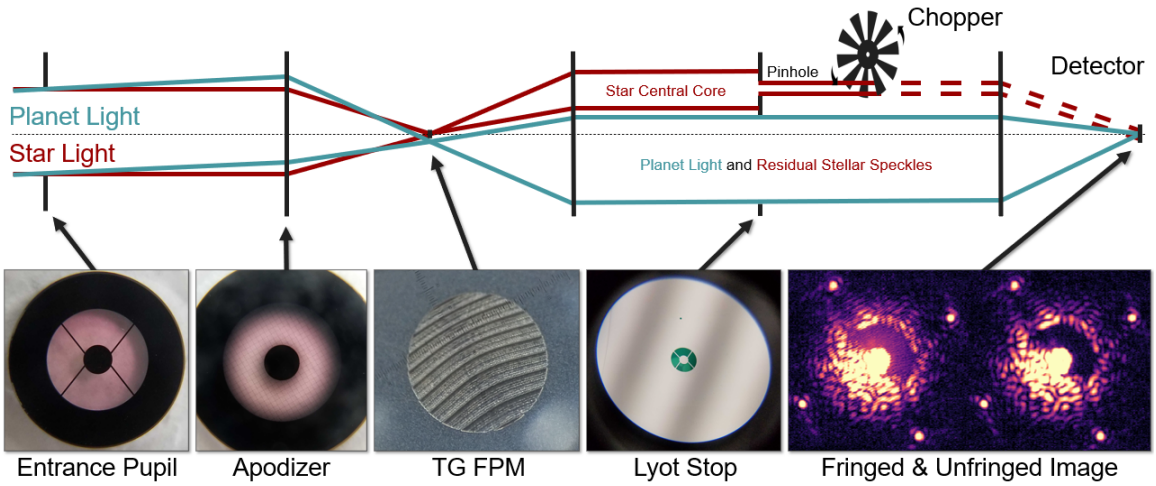

Figure 2.24: A portion of the optical layout for the SPIDERS instrument, from left to right: the Subaru entrance pupil mask; the apodizer for the Apodized Pupil Lyot Coronagraph (APLC) [118] system; The Tilt-Gaussian (TG) Focal Plane Mask (FPM) [102]; the reflective Lyot stop for LLOWFS [116]; and the resulting images on the detector plane [91]. The SPIDERS instrument is currently being assembled and will be tested on-sky in 2023 at the 8.2 m Subaru telescope.

The CAL 2.0 Upgrade for the Gemini Planet Imager

A second planned application for the ULSOC will be for the Gemini Planet Imager (GPI) instrument CALibration unit (CAL) 2.0 upgrade [119]. The upgrade aims to implement FAST and other techniques to improve speckle correction and achieve higher-contrast closed-loop imaging. The chopper will be used for the same tenths

to tens of Hertz range as SPIDERS to calibrate the wavefront as it comes into the instrument. The chopper will be positioned similarly in the optical path of CAL 2.0 (just behind the reflective Lyot stop), but with the added complexity of operating on a variably oriented platform subject to strict constraints on thermal emission, mechanical vibration, optical cleanliness, and other system-specific requirements. The CAL 2.0 ULSOC is discussed in §3.1.3.

2.3.3 Operational Principles

The input of the optical chopping system consists of a triggering source to receive the target chopping frequency, and PC communications for stopping, starting, and providing status updates. The trigger source symbolizes a train of 3.3 V or 5.0 V logical pulses that the optical chopping is required to follow. A phase-locked loop matches the leading edge of the trigger source pulse train with the leading edge of the optical chopping to synchronize the detector and the beam chopping. To ensure smooth and continuous motor operation, an additional current loop is required to make sure the motor has enough power to achieve the required speed, and a velocity loop to measure the actual speed of the chopper. A block diagram of this configuration is shown below in Figure 2.25.

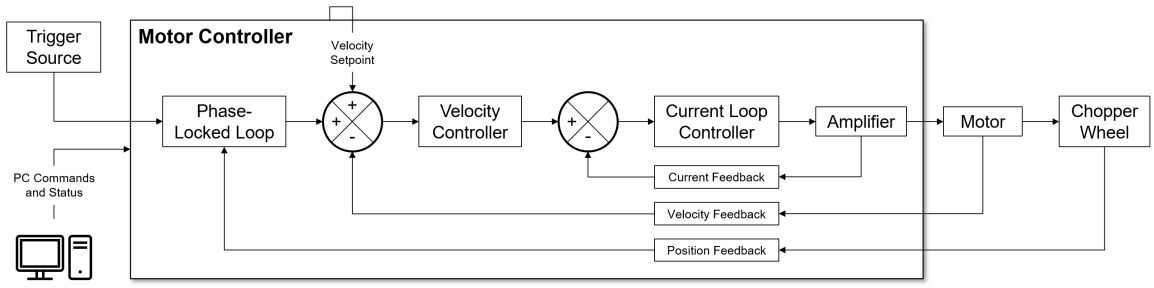

Figure 2.25: The block diagram of a current controlled, closed-loop stepper motor system with a phase-locked loop.

Closed-loop 'smart motors' are a motor, driver, encoder, and controller all-in-one for current sensing and velocity feedback to provide high-accuracy control, often called a 'stepper-servo'. The TSM11 [120] stepper-servo uses a 4096 count per revolution encoder to provide velocity feedback, and a current sensing loop to provide space vector current control. Being a stepper motor, it can operate between 200 and 51,200 steps per revolution for intermediate positioning and smoother motion between posi-

tions. The integrated smart motor package is controlled via Modbus RTU protocols and performs the closed-loop current and velocity control without any input from the user. A position, speed, or acceleration command can be sent to the motor and the TSM11 will close its own loops in an attempt to perform the commanded action. Since the smart motor does this in the background, the chopper system can be simplified to a single feedback loop for the trigger phase-locking, as shown in Figure 2.26 below.

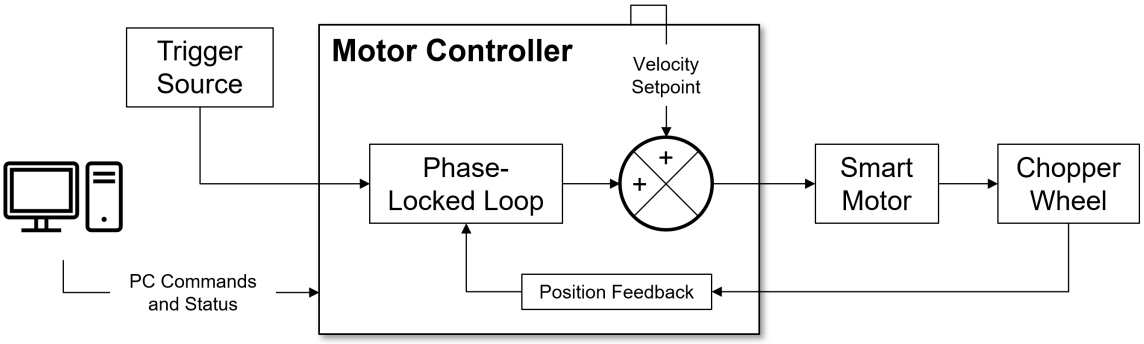

Figure 2.26: The same block diagram of the chopper system from Figure 2.25 but simplified by the use of a smart motor.

2.3.4 Technical Design

The technical design and discussion in this paper is specific to the SPIDERS instrument, with considerations for future instruments such as the CAL 2.0 upgrade and other 10-30m class telescope projects. The technical details are broken up into the mechanical chopper design and the system electrical design: the chopper mechanism is instrument specific, while the electrical design should remain the same or similar between instruments.

Chopper Mechanical Design

The mechanical design development of the chopper mechanism thus far has focused on the SPIDERS instrument which requires the reference beam to be above the main beam, with respect to the bench. This means that in order to mount the chopper to the optical breadboard, it must be hung upside down. Using off-the-shelf adjustable vertical posts and translational base mounts, easy manipulation of the chopper can

be made during the system alignment. Figure 2.27 below shows an exploded view on the left, and two isometric views on the right of the chopper design for the SPIDERS instrument.

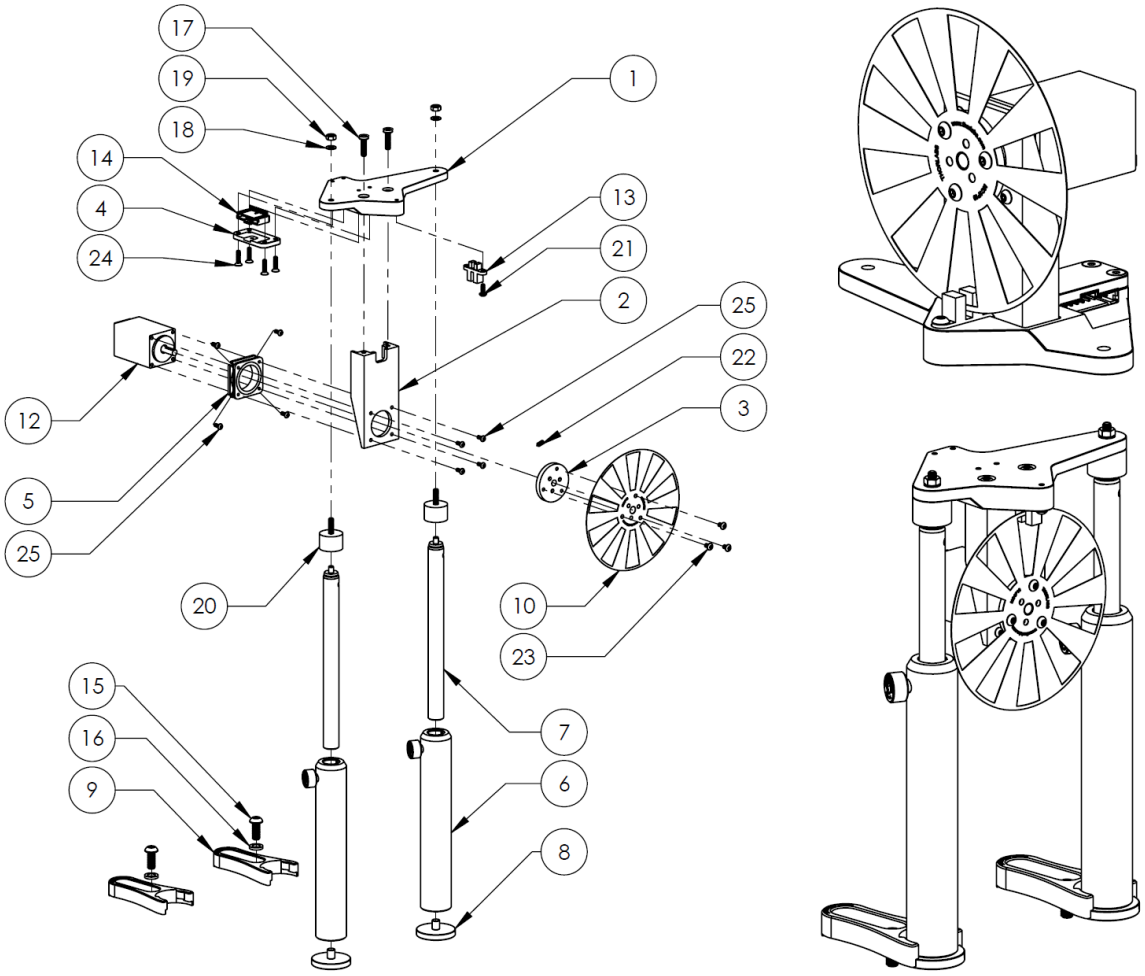

Figure 2.27: The initial mechanical design of the ULSOC (top right), and the custom assembly for the SPIDERS instrument exploded (left) and isometric (bottom right) view.

The mechanical design consists of five custom components and includes a optional silicone damper - shown in Figure 2.27, items 1, 2, 3, 4, and 5, respectively. The optional damper will be tested in situ for its vibrational response and its use determined when the system is prototyped. The remaining components are off-the-shelf and specific to the SPIDERS optical design. Of the five custom components, only the mounting bolt hole pattern of the base (item 1) should need modification to fit any other instrument.

For future projects, such as the CAL 2.0 upgrade, it is expected that additional custom components will be required. On instruments where the optical axis of the reference beam and main beam are closer together, a custom chopper blade (item 10) that does not have solid portions joining the blade segments is required to mitigate vignetting. Furthermore, instruments with variable gravity vectors (such as those mounted directly to a telescope at the Cassegrain focus), will require a different damper design to minimize sway, and more considerations for thermal emission and shielding. The optical sensor (item 13) is also expected to change to a different sensor that would ideally not use light at all.

Electrical Design

The electrical design for SPIDERS needs to be simple and easy to use. The design must be self-calibrating and work autonomously with the rest of the instrument, while also allowing manual control from the PC. Since the ULSOC must have minimal impact on the space it is occupying inside the instrument, the controlling electronics and power supply are housed separately in a control box connected by a 2.5 m cable. The cable to the chopper mechanism is detachable at both ends for the added convenience of shipping and storage. A BNC trigger input and PC communication line is attached to the control box, where it is assumed the control box should be kept near the trigger source and PC, but is not required.

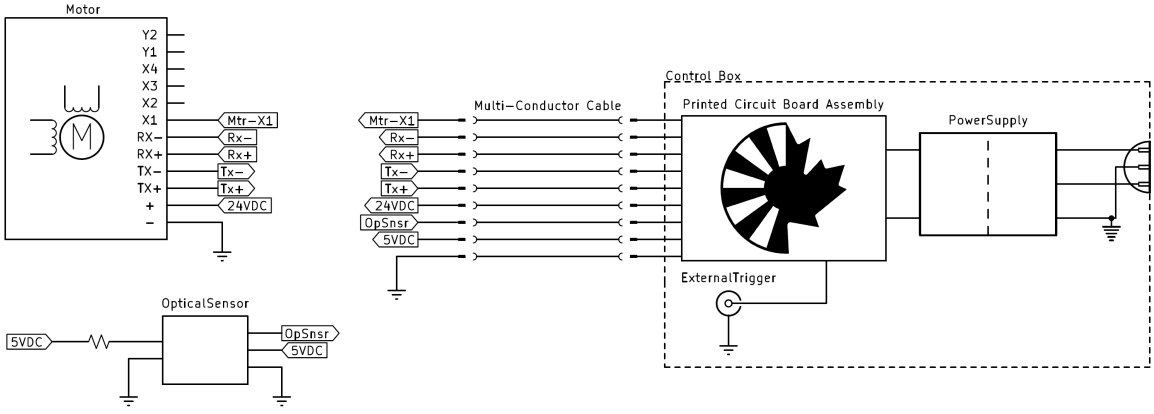

Figure 2.28: The initial electrical design concept for the ULSOC for the SPIDERS instrument.

The concept electrical design for the SPIDERS instrument is shown in Figure 2.28 above using the TSM11 smart motor, an optical sensor, detachable communications

and power cable, and control box. The control box houses a custom Printed Circuit Board (PCB) that will process the trigger signal and the optical sensor position feedback to establish a phase-locked chopping response with the motor. The power supply receives 120 VAC and provides 24 VDC to the PCB which is given directly to the motor and to another transformer for logic level voltages. The power entry module is fused and has a built in filtering circuit for safety and noise reduction.

Other instruments are expected to require the same basic electrical functions, including a phase-locked loop with an input trigger source, and the ability to communicate with a PC. Facility-class instruments like the CAL 2.0 upgrade will require additional safety mechanisms and electrical stages, but it is expected that the core control mechanism and electronics will stay the same. With the advantage of the smart motor controlling itself in the background, the trigger handling and commands are considered instrument and observation specific, implying that only the software will require updating for new instruments.

2.3.5 Preliminary Design and Results

The ULSOC preliminary design is rated for the harsh conditions of high-altitude telescopes, and designed for a long life of continuous and maintenance-free operation. The ULSOC is rated for 5000 m altitude and temperatures as low as -30 °C. The stepper motor ball bearings are the limiting component in the lifespan of the device, but are expected to last for over 10 years being used for 8 hr observations, 3-5 nights a week - around 20,000 operational hours [121]. A rendering of the control box concept and a photo of the finalized chopper mechanism for the SPIDERS instrument are shown below in Figure 2.29.

The version 2 (V2) control box shown in Figure 2.29 rests on four rubber feet and sits 120 mm wide, 220 mm deep, and stands 64 mm tall. The SPIDERS chopper mechanism sits 134 mm wide, 81 mm deep, and stands 117 mm tall with a 101.6 mm diameter off-the-shelf chopper wheel. Missing from the figure is the PC COMM cable used for sending commands to and receiving status updates from the ULSOC, the CHOPPER cable that connects the chopper mechanism to the control box, and an external trigger BNC connection for the chopper to synchronize to.

Initial motor response tests prove that stopping and starting in the ‘on’ and ‘off’ position can be done smoothly and accurately with PC communications. Chopping frequencies from 0.01 Hz up to 120 Hz with a 10-segment chopping blade were shown

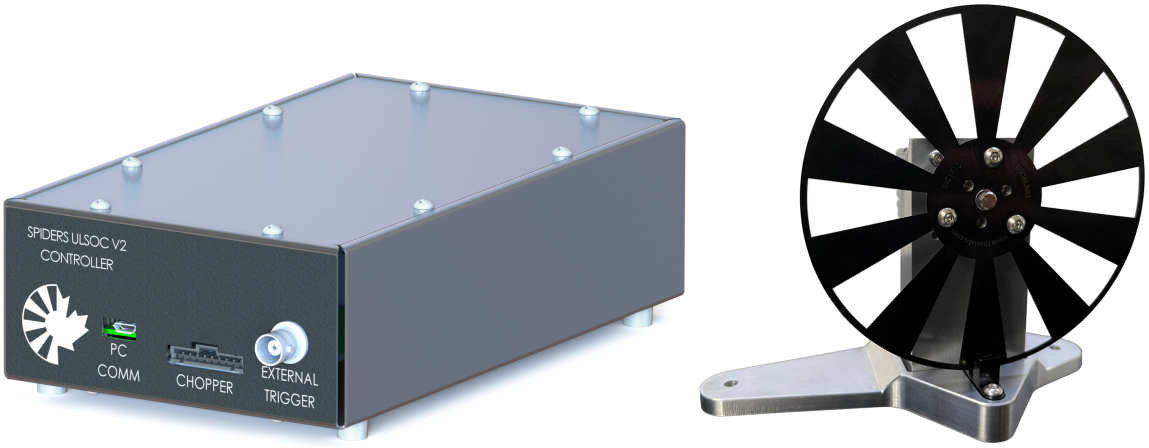

Figure 2.29: On the left, a rendering of the control box V2 concept. On the right, the manufactured chopper mechanism for SPIDERS.

to operate almost vibration-free. Using a standard NEMA 11 stepper motor without smart motor control, the motor passed through its natural frequency between a chopping frequency of 10 Hz and 12 Hz. Separating the stepper motor from the motor frame with the inclusion of the optional damper raised the natural frequency of the motor and slightly magnified the intensity of the vibration at the higher natural frequency. This effect has yet to be studied for the TSM11 smart motor, where the more advanced closed-loop system will produce less noise and use less current for driving. The optional damper will be tested on the bench before a final choice is made on using it in the final design. The CAL 2.0 ULSOC and other future projects may require a different approach to vibration isolation when the instrument has a variable gravity vector.

2.3.6 Next Steps and What to Expect

The ULSOC system for the SPIDERS instrument is still waiting on the finalization of the electrical design, and the manufacturing of control box including the custom PCB. With the mechanical design of the chopper mechanism complete and ready to install on the bench, the electrical design is expected to operate on a prototyping breadboard for initial testing and verification, before being pushed to a first prototyped package. The first control box prototype was developed in 2022, and a fully integrated system installed on SPIDERS in early 2024. Development of the CAL 2.0 ULSOC mechanical design has begun already with the aim to prepare and assist the primary mechanical

designers of the CAL 2.0 instrument. The electrical design for CAL 2.0 will require more safety and facility-class level considerations, requiring more collaboration with the GPI electronics and software teams. Other future projects will allow adaptations to the ULSOC and a case-by-case basis.

The expected results from the ULSOC in the SPIDERS instrument are the steady and accurate chopping of reference beam light, resulting in the interference-born fringes blinking on the detector. The fringe and unfringed image can be subtracted to produce a differential image that contains the PSF of the pinhole, known as the 'differential image vector'. This differential image vector is multiplied with an interaction matrix and used to retrieve an updated phase measurement of the wavefront [22]. Using a portion of this new phase measurement, a command is sent to update the shape of deformable mirror (DM), and the coherent starlight speckles can be removed from the recorded image. This process is repeated in real-time to suppress static speckles and quasi-static speckles evolving slower than the exposure time between chopped images. The resulting closed-loop system produces a 'dark-hole' around the star where the DM is able to actively reshape the wavefront back to flat, exposing faint and hidden exoplanets. The differential image is also utilized for coherent differential imaging (CDI), enabling the recovery of the pinhole PSF and subsequent subtraction of stellar static and quasi-static speckles, as detailed in §1.3.8. The resulting images are shown in Figure 2.30 below.

The images above were captured on the NEW EARTH Lab bench with a commercially available chopper system [114] running at 400 Hz with a super bright simulated star on a similar optical layout to SPIDERS. With the bright star on the bench, the differential imaging loop can generate a deep dark-hole around the star in only a few chopping cycles. It can be seen in the 'Loop Closed' images that the resulting differential image on the bottom right shows residual photon noise and fringe patterns surrounding the star which cannot easily be removed with this real-time method. Having the bright pinhole light for the SCC in the FAST method helps dramatically with fringe visibility, but reduces the achievable contrast within the dark-hole, which is why the chopped unfringed image is highly valuable for the actual science image. Being able to go much slower with the ULSOC will allow us to perform this technique on much dimmer and more realistic targets in preparation for on-sky observations with SPIDERS.

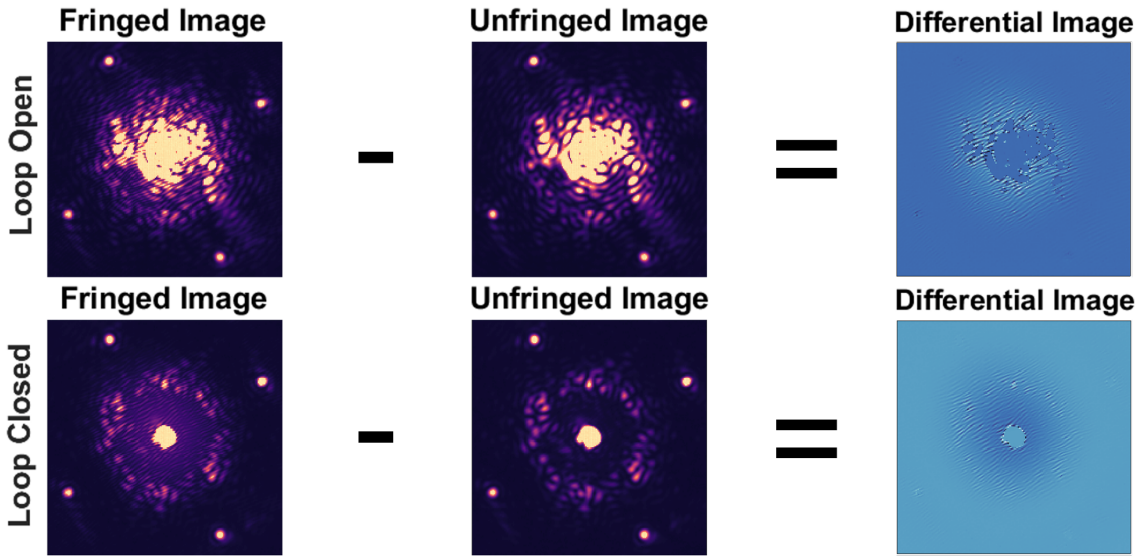

Figure 2.30: A comparison of fringed (left, unchopped), unfringed (centre, chopped), and differential (right) images, with the differential image containing the PSF of the pinhole for the self-coherent camera (SCC). The top and bottom rows represent the loop-open and loop-closed configurations, respectively. All images are colour-mapped for clarity. Detector saturation near the core, caused by excessive illumination, leads to missing fringe information and gaps in the differential image.

2.3.7 Conclusions

The ULSOC system is an unreached extension of commercial optical chopping systems available on the market today, and a powerful solution for high-contrast imaging systems. It reaches into a lower frequency range and is highly adaptable to provide instrument specific capabilities with high-resolution performance. The use of an off-the-shelf smart motor solution reduces system complexity and provides a quicker path forward with less design and development risk. The development of the ULSOC for SPIDERS has lead to the fully prototyped chopper mechanism and a concept of the almost finalized control box and electrical design. The ULSOC is expected to be tested on the bench in late 2022 where the artificial point source on the NEW EARTH Lab bench can be dimmed and a low-frequency loop can be closed for the first time. The advantage of using the ULSOC with the FAST SCC technique is the ability to directly subtract detector noise from the paired images and recover higher contrast images. The variations required for the ULSOC in the CAL 2.0 upgrade have already begun and initial prototyping is expected to take place in 2023.

2.4 Exoplanet Detection and Characterization: Development and Results of a New Generation Imaging Fourier Transform Spectrometer

This chapter is based on material published in the proceedings of the AO4ELT 7 conference in 2023 (10.13009/AO4ELT7-2023-130). Authors: Adam B. Johnson, William Thompson, Kris Caputa, Frédéric Grandmont, Christian Marois, Tim Hardy, Joel-eff Fitzsimmons, Olivier Lardière, Colin Bradley. *My contribution to this work was as the lead author, encompassing the mechanical design, electrical design, software design, testing, validation, and final integration of the device. W. Thompson facilitated the integration of the device into the SPIDERS system. K. Caputa provided expert guidance and review on the electrical design. F. Grandmont supervised my internship at ABB, where he assisted in the development of the quadrature feedback algorithm. C. Marois served as the Principal Investigator for the NEW EARTH Lab, providing essential laboratory support. T. Hardy, J. Fitzsimmons, and O. Lardière offered valuable insights and design advice throughout the project. C. Bradley facilitated institutional support from the university.*

2.4.1 Introduction

The NEW EARTH laboratory team at the National Research Council Canada (NRC) Herzberg Astronomy & Astrophysics (HAA) observatory in Victoria BC Canada have been working on new high-contrast imaging technologies and ideas since 2018 [122]. The current project, the Subaru Pathfinder Instrument for Detecting Exoplanets & Retrieving Spectra (SPIDERS) [103] deploys many new technologies designed specifically for the detection and characterization of exoplanets using the 8.2m Subaru telescope on Maunakea, in Hawaii [123].

In addition to the identification of molecules in the atmospheres of exoplanets using mid to high spectral resolution (discussed in §1.1.6 and §1.2.5), an imaging spectrograph can use low spectral resolution to optimize SDI and CDI post-processing in a large field of view (FOV) with approaches like the fast atmospheric self-coherent camera technique (FAST) [22] and new self-coherent camera (SCC) algorithms [91] (discussed in §1.3.8 and §1.3.10). Higher spectral resolution imaging around key bands, such as CH_4 or H_2O, could also be used to search for planets hidden in the star speckle noise. Furthermore, at very high spectral resolution the IFTS can be

used to do velocity mapping of emission lines. With its capability to handle both low and high dynamic resolution, the IFTS is well-positioned to become a powerful tool for advancing exoplanet science.

2.4.2 Operational Principles

Before its use in exoplanet imaging, Fourier transform spectroscopy has long been and continues to be a widely used process in industries that require the precision measurement and analysis of a material, compound, or light source. Commercially available devices like ABB's Fourier Transform Near-Infrared Process Analyzer FTPA2000-300 [124] use a bright internal source to create a strong signal for spectral analysis of any sample that light can transmit through. Using this device on SPIDERS, spectral analysis can be performed on a star and its companions.

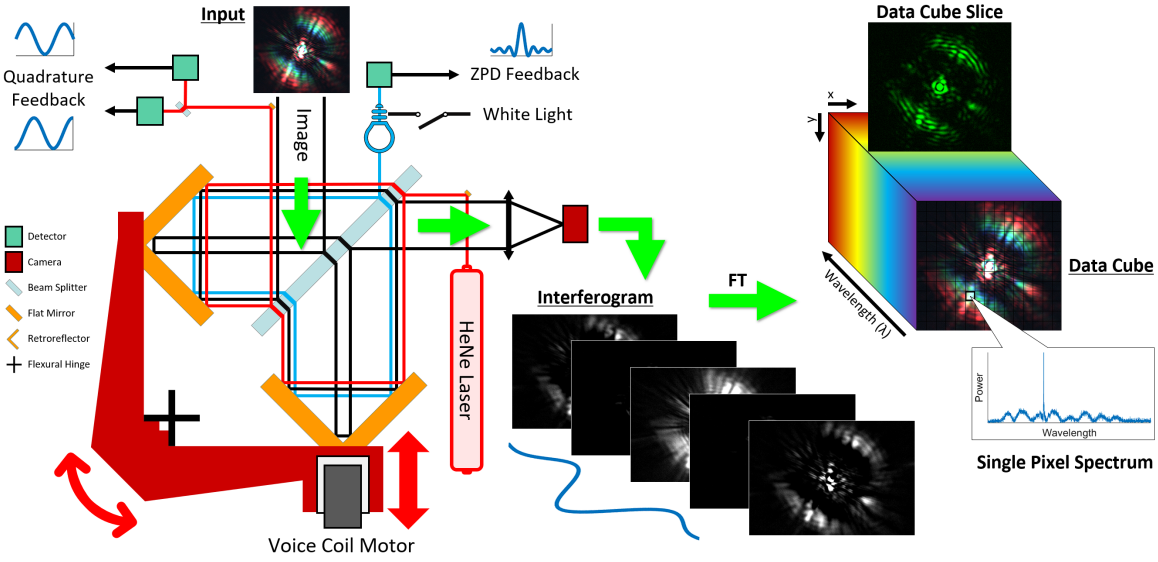

Figure 2.31: A scanning Michelson interferometer receives an image input and outputs an interferogram. A Fourier transform along each pixel yields the spectral data cube of the input image. A helium-neon (HeNe) laser provides positional feedback, while a white light source identifies the absolute centre.

The Michelson Interferometer Design

At the core of the SPIDERS IFTS is a Michelson interferometer equipped with two retroreflector mirrors mounted on an arm with a flexural hinge. This configuration facilitates interference of an image along a varying optical path difference (OPD), as shown in Figure 2.31. The interferometer scans continuously over an OPD window

using a voice coil motor to position the arm in space, a helium-neon (HeNe) laser to provide positional feedback, and an internal white light to find the scan centre (zero-OPD, or ZPD). An incoming chromatic (broadband) image is interfered with itself to produce an interferogram on the detector of a monochromatic camera. The interferogram recorded at each pixel is then Fourier transformed (FT) to recover the spectrum of the image for each pixel. The resulting wavelength specific images represent the spectral components (slices) of the input image and make up the data cube. Stacking and assigning colour to the data cube images can provide an insightful visualization of the original chromatic image.

2.4.3 Closed-Loop Velocity Control

Using the HeNe laser fringe signals, a quadrature algorithm was developed with the help of ABB to recover the OPD of the IFTS [125, 126], similar to the method used on SITELLE [59]. With a robust method to recover the position of the IFTS along its scan, a closed-loop controller was designed to ensure scan stability and repeatability over long-term operation. Without closed-loop control, external disturbances such as mechanical vibration or turbulent air pushing on the IFTS arm will cause the system to deviate from the commanded trajectory and significantly deteriorate the IFTS scan performance. Keeping the velocity constant over the duration of the scan is critical to ensuring each camera image gets an equal exposure time and are captured at near-equidistant OPD. Because the voice coil is driven through discrete position commands proportional to the current it is drawing, the regulated velocity command must be changed into a position command before it is used. Ultimately, the constant-speed motion during a scan is achieved by providing small linearly increasing position commands to the voice coil while taking advantage of the heavy IFTS arm that increases inertia and filters the discrete step motion. The controller block diagram is shown in Figure 2.32 below.

Various controllers were explored in simulation and on the bench including position-velocity cascade and pole-placement, but in the end, the velocity-current cascade controller shown in Figure 2.32 was the simplest to tune and optimize on the bench with a constant positive or negative velocity input. The inner current controller loop is implemented via hardware and does not require any tuning. Although some FTS devices operate in a step-scan mode to increase integration time at specific OPD, this system is designed to work at a constant speed only, also referred to as the

continuous-scanning mode.

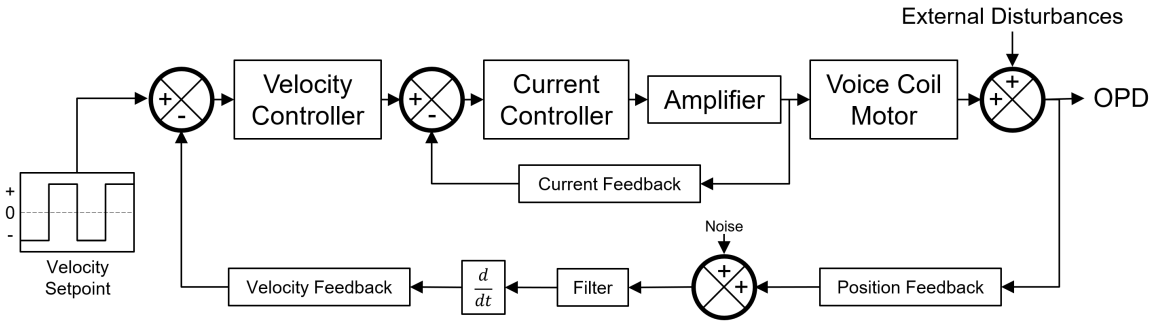

Figure 2.32: A closed-loop velocity-current cascade controller to regulate the voice coil motor scan speed.

2.4.4 Implementation, Performance, and Early Results

To acquire the position feedback, drive the voice coil, and implement closed-loop control for the IFTS system, custom electronics and software were developed. A printed circuit board (PCB) was designed to mount off-the-shelf analog-to-digital converters (ADC) to measure the fringe signals, a digital-to-analog (DAC) converter to command the voice coil current controller, and support for a microcontroller unit (MCU) to control the system. Every 10 μs (or at a rate of 100 kHz) the 16-bit ADCs measure and sends the analog fringe signals to the MCU, the MCU determines the current position, a new command is sent to the 16-bit DAC, and the current controller provides a new position command to the voice coil. A sheet metal enclosure was designed to house a power supply, fan, and PCB assembly while fitting comfortably on a *1U* server rack shelf ($<$ 1.75 in tall). BNC connectors on the front allow the input or output of 3.3 V triggers while a USB can be connected to set the scan speed and window serially from any PC, Figure 2.33 (left). A custom cable connects the IFTS controller to the ABB FTS voice coil and fringe signal detectors, mitigating any addition of heat or vibration from the controller by housing it away from the system.

The closed-loop controller was developed first in the NEW EARTH lab before being optimized on the SPIDERS bench for speeds between 0.36 mm/s and 1.2 mm/s, scanning back and forth indefinitely over ZPD. An OPD window can be selected anywhere within the range of -10 mm to $+10$ mm, with sizes as small as 100 μm, for either double-sided or single-sided scans. Using a scan speed of 0.36 mm/s in an

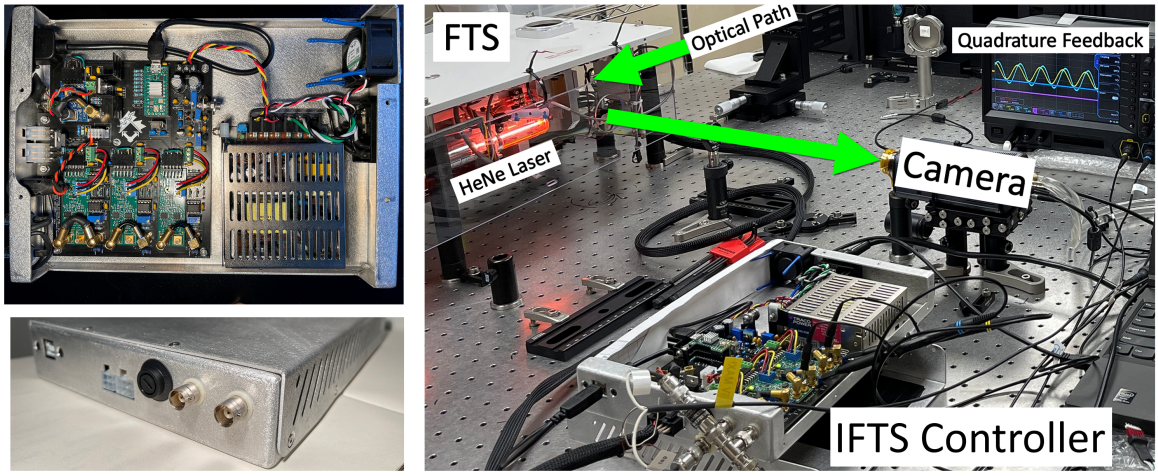

Figure 2.33: The custom IFTS controller system (left) and early experimental setup in the NEW EARTH lab (right).

OPD window from −3 mm to +3 mm, the IFTS position and velocity response are shown in Figure 2.34 below from left to right, respectively, for the system in open and closed-loop control.

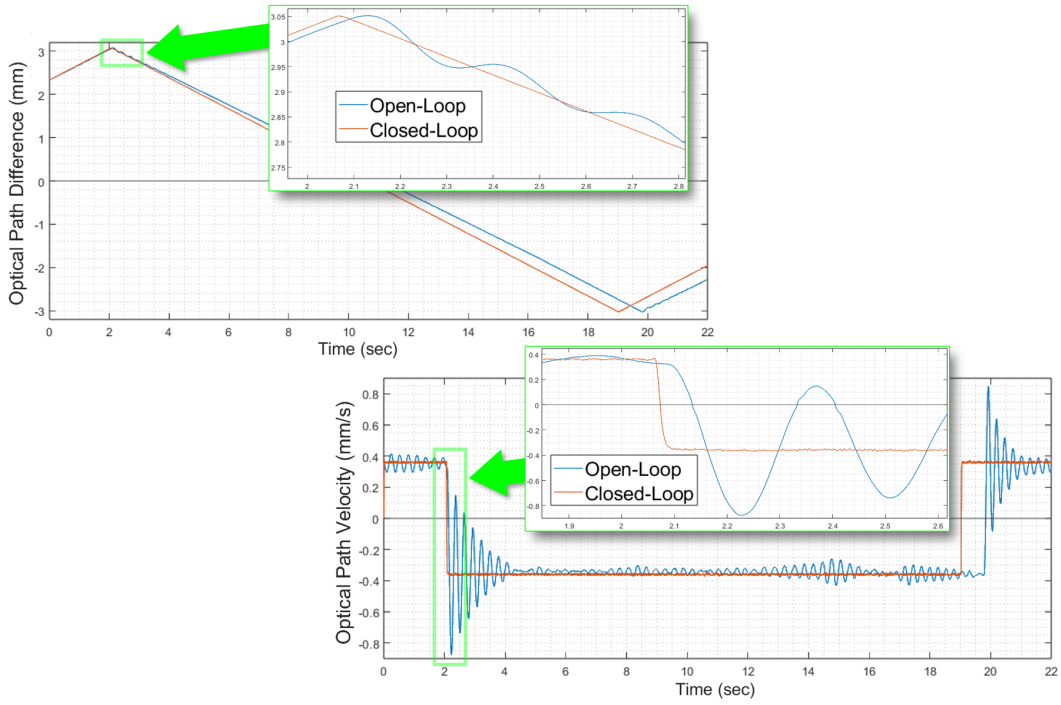

Figure 2.34: The open and closed-loop response in position and velocity for a 0.36 mm/s continuous-scan.

When the speed setpoint changes sign (the system reaches the edge of a scan window), the open-loop system takes over 2 seconds to settle and never fully settles due to external vibrations combined with its highly under-damped response. Furthermore, the open-loop control suffers from steady-state error and on average does not reach the scan speed setpoint, leading to longer than expected scan times. By comparison, the closed-loop system settles in about 35 ms (or in under 15 μm of OPD) and minimized the effect of benchtop vibrations seen in the open-loop control.

Linking the camera images to the OPD, the IFTS controller can either output a 3.3 V trigger at equidistant OPD intervals with non-uniformly triggered camera exposures, or a non-equidistant OPD can be output in Angstroms over serial communication with uniformly triggered camera exposures. In either the equidistant OPD or non-equidistant OPD case, the camera images from a complete scan produce the raw interferogram. The interferogram at equidistant OPD intervals can utilize a standard fast Fourier transform (FFT) to recover the spectrum, while the uniform triggering at non-equidistant OPD intervals require a non-uniform FFT (NUFFT) to interpolate the interferogram and resample to use the standard FFT. Details on these operations are not discussed in this paper but can found in publications such as [127] and [128].

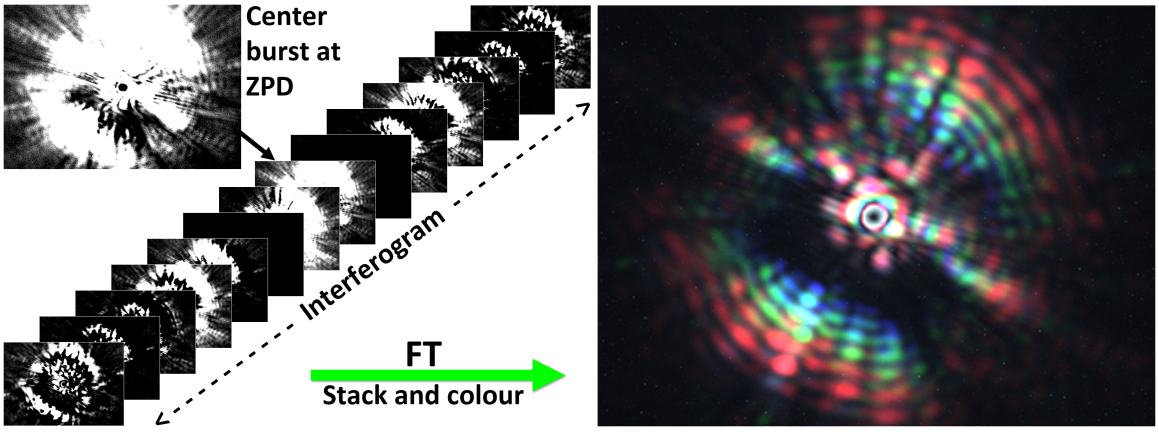

Figure 2.35: The interferogram produced and recorded by the SPIDERS IFTS (left) and the processed broadband image (right).

To evaluate the spectroscopic performance of the IFTS system, a SuperK COMPACT supercontinuum white light laser [129] was used as an infrared light source on the SPIDERS bench with a C-RED 2 infrared camera [130]. The camera took images at equidistant OPD locations every 400 nm along a -3 mm to $+3$ mm window at a constant speed of 0.36 mm/s, requiring an average frame rate of 900 Hz. The $15,000$

images recorded by the monochromatic camera produce the interferogram - a subset of black and white images around the ZPD shown in Figure 2.35 on the left - where each pixel is Fourier transformed (FT) to produce a wavenumber spectrum at each pixel in the FOV. The data cube of wavenumber (or wavelength) specific images can be stacked and coloured to produce the original chromatic input image (Fig. 2.35, right), with wavelength from red (long) to blue (short).

Using the adaptive optics (AO) system within SPIDERS, speckle suppression methods like *Thompson 2023* [79] can be used to remove the bright light directly surrounding the star (or benchtop light source in this case) to see potentially hidden planets that might exist. The dark region immediately surrounding the centre in Figure 2.35 demonstrates how a deformable mirror (DM) can target bright speckles, improving image clarity near a bright source. This method, along with dynamic correction of atmospheric effects, is discussed in *Thompson 2023* and §1.3.10.

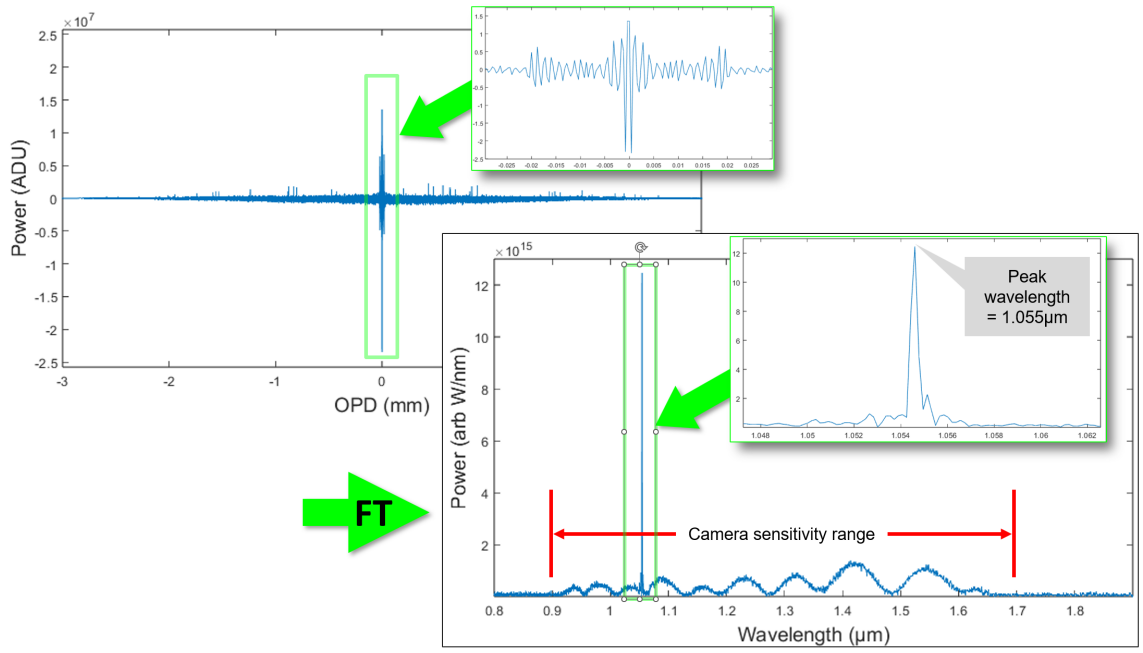

Figure 2.36: The 2D interferogram (left) and wavelength spectrum (right) of a benchtop supercontinuum white light source.

Analyzing the bright regions in the FOV surrounding the core of the image (to negate chromatic effects caused by the coronagraph removing the central core light, currently installed on SPIDERS), an average 2D interferogram and wavelength spectrum of the light source can be acquired, shown in Figure 2.36 above, respectively.

The obtained spectrum confirms that the C-RED 2 camera is only sensitive between 0.9 and 1.7 μm, with a peak intensity around 1.06 μm. The spectral resolution of this 3 mm double-sided scan is around R 6,000, where a possible 10 mm scan could produce an R 20,000 spectrum, or R 100 for a 100 μm scan. The interferogram can always be trimmed in post processing to reduce the resolution, but a longer scan must be performed to increase it. During this initial test on the SPIDERS bench, it was discovered that the final folding mirror was not optimal for the infrared waveband we were imaging in, and resulted in the strange and lumpy spectrum we see in Figure 2.36, rather than the unique spectrum published by the laser manufacturer [129]. Verifying the measured peak intensity and confirming the camera sensitivity range shows that the IFTS controller and system are working as expected.

2.4.5 Conclusions and Future Work

Initial results of the IFTS system on SPIDERS indicate that we are able to recover high-resolution spectra over a full FOV on the bench. Tests using a supercontinuum white light source and equidistant OPD intervals proved the success of the new IFTS system and its ability to provide highly-stable motion for long-term continuous-scanning operation. With the ability to reprogram the scan speed and window for use with different triggering modes (equidistant or non-uniform OPD), the system is able to provide unique capabilities for current state-of-the-art and future high-contrast imaging instruments to use for exoplanet imaging and characterization. Current development with non-equidistant OPD serial output and uniform triggering is proving to be easier to integrate with cameras and the rest of the system, while adding some complexity to the post processing. As we prepare for the planned 2025 commissioning of SPIDERS, we are refining the data cube processing algorithm to support extended observing sessions. This will also enable more comprehensive performance analysis and more detailed publications.

Chapter 3

GPI, CAL 2.0: The Gemini Planet Imager Calibration Unit 2.0 Upgrade

The Gemini Planet Imager Calibration Unit 2.0 (GPI CAL 2.0) is a facility-class upgrade to the original GPI CAL system, developed to enhance high-contrast imaging through improved focal plane wavefront sensing, control, and post-processing techniques at the Gemini North Telescope. *This chapter focuses on my contributions to the project, including the design, assembly, validation, and integration of three primary mechanical subsystems: the focal plane mask (FPM) wheel, adapted from the CAL 1 design developed at the NASA Jet Propulsion Laboratory (JPL); the polarization modulator (PolMod), based on a CAL 1 design from NRC HAA; and an ultra-low speed optical chopper, newly engineered for CAL 2.0 with prototyping and validation on SPIDERS, co-developed with experienced electrical engineer D. Gamroth. As CAL 2.0 and its subsystems remain in active development, this chapter presents final mechanical designs and early-stage assembly progress. The continued success of the project has been made possible through close collaboration with Principal Investigator C. Marois, Mechanical Lead and Project Manager J. Fitzsimmons, Mechanical Engineer M. Demers, Optical Engineer O. Lardière, and contributors W. Thompson, T. Hardy, E. Chapin, and K. Caputa, as part of a broad, multinational effort involving institutions such as the NRC, Opto-Mécanique de Précision (OMP), the University of Victoria, the University of Toronto, and the University of California, Santa Cruz.*

3.1 CAL 2.0: Introduction and System Overview

Building upon the SPIDERS instrument developed for the Subaru Telescope (§2), CAL 2.0 represents the next stage in the evolution of facility-class focal plane wavefront sensing for ground-based exoplanet imaging. As a critical technology demonstrator, SPIDERS validated the FAST self-coherent camera (SCC) architecture and established the foundation on which CAL 2.0 builds, including the integration of specialized focal plane masks, closed-loop speckle suppression, and coherent differential imaging (CDI) techniques, introduced in §1.3.8 and §1.3.10. The lessons learned from its optical, mechanical, and control system implementation, along with the operational challenges encountered, directly informed the design and engineering of CAL 2.0. While SPIDERS served as a pathfinder for focal plane wavefront sensing, CAL 2.0 advances the approach into a robust, observatory-grade subsystem designed for autonomous, continuous operation at the 8.1 m Gemini North Telescope, with the goal of improving contrast by up to a factor of 100 on bright stars [131].

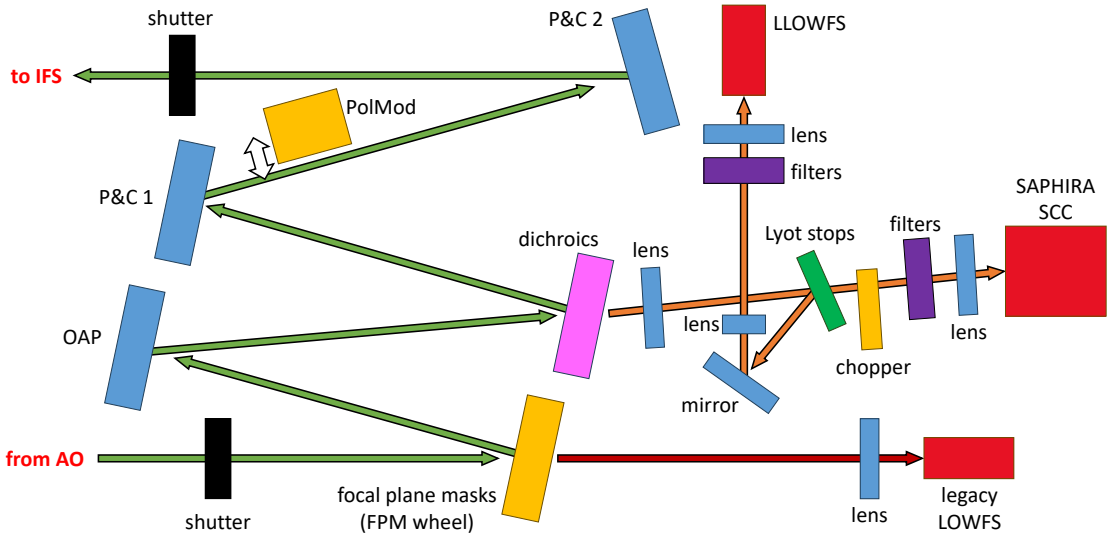

Figure 3.1: Optical layout of CAL 2.0, illustrating the light shared between the integral field spectrograph (IFS) and the wavefront sensing arms. A legacy low-order wavefront sensor (LOWFS) is positioned behind the focal plane mask (FPM) wheel, providing fallback support for the original non-common path CAL architecture.

As part of the Gemini Planet Imager 2 (GPI 2) upgrade, CAL 2.0 introduces a new optical and control architecture that replaces the original GPI CAL system. A key advancement is the shift from a non-common path to a common-path configuration, minimizing non-common path aberrations (NCPAs) that previously limited contrast

performance. Unlike SPIDERS, which includes a local deformable mirror (DM) for wavefront correction, CAL 2.0 is a sensing-only system operating downstream of the GPI adaptive optics (AO) system. It receives light already corrected by the facility DM and measures residual aberrations in the science focal plane using the SCC for high-order modes and a Lyot-based low-order wavefront sensor (LLOWFS) for slow drifting aberrations such as tip, tilt, and focus. These measurements are sent upstream in real time to the GPI AO controller, implemented within the NRC-developed HEART real-time control framework, which applies the corrections to the shared DM at rates up to 100 Hz for high-order and several hundred hertz for low-order modes [132].

Following AO correction by GPI, the science beam enters CAL 2.0 for wavefront sensing before continuing downstream to the integral field spectrograph (IFS), as shown in the Figure 3.1 optical layout. Within CAL 2.0, a motorized dichroic wheel splits the post-AO near-infrared light between the science channel and two sensing arms. The focal plane wavefront sensing system, based on the FAST SCC architecture, uses a cryogenically cooled SAPHIRA detector to measure high-order residual speckles in real time, while the LLOWFS measures low-order aberrations.

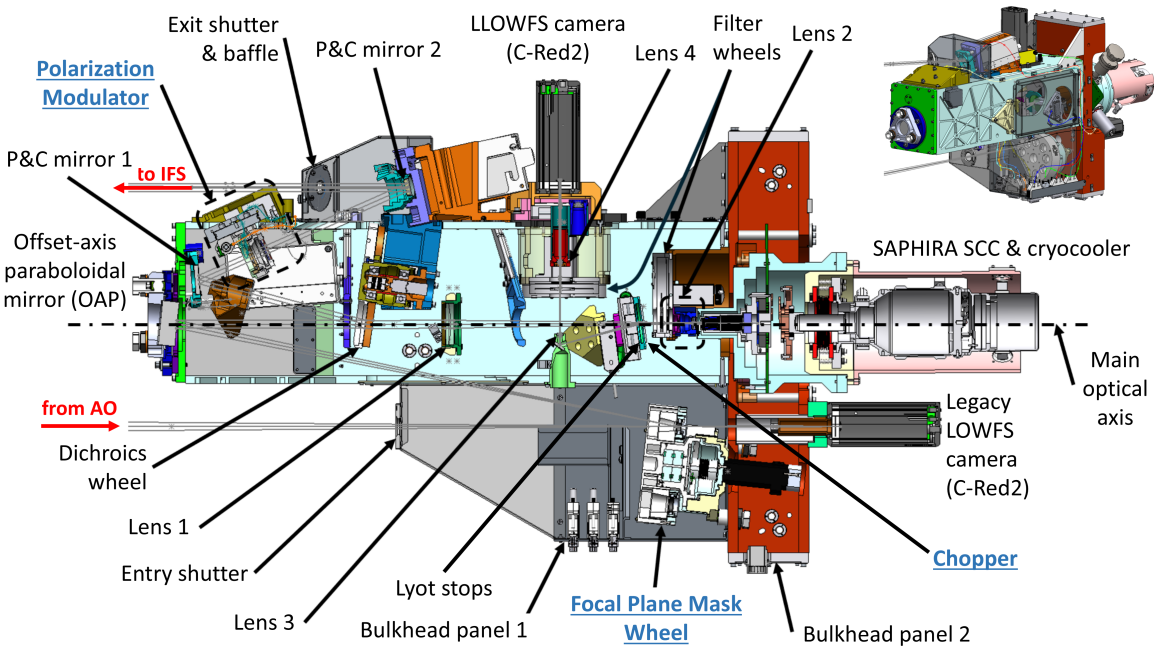

Figure 3.2: Section view of CAL 2.0 mechanical structure and labeled main subsystems, with isometric view in the top right. Figures courtesy of C. Marois [131].

To ensure system resilience and continuity with GPI's original control strategies,

CAL 2.0 includes a fallback configuration that preserves the non-common path architecture of the original CAL design. A legacy low-order wavefront sensor (LOWFS), positioned behind the focal plane mask (FPM) wheel, supports the use of traditional masks and control algorithms that let the core PSF light through a central hole to an imaging camera. This mode ensures continued operation in a validated configuration if the CAL 2.0 sensing path becomes non-functional during commissioning, supporting a reliable transition from legacy methods to advanced focal plane wavefront sensing.

Mechanically, CAL 2.0 is enclosed in a compact, rigid structure that supports all optical and electromechanical components while providing thermal and mechanical stability, as shown in Figure 3.2. Several proven mechanisms from the original CAL design have been retained, including the Focal Plane Mask Wheel and Polarization Modulator, while a new Ultra-Low Speed Optical Chopper has been added to support SCC fringe modulation. The remainder of this chapter describes the development of these three systems, as CAL 2.0 and its subsystems remain in active development to be fully assembled and integrated by early 2026. These components support high-precision focal plane sensing and correction, contributing to both the contrast enhancement targets and the broader scientific goals of the GPI 2.0 upgrade.

3.1.1 Focal Plane Mask Wheel

Overview and Requirements

The focal plane mask (FPM) wheel enables precise and repeatable positioning of up to nine custom masks used in the self-coherent camera (SCC) path for wavefront sensing. Originally developed for the GPI CAL system and successfully deployed at Gemini South in 2013, the mechanism has been carried forward into CAL 2.0 with minimal modification. This reuse capitalizes on a proven optomechanical design, reducing development time and integration risk while ensuring consistent performance. However, due to the age of the original design, components such as adhesives, motors, sensors, paints, and mechanical hardware such as fasteners and bearings required resourcing. When direct replacements were unavailable, equivalent parts were identified or the design was modified accordingly. In cases where the original design remained applicable, it was treated as a validated baseline, enabling targeted analysis only when necessitated by changes in component availability or material substitutions, rather than requiring a full re-evaluation of all design elements. A summary of the system-level requirements for the CAL 2.0 FPM wheel is provided in Table 3.1.

Table 3.1: Mechanical and control constraints for the CAL 2.0 focal plane mask wheel.

Requirement	**Specification**
Forward and backward compatibility	Compatible with CAL 2.0 controllers Preserves original CAL design configuration
Support for multiple focal plane masks	Mask capacity: 9 Mask Diameter: 25.0 mm ($+0.0/-0.1$ mm) Mask Thickness: 1.0, 1.6, 6.0, or 6.35 mm
Time between mask changes	$\leq$ 30 s (encoder referenced) $\leq$ 60 s (encoder not referenced)
Positioning accuracy	$\leq$ 50 µm from nominal position
Positioning repeatability	$\leq$ 50 µm
Mask changes per day	$\leq$ 10
Operational lifetime	$\geq$ 10 years
Operating temperature range	-5 °C to 20 °C
Thermal emission limits	System $\leq$ 2 °C above ambient Must not emit 0.8 to 3.5 µm infrared light

Design Summary

The FPM wheel is built around a central rotatable platform that holds nine focal plane masks, each secured against an optically flat Zerodur reference surface. This reference provides a stable mechanical interface that ensures precise mask alignment and consistent positioning across the expected operating temperature range. To accommodate optics of varying thicknesses, shim stacks combined with a wave spring apply uniform retention pressure.

Flexural features integrated into the rotating platform allow manual adjustment of perpendicularity between the Zerodur surface and motor axis, maintaining alignment throughout rotation. Additional flexural elements within each mask pocket enable fine radial positioning of individual masks relative to the incoming beam. Prior to integration, the Zerodur flat is aligned to the motor axis to establish perpendicularity. Radial alignment of each mask is first performed coarsely using mirror dummies and later refined following integration into the complete CAL 2.0 system.

Mask selection is achieved using a DC motor coupled to a harmonic gearhead with a 100:1 reduction ratio. This provides backlash-free, non-backdrivable motion with precise rotational control. An internal 15-bit infrared encoder is directly coupled to the hub, providing incremental position feedback with a resolution of 10 µm and an accuracy of ± 1 µm relative to the main CAL 2.0 optical axis. To suppress stray

infrared light from the encoder, a custom light shield and revised motor mount were introduced during the CAL 2.0 implementation. As the motor operates only briefly between observations and is non-backdrivable, no significant heat is generated under normal operating conditions.

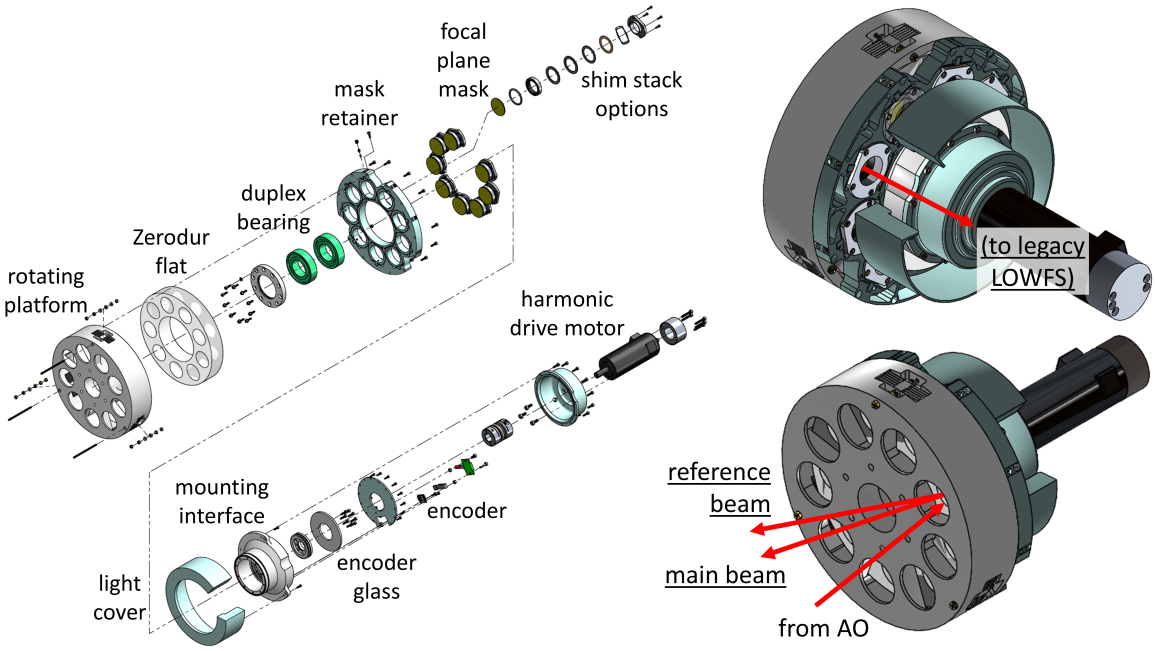

Figure 3.3: Exploded CAD view of the CAL 2.0 FPM Wheel assembly with labeled critical components (left). Isometric views are shown with the beam path (right)

Material selection prioritizes thermal and optical cleanliness. Low-volatility greases, oils, adhesives, and paints are used to prevent corrosion, avoid galling between stainless steel components, and eliminate contamination from off-gassing that could degrade optical surfaces. An oleophobic (oil repelling) surface coating (Nyebar Type T 0.2% [133]) is applied around the bearings and motor mount to prevent grease migration toward the masks, encoder, or other critical regions. Optically flat black paint (Aeroglaze Z306 [134, 135]) is applied to the front surface of the rotating platform to absorb stray infrared light from the primary beam, and to the motor mount shielding to suppress stray light originating from the internal encoder.

Together, these features ensure the FPM wheel meets all mechanical stability, optical cleanliness, and motion control requirements specified in Table 3.1, with the final design and key components illustrated in Figure 3.3.

Current Assembly and Next Steps

At the current stage of development, the final mechanical assembly of the FPM wheel has been completed. As shown in Figure 3.4, the integrated drive system and rotating platform assembly are shown prior to temporary mounting on a 3D-printed base structure for alignment and performance validation. Optical masks have not yet been installed at this stage.

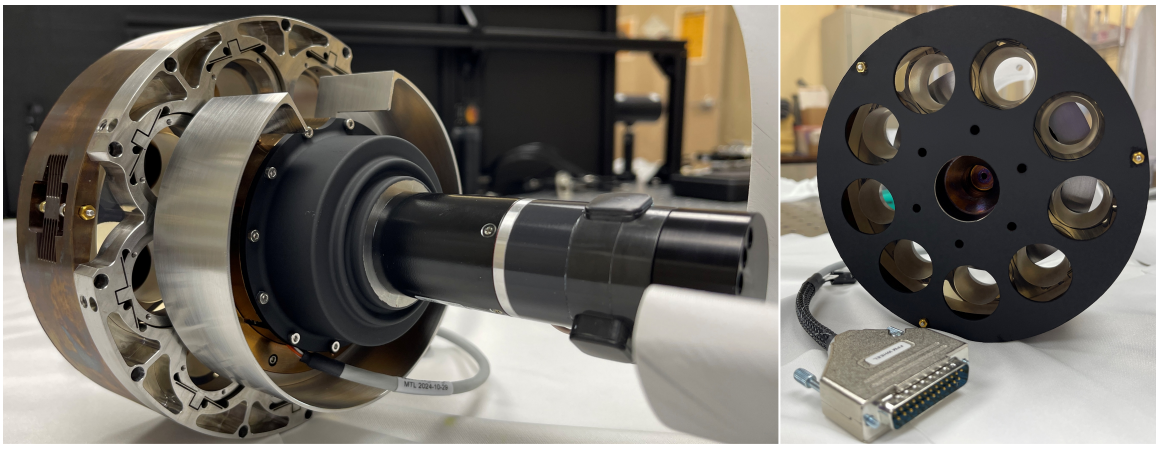

Figure 3.4: Initial laboratory assembly of the CAL 2.0 focal plane mask wheel side (left) and front (right) view.

Prior to final assembly, preliminary cold testing was conducted to evaluate the performance of the harmonic gearhead grease, which is nominally rated for operation down to 0 °C. In this test, the motor was run independently, outside of the system, and repeatedly completed full wheel rotations in approximately 15 seconds at −10 °C, demonstrating that the grease performs reliably under sub-nominal temperature conditions.

The next phase of development will focus on completing motion and repeatability testing under operational loads across both ambient and low-temperature conditions. This will be followed by alignment procedures, including precision alignment of the Zerodur reference flat and initial coarse positioning of the mask retainers using mask dummies. Upon completion of these steps, the final mechanical integration of the FPM wheel into the CAL 2.0 system will take place. In parallel, software integration with the CAL 2.0 control framework will continue. Once the FPM wheel is installed, it will undergo a final revalidation phase to confirm mechanical performance, alignment stability, and overall readiness for observatory deployment.

3.1.2 Polarization Modulator

Overview and Requirements

The polarization modulator (PolMod) is a dual axis optomechanical assembly that enables polarimetric calibration and supports polarization differential imaging (PDI, see §1.3.8). It consists of a linear translation stage that moves a polarization optic into and out of the science beam, and a rotational stage that provides continuous angular adjustment to the polarization optic during observation.

Mechanically, the PolMod is mounted within the CAL 2.0 system, situated after the pointing and centring mirrors that feed the integral field spectrograph (IFS). When needed during an observation, the device inserts the optic, rotates it to one or more commanded angles, and retracts when not in use. All components are selected and finished for thermal stability and optical cleanliness to prevent contamination or stray light within the science path. Key system requirements and constraints are summarized in Table 3.2.

Table 3.2: Mechanical and control constraints for the CAL 2.0 polarization modulator.

Requirement	**Specification**
Forward and backward compatibility	Compatible with CAL 2.0 controllers Preserves original CAL system configuration
Linear positioning range	+50/−0 mm from home position (fully into and out of main beam path)
Linear positioning accuracy	$\leq$ 50 µm from nominal position
Linear repeatability	$\leq$ 50 µm
Rotational positioning range	± 360° from home, no limit
Rotational positioning accuracy	$\leq$ 8.7 mrad (0.5 °)
Rotational repeatability	$\leq$ 8.7 mrad (0.5 °)
Operational lifetime	$\geq$ 10 years
Operating temperature range	-5 °C to 20 °C
Thermal emission limits	System $\leq$ 2 °C above ambient Must not emit 0.8 to 3.5 µm infrared light

Design Summary

The CAL 2.0 PolMod builds upon the original polarization modulator developed for the GPI CAL system at NRC HAA in 2009. The core mechanical design has been retained with minor modifications to ensure compatibility with the upgraded control framework while maintaining stringent optical cleanliness standards.

The mechanism consists of a commercial high-precision linear translation stage paired with a custom rotational stage mounted above. Both axes are actuated by DC motors with integrated 9-bit magnetic encoders, providing precise motion control without introducing optical emission. The linear stage uses a 22:1 gearhead driving a 1.27 mm pitch lead screw attached to an anti-backlash nut, enabling smooth and accurate insertion of the optic. The rotational stage employs a 900:1 gearhead driving an anti-backlash spur gear system, supported by a four-point contact bearing for enhanced stability. As the rotary motor gearhead has a high reduction with minimal load, the lead screw configuration is non-backdrivable, and both motors only operate intermittently between observations, thermal output to maintain position remains negligible. An exploded view of the full assembly is shown in Figure 3.5.

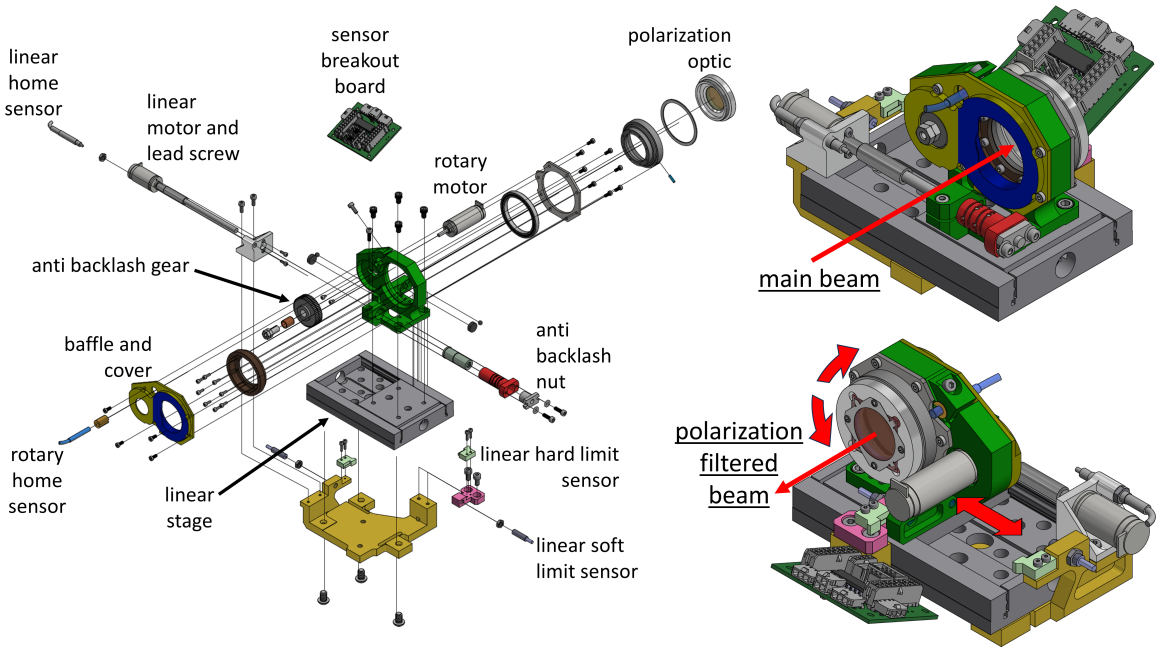

Figure 3.5: Exploded CAD view of the CAL 2.0 polarization modulator with labeled components (left). Front and rear isometric views illustrate the beam path through the mechanism (right). Component colours are for visualization purposes only.

Accurate and repeatable motion is achieved through closed loop encoder feedback, mechanical preload, and a set of integrated sensors. The encoders provide resolutions of approximately 0.11 µm for linear motion and 13.6 µrad for angular motion per count. Linear homing is defined by a plunger style push button sensor with 5 µm repeatability, backed by secondary plunger style soft limit switches and snap action hard limit switches. For the rotational axis, which supports continuous 360° motion,

homing is referenced using an inductive proximity sensor with less than 1 mrad of repeatability, eliminating the need for mechanical limit sensors.

To ensure long-term performance under variable thermal conditions, all mechanical interfaces are assembled with low-outgassing, thermally stable materials. Fomblin UT18 grease [136] is used for gear and lead screw lubrication, while Armstrong A-12 epoxy [137] is used to secure sensor touch pads, the rotary homing sensor pin, and fastener heads in place, ensuring long-term mechanical stability.

The polarization optic is an achromatic wave plate composed of MgF_2 and quartz, mounted in a cylindrical holder with a 24.5 mm clear aperture and 0.5° internal tilt to reduce ghost reflections. To suppress stray near-infrared light, all internal surfaces near the beam path, including the front cover and baffle, are coated with Aeroglaze Z306 black paint [134], selected for its low reflectivity and durability [135].

Current Assembly and Next Steps

With the mechanical design finalized, the CAL 2.0 PolMod has been fully assembled and mounted to a temporary test fixture for operational validation. This setup enables verification of system performance in a controlled environment prior to full integration. Figure 3.6 shows the completed assembly, including the installed linear and rotational stages, wiring, and sensor harnesses.

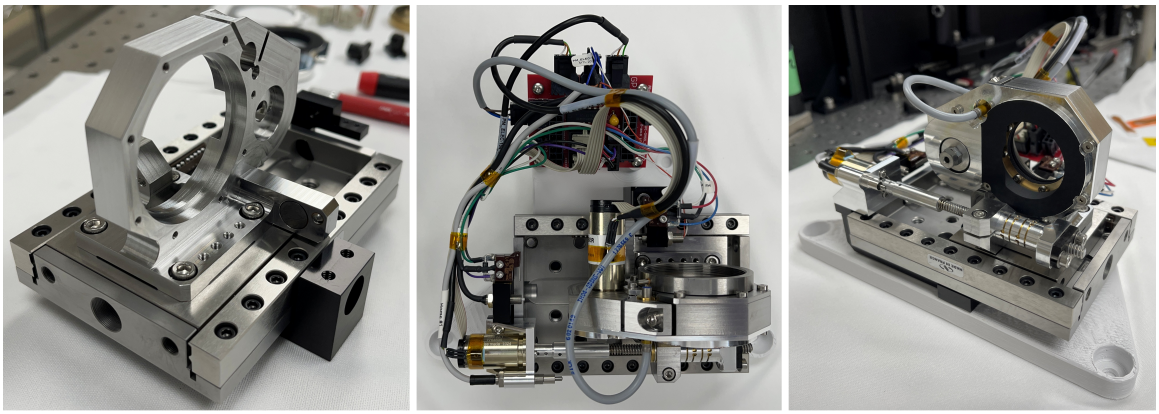

Figure 3.6: Partial (left) and complete (middle and right) laboratory assembly of the CAL 2.0 polarization modulator with linear and rotational stages, wiring, and sensor harnessing installed. The polarization optic will be installed following system validation and prior to final CAL 2.0 integration.

The next phase of development will focus on environmental and functional testing. Beginning in summer 2025, initial evaluations will assess encoder readout fidelity,

verify full range of motion along both translational and rotational axes, and validate the accuracy and repeatability of the homing and limit switch sensors. These tests will be conducted under both ambient and cold operating conditions to ensure compliance with the specifications outlined in Table 3.2.

Upon successful completion of mechanical testing, the PolMod will proceed to software integration with the CAL 2.0 control framework. Once integrated, the mechanism will undergo optical alignment to the common axis shared with the FPM wheel and IFS, followed by a final round of revalidation to confirm system readiness for commissioning.

3.1.3 Ultra-Low Speed Optical Chopper

Overview and Requirements

The ultra-low speed optical chopper (ULSOC) is a newly developed mechanism for CAL 2.0, engineered to provide slow, precise fringe modulation for the FAST self-coherent camera (SCC) architecture. By modulating the SCC reference beam at a precisely controlled rate, the ULSOC enables real-time recovery of the reference pinhole point spread function (PSF), facilitating focal plane wavefront sensing and enhancing post-processing techniques such as coherent differential imaging (CDI), discussed in §1.3.10.

First prototyped as part of the SPIDERS instrument (see §2.3), the ULSOC has since been developed into a facility class system offering robust performance and seamless integration into CAL 2.0. Unlike commercial choppers, which typically operate at kilohertz frequencies, this mechanism supports chopping from hundreds of hertz down to subhertz and can hold fixed positions in either the chopped or unchopped state. It is designed to meet strict requirements for low vibration and minimal thermal emission, ensuring compatibility with nearby sensitive optical components within CAL 2.0. A summary of the design constraints is provided in Table 3.3.

Table 3.3: Mechanical and control constraints for the CAL 2.0 optical chopper.

Requirement	Specification
Chopping frequency range	0.1–100 Hz, or maintain chopped/unchopped state
Chopping frequency accuracy	$\leq 0.1°$ RMS chopping phase jitter per revolution
Chopping frequency stability	$\leq 0.1\%$ RMS variation from input trigger over 10 min
Chopping frequency transition time	≤ 10 seconds

Chopping position accuracy	$\leq$ 1 mm from nominal position
Chopper blade characteristics	Outer diameter: 101.6 mm Clearance for unchopped beam: $\geq$ 3 mm Chopping cycles per revolution: 8
Operational lifetime	$\geq$ 10 years
Operating temperature range	-5 °C to 20 °C
Thermal emission limits	System $\leq$ 2 °C above ambient Must not emit 0.8 to 3.5 µm infrared light
Optical cleanliness	Minimize scattering around beam path Gold coating on blade side facing camera
Vibration limits	No detectable vibration at CAL 2.0 interface

Design Summary

The CAL 2.0 ULSOC is driven by a NEMA 11 DC stepper motor directly coupled to a custom stainless steel blade with alternating transmissive and blocking regions. An 18-bit absolute magnetic encoder, mounted on the back end of the motor, provides closed-loop feedback for precise control of rotational speed and angular position. It enables millidegree-scale, non-volatile position tracking, allowing the blade to maintain its phasing across power cycles without requiring recalibration. An external optical sensor is used for initial alignment during system setup but is disabled during normal operation to prevent light generation.

Fringe modulation control is handled by a custom driver board developed by electrical engineer D. Gamroth, located with the main CAL 2.0 electronics outside the primary optomechanical enclosure. The board provides high-resolution speed regulation through field-oriented control, motor current limiting, and phase locking with an external trigger source to support stable, synchronized fringe modulation.

To maintain optical cleanliness and ensure high fidelity modulation, one side of the chopper blade and the upstream baffle are coated with Aeroglaze Z306 [134] to suppress stray light and reduce associated scattering. The opposite face of the blade is gold coated to reflect radiation from the SCC's cryogenically cooled detector, minimizing thermal background downstream at the focal plane. An oleophobic surface treatment (Nyebar Type T 0.2% [133]) is applied around the bearings and motor shaft to prevent grease migration toward the blade, encoder, or other sensitive components.

Thermal management is critical due to the motor's continuous operation during observations. A custom aluminum heat sink, attached using low-outgassing thermal

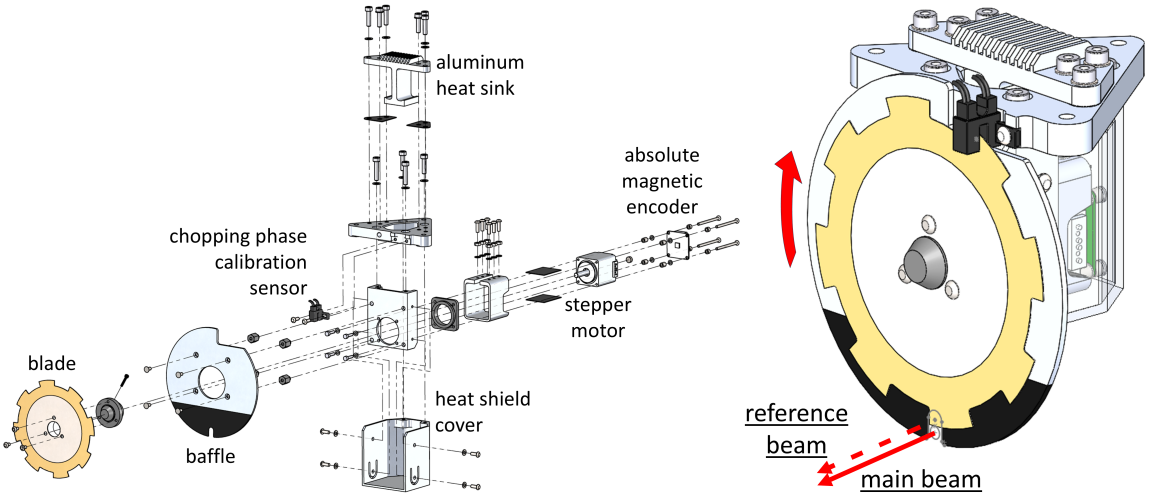

Figure 3.7: Exploded CAD view of the CAL 2.0 chopper with critical components labeled (left), and isometric views with the main/reference beam path shown (right).

pads and secured by an aluminum strap, increases surface area for passive cooling. This assembly is thermally coupled to the ULSOC base frame through an additional thermal pad, allowing heat dissipation via conduction and natural convection, even within the telescope's low-pressure, low-airflow environment. The system is designed to handle a peak combined thermal load of 0.3 W from the motor and encoder, maintaining a temperature rise of less than 2 °C above ambient under nominal conditions. Delrin spacers thermally isolate the baffle and blade from the motor while preserving mechanical alignment. A thin aluminum shroud encloses the motor assembly, adding thermal mass, surface area, and infrared shielding. To improve long-term mechanical reliability, Armstrong A-12 epoxy [137] is applied at critical fastening points, including the encoder magnet and screw heads, to prevent loosening under operational stress and thermal cycling.

The complete chopper assembly is rigidly mounted to the CAL 2.0 frame, with final alignment achieved through manual adjustment and shimming. Figure 3.7 shows the full mechanism, including the blade, motor, encoder, and optical paths for reference.

Current Assembly and Next Steps

With final mechanical components fabricated, the CAL 2.0 ULSOC has been fully assembled and is currently undergoing laboratory testing. Figure 3.8 shows the system mounted on a test bracket with an uncoated blade installed for testing.

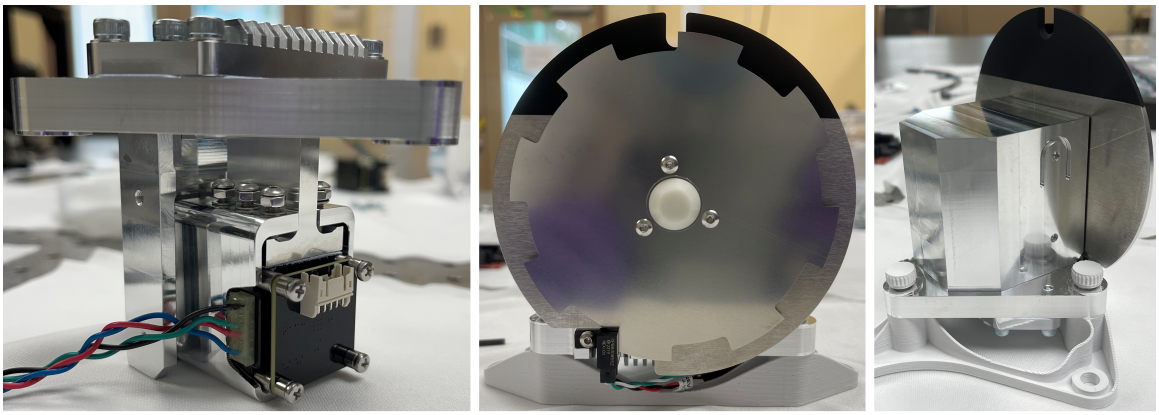

Figure 3.8: Laboratory assembly of the CAL 2.0 chopper, showing the partially assembled configuration (left), and the uncoated chopper blade installed in the fully assembled system mounted on a test bracket (middle and right).

Initial room temperature tests of the SPIDERS prototype, which serves as the foundation for the CAL 2.0 design, demonstrated stable operation across the required speed range with no detectable vibration and no measurable thermal rise above ambient. These results meet the environmental and performance criteria listed in Table 3.3 and establish a solid baseline for validating the CAL 2.0 implementation. While the underlying modulation scheme and software interface were proven on SPIDERS, the CAL 2.0 version features a complete redesign of the control electronics for facility-class operation, with software integration currently underway.

The next phase will focus on verifying both short- and long-term stability, followed by environmental testing at room and low temperatures to confirm reliable operation under expected conditions. Once bench validation is complete, final mechanical integration into the CAL 2.0 system will proceed in parallel with continued software development and real-time interface testing using the HEART control system. After installation, the ULSOC will be revalidated to confirm stability and alignment within the system before being used to support SCC fringe modulation during on-sky operation.

Chapter 4

STARLITE: Superluminous Tomographic Atmospheric Reconstruction with Laser-beacons for Imaging Terrestrial Exoplanets

4.1 A SmallSat Mission Study for STARLITE

This section is based on material published in the proceedings of the SPIE Volume 13092, Adaptive Optics Systems IX in 2024 (10.1117/12.3018042). Authors: Adam B. Johnson, Ashley Padres, Ryan Hughes, Carmine Buonagura, Zane Chapman, Alexia Kubas, Veronica Hegelein, Ishan Mishra, Adler Smith, Abu Taqui Md Tahsin, Akshiti Parashar, Rafid Bendimerad, Yizhou Chen, Qizhi Lu, Asterios Aidan Kounios, Devin Desilva, Verena Padres, Jamie Lloyd, Dmitry Svransky, Joshua Umansky-Castro, Andrew van Paridon, Elaine Petro. *My contribution to this work was as the lead author and Principal Investigator for the Cornell Smallsat Mission Design School 2023 course, during which this project was completed. I initiated the project and led the efforts of the multidisciplinary science and engineering subsystem teams, composed of students from various international universities. A. Padres, R. Hughes, C. Buonagura, Z. Chapman, A. Kubas, V. Hegelein, I. Mishra, A. Smith, A. T. Md Tahsin, A. Parashar, R. Bendimerad, Y. Chen, Q. Lu, A. A. Kounios, D. Desilva, and V. Padres were fellow students in the course, with their specific roles detailed in Section 4.1.17. J. Lloyd and D. Svransky provided expert guidance and support during the*

in-person segment of the course at Cornell University. J. Umansky-Castro, A. van Paridon, and E. Petro served as course instructors, organizing and facilitating the program both on-campus and remotely.

4.1.1 Introduction

One of the biggest challenges of imaging Earth-like exoplanets from Earth is the turbulent atmosphere that distorts the incoming wavefront, adding speckles to the captured images and hiding potential exoplanets [75]. Commissioning telescopes in space allows us to avoid the turbulent atmosphere, but at a substantial cost and constrained size. Dedicated space observatories like the James Webb Space Telescope (JWST) with a 6.5 m primary mirror cost many billions of dollars to commission [138] compared to ground-based observatories like Keck I and II with 10 m primaries costing around $100 M each [139]. Using existing 8-10 m and future 30 m+ ground-based telescopes, adaptive optics (AO) can help us correct and see through the turbulent atmosphere, unlocking the resolving power of larger and cheaper telescopes on Earth.

Discussed in various papers, [2, 140, 141, 142, 143] the concept of an artificial guide star constellation being launched into orbit to act as reference sources for an extreme adaptive optics system has substantial potential. Although calibrated light sourced on satellites is used in many applications, a full-scale beacon mission dedicated to exoplanet imaging and characterization specifically for large ground-based observatories has yet to be implemented. The Orbiting Configurable Artificial Star (ORCAS) team and mission [143] have exemplified how a mission like this could be feasible. Further, the wavefront control architecture necessary for such a mission is well discussed within *Douglas et al 2019*. [2]

Continuing the approach discussed in *Thompson 2019* [142], the STARLITE constellation of satellites uses principles of AO and tomography to reconstruct and correct multiple layers of the atmosphere in real-time to enable higher contrast and more efficient detection and characterization of exoplanets. Using a constellation of small satellites equipped with lasers as artificial guide stars, STARLITE can take full advantage of multi-conjugate adaptive optics (MCAO) to improve imaging detection and characterization of Earth-like planets orbiting nearby Sun-like stars using observatories on Earth. This paper will discuss the satellite mission and conceptual design of the STARLITE satellite, while atmospheric modeling, reconstruction, and optical simulation with ground station design considerations are discussed in [144] (§4.2).

4.1.2 Concept Overview

The space-based portion of the STARLITE mission consists of a constellation of small satellites, (i.e., CubeSats), in a highly elliptical orbit. At apogee during a given orbit, the constellation will approach alignment with a ground-based observatory, and then for a 1-2 hour window, onboard lasers on each satellite pointed at the observatory generate super bright ∼on and off-axis guide stars. Using a 1 W onboard laser, upwards of a -10 magnitude guide star is generated during the observation window. In a 1 % bandpass, science images can be acquired between the bright calibration images. The concept for a five-beacon constellation is shown below in Figure 4.1.

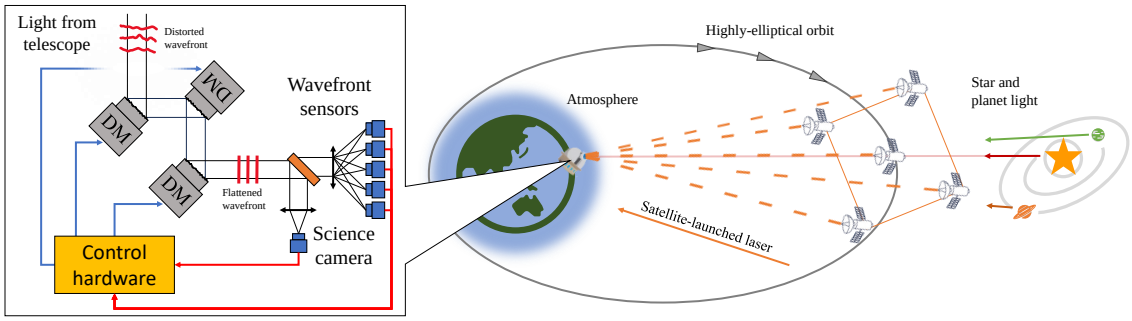

Figure 4.1: STARLITE five-beacon constellation concept design with generalized MCAO ground station system. The constellation aligns with the target star at apogee during a highly-elliptical orbit, and the laser light is used to enhance the system's ability to correct the wavefront and acquire signal from any potential exoplanets.

Before and after observation, small station-keeping maneuvers are made to keep the constellation on a stable and desired trajectory or to adjust the orbit for other nearby observations (e.g., via Global Positioning System (GPS)). During the observation, the constellation moves into and out of the field of view (FOV), momentarily appearing to stop at apogee when the central beacon will ideally be nearly on-axis. Because the beacons are in space (above the atmosphere) and far away, the off-axis beacons will not be resolved and not suffer from the cone-effect that laser guide stars on Earth experience [18]. Furthermore, the ideal tomographic reconstructor will take advantage of better information closer to the target as the constellation moves in and out of the FOV [144].

For this mission, a constellation of five 12U CubeSats, with each CubeSat individually weighing less than 24 kg, as per specifications [145], has been chosen. Following CubeSat standards, where 1U is equal to a $10x10x10$ cm volume, each of the constel-

lation's CubeSats will be constructed out of four 3U long CubeSats. This choice of size and shape, along with decisions regarding launch and integration requirements, comes directly from the Pioneers Solicitation [146]. The team has currently selected this solicitation as the primary source for funding the mission and therefore will use the solicitation's recommendations and guidelines for the various mission criteria discussed later.

Although this paper will only discuss the five-beacon constellation under the constraints of the Pioneers Solicitation, the concept can be extended or simplified to utilize any number of beacons, given the appropriate ground station design. An initial single beacon that is flown nearly on-axis could be used for preliminary detection and investigation of one or multiple exoplanet systems, and a more complex multi-agent constellation (like that shown in Figure 4.1) could be launched to provide dedicated follow-up missions.

4.1.3 Mission Profile

The concept of operations (ConOps) outlines and details the order of operations for the STARLITE mission to reach its primary goals, detailed in Figure 4.2. Our mission-specific operations are divided into five phases: 1) Launch and Early Operations (LEOP) and Trans-Lunar Injection (TLI); 2) Commissioning; 3) Transfer; 4) Operative, and; 5) End-of-Life. During the first phase (LEOP and TLI), the STARLITE CubeSats are switched off inside the deployer, and power connection between them and the carrier bus keep the batteries charged. This phase ends with the release of all STARLITE CubeSats, which will then continue their cruise toward the Moon. Some number of days before the close encounter with the Moon, each CubeSat will perform a Deep Space Maneuver (DSM) to fly by the Moon and insert into a Transfer trajectory that will end with the Highly Elliptical Orbit Injection Maneuver (HEOIM). After this maneuver is performed, the Operative phase, lasting 4.6 *years*, will begin. In this phase, at the orbital apogee, STARLITE will enable extreme MCAO for a ground station on Maunakea, providing unprecedented guide star brightness and AO capabilities. The Operative phase ends with the STARLITE CubeSats raising their apogee with the remaining propellant available, increasing the orbital instability, and leaving the Earth-Moon system for the End-of-Life Maneuver (EoLM) at the perigee of the orbit. An analysis of the probability of the spacecraft being captured again by the Earth-Moon system will be assessed in the following

phase of the mission.

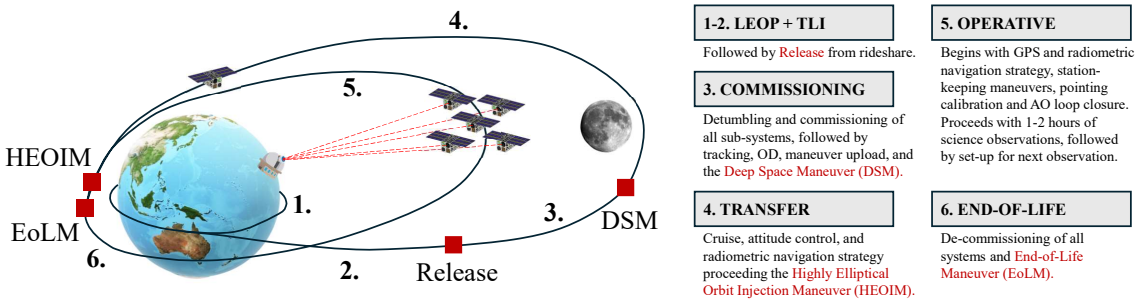

Figure 4.2: STARLITE concept of operations (ConOps), from launch to end of life.

4.1.4 Science Overview

So far, the vast majority of exoplanets have been discovered via radial velocity and transit methods [34], while direct detection of Earth-like exoplanets has proven difficult due to a number of factors (also discussed in §1.1.3). Not only are distant stellar systems dim ($Flux \propto distance^{-2}$), but exoplanet signals are minuscule compared to their host stars ($F_{Earth}/F_{Sun} \sim 10^{-10}$) [2], making them impractical and nearly impossible to directly observe unless they are several orders of magnitude more massive than Earth and 10 s of AU away from their host stars. Additionally, considering Earth's atmospheric distortion of incoming light, direct detection of Earth-like exoplanets in the habitable zones of their host stars from ground-based observatories has not yet been possible.

Since the first detections of Sun-like stars in the 90s, the number of exoplanets cataloged each year has been growing steadily, with more methods and approaches becoming optimized and more available. With its many challenges, direct imaging makes up for only a small portion of the total number of detections today, only 66 of the total $5,616$ confirmed planets as of April 30th, 2024, according to NASA's Exoplanet Archive [34]. Shown in Figure 4.3, we see the distribution of detection methods by Semi-Major Axis and Earth-Masses, where direct imaging has so far been limited to large separations and mass only. To reach the sensitivity required to directly image rocky planets like Earth in the habitable zone of the other Sun-like systems, new approaches like STARLITE must be pursued to overcome the current physical limitations of direct imaging and AO from Earth.

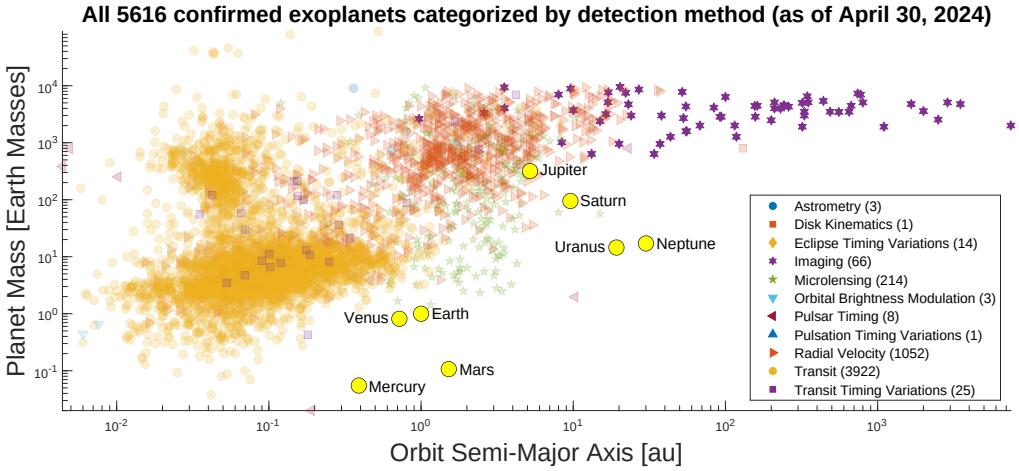

Figure 4.3: Planet mass (in Earth masses) versus orbital distance (in AU) of current confirmed exoplanets sorted by detection method. The plot was created using data retrieved from the NASA Exoplanet Archive [34].

The aims of STARLITE align with one of NASA's long-standing goals to search for life elsewhere in the universe and to develop instrumentation to detect potentially habitable exoplanets, stated in NASA's 2022 Strategic Plan and the 2020 Astrophysics Decadal Survey [147, 148]. As we look out into the universe to search for life as we know it, a logical first step would suggest to look for Earth-like planets around nearby Sun-like stars. STARLITE will allow us to both directly image the habitable zones of nearby Sun-like stars and characterize close-in exoplanets, where spectroscopic characterization can provide insight and evidence on potential habitability. The science traceability matrix shown in Table 4.1 below outlines the science goals of the mission and lays a path to achieving these goals through a basic set of specifications and requirements.

Detection

Looking for potential candidates that STARLITE could aid in the detection and characterization of, our research uses a list of 164 F, G, K, or M-type nearby stars (<25 *pc* away) compiled by the Exoplanet Exploration (ExEP) for the future Habitable Worlds Observatory (HWO) to directly image select habitable zones [149]. Assuming STARLITE will be commissioned using a telescope on the summit of Maunakea in Hawaii, targets outside of this observing window (-40° < declination < 80°) were removed, leaving us with 127 potential target systems observable from the telescope site but not on the same orbit. The ExEP HWO Catalog is further divided into Tiers A,

Table 4.1: The science traceability matrix for the STARLITE mission.

Science Goals	Science Objectives	Physical Parameters	Observables	Instrument Requirements	Projected Performance	Mission-Level Requirements
Potential Science Goals Identified from 2022 NASA Strategic Plan: **Strategic Objective 1.2 -** **Understand the Sun, solar system, and universe.** *Searching for Life Elsewhere* 1. *Improve the knowledge of environmental requirements for habitability* 2. *Develop tools for detecting life* 3. *Develop tools for determining the relative habitability of present or ancient environments*	Directly image Earth-like exoplanets around Sun-like stars and their system in visible to NIR wavelengths	Flux from exoplanet around the host star with a statistical confidence of at least 5 sigma	Achieve 1e-8 planet-to-star contrast through AO correction using super-bright off-axis artificial guide stars and further 1e-10 contrast with post-processing and integration Observe exoplanets at star-to-planet separations down to ~5λ/D, near the IWA and around the system's habitable zone	**Brightness:** Minimum apparent magnitude brighter than -10, while on target at apogee **Laser Size and Pointing:** 10cm launch aperture ~4mas pointing **Ion Thruster Capability:** Thrust = 100-1000mN ~50(m/s)/year station keeping ~30 (m/sec)/deg for target changing ~700 m/s launch ~2000-10000 m/s of total fuel **HEO Requirements:** a = 150,000km - 300,000km e = 0.75 - 0.95 T = 3-9 day period 1.5-3 hrs on target for observation **Narrowband Observations within:** 500-1200nm **Spectroscopy for biomarkers within:** 500-1200nm	**Brightness:** Apparent magnitude -10, while on target at apogee **Laser Size and Pointing:** 10cm launch aperture ~1mas pointing **Ion Thruster Capability:** Thrust = 100mN 4100m/s of fuel **HEO Requirements:** a = 182,000km e = 0.78 T = 9 day period 0.5-1.2 hrs on target for observation **Narrowband Observations:** 760nm **High-res. Spectroscopy:** 760nm (O2 A-band)	1. Achieve a minimum off-axis guide-star apparent magnitude of -10 mag through the use of STARLITE's onboard laser 2. Observe exoplanets at, at least, a 5λ/D separation 3. Observe at least 2 different star systems over the total mission lifetime 4. Observe Earth-like exoplanets within 10 parsecs 5. Stay on target for at least 1 hour
	Determine if the surface and atmosphere of exoplanet(s) have a composition with biomarkers, similar to that of Earth, that are known to sustain life and/or provide habitability (i.e. is the atmosphere Earth-like or similar)	**Chemical Composition:** Presence of H2O, O2, CO2, CH4, NH3 **Bulk Composition:** Whether exoplanet is icy, rocky, or gaseous **Orbital Zone:** The location of the exoplanet in relation to its star	Look for biomarker absorption lines in exoplanet spectrums in VIS to NIR wavelengths Conduct photometry of exoplanets in R, I, J, and H bands to determine color of exoplanet			

B, and C based on imaging feasibility, which depends on the inner working angle (IWA), whether or not a disk is present (i.e., dust or debris disk present), the nature of the primary star (i.e., whether or not it is a binary system and the separation between them), etc. [149]. In addition, it is worth noting that targets further away from 0 declination will be more difficult to detect as this further limits the available observational time.

- Tier A stars have a large IWA ($> 83\ mas$), no known dust disks, and are single stars or binaries with $>$ 10" separation.
- Tier B stars have a median IWA ($> 72\ mas$), may have a dust disk with a minimum contrast ($L_{disk}/L_{star} \leq 10^{-4}$), and are single stars or binaries with 5"–10" separation.
- Tier C stars have the lowest IWA ($> 65\ mas$), may have any type of dust disk, and are single stars or binaries with 3"–5" separation.

While Tier A stars are the highest priority (of which there are 39), our current estimated orbit (presented in §4.1.6) only permits us to observe five total nearby targets within 10 pc (three Tier A, one Tier B, and one Tier C), of which the most on-orbit and highest priority is 61 Cygni A, 3.5 pc away from Earth and in spectral class K. The potential declination range is simulated and discussed later in §4.1.6, while the right ascension can be selected. The green ring in Figure 4.4 below indicates the potential target stars from the ExEP HWO list. If we are able to directly image just one close-in exoplanet, we will achieve a scientific goal that has not yet been met.

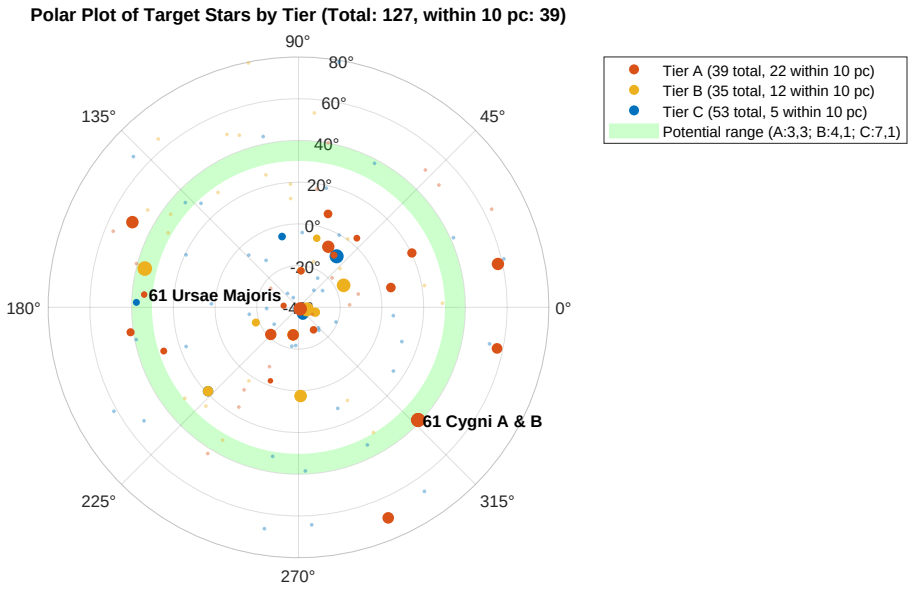

Figure 4.4: Candidate target stars, coloured by tier, dot size inversely proportional to distance from Earth, and translucent when farther than 10 *pc* away. Concentric circles denote declination and angular ticks denote right ascension. The number of targets in the potential orbit are identified in the legend above as *(-TIER- : -TOTAL TARGETS- , -WITHIN* 10 *pc-)*.

Characterization

Direct imaging enables the use of spectroscopy for astronomers to analyze the composition, and in turn, potential habitability, of an exoplanet. For reference, spectroscopic characterization of a bright celestial body is performed by analyzing the intensities of different broad and narrow spectral bands of the measured electromagnetic spectrum (discussed in §1.1.6 and §1.2.5). This method has been performed on planetary bodies within our solar system and found that gas, icy, and rocky planets can be separated by their R-J and J-K colours. Using these same methods, we will be able to identify if any of the detected exoplanets are Earth-like in composition. Investigating identified Earth-like planets, narrowband spectroscopy can provide information on the molecular composition of their atmosphere. Potential targets like H_2O, O_3, O_2, and CO_2 at wavelengths around 0.75, 1.4, and 1.6 μm are of interest as these can provide crucial information about the habitability of the planet. However, the CubeSat would require different on-board lasers of wavelengths nearby the various target molecules for detection of those molecules. For this mission, the team

has chosen to focus on the detection of O_2, resulting in the selection of a laser in the 750 nm range for STARLITE.

4.1.5 Instrument / Laser Payload

To ensure STARLITE's mission requirements are met, the constellation of artificial guide stars must reach a brightness of at least -10 apparent magnitude each to meet the requirements outlined in Table 4.1. From preliminary calculations, a 1 W laser with a ~759 nm wavelength and ~0.1% bandwidth was selected for each of STARLITE's CubeSats. Shown in Figure 4.5, this wavelength falls in a high atmospheric transmission region, but also near the O_2 A-band, based on the Echelle Spectro Polarimetric Device for the Observation of Stars ((ESPaDOnS) processed data from the Canada-France-Hawaii Telescope (CFHT) [150]. Because the exoplanet system is moving relative to Earth, the same absorption features seen in the atmosphere of the exoplanet compared to Earth's spectrum will be Doppler shifted based on the relative motion. Observation of these signals at various times throughout the year will allow us to detect modulation of these absorption features with a telescope on Earth.

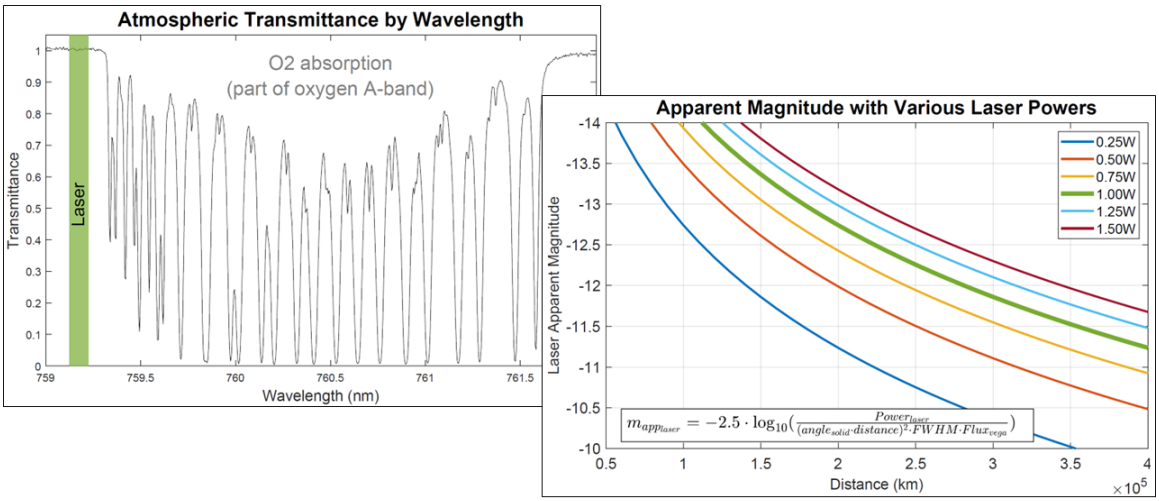

Figure 4.5: The designed laser wavelength next to the blue side of the oxygen A-band (left). The apparent magnitude of various laser powers is plotted over the distance from the beacon to the telescope (right).

At an apogee of around 350,000 km, a laser power of at least 250 mW is needed to meet the brightness requirements. A 1 W laser power was chosen to ensure we still meet our requirements after including optical inefficiencies through the many surfaces

in the end-to-end optical path. The relationship between apparent magnitude and distance from the telescope to the beacon is shown in Figure 4.5 on the right.

Commercially, not a wide variety of current space-rated lasers exist or meet STARLITE's specific requirements for output power, wavelength, and bandwidth, so it is likely that STARLITE will require a custom laser system. On each STARLITE CubeSat, an on-axis optical system will be used to magnify and collimate the laser light, with a tip/tilt fast-steering mirror (FSM) to allow guiding of the laser in a small window. The FSM will be used for calibrating the system alignment at apogee and enables fine-resolution pointing toward the telescope.

To feed the laser to the launching telescope, the laser light will go through a fiber with an opening width of a few microns and land on the FSM with milliarcsecond precision. After the FSM, the secondary mirror of approximately 1.5 cm will direct the beam towards the 10 cm primary mirror that finally collimates the light so it can leave the system, shown below in Figure 4.6. The combination of mirrors provides a collimated beam with a magnification of $\sim$50 so that the angular precision of the beam coming out is within an arcsecond. The telescopic system provides a $\sim$1 arcsecond beam with a pointing accuracy of less than 0.5 arcseconds.

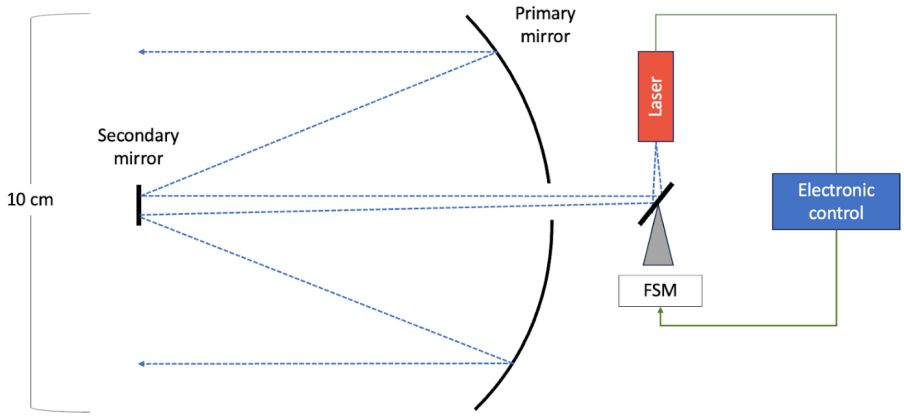

Figure 4.6: Conceptual optical layout for a single STARLITE CubeSat.

To calibrate the precision pointing at apogee before observation, a predetermined raster pattern can be performed by the accurate and high-resolution FSM. The ground instrument will record the raster pattern and communicate back to the satellite what the optimal pointing position is to maximize the apparent brightness of each beacon. Careful design of the optics and selection of coatings will need further analysis as the high-power laser requirement could be problematic for standard optics.

4.1.6 Trajectory

Using STARLITE's science orbit requirements to find a suitable trajectory for the mission, the constellation orbit is defined by a stability requirement, minimum altitude and astro-stationary requirement, a near/super synchronous requirement, and a phasing requirement.

- The mission shall have repeat observation targets over a mission duration of no more than 5 years.
- Minimum observational window of 30 minutes while within a 35 arcsecond FOV on target at apogee.
- The orbital period shall be an integer multiple of 24 hours.
- STARLITE's orbital apogee shall be within 25° of azimuth with respect to Maunakea Observatories during the operational window.

With these requirements in mind, the team has identified the P2/P3 Lunar Resonance Orbits and Northern Group L1 Halo Orbits as potential target trajectories that could be suitable for the mission profile. Analysis of the mission profile assuming a TESS P2 orbit helps bring the mission beyond the Earth-Moon L1 point [151]. In this scenario, a direct lunar intercept rideshare would be utilized, followed by a lunar fly-by to release toward an operational orbit. The total delta-v costs associated with this type of target trajectory would be relatively low, on the order of approximately 215 m/s. A TESS P2 orbit would only allow for approximately 18.3 minutes for a single target however due to the phasing and precession of the orbital elements over the observational window with the target.

For STARLITE to obtain sufficient observational window times, a dedicated launch is likely required. A dedicated launch would allow the constellation to achieve a higher orbit eccentricity (e $\sim$ 0.78), however, the associated costs may be beyond the scope of the Pioneers Solicitation [146]. In order to develop a preliminary simulation of the constellation's orbit, the team focused on any potential orbits that most closely matched the lateral velocity of the CubeSat constellation to the lateral speed of the Keck Observatory on the ground, as an example ground-based 10 m telescope on Maunakea. After analyzing the resulting orbit and observational window for an optimal dedicated-launch orbit (Figure 4.7), we are able to achieve an observation

time of ∼68 minutes with an estimated precession pattern resulting in a declination range between 31.14° - 39.85° while the right ascension can be selected.

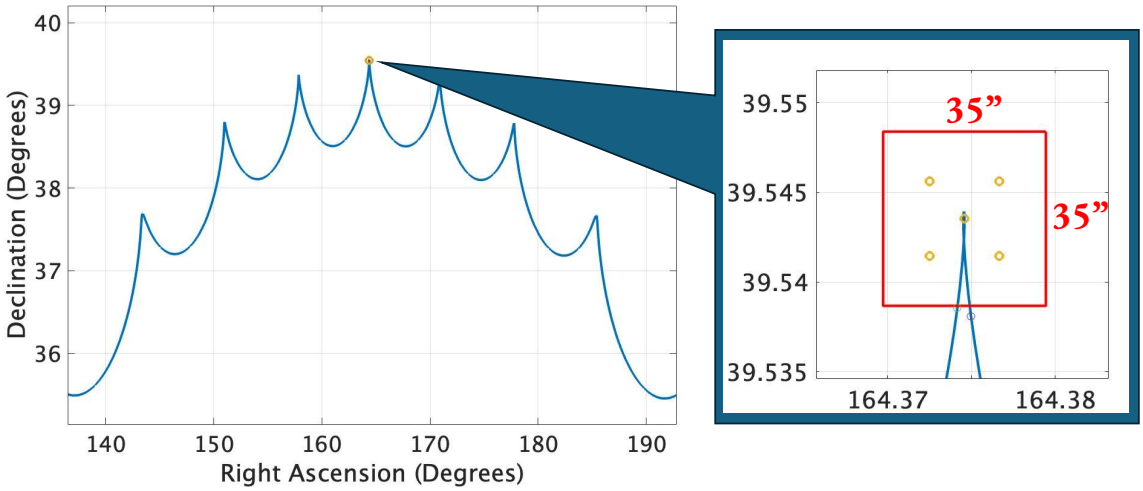

Figure 4.7: Conceptual trajectory of CubeSat constellation in isoplanatic field of view relative to Keck Telescope (left) and close-up view of observation window size relative to constellation positioning (right).

The ideal orbit may be possible with some Lunar Rideshare missions, but, more research is needed to further refine and select an optimal trajectory for the mission. The trajectory simulated above is proof-of-concept and would need further refining in later mission development.

4.1.7 Propulsion and Launch

Considering the options for propulsion and launch of STARLITE, a handful of potential lunar rideshares have been identified that the mission could make use of. These options include the Falcon 9 from SpaceX [152], the Ariane 6 from the ArianeGroup [153], or the Vulcan Centaur from the United Launch Alliance [154]. The CubeSats would attach to an Evolved Expandable Launch Vehicle Secondary Payload Adapter (ESPA) ring and then launched using a standard 12U CubeSat dispenser, such as one from Exolaunch [155] or Maverick Space Systems [156], both of which have extensive flight heritage.

Based on preliminary calculations for STARLITE, each CubeSat will require a propulsion system with a long (t > 20,000 hours) firing time and an approximately 1 $MN-s$ total impulse, like a radio frequency ion thruster such as the RIT 10 EVO

from ArianeGroup [157]. For STARLITE's reaction control system (RCS) thrusters, the requirement for precise pointing using micronewton-level control has led to the initial choice of using the TRL9 SVT01 Cold Gas Thruster from Nammo Space [158]. Further calculations based on the CubeSat dry mass and approximate delta-v requirements estimate 0.5 kg of Xenon propellant required per CubeSat, with fuel split between the RCS thrusters and main ion thruster. A standard chemical-based propulsion system would be the cheapest and most reliable selection for the purposes of the mission.

4.1.8 Attitude Dynamics and Control

The attitude, dynamics, and control (ADC) subsystem is responsible for controlling the CubeSat constellation throughout the mission lifetime. The components for the subsystem can be selected by evaluating the significant point-of-controls as faced by each CubeSat in its orbit. The perturbations to be considered here are those due to the gravity field, gravity gradient, and solar radiation pressure. The orbit is beyond the High Earth Orbit (HEO), so the perturbations caused by the gravity field and gravity gradient are not particularly significant. The torque due to solar radiation pressure should not be very significant given the planned trajectory, but over time would necessitate a periodic correction in orientation.

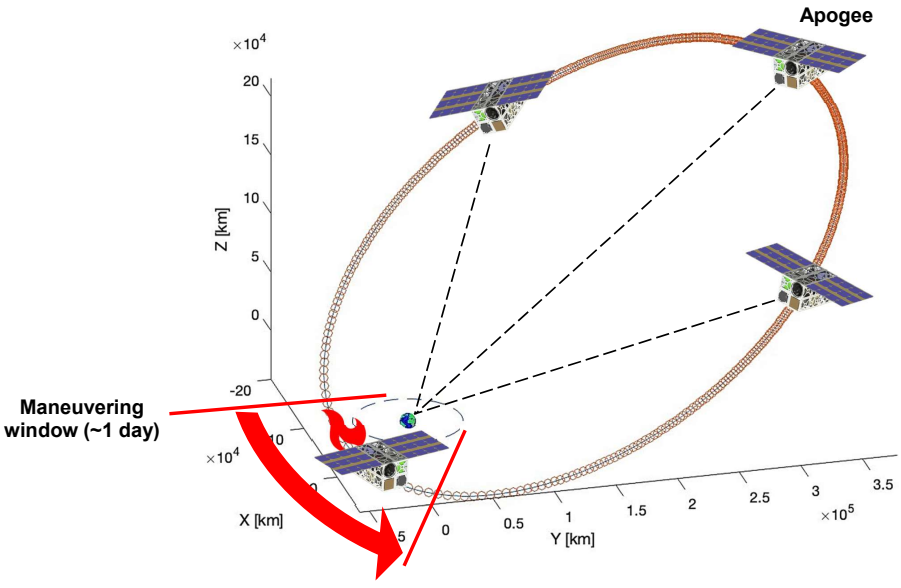

Figure 4.8: Conceptual representation of the satellite in orbit and the maneuvering window at perigee.

Leveraging the Oberth effect, a small maneuvering window (1 day) can be defined near the perigee where the satellite will use cold gas RCS thrusters to accelerate, as shown in Figure 4.8. Six RCS thrusters will be used to cover the 3-axis of rotational motion. The satellite should be Nadir-pointing throughout the orbit except for the time when it is in this maneuvering window. At the apogee, the controls for each satellite must be precise and accurate for the mission ($<$ 1 arcsecond), indicating a need for an Inertial Measurement Unit (IMU), star tracker, and reaction wheels. A four-wheel configuration of the reaction wheels provides the required actuation, with one reaction wheel for redundancy. Combined with the laser's fast steering mirror accuracy, the components have the capability of achieving the desired accuracy.

4.1.9 Data Processing

The ground-based station must possess the capability to accurately monitor and control the spacecraft with meter-level precision at apogee. The fulfillment of this orbit precision criterion will be achieved through the implementation of radio frequency (RF) ranging within the S-band ($2-4\,GHz$) via the Near Earth Network (NEN). Concurrently, GPS location determination will be employed up to a distance of 200,000 kilometers. The utilization of GPS at substantial altitudes has been empirically validated by the Magnetospheric Multiscale (MMS) mission [159], and it is suggested for deployment in the ORCAS mission at an altitude of 200,000 kilometers [143]. The incorporation of GPS will add redundancy to the tracking system and facilitate the recognition of the STARLITE constellation among other SmallSats after their ejection from the launch vehicle.

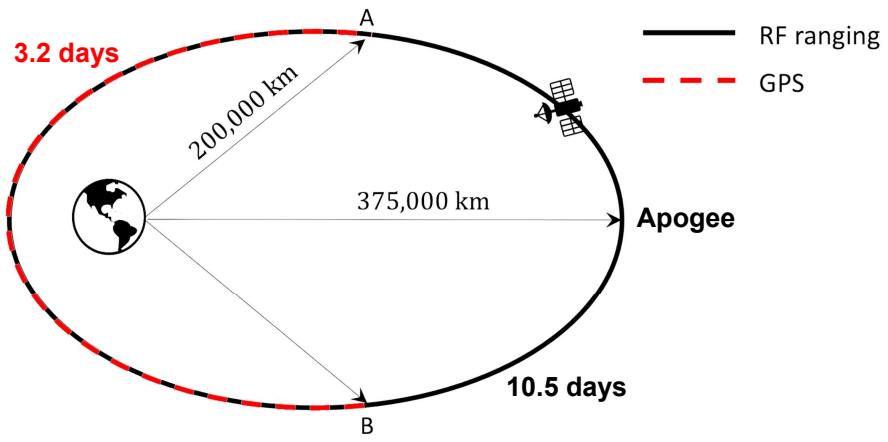

Figure 4.9: STARLITE orbit with RF (black) and GPS coverage (dashed red).

The spacecraft will spend 3.2 days within the GPS range and 10.45 days out of the GPS range as illustrated in Figure 4.9. The critical region for orbit determination is between point A and apogee as exoplanet observations will be executed at apogee. Based on the consideration that major perturbations are predictable and accounted for in orbit calculations, ground-space communication every 24 hours is deemed sufficient to ensure that the spacecraft is on the right path.

4.1.10 Telemetry Tracking and Command

The telemetry, tracking, and command (TT&C) system will be responsible for the uplink, downlink, and orbital determination of STARLITE satellites. Given the highly elliptical orbit required by the mission, a relatively low data rate is needed. An S-band frequency was chosen for long-distance communication and altitude determination using the NEN and Near Space Network (NSN), respectively. Because the S-band is in a relatively low-frequency range, lower data loss and higher power efficiency is achievable. For nearby altitude determination (within 200,000 km), GPS will provide more accurate positional data.

S-Band Communication and Tracking

To maximize the space utilization efficiency, the Satlab SRS-3 Full-duplex transceiver [160] combined with a small form factor patch antenna from Anywaves [161] was chosen. The pointing requirement for a patch antenna is relatively loose, for gain larger than 5 dB, the ground stations only have to be within 90° of the antenna centre. Using one of the NEN Ground Stations located in Hawaii, USHI01 [162], we were able to calculate the link budget. As shown in Table 4.2, at apogee, we are able to achieve a positive link margin with a min $E_b/N_0 = 14$ calculated from Gaussian Minimum Shift Keying (GMSK) modulation and a projected bit-error rate of 10^{-6}.

Table 4.2: S-band communication link budget

	$\boldsymbol{E_b/N_0}$ **(dB)**	**RSSI (dB)**	**Link Margin (dB)**
Downlink (128 *kbps*)	25.74	-130.48	11.74
Downlink (512 *kbps*)	19.72	-130.48	5.72
Uplink (128 *kbps*)	57.74	-98.48	43.74

GPS Tracking

The NGPS-03-422 GPS Receiver and piPATCH-MAX Patch Antenna were chosen for GPS communication for their small form factor and proven flight readiness. As STARLITE is constantly above the GPS constellation, we are projecting an effective GPS antenna gain of -15 dB [163] Using the same BER = 10^{-6} as the S-band, and a Data Rate = 2 $kbps$, the link budget is tabulated in Table 4.3.

Table 4.3: GPS communication link budget

	E_b/N_0 (dB)	RSSI (dB)	Link Margin (dB)
Uplink (200,000 km)	21.91	-152.37	11.41
Uplink (380,000 km)	16.33	-157.95	5.84

It is shown that the GPS tracking is also achieving a positive budget, but with less margin to maintain a 2 $kbps$ data rate. However, a recent study suggests the possibility that GPS signals leaking from the opposite side of Earth can enhance signal gain [164], which would improve gain when in higher orbits. More research is required for longer-range GPS communications.

4.1.11 Power

Power is an important consideration for the STARLITE mission with long-range communications and a high-powered laser. When the payload laser is not in operation, during 'Idle' mode that spans approximately 13.4 days, the system draws 39.2 W of power to maintain critical station-keeping functions and communication with the ground station only. This mode is contrasted by a 'Science' mode which spans only $\sim$2.5 hours while requiring a considerably higher power of 126.8 W, even with the main propulsion inactive. During an 'Eclipse' mode that lasts 4 hours, both payload and main propulsion remain inactive, and the system draws a power of 21.0 W.

With a specific power of 100 W/kg and an efficiency rate of 30%, the 3U Deployable Multifunction Solar Array (DMSA) can provide robust performance for the primary BA01 High Energy Density Battery Array power source [165, 166]. However, like all solar technologies, degradation is inevitable with the inherent degradation at 23% and an additional 0.5% degradation per year. Despite these challenges, the panel's life expectancy exceeds 5 years.

Space-ready solar panels with flight heritage like the selected DMSA integrates a built-in deployable mechanism and embedded sensors. The Starbuck NANO Power Distribution Unit, weighing 148 g, promises to be a pivotal element in the entire assembly with its high throughput, small form factor, and flight heritage [167]. The total power from each subsystem is tabulated in Table 4.4, outlining the approximate but conservative power requirements for each of the three modes.

Table 4.4: Power requirements of each CubeSat for each of the three modes: Science, Idle, and Eclipse.

Mode	**Science Power** $[W]$	**Idle Power** $[W]$	**Eclipse Power** $[W]$
Telemetry, Tracking, & Command	18.0	14.4	10.8
Attitude Dynamics & Control	5.6	2.9	-
Payload	90.0	-	-
Propulsion & Launch	-	8.7	-
Load Structure & Mechanisms	6.0	6.0	6.0
Environmental Protection	6.0	6.0	3.0
Power	1.2	1.2	1.2
TOTAL:	126.8	39.2	21.0

4.1.12 Environmental Protection

The Environmental Protection subteam is responsible for researching and providing protection for the STARLITE satellites from internal and external threats. The primary areas for focused analysis include Radiation Protection and the internal thermal stability of the satellites, while secondary concerns like material out-gassing and Electrostatic Discharge (ESD) potential are also analyzed but to a lesser degree.

As the mission shall not directly pass through Van Allen Belts, the main concern in terms of radiation is solar radiation experienced while in orbit. A passive shielding strategy has been identified for use in protecting the mission from solar radiation - specifically, 12 gauge 6061 aluminum panels may be sufficient given the mission lifetime [168]. In addition, sensitive equipment such as the optics, electronics, and instrument payload have been identified for additional shielding and thermal control in order to ensure the systems do not experience significant temperature gradients across the extremes of the orbit.

A more detailed environmental study and analysis of the specific compatibility and requirements for space-commissioning of components with minimal or no flight-heritage will be required as the detailed design materializes. It is expected that many

or all components used in STARLITE will need to be radiation-hardened and space-tested prior to selection for the mission, to ensure a high level of reliability for each satellite deployed.

4.1.13 Assembly and Structures

The components inside each STARLITE satellite fit into a standard 12U CubeSat-sized frame made of 6061 aluminum that will be designed and sourced in later stages of development. Standardized and commercially available CubeSat frames could be utilized, but the specific structural design and component placement are still in development and could necessitate a completely custom frame. The 6061 aluminum material chose provides sufficient strength for STARLITE's frame while also being lightweight, easily machinable, easily sourced, and able to absorb the harsh radiation in space (discussed in 4.1.12), making it suitable to withstand the demands of our mission. Additional panels will cover the chassis walls to protect the internal components during the mission's lifetime.

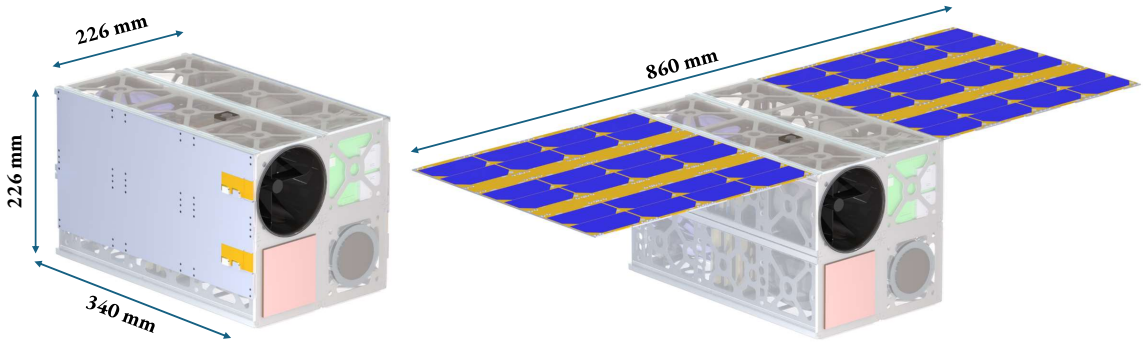

Figure 4.10: Rendering of the preliminary STARLITE CubeSat concept in launch (left) and deployed (right) configurations.

A preliminary 3D model was generated to validate the fit and relative location of critical components within the frame while also providing a starting point to prepare for the detailed design in the next phase of the mission. CAD models of the off-the-shelf components were used wherever possible, while placeholder models generated from data sheet dimensions and mass estimates were used when models were not available from the vendors. The assembled structure weighs approximately 19 kg and uses a standard 12U CubeSat form factor (4U x 3U). The solar panels mechanically fold in half to fit close to the mainframe during launch, and deploy after the release

from the rideshare. The launch and deployed configurations with overall dimensions are shown in Figure 4.10, with the external radiation covers translucent for internal visibility.

The critical components that were considered, and will be further detailed in later stages of development, include: the instrument laser, laser fiber, fast-steering mirror, and telescope that comprise the Laser Assembly; the insulation layers, ESD protection, and passive radiators associated with thermal and environmental protection; and the miscellaneous components such as propellant lines, IMUs, electrical harnessing, and mounting hardware that make up the the support hardware. Custom fittings, housings, and connections are not shown or considered at this stage of the mission design. An exploded view of the STARLITE concept is shown in Figure 4.11 to outline critical components.

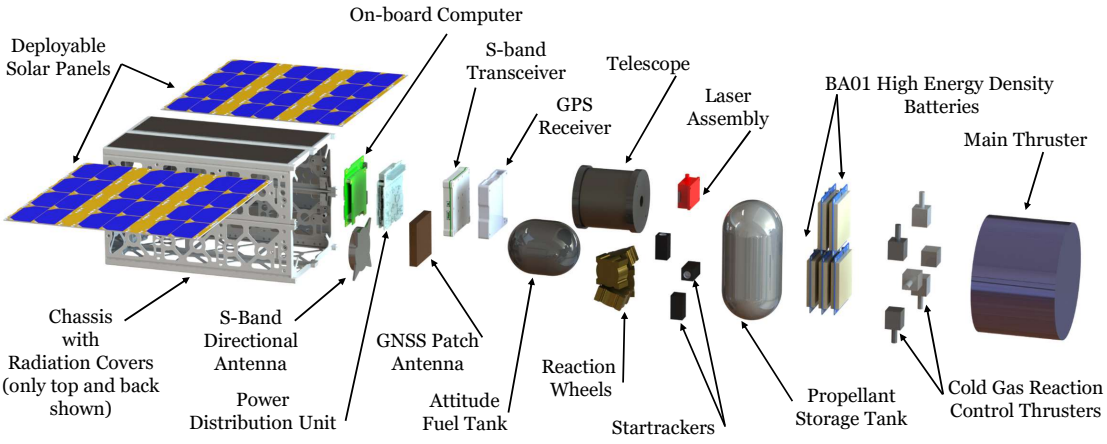

Figure 4.11: Exploded view of the STARLITE system with critical components and subsystems labeled.

4.1.14 Integration and Testing

The Integration and Testing subteam is responsible for planning and managing all subsystem interfaces and hardware testing for the STARLITE CubeSats. In preparation for the testing, the subteam must review and compile information from the rideshare user's guide for STARLITE's launch vehicle and any other commissioning guidelines and requirements identified by the launch provider.

Full System Integration and Testing

Throughout the integration process, each 12U STARLITE CubeSat will follow the Cal Poly CubeSat Design Specification [169] to ensure compatibility with a variety of CubeSat dispensers. Suggestions and requirements including the location of the CubeSat's centre of gravity, mass, sizing specifications, and more will be considered from the aforementioned document and from the dispenser provider, whether that be for the ESPA ring (per Pioneers Solicitation guidance [146]) or any other launch vehicle with rideshare potential.

The required testing of the assembled CubeSats will primarily come from the Payload User's Guide supplied by the launch provider. Beyond conducting system-specific simulations throughout the design phase to verify that our CubeSats meet the given requirements, the following critically tests have been identified: random and prescribed vibration tests, shock tests, static load tests, electromagnetic compatibility verification, acoustic testing, and combined thermal vacuum and thermal cycle tests. As the system design matures, the definitions of success or failure for the above tests will require careful consideration.

The vibration, shock, acoustic, and compatibility testing will likely be outsourced to a professional and experienced service. Some static load testing can be conducted in-house, but more comprehensive testing is needed to validate launch survivability. Additionally, thermal cycling and vacuum testing could be outsourced to professional services if the team lacks a large enough vacuum chamber or has insufficient thermal equipment. The capacity and capabilities of the yet to be chosen assembly facility will guide what testing will require outsourcing and what can be done in-house.

Subsystem Integration and Testing

Before final integration and assembly of the full system, each completed subsystem will be tested to confirm performance is within margin and is fully functional as needed for the mission. All subsystems will be tested together and/or separately during/after integration, but dedicated tests to validate subsystem performance before systems are joined and can interfere with each other are required.

The instrument assembly, which includes the launching telescope, high-powered laser, and pointing system, will require thorough testing, as failure of this subsystem effectively decommissions the CubeSat with the dysfunctional laser system. Vibration and shock testing of this system must confirm that the system can achieve a resolution

within 5 milliarcseconds following launch. Additionally, calibration will be conducted on an optical bench to verify that the final system throughput before and after testing is at least 90% to keep the apparent magnitude of each laser guide star within margins.

Beyond this, the reaction wheels will be thoroughly tested to validate that the output torque is consistently able to meet the pointing requirements and the power consumption will be validated by monitoring consumption during testing of each operational mode. All of the listed tests will be run multiple times to verify the repeatability of results, and statistical methods used to predict the probability of failure and where risk mitigation strategies and efforts should be put.

4.1.15 Cost Budget

The Pioneers Solicitation [146] constrains STARLITE's final cost to no more than \$20 M total for the entire mission [170]. Preliminary calculations were performed by first analyzing the cost per sub-system for a single satellite and its corresponding costs in terms of operations, systems engineering, and management. From this preliminary estimate, a significant margin is added due to the fact the mission is still very much in the early design phase of mission concept review. Margin was added per sub-system based on its associated risk and Technology Readiness Level (TRL), with most receiving 25% margin and the most critical subsystems, namely propulsion and the instrumentation payload, having an added margin of 50%. The final cost, in terms of the hardware cost per satellite, was estimated to be approximately \$2.7 M with a 39% margin. After factoring in costs in terms of wages, human-power, and operations, the final estimated cost for the mission is approximately \$19.9 M with a 32% margin. The total cost with margin for the mission leaves the project with less 1% left over from the original \$20 M constraint. The detailed breakdown is shown in Table 4.5.

4.1.16 Conclusion

STARLITE provides a relatively low-cost and innovative platform to resolve current limitations in modern AO systems. The mission concept and preparation outlined in this paper detail the use of a constellation of artificial guide stars used for the next generation of extreme MCAO. STARLITE provides the tools necessary to reconstruct the atmosphere with enough speed and accuracy to produce clearer and faster direct images of exoplanets.

Table 4.5: Cost estimate per STARLITE satellite and for a five-beacon constellation.

Organization and Overhead Costs	**Estimate**	**Margin %**	**Final Cost**
Management	$1,500,000	15	$1,725,000
Systems Engineering	$2,000,000	15	$2,300,000
Operations	$850,000	30	$1,105,000
Safety	$100,000	30	$130,000
Near-Space Network Usage	$850,000	30	$1,105,000
Individual CubeSat Costs	-	-	-
Telemetry, Tracking, Command	$60,000	25	$75,000
Attitude Dynamics & Control	$175,000	25	$218,750
Instrumentation	$60,000	50	$90,000
Propulsion and Launch	$1,000,000	50	$1,500,000
Load Structure & Mechanisms	$30,000	25	$37,500
Environmental Protection	$10,000	25	$12,500
Power	$120,000	25	$150,000
Integration and Testing	$500,000	25	$625,000
TOTAL Individual CubeSat Cost	$1,955,000	(∼39)	$2,708,750
TOTAL for CubeSat Constellation	$15,435,000	(∼32)	$19,908,750

The most significant cost for the mission was identified to be the cost of launch, where a typical CubeSat LEO or GEO trajectory is inappropriate for the science goals of STARLITE. Given the perfect rideshare or a funded launch (from a different SmallSat solicitation program, or government/private sponsorship) that could get STARLITE into its ideal orbit, a $\sim$ \$20 M five-beacon constellation is a low-cost solution, especially considering the cost of other space-based exoplanet instruments.

While more work is required to both accurately and precisely simulate the optimal satellite configurations and orbital parameters of the mission, the STARLITE mission depicted in this paper presents a feasible path forward as a technology that could aid in our ability to search for life beyond our own solar system. While the ability to improve our current state of AO is not limited to just STARLITE, a dedicated artificial guide-star mission has the potential to significantly enhance our ability, to understand, image, and analyze exoplanets in the search for Earth-like exoplanets and proof of life elsewhere in the universe.

4.1.17 Acknowledgments

The team would like to give a big thank you to Cornell University SmallSat Mission Design School (SMDS), their instructors, teaching assistants, and company sponsors

which enabled the work conducted within this paper.

SMDS is a summer program provided by Cornell University designed to teach space mission design via a hands-on format and bring together students and professionals from around the world to investigate unique space science missions relevant to NASA's Decadal Survey science priorities [171]. Participating students work to develop a mission concept within the constraint of the NASA Pioneers Solicitation [146] with science and technology innovators over a 5-week online series with a 6th week of in-person design and review preparation at Cornell. Each student is assigned a critical mission role and responsibility that they must learn and contribute to in the final weeks of the course. The team photo and organizational chart are shown in Figure 4.12.

Students directly benefit from the combined expertise of Cornell faculty in Mechanical and Aerospace Engineering, Astronomy, and Planetary Sciences, as well as various external scientists from industry partners. Since 2023, the program has been open to graduate students and postdocs of partner universities, including international students, as well as a small number of undergraduate students from Cornell.

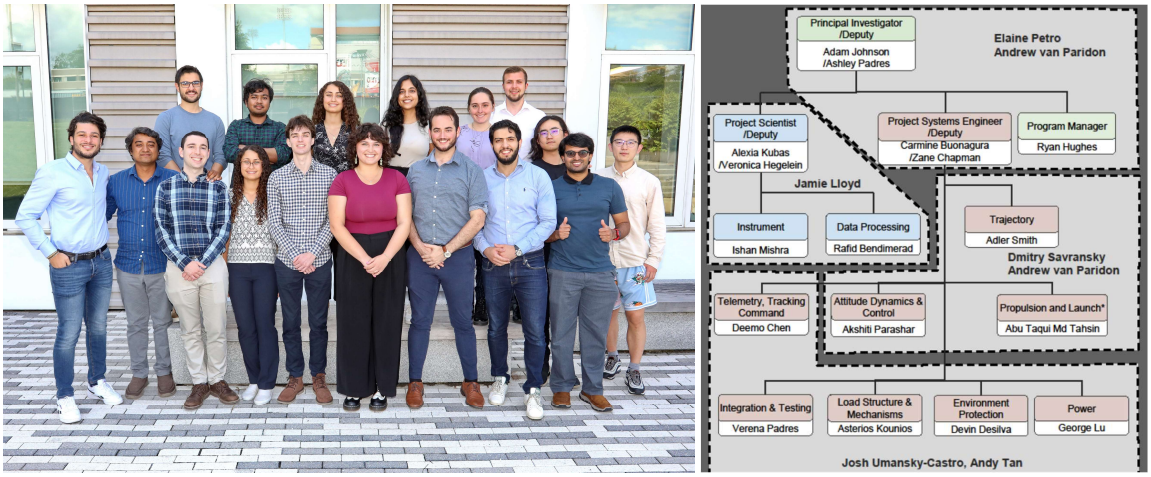

Figure 4.12: The SMDS class of 2023 after the final Mission Concept Review (MCR) at Cornell University (left). The organizational chart including support instructors and teaching assistants (right).

4.2 An Optical Feasibility Study for STARLITE

This section is based on material published in the proceedings of the SPIE Volume 13097, Adaptive Optics Systems IX in 2024 (10.1117/12.3018040). Authors: Adam B. Johnson, Christian Marois, William Thompson, Kate Jackson, Jean-Pierre Véran, Maaike A. van Kooten, Olivier Lardière, Darryl Gamroth, Colin Bradley. *My contribution to this work was as the lead author and primary contributor to the tomographic reconstruction development. C. Marois originated the concept and met with me regularly to refine and guide the work. W. Thompson also contributed to the initial orbital-laser concept and participated in regular discussions, offering key ideas throughout the project. K. Jackson provided valuable consultation on the tomographic reconstruction efforts through a series of in-depth meetings. J.-P. Véran and M. A. van Kooten offered technical guidance related to the simulation aspects of the work. O. Lardière contributed optical engineering insights for the conceptual design of the STARLITE system. D. Gamroth advised on real-time control strategies and the electrical hardware requirements for STARLITE. C. Bradley facilitated institutional support from the university.*

4.2.1 Introduction

The search for Earth-like exoplanets around Sun-like stars with the aim of detecting life signatures, presents an immense challenge. Achieving the necessary $\sim 10^{10}$ contrast to detect these exoplanets at small angular separations requires advanced coronagraph designs and picometer-level wavefront control [75, 172, 173]. Currently, several ground-based and space-based instruments are dedicated to the direct imaging and characterization of exoplanets. Space missions like the 6.5 m James Webb Space Telescope (JWST) and future Habitable Worlds Observatory (HWO) leverage their position beyond Earth's atmosphere to avoid atmospheric turbulence and the bright sky background to capture images and perform detailed spectroscopic analysis of exoplanet atmospheres [20, 174]. However, these space-based observations come with extraordinary financial costs, up to tens of billions of dollars, along with decades of planning and higher risks associated with operating in space. In comparison, ground-based telescopes like the twin 10 m Keck, 8.2 m Subaru, and 8.1 m Gemini north telescope on the summit of Maunakea in Hawaii offer higher resolving power with their bigger diameter and a more cost-effective approach being assembled and maintained on Earth, in the range of hundreds of millions of dollars [175, 176, 177]. High-quality

observation sites like Maunakea at an altitude of $\sim 4200\ m$ offer a way to get partially above and reduce the effects of the atmosphere [178]. Even at sites like these, sensing the incoming wavefront fast enough and with enough accuracy to keep up with the continuously and randomly evolving atmospheric turbulence becomes a fundamental barrier.

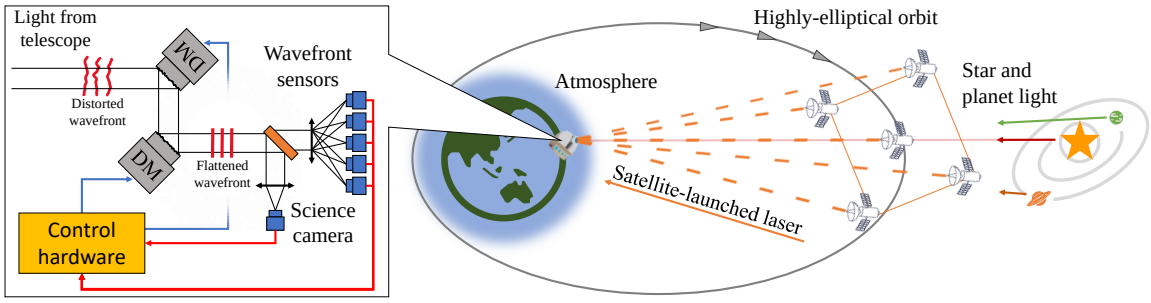

Figure 4.13: STARLITE five-beacon constellation concept with generalized ground station system. The constellation aligns with a science target at apogee where onboard lasers generate superluminous guide stars for adaptive optics on the ground.

To bridge the gap between ground-based accessibility and the demanding observational requirements needed for exoplanet imaging and characterization, the concept of STARLITE (Superluminous Tomographic Atmospheric Reconstruction with Laser-beacons for Imaging Terrestrial Exoplanets) has been proposed. This concept builds upon and refines earlier concepts and discussions on space-based laser guide stars for calibration and extreme adaptive optics (AO) [140, 141, 142, 143, 173, 179]. STARLITE ultimately aims to achieve an intermediate sky-limited contrast of approximately 10^8 in the visible band using ground-based telescopes ranging from 8 to 30 m in diameter. Central to the STARLITE concept is a satellite constellation in a highly-elliptical orbit (HEO) that aligns at apogee with nearby Sun-like star targets to provide super-bright guide stars for up to a few hours every several days. Each satellite in the constellation utilizes an onboard laser to generate extremely bright and unresolved off-axis guide stars for atmospheric tomography to reconstruct the (on-axis) science wavefront towards the target. This will enable extreme AO capabilities, with the objective to attain closed-loop Angstrom-level wavefront residuals on the science target. This paper will present preliminary considerations for end-to-end optical simulations of the STARLITE system and provide theoretical "best-case" estimates of the wavefront reconstruction accuracy through the Earth's atmosphere towards a target. The satellite mission and preliminary design is presented and discussed in

[144] (§4.1), with the concept discussed in this paper shown in Figure 4.13.

4.2.2 Optical System Overview

Many methods and approaches can be used to measure and correct wavefront errors with AO, but for the purposes of this discussion, AO is generalized into single-conjugate AO (SCAO) and multi-conjugate AO (MCAO), where each use the same fundamentals of operation but differ in their architecture and capabilities [18]. SCAO is the simpler approach, where the phase errors in the wavefront caused by the turbulent atmosphere are measured and corrected at a single altitude using one or multiple deformable mirrors (DMs). Typically, the ground layer near the telescope is chosen where the phase errors are the sum of the errors throughout the full volume of the atmosphere, but any altitude could be chosen if the atmosphere can be reconstructed and a DM conjugated to a targeted altitude. MCAO employs the use of multiple wavefront sensors (WFSs) and guide stars (natural or laser) to measure the wavefront phase along different lines of sight through the atmosphere for tomographic reconstruction, and multiple DMs to provide altitude-targeted corrections. It is assumed that there are no wavefront errors accumulating between the target, beacons, and the edge of the atmosphere (meaning they are all ~flat before entering the atmosphere). The simplified MCAO system discussed in this paper is shown in Figure 4.14.

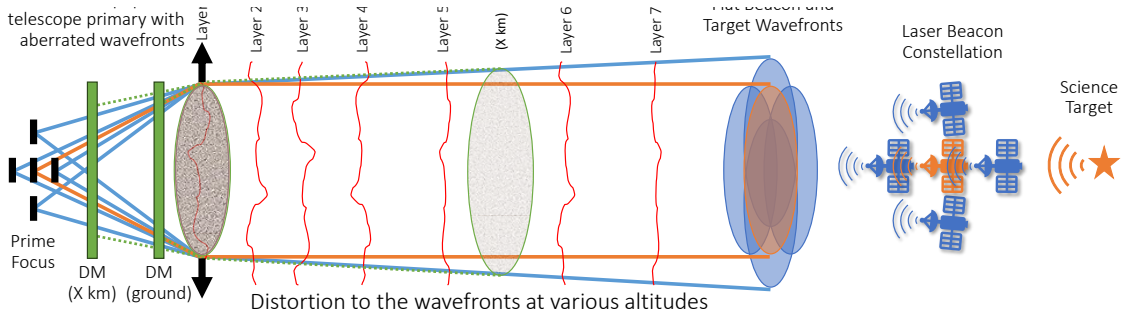

Figure 4.14: Simplified MCAO layout at apogee with the on-and off-axis beacons in front of the target to provide different lines of sight through the atmosphere to reconstruct the on-axis wavefront throughout the duration of the observation.

While MCAO is typically employed to improve imaging in a wider field of view, it is being investigated here to see if the on-axis wavefront can be reconstructed in a narrow field of view to meet the accuracy requirements without burning fuel to keep the beacons on-axis at their apogee during the observation. The direction-specific

correction and ability to correct scintillation effects with a DM conjugated to a high altitude also make MCAO an attractive approach for STARLITE.

Components traditionally in high-contrast imagers and imaging spectrograph systems like a coronagraph, beam splitters for wavefront sensing, wavefront sensors, filters, cameras, etc. are not analyzed in this paper to isolate the performance of the reconstruction.

4.2.3 Designing an Atmospheric Turbulence Model

To approach the problem, the first step is developing an appropriate atmospheric model to generate realistic turbulence maps (screens) of the phase distortion seen when looking through the atmosphere. Simulating atmospheric turbulence with phase screens is a common approach that has been used over many decades to simplify the three-dimensional atmosphere volume into a single two-dimensional map of the phase delay or advancement (error from zero) across a spatial domain, for some given observing conditions [18]. The distribution and power of the spatial-frequencies in atmospheric turbulence can be defined by the power-spectral density (PSD). It has been shown to follow a -5/3 power law relationship (Kolmogorov turbulence), and can be properly scaled to incorporate the telescope diameter and the Fried parameter, r_0, which characterizes the turbulence strength [180] (presented in §1.3.4).

To avoid the zero inner scale and infinite outer scale energy in the Kolmogorov PSD, a modified von Kármán spectrum with an -11/6 power law can be used [181, 182]. The Equation 1.45 Kolmogorov PSD is modified to form the von Kármán PSD:

$$\Phi_{\phi,vk}(f) = 0.0229\, r_0^{-\frac{5}{3}} \frac{e^{-(f/f_m)^2}}{(f^2 + f_0^2)^{11/6}} \tag{4.1}$$

where $f_0 = 1/L_0$ and $f_m = 1/l_0$, with L_0 and l_0 in meters denoting the outer and inner turbulence scales, respectively. The radial spatial frequency is given by $f = \sqrt{f_x^2 + f_y^2}$, based on the Cartesian frequency grid coordinates. The outer scale L_0 limits low-frequency energy by bounding the largest eddies, while the inner scale l_0 attenuates high-frequency content by constraining the smallest eddies.

Mapping the PSD onto a 2D polar grid and multiplying by random Fourier coefficients, the 2D PSD can be inverse Fourier transformed to produce the phase map in the spatial domain. The 2D map can be shifted using an exponential phase ramp where the ramp slope is proportional to an input wind speed and sample rate, and

gradient in the wind direction to simulate bulk motion of the layer. Multiple layers can be generated and motion imposed in different directions and speeds to simulate a temporally evolving multi-layer atmosphere. A detailed description of how to implement the PSD and simulate atmospheric turbulence is provided in §A.3.

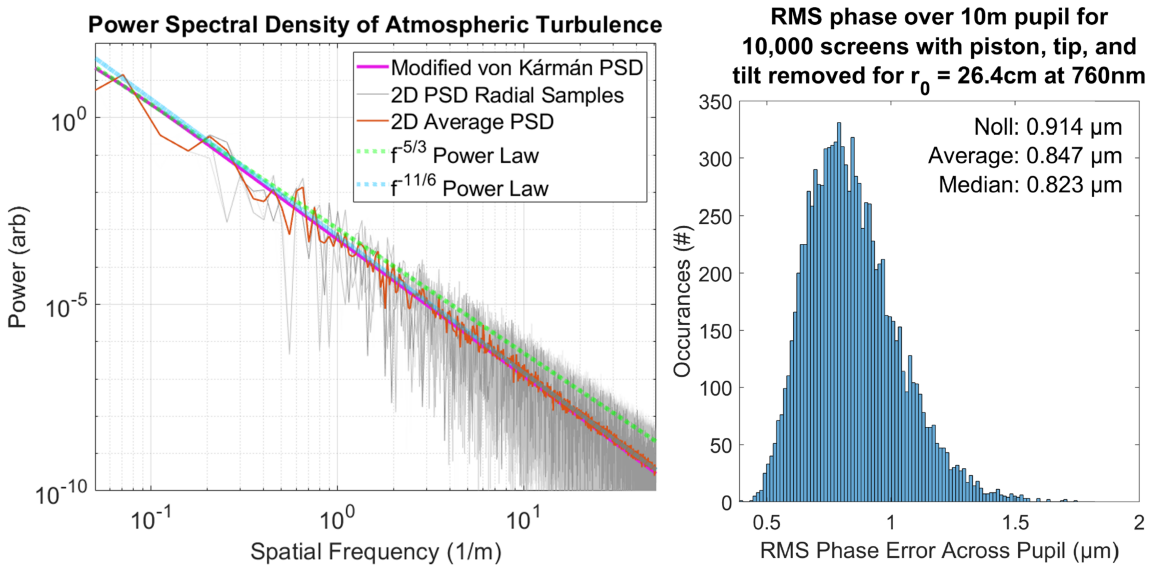

Figure 4.15: PSD model and result comparison (left) and RMS error validation (right).

Atmospheric characteristics like the Fried parameter, its fractional distribution through the atmosphere, wind speeds, and directions are difficult to predict with momentary, daily, seasonal, and yearly variability. Utilizing measured and published conditions from the 2007 Maunakea Ridge (MKR) Turbulence Models, a 7-layer model can be simulated from 50th percentile fractional r_0 and wind speeds at specific altitudes, for "median" seeing conditions ($r_0 = 16\ cm$) [73]. Combining this information with suggestions from *Tyson* [18] to use a 1 mm inner and 40 m outer scale for the modified von Kármán PSD, the resulting screen variance and standard deviation (or root-mean-square deviation/error (RMS)) can be validated against analytical results from papers like *Noll 1976* [72] and *Conan 2008* [183] (presented and discussed in §A.3.1). The designed PSD is shown in Figure 4.15 on the left with radial samples of the generated 2D PSD and its average overlaid on top to validate that the output PSD roughly matches the input PSD. -5/3 and -11/6 power law curves are shown for reference to illustrate the attenuation of inner and outer scale power. The RMS of the wavefront phase across the pupil with the first three Zernike modes removed (piston, tip, and tilt) is calculated for 10,000 randomly generated screens and a histogram

shown on the right to validate that the expected variance is observed on average. It is expected to see a slightly lower RMS for the von Kármán model compared to the the pure Kolmogorov model derived by *Noll* for these conditions, due to the attenuated inner and outer scales incorporated into the input PSD. These results indicate the model matches the literature and median observing conditions at the Maunakea site.

4.2.4 On-Axis Phase Residuals at the Focal Plane

Without the wavefront errors imposed by the atmosphere, the best possible image of a point source (or distant star) through a simple circular pupil telescope is dependent on its diameter and the observed wavelength, where the the resolution limit can be given by the *Rayleigh Criterion* [184, 185, 186, 187], discussed in §1.2.1. The image formed on the science camera detector can be represented by the the intensity of the point-spread-function (PSF) at the prime focus of the telescope after going through a circular pupil and primary mirror (Figure 4.14), and can be approximated using Fraunhofer propagation [18, 68] (§1.3.2).

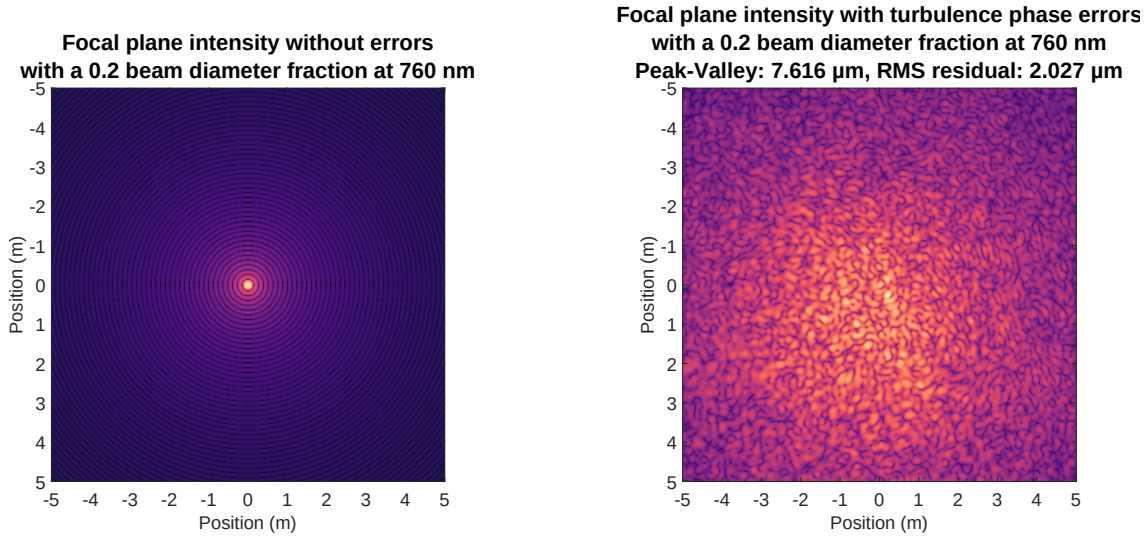

Figure 4.16: PSF of $10m$ telescope with circular aperture without errors (left) and with errors from the atmosphere (right). Peak-valley and RMS error across the pupil includes piston, tip, and tilt - compared to the expected RMS in Figure 4.15.

To simulate an image of an on-axis science target with the science camera including atmospheric turbulence, the entire optical system must be modelled and a

wavefront propagated through it. Assuming the target is far enough away from Earth that the phase of the wavefront is essentially flat when it reaches the atmosphere, the contribution of phase distortion to the wavefront will simply be that of the atmospheric turbulence phase map. Effects like scintillation will affect the amplitude of the wavefront, but will be investigated in later phases of the project. For preliminary analysis and simplicity, it is assumed that the phase can be perfectly measured from the wavefront, while a Shack-Hartmann or Pyramid wavefront sensor (WFS) would typically be modelled to simulate measurement error [188]. Additionally, surface errors from optics and detection noise are also not considered for this preliminary work. The intensity of the PSF at the focal plane of a 10 m telescope on a without (left) and with (right) atmospheric turbulence is shown in Figure 4.16. The intensity values in the images shown in this paper are exponentially scaled to improve the visibility over a wide range.

A continuous surface DM like ones from Boston [189] or ALPAO [190] are typically used to correct the phase distortion introduced by the atmosphere, where the surface can be shaped and the incoming wavefront inversely deformed (flattened) at speeds up to tens of kHz. A DM can be simulated by fitting the 2D phase screen to a grid of actuators and applying an influence function between them to provide a good approximation [18, 191]. DM fitting is important to analyze and design around, but is not incorporated into the simulation at this stage. However, the time taken to measure the wavefront, apply the DM command, and get the surface to that position (latency or time lag) is a significant challenge when the atmospheric turbulence is evolving quickly, and is considered below.

Temporal Prediction

When the atmosphere has fast moving layers, the AO system must be fast enough to keep up with the high and low spatial frequencies errors. *Tyson* [18] suggests some approaches to determining DM stroke and resolution requirements, while approximations for speed requirements depend on many factors but are driven by the RMS phase residuals required to reach the contrast goals. To get ahead of time lag, an extrapolation from previous measurements can be used on each pixel to predict the next measurement instead of only applying correction to the most recent measurement, known as a predictor. Many predictors are discussed in literature for various applications and needs, such as a simple linear, quadratic, or cubic polynomial fitting

[192, 193]. More complex predictors like Kalman and Weiner filters can be used to handle noise in the measurement and provide better prediction with some added complexity [194]. Since we are not considering sources of noise for this paper, a simple polynomial predictor using a least squares fit is explored here.

The next phase map $\hat{\phi}_{n+1}$ is predicted by fitting a polynomial to the most recent measurements $\phi_{n-k+1}, \ldots, \phi_n$ at each pixel, then evaluating the fit at the next time step. Depending on the prediction order (linear, quadratic, or cubic), this is done using either forward differencing or least-squares polynomial fitting with Vandermonde matrices. Flattened phase maps are arranged as columns of a matrix Y with M rows and k columns, where $M = N \times N$ is the total number of spatial pixels and k is the number of time steps used in the fit. The specific formulation depends on the chosen prediction order, as outlined below.

The linear predictor employs a simple forward differencing over two time steps:

$$\hat{\phi}_{n+1} = \phi_n + (\phi_n - \phi_{n-1}) \tag{4.2}$$

In the quadratic case, a second-order polynomial is fitted using three time steps:

$$\begin{gathered} A = \begin{bmatrix} 1 & 1 & 1^2 \\ 1 & 2 & 2^2 \\ 1 & 3 & 3^2 \end{bmatrix}, \quad Y = \text{reshape}([\phi_{n-2}\ \phi_{n-1}\ \phi_n], M, 3), \quad \mathbf{C} = A^{-1}Y^\top \\ \hat{\phi}_{n+1} = \text{reshape}(\mathbf{C}_0 + 4\,\mathbf{C}_1 + 16\,\mathbf{C}_2,\ N, N) \end{gathered} \tag{4.3}$$

Cubic extrapolation extends this approach by fitting a third-order polynomial over four time steps:

$$\begin{gathered} A = \begin{bmatrix} 1 & 1 & 1^2 & 1^3 \\ 1 & 2 & 2^2 & 2^3 \\ 1 & 3 & 3^2 & 3^3 \\ 1 & 4 & 4^2 & 4^3 \end{bmatrix}, \quad Y = \text{reshape}([\phi_{n-3}\ \phi_{n-2}\ \phi_{n-1}\ \phi_n], M, 4), \quad \mathbf{C} = A^{-1}Y^\top \\ \hat{\phi}_{n+1} = \text{reshape}(\mathbf{C}_0 + 5\,\mathbf{C}_1 + 25\,\mathbf{C}_2 + 125\,\mathbf{C}_3,\ N, N) \end{gathered} \tag{4.4}$$

For the second and third order predictors, a polynomial is fit independently at each pixel using its temporal phase history, stored as a row in Y. The fitted coefficients are stored in a matrix $\mathbf{C}$, where columns correspond to pixels and rows to polynomial terms. Row C_i contains the i-th coefficient for all pixels. The prediction is computed

by multiplying each coefficient row by a fixed scalar based on its term, such as $1, 4, 16$ for quadratic or $1, 5, 25, 125$ for cubic, and summing the result. The result is reshaped into the full $N \times N$ map representing the predicted phase $\hat{\phi}_{n+1}$.

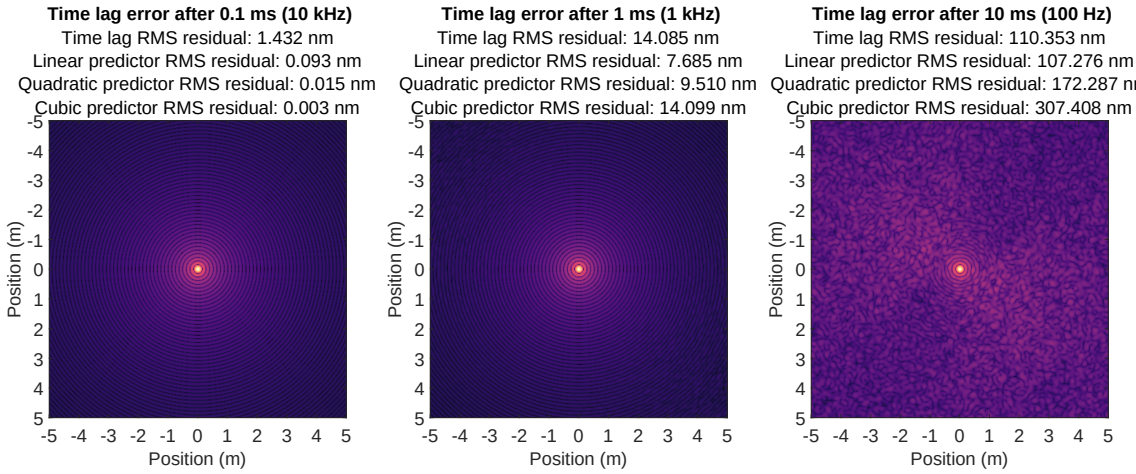

Figure 4.17: RMS error and visual comparison of on-axis first, second, and third order polynomial predictors applied to 10, 1, and 0.1 kHz atmosphere model samples with the best predictor residual PSF shown (cubic, linear, and linear, respectively).

To evaluate prediction performance under realistic conditions, time lag error is simulated for 10, 1, and 0.1 kHz in Figure 4.17, with three predictors simulated using Equations 4.2 through 4.4 to compare the resulting PSFs and residuals. The RMS residual of the time lag and each predictor is shown above each plot, with the best predictor residual PSF shown.

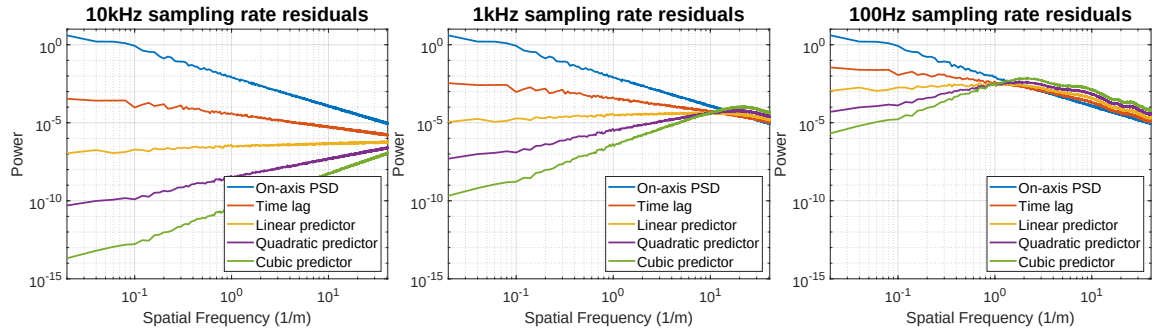

Figure 4.18: Comparison of on-axis PSD with time lag and first, second, and third order polynomial predictors applied to 10, 1, and 0.1 kHz atmosphere model samples.

Analyzing the PSD residuals in Figure 4.18, it can be seen that higher-order predictors are more effective at lower spatial frequencies, however, to see the same

gains at higher spatial frequencies, the sampling rate needs to be sufficiently high.

The prediction approach detailed above can be applied to each of the off-axis wavefront measurements before the next steps are taken to acquire the on-axis phase errors, discussed in the following section. However, if the reconstruction operations are mathematically linear, then the prediction can be made on the final reconstructed wavefront only to minimize the number of computations.

4.2.5 Off-Axis Tomographic Reconstruction Phase Residuals

As a STARLITE constellation is kept on an HEO and does not stay on-axis during observation, the limitations of phase reconstruction towards the target must be analyzed and optimized. To look at the off-axis reconstruction performance independent of the on-axis performance, four beacons are placed at equal distances from the centre without a central beacon. The angular separation between the centre and the beacons is modulated to analyze the RMS residuals of the constellation at various radii. Given a ~ 35" observational window, constellation radii from 10" down to 0.1" will be analyzed, where the performance of the reconstruction is directly dependent on the distance between the guide star and the target [195] and hence a good indicator of reconstruction effectiveness. Motion through the observation window will be not analyzed in this paper, but it is noted that the beacons closer to the target can be weighted more heavily in the reconstruction as they are more representative of the on-axis wavefront, and that certain beacons will get closer to the target during the observation as the constellations moves in and out of the observation window. Figure 4.19 illustrates the setup of the reconstruction where the beacons locations and their fields of view are show in white circles with the on-axis target and telescope pupil shown in green in the middle of the grid.

There are various approaches to reconstructing the on-axis phase from off-axis measurements with tomographic reconstruction of the atmosphere using statistical fitting, iterative, and/or interpolation methods to preserve the structure while minimizing noise and error [192, 193, 196, 197, 198, 199, 200, 201]. Given the small separations and ignoring noise for now, this paper will look at the expected performance that could be possible from a simple polynomial interpolation method, where the measured phase from each beacon placed at a specific altitude, spatially interpolated towards the on-axis target, and an average of the four screens taken as the reconstructed on-axis phase. A prediction of the next reconstructed on-axis phase

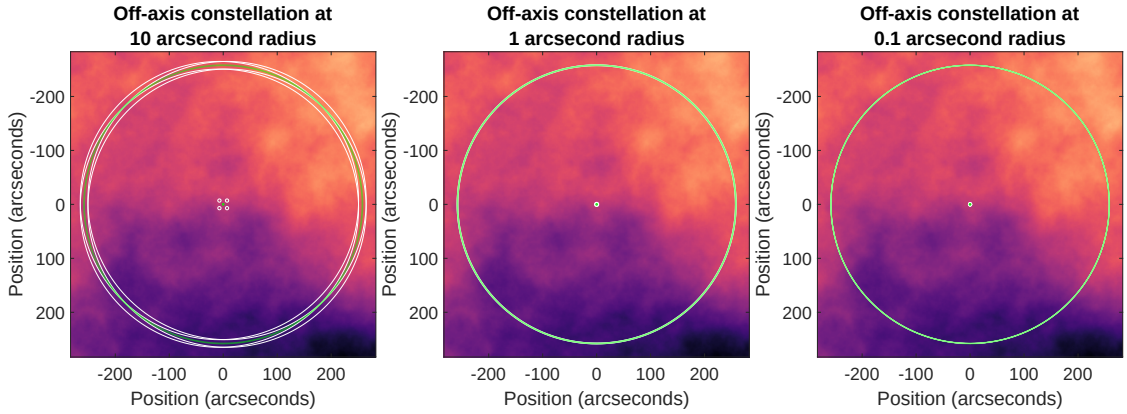

Figure 4.19: Beacon fields of view (lines of sight) around on-axis target for reconstruction (white circles), with on-axis target and field of view (green circle and dot) for a targeted reconstruction altitude of 4 km above the 10 m telescope.

measurement can be used to minimize the time lag of the measurement (as discussed in the previous section) and a subtraction from the true on-axis phase error performed to analyze the residual phase error left over from the combined time lag and reconstruction.

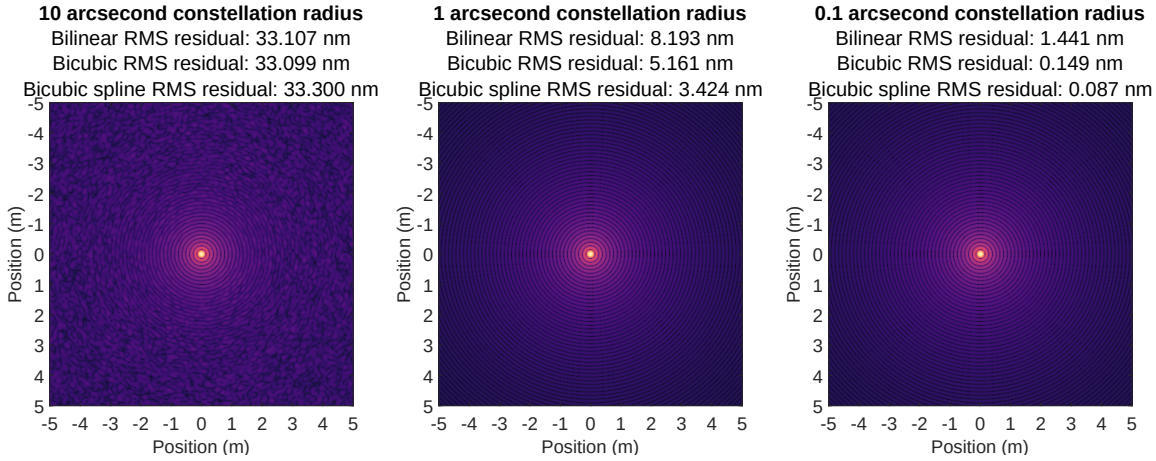

Figure 4.20: PSF of the residual phase error after reconstruction of 10", 1", and 0.1", with reconstructor type and RMS of each simulation above their plot.

The RMS residuals for each constellation radii is calculated and the PSF shown in Figure 4.20 for a bilinear, bicubic, and bicubic spline interpolation reconstructor at an altitude of 4 km above the telescope and sampling rate of 10 kHz with a cubic predictor. The RMS residual after each interpolation is shown above each plot. 4 km was chosen to get above the average height of the turbulence in the atmosphere

model, while 10 km might be considered to be above the majority of it and to be considered later. It is noted that reconstruction accuracy increases as separation decreases (as expected) and that accuracy is only improved with the use of higher order interpolation when the separation is small.

Looking at the PSDs of the reconstructor residuals illustrated in Figure 4.21, both bilinear and bicubic interpolation exhibit similar structures. Bicubic interpolation shows slight improvements over bilinear interpolation at higher spatial frequencies. Bicubic spline interpolation, which ensures continuity of the first and second derivatives for a smoother and more continuous result, is identified as the superior reconstructor when separations are small, demonstrating a more linear residual trend initially. However, at larger separations, bicubic spline interpolation attenuates higher spatial frequencies and can underperform compared to simpler interpolators. It was observed that the accuracy of bicubic spline interpolation showed some dependency on computational grid size, necessitating further study before definitive conclusions can be drawn and further optimizations implemented.

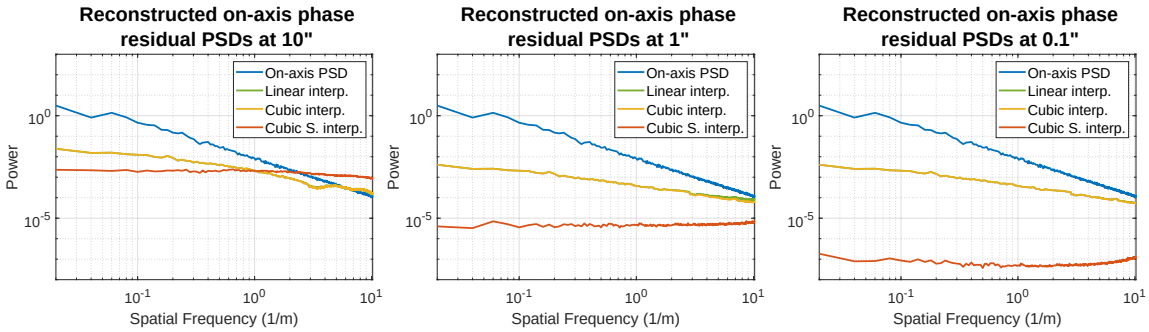

Figure 4.21: On-axis average and reconstructor residual PSDs for 10", 1", and 0.1" constellation radii with bilinear, bicubic, and bicubic spline interpolation reconstruction.

For all three interpolators, low spatial frequency components are reconstructed effectively, while smoothing effects attenuate high spatial frequency components that are crucial to preserve. These findings suggest that at small separations, approximately $\sim$ 1" or less, bicubic spline interpolation could effectively reconstruct the on-axis phase from off-axis measurements, achieving residuals at nanometer to sub-Angstrom levels. For larger separations, bilinear interpolation could serve as a suitable initial estimate for more robust fitting methods to improve accuracy and reduce residuals. Bayesian statistical methods such as Maximum A Posteriori (MAP) esti-

mation could leverage known characteristics about the phase map structure derived from off-axis or real-time atmospheric measurements to infer the most likely reconstructed phase map considering all available information [202, 203]. Integration of these approaches with interpolation methods to provide a strong initial estimate could establish the groundwork for achieving Angstrom-level residuals up to separations of 10" and will be thoroughly investigated in the subsequent phase of this study.

4.2.6 Conclusions

STARLITE aims to bridge the gap between ground-based accessibility and the demanding observational requirements needed for exoplanet imaging and characterization. Each satellite in the constellation uses a 1 W onboard laser at 760 nm to generate extremely bright -10 mag, unresolved off-axis guide stars for tomographic reconstruction towards the target, enabling extreme AO capabilities in a narrow 0.1-1% bandpass . This paper presents a preliminary theoretical 'best-case' end-to-end optical simulation of the STARLITE system, providing estimates of wavefront reconstruction accuracy and residuals through the Earth's atmosphere towards a target.

Polynomial predictors at a high enough sample rate (>10 kHz) were shown to minimize the wavefront error to less than 0.1 nm for linear prediction and less than 0.01 nm for cubic prediction in the on-axis case. Polynomial prediction with orders higher than one (non-linear) performed very well at higher sample rates up to a certain spatial frequency cutoff, beyond which lower-order predictors began to perform better. However, even at lower sample rates down to 100 Hz, higher-order polynomials remained effective at predicting lower spatial frequencies, indicating their usefulness primarily for low-order prediction.

Utilizing a cubic predictor at 10 kHz with 2D polynomial interpolation to reconstruct on-axis phase from off-axis measurements (tomography) was shown to be an reasonable starting point for angular separations up to 10 arcseconds, while bicubic spline interpolation showed to have good potential for smaller separations around 1 arcsecond or less. In each reconstructor case, the interpolation and averaging had a blurring effect on the resulting reconstructed phase map and caused the attenuation of high spatial frequency components. Considering computational complexity and the high-speed sampling rate needed, bilinear interpolation could be an appropriate starting point for reconstruction at any separation if statistical methods could be implemented to better match the structure of the solution with known atmospheric

characteristics.

While more work and research is needed, we found that at a sampling rate of at least 10 kHz and separations near 0.1" could theoretically allow us to achieve the 10^8 contrast goal needed for Earth-like exoplanet imaging around nearby Sun-like stars. Optimal constellation geometries and statistical reconstruction methods will need to be studied to see if the constellation size can be increased to allow longer a observing time per constellation during the science target transit.

4.2.7 Future Work

Based on the findings of this paper, a more robust statistical method for reconstructing the on-axis phase is needed to preserve high-frequency details without introducing unwanted smoothing or noise. Additionally, it is important to consider a realistic entrance pupil design that includes a central obscuration and secondary mirror supports. Optimal design of a coronagraph tailored for this setup to efficiently block the bright target light and minimize diffraction effects caused by sharp edges in the pupil should also be studied and designed. Selecting and simulating a wavefront sensor (WFS) scheme/design, and subsequently fitting it to a deformable mirror (DM) surface, will enable analysis of measurement and fitting errors while also providing an estimate for the optimal number of DM actuators required. Lastly, it is essential to investigate scintillation effects and amplitude errors in the wavefront due to atmospheric conditions. Understanding these factors is crucial for extreme AO applications and ensuring STARLITE can mitigate or avoid potential issues stemming from them.

Chapter 5

Conclusions

This dissertation has presented a focused body of work aimed at advancing the state of high-contrast imaging for the direct detection and characterization of exoplanets. Through the development of three interrelated projects, SPIDERS, CAL 2.0, and STARLITE, this research addresses persistent challenges in instrumentation, wavefront control, and atmospheric correction. Collectively, these efforts contribute to the long-term objective of imaging and analyzing Jupiter- and Earth-class exoplanets orbiting nearby stars.

The State of the Field

Direct imaging remains among the most technically demanding approaches in exoplanetary science, requiring suppression of stellar light by factors of up to ten billion in order to detect planetary signals at sub-arcsecond angular separations. Present-day adaptive optics (AO) systems have achieved raw contrast levels of 10^{-6} to 10^{-7}, sufficient for detecting young gas giants that remain luminous in the infrared. However, imaging mature Jupiter or Earth-like exoplanets in reflected light requires contrast levels approaching $10^{-9} - 10^{-10}$, which remain beyond the capabilities of existing ground-based instruments.

In response to these challenges, the research presented here contributes practical tools and strategies for improving contrast performance. Developments in focal plane wavefront sensing and correction, post-processing techniques, and atmospheric tomography help advance achievable contrast into the 10^{-7} to 10^{-8} regime. These capabilities provide the foundation for future observatories to detect and characterize potentially habitable terrestrial exoplanets, marking a critical step forward for direct imaging science.

SPIDERS: Subaru Pathfinder Instrument for Detecting Exoplanets and Retrieving Spectra

SPIDERS was developed as a testbed for combining focal plane wavefront sensing and imaging spectroscopy within a common-path optical architecture. Designed for deployment on the Subaru Telescope and compatible with the AO3k system, SPIDERS targets contrast levels in the range of 10^{-6} to 10^{-7}, enabling the detection and spectral retrieval of young self-luminous exoplanets. In addition to validating real-time wavefront control and broadband spectral analysis, SPIDERS demonstrates the potential for significant post-processing contrast gains using coherent and spectral differential imaging (CDI and SDI). Preliminary results show contrast improvements by factors of 10 to 100 compared to instruments currently deployed in the field.

To support these goals, my work focused on the mechanical and optomechanical design and integration of key subsystems. This included the design and integration of a structural frame with a six degree-of-freedom hexapod alignment system, a custom ultra-low speed optical chopper (ULSOC) for fringe modulation, and the motion control system for a full-field imaging Fourier transform spectrometer (IFTS). Together, these components support real-time speckle suppression and broadband spectral retrieval within a unified science path, establishing a framework for future exoplanet instruments with enhanced contrast and characterization capabilities.

CAL 2.0: The Gemini Planet Imager Calibration Unit Upgrade

CAL 2.0 is a facility-class upgrade to the Gemini Planet Imager's internal calibration system, designed to enable real-time focal plane wavefront sensing and correction through an integrated optomechanical and control architecture. Building on the principles and operational experience of the SPIDERS instrument, CAL 2.0 represents a major advancement in large-scale facility-level focal plane wavefront sensing for ground-based exoplanet imaging. The system is built for the Gemini North Telescope and targets contrast performance in the range of 10^{-7} to 10^{-8} for bright stars.

As part of this effort, I led the mechanical design, assembly, and integration of three major subsystems: the focal plane mask (FPM) wheel, the polarization modulator (PolMod), and the ultra-low speed optical chopper (ULSOC). The FPM wheel and PolMod are both based on original CAL 1 designs, developed by NASA JPL and NRC HAA respectively, and were adapted with updated components and electronics to replace obsolete commercial parts. The FPM wheel allows for the selection of specialized masks used for the self-coherent camera (SCC), while the PolMod provides

precise positioning and angular control of a polarization optic for calibration and science observations. The ULSOC, derived from the SPIDERS prototype, delivers stable fringe modulation at subhertz speeds with minimal thermal and vibrational noise, enabling SCC operation on faint targets.

With final fabrication and assembly complete, all three mechanisms are currently undergoing functional and environmental testing in preparation for integration into the CAL 2.0 optomechanical structure. Alignment and software commissioning will proceed in parallel with interface validation through the HEART real-time control system. Following its deployment at Gemini North, CAL 2.0 is expected to improve GPI's contrast floor through closed-loop focal plane wavefront correction and enhanced post-processing with coherent differential imaging (CDI), increasing sensitivity by up to a factor of 100 for faint companions at smaller angular separations.

STARLITE: Superluminous Tomographic Atmospheric Reconstruction with Laser Beacons

STARLITE investigates a combined ground- and space-based approach to atmospheric tomography, using laser beacons deployed on satellites to enhance AO correction for high-contrast ground-based imaging. The approach involves a constellation of small satellites in highly-elliptical orbits that periodically align with a target field. During these alignments, the satellites project extremely bright artificial guide stars around the science target, creating short observational windows that repeat approximately every two weeks and last a few hours. This beacon configuration enables tomographic wavefront reconstruction for a significantly improved signal-to-noise ratio in the direction of the science target, increasing the accuracy of wavefront measurement and correction. The resulting reduction in speckle noise improves image fidelity, decreases integration times, and accelerates detection. The mission concept is designed to achieve near diffraction-limited performance with raw contrast levels between 10^{-8} and 10^{-9}, providing a foundation for post-processing techniques that can further suppress residual speckle noise and potentially enable reflected-light exoplanet detection at contrasts below 10^{-10}, beyond the reach of current ground-based systems.

To evaluate the feasibility of this architecture, my work focused on developing a comprehensive mission framework incorporating compact CubeSat-based laser beacons and their orbital dynamics. This effort was complemented by a high-fidelity simulation environment designed to assess tomographic reconstruction performance

under typical atmospheric conditions for a variety of beacon configurations and sampling rates. Results indicate that an optimally configured satellite constellation with sufficient temporal resolution can achieve the low residual wavefront error required across the exoplanet imaging field of view, supporting the system's promise for future implementation. Although STARLITE remains a conceptual study, the analysis establishes the viability of integrated ground- and space-based platforms for overcoming atmospheric limitations in direct exoplanet imaging.

Final Remarks

This dissertation has presented a set of coordinated developments that advance the capabilities of high-contrast imaging through improvements in focal plane wavefront sensing, calibration hardware, and atmospheric correction strategies. Each project contributes to addressing specific limitations that constrain the detection and characterization of exoplanets, particularly at small angular separations and high contrast ratios.

While tailored to specific instruments, these developments help pave the way for future advances in high-contrast imaging technologies and observing strategies across both current and next-generation observatories. Together, they support a broader architecture for improving contrast performance and extending the sensitivity of direct imaging systems. The work spans a range of technical maturity, from early-stage feasibility studies to fully engineered hardware now prepared for integration, and establishes a foundation for continued advancement in the field.

Looking ahead, sustained progress in direct imaging will require the integration of precision optics, real-time control systems, and coordinated observing strategies that support advanced post-processing techniques. The methods and systems developed in this research contribute directly to that trajectory, enabling future instruments to investigate planetary atmospheres, surfaces, and potential biomarkers beyond our solar system.

Appendix A

Additional Information

A.1 Detector Types, Readout Strategies, and the Photo-Electric Relationship

This section provides a concise overview of detector types, readout strategies, and the photoelectric relationship in the context of observational astronomy. Detectors used in observational astronomy, particularly for high-contrast exoplanet imaging, rely on advanced material designs and readout mechanisms that significantly impact performance. These mechanisms dictate how signals are captured, processed, and interpreted, directly influencing sensitivity, noise characteristics, and the overall signal-to-noise ratio (SNR) [62]. Selecting the appropriate detector type, in combination with an optimized readout strategy, is crucial for enhancing the detection of the faint signals emitted by exoplanets. The most commonly used detector types include:

- **Charge-Coupled Devices (CCDs):** CCDs are widely employed due to their high quantum efficiency and low noise characteristics, making them well-suited for capturing faint astronomical signals in the visible to near-infrared wavelengths. These detectors consist of an array of photoactive regions that accumulate charge proportional to the incident photon flux. The collected charge is then transferred across the array to a readout register for digitization.

- **Electron-Multiplying CCDs (EMCCDs):** EMCCDs enhance the detection of extremely faint light levels by incorporating an electron multiplication stage for visible to near-infrared wavelengths. This high-voltage gain register amplifies weak signals before readout, effectively increasing the SNR in low-light

conditions while minimizing additional noise.

- **Complementary Metal-Oxide-Semiconductor (CMOS) detectors:** CMOS detectors offer advantages such as faster readout speeds, lower power consumption, and greater readout flexibility compared to CCDs. Each pixel contains its own amplifier and readout circuit, allowing for parallel data processing across the array. This architecture enables selective readout, making CMOS sensors particularly useful for high-speed imaging applications in the visible to near-infrared wavelengths.

Beyond CCDs, EMCCDs, and CMOS sensors, several advanced detector technologies are increasingly employed in exoplanet imaging to address specific observational requirements:

- **Microwave Kinetic Inductance Detectors (MKIDs):** MKIDs provide high sensitivity with intrinsic energy resolution, making them ideal for simultaneous imaging and spectroscopy [204]. These detectors operate by measuring shifts in inductance caused by photon absorption, allowing them to distinguish between photons of different energies (or wavelengths) across the visible to infrared wavelengths.

- **Single-Photon Avalanche Diodes (SPADs):** SPADs are highly sensitive detectors capable of counting individual photons with high temporal resolution in visible to near-infrared wavelengths [205]. They utilize avalanche multiplication, where a single photon triggers a rapid cascade of charge carriers, significantly amplifying the signal. This process enables SPADs to detect faint signals in low-light conditions with minimal noise and highly precise timing.

- **Superconducting Nanowire Single-Photon Detectors (SNSPDs):** SNSPDs offer exceptional photon-counting efficiency with ultra-low dark noise [206]. These detectors employ superconducting materials cooled to cryogenic temperatures and operate near their critical current, enabling the detection of single photons with extremely high efficiency. They are particularly valuable for high-sensitivity infrared and visible imaging applications.

- **Mercury Cadmium Telluride (MCT) Detectors:** MCT detectors are widely used in infrared astronomy due to their broad wavelength sensitivity, covering both near and mid-infrared regions [207]. These detectors leverage the

tunable semiconductor properties of mercury cadmium telluride to efficiently absorb infrared photons and convert them into measurable electrical signals.

Selecting the appropriate detector type and readout mechanism is essential to meet the specific demands of an observation, including wavelength coverage, temporal resolution, and noise performance. The strategic compromise between detector technology, readout approach, and system design plays a critical role in optimizing the performance of high-contrast imaging systems.

Readout Strategies

Optimizing detector performance requires carefully chosen readout methods, each with distinct advantages and trade-offs. These strategies determine how data is retrieved from the detector array, affecting image quality, acquisition speed, and noise characteristics. The primary readout methods used in modern astronomical detectors include:

- **Full-frame readout:** Captures the entire detector array, either row-by-row or pixel-by-pixel. While this method ensures complete image acquisition with high spatial resolution, it increases readout time and introduces potential readout noise. Full-frame readout is commonly used in CCDs, EMCCDs, and some CMOS detectors for high-resolution imaging and calibration.
- **Selective readout:** Retrieves data from specific regions of interest, reducing acquisition time and minimizing unnecessary noise. CMOS detectors allow for efficient access to individual pixels or subarrays without affecting the rest of the sensor.

Readout methods can further be classified based on pixel charge retention during acquisition:

- **Destructive readout:** Clears pixel charge after each readout, preventing repeated measurements of the same pixel. This method, standard in traditional CCDs, introduces readout noise and limits temporal resolution, making it less suitable for applications requiring multiple exposures of the same region.
- **Non-destructive readout:** Enables repeated sampling of pixels without erasing their charge, improving dynamic range and reducing noise accumulation over time. This technique is particularly advantageous for high-contrast and

long-duration observations, widely used in CMOS and MCT detectors [208]. Common non-destructive readout strategies include:

- **Correlated Double Sampling (CDS):** A pair of non-destructive reads are differenced to remove reset noise and reduce read noise, one immediately after reset and one at the end of the integration.
- **Fowler (Multiple CDS) Sampling:** Multiple reads are taken at both the start and end of the exposure, their averages differenced to reduce read noise roughly by $1/\sqrt{N}$ for N samples.
- **Other methods (e.g., Up-the-Ramp / Multi-Accumulate):** Continuous or group-averaged non-destructive reads during integration allow slope fitting, cosmic-ray detection, and flexible noise-weighted stacking.

By selecting an appropriate readout strategy, data collection can be optimized for specific observational needs, balancing sensitivity, temporal resolution, and noise minimization.

Detector Signal Relationship

In detector-based imaging systems, the relationship between the digital readout (in bits) and the number of electrons generated on the detector array by incident photons is important to establish for calibration. This conversion is typically expressed by the equation:

$$\text{Signal}_{\text{electron}} = G \times \text{Signal}_{\text{ADU}}, \tag{A.1}$$

where $\text{Signal}_{\text{electron}}$ is the number of electrons converted from incident photons on the detector, G is the detector's gain in electrons per Analog-to-Digital Unit (ADU), and $\text{Signal}_{\text{ADU}}$ is the measured signal in detector units. This relationship provides a means to calibrate the digital output to the actual physical signal, enabling accurate flux measurements and calibration. However, the electron-to-photon conversion can vary between detectors based on the detector type, sensitivity, and any signal amplification. Moreover, photon noise and other sources of signal contamination add complexity to this conversion, as discussed in §1.2.6.

A.2 Simulating a Chromatic Wavefront

In this section, the methods for simulating the chromatic intensity distribution of a point source at the focal plane of a telescope are presented. The simulation employs the 2D Fast Fourier Transform (FFT2) within the Fraunhofer approximation framework, providing an efficient means to calculate the Point Spread Function (PSF), which is essential for quantifying the optical system's impact on point sources. For theoretical background, refer to §1.3.1.

Spatial Grid Setup

The simulation begins by defining a spatial grid. The resolution of the grid must satisfy the Nyquist sampling criterion, which ensures proper representation of spatial frequencies without aliasing. The grid's spatial resolution is determined by the aperture diameter D in meters, beam ratio b_r, and the number of grid points across each grid axes np. The beam ratio, which is the fraction of the aperture used to define the beam, should not exceed 0.5 to meet the Nyquist criterion. However, lower beam ratios (e.g., 0.2 or 0.3) may be used to oversample the aperture and increase the resolution of the focal plane image. The beam ratio is defined as:

$$b_r = \frac{D}{L}, \tag{A.2}$$

where L is the total grid size in meters. The spacing between adjacent grid points, Δx, is then calculated by:

$$\Delta x = \frac{D}{b_r \cdot np} = \frac{L}{np}, \tag{A.3}$$

where np is the number of grid points along each axis. For computational efficiency, np is typically chosen as a power of 2, i.e., $np = 2^n$, where n is a positive integer. The spatial grid typically spans the domain $[-L/2, L/2]$ with equal spacing Δx along both the x and y axes.

Aperture Function

The aperture function models the spatial distribution of light passing through the telescope's aperture, and is directly related to the angle of diffraction at the focal plane. While the aperture shape can vary to represent different optical systems, a circular aperture is considered here for simplicity. If both the amplitude and phase functions are known and spatially scalable, chromatic broadening of the diffraction

pattern can be simulated using an aperture radius r^{aperture} scaled for each wavelength λ_i according to the angular diffraction relationship between the aperture diameter and the wavelength, defined as:

$$r_i^{\text{aperture}} = \frac{D}{2} \cdot \frac{\lambda_1}{\lambda_i}, \quad \text{where} \;\; i = 1, 2, 3, \ldots \;\; \text{and} \;\; \lambda_1 < \lambda_2 < \lambda_3 < \ldots \tag{A.4}$$

where λ_1 is the reference wavelength. This approach can be used to scale pupil plane apertures and masks to simulate multiple wavelengths by broadening the PSF. The aperture function $A_i(x, y)$ for a circular pupil centred on the grid is then defined as:

$$A_i(x, y, \lambda) = \begin{cases} 1, & \text{if } \sqrt{x^2 + y^2} \leq r_i^{\text{aperture}}, \\ 0, & \text{otherwise.} \end{cases} \tag{A.5}$$

This simple circular aperture can be replaced with a more complex function to represent real-world aperture shapes, such as those with secondary obscurations or apodization, as discussed in §1.3.5. Regardless of the shape, the aperture function must satisfy the beam ratio limit and be bounded between 0 and 1. To reduce the pixel edge effects that arise from the finite nature of the simulation, grey-pixel approximations or apodization approaches can be used. These methods effectively smooth the sharp change from 0 to 1 in the aperture function, minimizing discretization artifacts that would not appear in a real system.

For a system with wavefront phase errors and multiple optical elements at different planes, careful consideration of scaling for chromatic simulations is essential. Conversely, magnifying the wavefront intensity at the focal plane (which includes the phase and amplitude/aperture) can be achieved using a Fourier-domain zero-padding approach, which is discussed later in this section.

Wavefront Phase

The wavefront phase, $\phi_i(x, y, \lambda)$, models distortions and aberrations in the optical system in units of radians. In this simulation, we assume an initially zero-phase condition for all wavelengths:

$$\phi_i(x, y, \lambda) = 0. \tag{A.6}$$

This phase term can be modified to account for optical aberrations such as surface errors or atmospheric turbulence, but must also undergo spatial domain magnification if considering a chromatic simulation via pupil plane aperture radius scaling.

For this reason, it can be easier to magnify the focal plane intensity rather than the amplitude and phase components separately, using a Fourier-domain zero-padding approach. Regardless, phase can be added to the wavefront either by modifying angles within the phase matrix $\phi_i(x, y)$ directly or equivalently by multiplying the wavefront with an exponential phase term, i.e., $e^{i(\phi_1+\phi_2)} = e^{i\phi_1}e^{i\phi_2}$.

Wavefront Energy Normalization

To standardize the system energy, the wavefront at the entrance pupil is normalized so that the total power, given by the sum of the squared magnitudes of all wavefront values, is equal to 1 across the grid. The normalization constant b_i that scales the wavefront is defined as:

$$b_i = \frac{1}{\sqrt{\sum_{x,y} |A_i(x, y, \lambda) \cdot e^{i\phi_i(x,y,\lambda)}|^2}} \, . \tag{A.7}$$

This normalization ensures that the total energy entering the system is standardized, which is essential to perform physically meaningful diffraction calculations.

Fourier Transform and Scaling

The propagated wavefront in the focal plane $\tilde{E}_i(f_x, f_y)$ is acquired by applying the 2D Fourier transform (FFT2) to the normalized wavefront:

$$\tilde{E}_i(f_x, f_y) = \mathrm{FFT2}\left(b_i \cdot A_i(x, y, \lambda) \cdot e^{i\phi_i(x,y,\lambda)}\right). \tag{A.8}$$

where (f_x, f_y) are the spatial frequency components of the diffraction pattern. To map these frequency components to the physical space in the focal plane, the focal plane grid must be established.

Focal Plane Grid Setup

Performing the 2D FFT on a spatial grid with sampling interval Δx, the corresponding frequency domain is already defined. The frequency grid spacing, Δf, is inversely proportional to the spatial sampling interval and its Nyquist limit f_{max}:

$$\Delta f = \frac{1}{np \cdot \Delta x}, \quad f_{\max} = \frac{1}{2\Delta x} \, . \tag{A.9}$$

Here, Δf specifies the interval between adjacent frequency points, and the frequency

grid extends from $-f_{\max}$ to $f_{\max}$. Frequencies exceeding the Nyquist limit ($f_{\max}$) are subject to aliasing; thus, only frequencies within this range are physically meaningful. This constraint is crucial when interpreting or analyzing diffraction patterns. Maintaining the correct scaling between spatial and frequency domains preserves the physical interpretation of diffraction patterns and intensity distributions. Depending on the application, the focal plane image can also be analyzed in terms of angular separation on the sky (λ/D), or other pertinent coordinate systems, presented later in this section.

Intensity Calculation

The intensity at the focal plane (or any observation plane) depends on the coherence of the light, as discussed in §1.3.2. For incoherent sources, the total intensity is the sum of the wavefront intensities:

$$I_{\text{total, incoherent}}(x, y) = \sum_{i=1}^{N_\lambda} \left| \frac{1}{\lambda_i} \cdot \tilde{E}_i(f_x, f_y) \right|^2 \tag{A.10}$$

where λ_i accounts for the wavelength dependence of the diffraction pattern, often left out if considering the monochromatic case and intensity is normalized or scaled for contrast. For coherent light, the total intensity is the intensity of the wavefronts summed:

$$I_{\text{total, coherent}}(x, y) = \left| \sum_{i=1}^{N_\lambda} \frac{1}{\lambda_i} \cdot \tilde{E}_i(f_x, f_y) \right|^2 . \tag{A.11}$$

Using these intensity formulas, the propagated wavefront can be simulated to generate the corresponding image in the focal plane.

Algorithm Summary

The steps for simulating the focal plane intensity are as follows:

1. Define the spatial grid, ensuring adequate resolution based on aperture diameter and beam ratio.
2. Compute the aperture function.
3. Apply phase and amplitude to the wavefront as applicable.
4. Normalize the wavefront to standardize the energy at the entrance pupil.

5. Perform a 2D FFT to propagate the wavefront to the focal plane.

6. Define the frequency grid at the focal plane, considering the Nyquist limits.

7. For coherent light, sum the fields before calculating the intensity; for incoherent light, sum the intensities. Employ wavelength magnification as applicable.

These steps produce a simulated image of a point source at the focal plane, which can be further processed to assess the optical system's performance, including the PSF, and its impact on observations. Implementing this algorithm, Figure A.1 presents the focal plane intensity distributions for different spectral conditions.

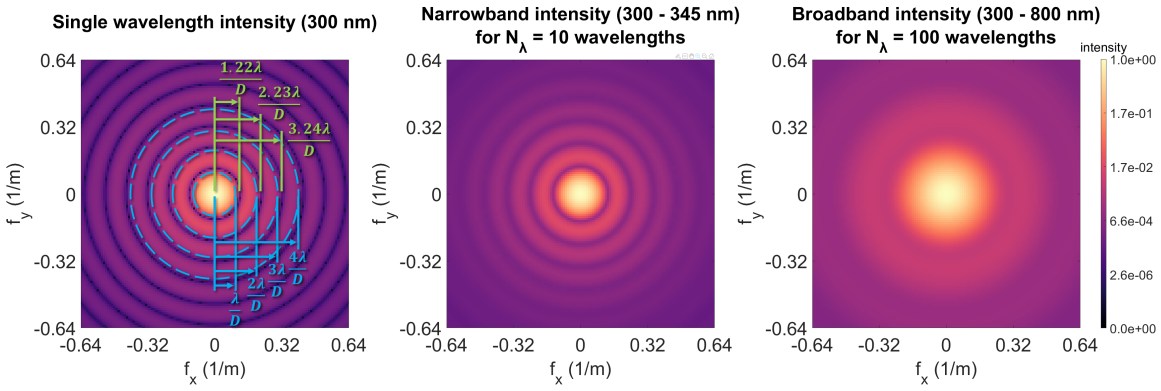

Figure A.1: Simulated focal plane intensity for monochromatic (left), narrowband (centre), and broadband (right) light spanning the U to R photometric bands (300–800 nm), using $np = 2048$, $D = 10$ m, and $b_r = 0.1$, the λ/D rings (in blue) illustrate the grid relationship with the wavelength and telescope diameter. Monochromatic light produces a distinct Airy disk, while chromatic broadening blurs these features and increases the PSF size. Exponential scaling of the intensity enhances image contrast globally without altering structure. The plotted intensities are zoomed in from the full Nyquist limit range, where $f_{\max} = 10.24$ cycles/m.

As shown, monochromatic light forms a well-defined Airy disk, revealing the PSF structure of the circular aperture. Conversely, broadband propagation induces chromatic broadening, which smears the diffraction rings and complicates PSF measurements. This effect underscores the necessity of narrowband filtering in high-contrast imaging applications to mitigate PSF degradation.

Relating λ/D to the Focal Plane Grid

In analyzing diffraction patterns, the Airy disk produced by a circular aperture is

defined by the wavelength of light and the aperture size. The first minimum of the Airy disk occurs at an angle θ, as defined by the Rayleigh criterion, $\theta \approx 1.22\ \lambda/D$, discussed in §1.2.1. This angle corresponds to the spatial frequency at which the first dark ring appears in the diffraction pattern. The Airy disk pattern at the focal plane is determined by the beam ratio (b_r), which provides a direct relationship with the grid spacing $\Delta\ \lambda/D$ as:

$$\frac{1}{b_r} = \frac{\text{pixels}}{\lambda/D} \quad \text{or} \quad b_r = \Delta\frac{\lambda}{D}\ . \tag{A.12}$$

Consequently, the first minimum of the Airy disk, occurring at $1.22\ \lambda/D$, spans $1.22/b_r$ from the centre of the grid. For example, $b_r = 0.5$ would put the first minimum of the Airy disk at 2.44 pixels from the centre, just enough to sample the oscillation between minimums. Comparatively, $b_r = 0.1$ would put the first Airy disk minimum at 12.2 pixels from the centre, oversampling the Airy disk structure but providing higher resolution. Proper configuration of the focal plane grid and a thorough understanding of sampling requirements are vital for accurate representation and analysis of diffraction patterns in optical systems.

Wavelength Magnification in the Focal Plane

In optical simulations that include phase and amplitude aberrations, chromatic broadening of the point spread function (PSF) can be efficiently modeled by magnifying the final focal plane rather than the pupil wavefront. This approach is particularly advantageous in systems with multiple intermediate planes, where full multi-wavelength propagation is computationally expensive and susceptible to interpolation artifacts.

A practical method to perform this magnification is through zero-padding in the Fourier domain. This operation increases the spatial sampling in the image plane, effectively magnifying the PSF without modifying the optical propagation itself [209]. The result is a higher-resolution PSF that emulates the effect of increasing the wavelength or reducing the aperture size. The magnification factor k is defined as:

$$k = \frac{\text{zero-padded grid size}}{\text{original grid size}} = \frac{zp + np}{np}, \tag{A.13}$$

where zp should be a multiple of 2 for symmetrical padding. This factor adjusts the effective wavelength λ_{eff} as:

$$\lambda_{\text{eff}} = k \cdot \lambda_{\text{ref}}, \tag{A.14}$$

where λ_{ref} is the reference wavelength used in the original simulation.

To maintain physical accuracy, any focal plane elements defined upstream of the final image, such as coronagraphic stops or focal plane masks (FPMs), must also be scaled. For a simple circular FPM with radius r_{FPM}, the scaled radius becomes:

$$r_{\text{FPM, scaled}} = \frac{r_{\text{FPM}}}{k}. \tag{A.15}$$

This adjustment ensures that the mask maintains its correct physical size relative to the scaled PSF, accurately capturing the effect of longer wavelengths interacting with the mask and partially diffracting around it. Discussed in §A.2.1, the tip/tilt phase ramp used to inject off-axis companions must be scaled by $1/k$ to ensure that their chromatic spreading occurs symmetrically about their respective optical axes.

To simulate the broadband image, individually scaled PSFs computed at different wavelengths must be combined incoherently across the spectral band, outlined in §1.3.3.

Algorithm Summary:

1. Select a reference wavelength λ_{ref} and compute the magnification factor k, either based on the target effective wavelength or the number of padding pixels.

2. Rescale all focal plane masks and off-axis companion phase ramps by $1/k$ to preserve their correct physical dimensions and positions following image magnification.

3. Simulate the intensity at the final focal plane for λ_{ref} using FFT-based propagation through the optical system.

4. Apply an FFT to the intensity image to convert it into the frequency domain.

5. Zero-pad the frequency-domain data symmetrically to achieve the final grid size corresponding to the magnification factor k.

6. Apply an inverse FFT (IFFT) to obtain the magnified PSF in the image domain.

7. Normalize the resulting intensity by $1/k^2$ to conserve energy:

$$I_{\text{scaled}} = \frac{1}{k^2} \left|\text{IFFT(zero-padded FFT(I))}\right|.$$

8. Trim the scaled intensity image by removing the same amount of padding applied in the Fourier domain, restoring the grid to its original size.

9. Repeat steps 1–8 for all wavelengths in the bandpass, adjusting k for each wavelength as required.

10. Incoherently sum the scaled intensities across all wavelengths to produce the final broadband PSF:

$$I_{\text{broadband}} = \sum_{\lambda} I_{\text{scaled}}(\lambda).$$

This approach allows for efficient broadband PSF simulation without the need for a more complex multi-wavelength propagation. By applying scaling directly in the final image, high spatial fidelity is achieved, while ensuring consistency across all focal plane modifications. Figure A.2 illustrates the algorithm for both narrowband and broadband simulations, incorporating phase and amplitude errors, a coronagraphic FPM, and multiple point sources with varying contrasts in the field.

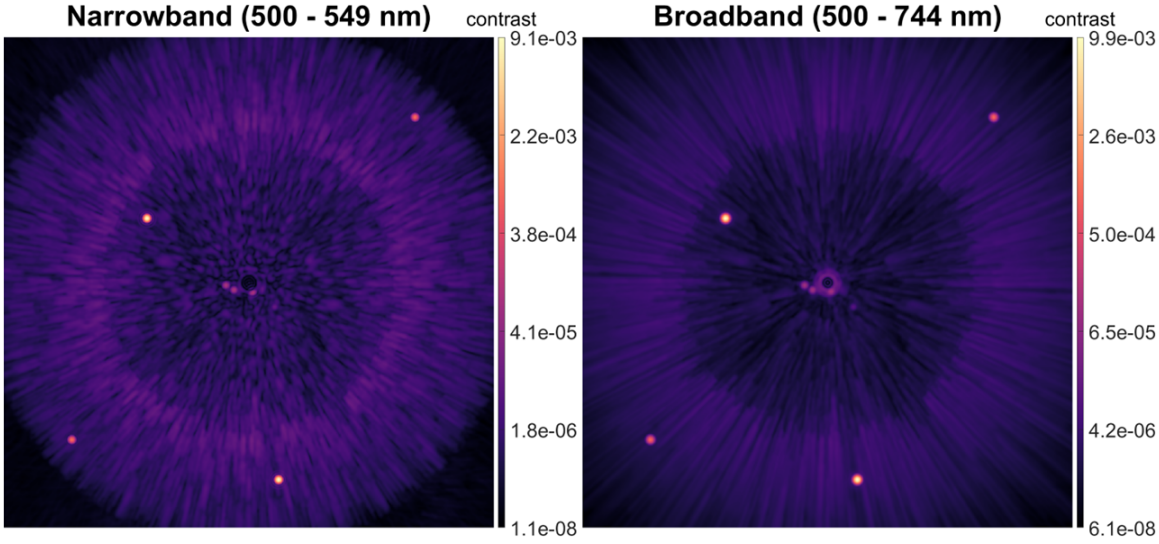

Figure A.2: Simulated intensity for a narrowband (left) and broadband (right) focal plane image with multiple point sources, including phase and amplitude errors. Chromatic blurring is modeled via Fourier-domain zero-padding, with wavelength-dependent focal plane intensities scaled and incoherently summed. A 124x124-actuator deformable mirror partially corrects the speckles around the on-axis occulted star, while faint point source companions with contrasts between 10^{-2} and 10^{-5} are visible. The coronagraphic FPM at the centre becomes progressively less effective at longer wavelengths, with diffraction around the mask becoming more prominent. A contrast scale based on the unocculted peak intensity is shown for reference.

Within this simulation framework, broadband images can be colour-coded to illustrate wavelength-dependent diffraction patterns, whether in the visible range or other spectral regions. An RGB-coloured image for the simulated narrow and broadband focal plane images from Figure A.2 are shown in Figure A.3.

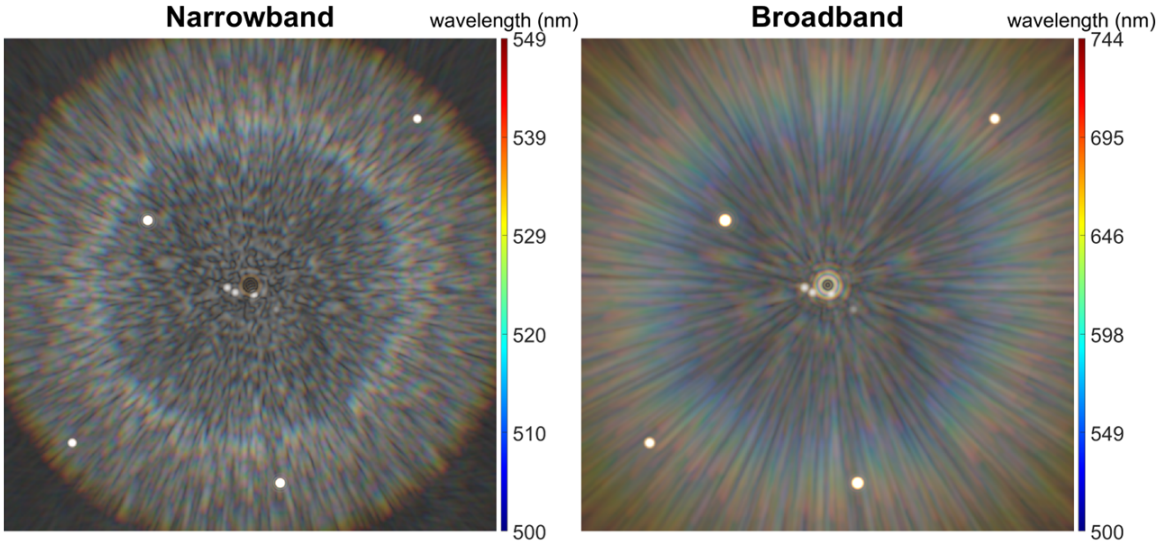

Figure A.3: Simulated colour-coded intensity for narrowband (left) and broadband (right) focal plane images containing multiple point sources. The simulations use the same environment and setup as Fig. A.2. Spectral channels are coloured by wavelength over the simulation range, with the scale shown for reference.

In typical observations with standard detectors, intensity at the focal plane is integrated over a spectral band, typically without resolving individual wavelength components, leading to an inherently blurred PSF. Imaging spectroscopy techniques discussed in §1.2.5 can provide a way to separate the wavelength components within the broadband PSF and recover the diffraction pattern for discrete wavebands, in the broadband spectral cube stack recovered by an imaging FTS in Figure 2.35.

A.2.1 Simulating an Exoplanet Companion

Simulating the focal plane intensity for a point source star can be extended to include the contribution of a nearby and faint exoplanet companion. In this section, the process of modeling the exoplanet's contribution to the focal plane intensity, considering factors such as angular separation, angular position (azimuthal angle), and contrast

ratio is outlined.

Planet's Angular Offset and Phase Ramp

To simulate an exoplanet at some angular separation, its displacement within the simulation grid must be calculated. The angular separation between the planet and the star θ_{planet} is determined using the distance and separation (Eq. 1.1), and expressed in units of radians or λ/D, while the angle ψ_{planet} specifies the planet's azimuthal angle in radians. Using the beam ratio b_r (Eq. A.2), magnification factor k if applicable, and spatial grid interval Δx (Eq. A.3), the angular offset for both the x and y directions is computed as:

$$r_x^{\text{planet}} = \theta_{\text{planet}} \cdot \cos(\psi_{\text{planet}}) \cdot \frac{\Delta x}{k \cdot b_r}, \tag{A.16}$$

$$r_y^{\text{planet}} = \theta_{\text{planet}} \cdot \sin(\psi_{\text{planet}}) \cdot \frac{\Delta x}{k \cdot b_r}. \tag{A.17}$$

Wavelength scaling of these offset components can be applied here with a factor of λ_i/λ_1 similar to the aperture radius Eq. A.4 if employing a pupil plane aperture scaling approach (not done in this example). However, computing these coefficients for the monochromatic case, and then scaling the intensity in the focal plane via Fourier-domain zero-padding is preferable as a simpler approach, discussed in §A.2. Next, a frequency grid is setup to map the x and y slopes to a 2D tip/tilt phase ramp:

$$[X_{\text{freq}}, Y_{\text{freq}}] = \text{meshgrid}\left(-\frac{np}{2} : \frac{np}{2} - 1\right) \frac{2\pi}{\Delta x \cdot np}\ , \tag{A.18}$$

where X_{freq} and Y_{freq} represent the spatial frequency components in the x and y directions, respectively, with grid spacing $\Delta X_{\text{freq}} = \frac{2\pi}{np \cdot \Delta x}$. The corresponding phase ramp is calculated as:

$$\phi_{\text{offset}} = r_x^{\text{planet}} \cdot X_{\text{freq}} + r_y^{\text{planet}} \cdot Y_{\text{freq}}\ . \tag{A.19}$$

This phase ramp is then applied to the wavefront in the spatial domain to shift the image in the focal plane, simulating the planet's offset position.

Planet Wavefront Simulation

To accurately model the wavefront of the exoplanet, the same aperture function used

for the star is applied to the planet. This ensures that both sources experience identical optical propagation, preserving the system's point spread function (PSF) for consistency across all point sources, like a companion exoplanet. The wavefront shift is implemented by multiplying the wavefront by an exponential phase ramp or, equivalently, by directly adding the phase offset to the planet's phase if it is known:

$$E_{\text{planet}} = A(x,y) \cdot e^{i\phi_{\text{planet}}} \cdot e^{i\phi_{\text{offset}}} = A(x,y) \cdot e^{i(\phi_{\text{planet}}+\phi_{\text{offset}})}, \tag{A.20}$$

where $A(x,y)$ denotes the aperture function, as defined in Eq. A.5 for this example. The planet's wavefront energy is normalized at the entrance pupil and propagated to the focal plane using a 2D FFT, following the same procedure applied to the star's wavefront, as described in Equations A.7, A.8, and A.10/A.11. If additional optical elements, such as a focal plane mask, apodization mask, or Lyot stop, are present in the optical path of the star, the off-axis planet wavefront must also pass through these elements. The resulting propagated planet wavefront in the focal plane is denoted as $\tilde{E}_{\text{planet}}$, with intensity I_{planet} in this simplified monochromatic case.

Planet Intensity using the Contrast

Normalizing the intensity of the planet to the star's intensity, the planet-to-star contrast ratio $C_{\text{P/S}}$ can be applied as:

$$I_{\text{planet}} = C_{\text{P/S}} \cdot \max(I_{\text{star}}) \cdot \frac{I_{\text{planet}}}{\max\left(I_{\text{planet}}\right)}, \tag{A.21}$$

where $\max(I_{\text{star}})$ is the peak intensity of the star, and I_{planet} is the as-calculated intensity of the planet's wavefront.

Final Intensity Calculation

The total intensity at the focal plane is then obtained by incoherently adding the planet's intensity with the star's intensity:

$$I_{\text{total}} = I_{\text{star}} + I_{\text{planet}}. \tag{A.22}$$

Algorithm Summary

The steps for simulating a companion exoplanet in the focal plane are as follows:

1. Define the planet's angular separation, and angular position, and contrast ratio.

2. Compute the angular offset of the planet using the angular separation, azimuthal angle, beam ratio, and grid size.
3. Generate the meshed grid frequency domain phase ramp.
4. Define the planet wavefront with an amplitude and phase using the same grid size and beam ratio as the star.
5. Apply the phase ramp to the wavefront in the spatial domain.
6. Normalize the planet's wavefront to standardize the energy at the entrance pupil.
7. Perform a 2D FFT to propagate the wavefront to the focal plane.
8. Compute the planet's focal plane intensity, scaled by the contrast ratio.
9. Define the frequency grid at the focal plane, considering the Nyquist limits.
10. Incoherently add the planet and star intensity to obtain the total focal plane intensity. Employ wavelength scaling as applicable.

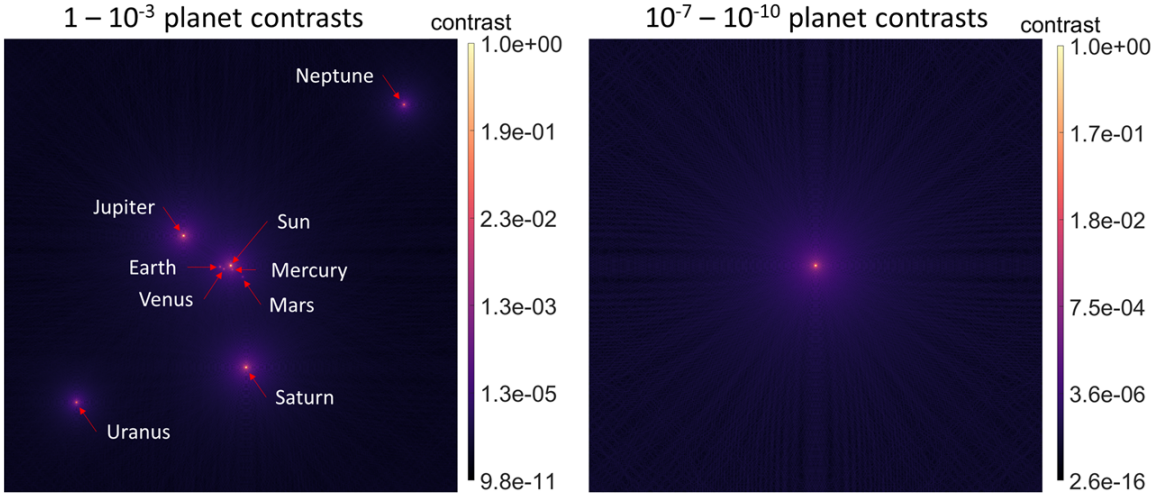

Figure A.4: The simulated diffraction-only focal plane intensity for monochromatic point sources at separations analogous to our solar system, as viewed from 10 parsecs away with a 10 m telescope at $10^7\times$ the contrasts in the visible (left). At visible wavelength contrasts, the planets are practically invisible compared to the overwhelmingly bright Sun (right). The contrast at each pixel is calculated by dividing each pixel of the final intensity image by the peak star intensity, the Sun in this case.

Applying this algorithm, a simulation using our solar system planets viewed from 10 parsecs as an example is shown in Figure A.4. The figure demonstrates the aperture PSF applied to each of the point sources and their incoherent additions, along with the reduction in visibility when the planet-to-star contrast ratio decreases.

These results emphasize the critical importance of starlight suppression in detecting faint exoplanets, both close to and far from their host stars. Coronagraphy is essential for achieving this suppression, blocking starlight at the centre of the image, thus improving the contrast in the surrounding regions, formally discussed in §1.3.6. Effective planet detection requires a careful balance between the angular separation of the target, the coronagraph's inner working angle, the telescope's resolution (§1.2.1), and other limiting factors like wavefront errors or noise.

A.3 Simulating Atmospheric Turbulence

Simulating atmospheric turbulence is critical for evaluating its effects on optical wavefronts, particularly in the design and optimization of adaptive optics (AO) systems. This section outlines the generation of phase screens based on the Kolmogorov power spectral density (PSD), as defined in Equation 1.45 and discussed in Section 1.3.4. An alternative model, the von Kármán PSD (Equation 4.1), is also introduced, which incorporates low- and high-frequency attenuation to better represent physical turbulence behavior. The simulation of spatiotemporal turbulence evolution is achieved by displacing multiple phase screen layers in different directions over time.

Generating a Turbulent Phase Screen

To generate a turbulent phase screen, a two-dimensional grid of spatial frequencies (f_x, f_y) over the aperture must first be established. The spatial frequencies are distributed on the grid over $\left(-\frac{np}{2}, \frac{np}{2} - 1\right) \cdot \left(\frac{1}{np\Delta x}\right)$, where $\Delta f = \frac{1}{np\Delta x}$ represents the grid spacing, and np is the grid size (Equation A.9). The spatial grid spacing Δx is determined by the aperture diameter D and beam ratio b_r (Equation A.3). To optimize computational efficiency, np is often chosen as a power of two, facilitating the use of fast Fourier transform (FFT) algorithms [71].

Next, random phase values $\theta(f_x, f_y)$ are generated for each spatial frequency, uniformly distributed within the interval $[-\pi, \pi]$ or $[0, 2\pi]$, ensuring circular randomness. The PSD $\Phi_\phi(f_x, f_y)$ is then used to scale the magnitude of the Fourier coefficients. The Fourier coefficients $\hat{\phi}(f_x, f_y)$ are expressed as:

$$\hat{\phi}(f_x, f_y) = \sqrt{\Phi_\phi(f_x, f_y)} \cdot e^{i\theta(f_x, f_y)}, \tag{A.23}$$

where $\Phi_\phi(f_x, f_y)$ is the PSD, and $\theta(f_x, f_y)$ the random phase values. To prevent aliasing, the Fourier coefficients outside the radius of $f_{\max} = \frac{1}{2\Delta x}$ (Eq. A.9) are masked by setting them to zero, ensuring that only spatial frequencies within the Nyquist limit are considered. The centre of the $\hat{\phi}(f_x, f_y)$ grid is also set to zero at $\left(\frac{np}{2} + 1, \frac{np}{2} + 1\right)$ for a square grid, ensuring no unwanted constant phase shifts (referred to as piston in Zernike polynomials, Figure 1.11).

Finally, the phase screen in the spatial domain is obtained by performing the inverse Fourier transform of the complex field. The 2D grid of phase angles, representing

the phase screen $\phi(x, y)$, is given by:

$$\phi(x, y) = \text{Re}\left(\mathcal{F}^{-1}\left\{\hat{\phi}(f_x, f_y)\right\}\right) \cdot \frac{np}{\Delta x}, \tag{A.24}$$

where $\mathcal{F}^{-1}$ denotes the 2D inverse Fourier transform and $\frac{np}{\Delta x}$ normalizes the solution over the grid. The real part of the inverse Fourier transform yields the final phase screen. Following the above outlined approach, the resulting phase and amplitude components of the Fourier coefficients, as well as the final phase screen, are shown in Figure A.5.

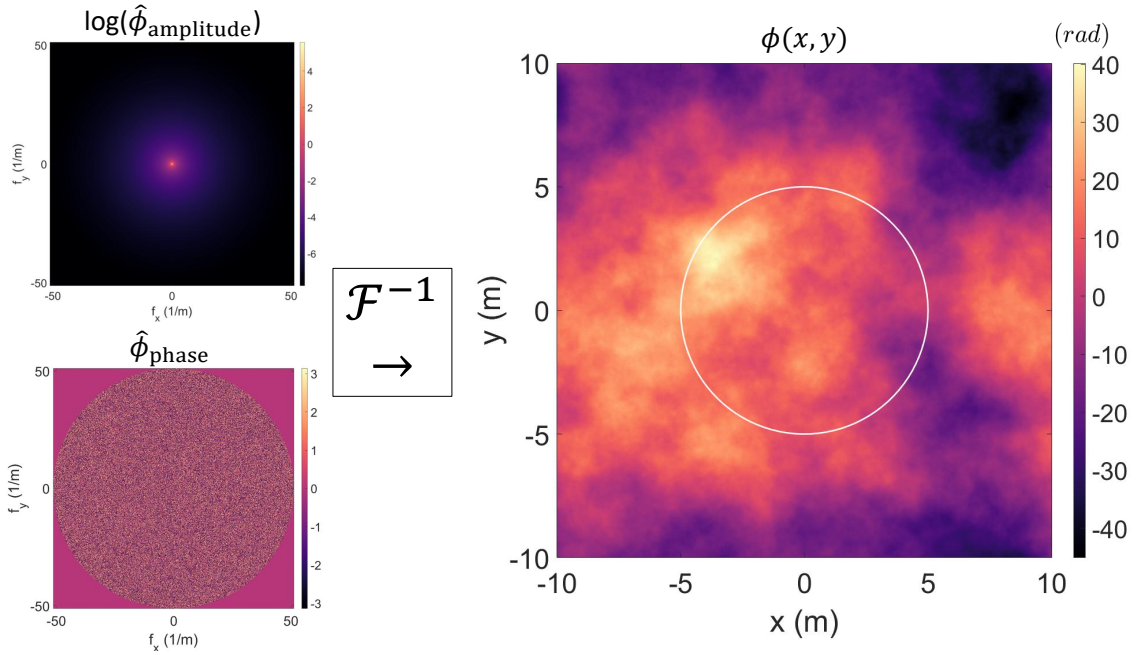

Figure A.5: The amplitude (top left, log-scale for visibility) and phase (bottom left) components of the random Fourier coefficients $\hat{\phi}(f_x, f_y)$. The resulting phase screen $\phi(x, y)$ (right) is shown with a $D = 10$ m aperture overlaid in white, using $np = 2048$, $b_r = 0.5$, $r_0 = 0.2$ m, and $\lambda = 500$ nm.

Multiple Moving Turbulent Layers

To introduce a spatially and temporally evolving turbulence simulation, a unique phase screen can be generated for multiple layers, with each layer individually moved at its own rate and direction, following Taylor's frozen flow hypothesis [74]. In these simulations, the PSD strength can be divided among each layer to account for varying turbulence strengths at different altitudes, a published phenomena with historical measured data from Maunakea Ridge [73]. These models provide 'good' to 'bad'

seeing conditions for AO observations, and include the wind speed, direction, altitude, and fractional contribution of the turbulence strength at each layer, measured during ongoing atmospheric measurement campaigns. The layer-specific PSD is given by including an additional term into Equation 1.45 for each layer i up to n layers:

$$\Phi_{\phi}^{(i)}(f_x, f_y) = 0.023\, f_{r_0}^{(i)}\, r_0^{(i)\,-5/3} \left(f_x^2 + f_y^2\right)^{-11/6}, \quad \text{for} \quad i = 1, 2, 3, \ldots, n. \tag{A.25}$$

where r_0 is the reference Fried parameter, and $\mathrm{f}_{r_0}^{(i)}$ is the fractional contribution of the PSD strength for the i-th atmospheric layer, sometimes called the fractional r_0, Cn^2, or Cn^2 distribution. It is important to ensure that $\sum_{i=1}^{n} \mathrm{f}_{r_0}^{(i)} = 1$ to preserve the total turbulence strength in the summed PSD over all included layers.

The wind-induced motion of each layer is determined by the wind speed and sampling rate, which influences how much the grid moves between frames. For the i-th atmospheric layer, the change in the grid location $\Delta\text{position}^{(i)}$ is calculated as:

$$\Delta\text{position}^{(i)} = \frac{np}{L} \cdot v_{wind}^{(i)} \cdot \Delta t, \tag{A.26}$$

where np is the number of pixels across the grid, L is the full size of the grid in meters (where $L = D/b_r$, as discussion in §A.2), $v_{wind}^{(i)}$ is the wind speed at the i-th layer, and Δt is the sample or frame rate of the simulation. The grid's positional change in the x- and y-directions is then given by:

$$\Delta\text{position}_x^{(i)} = \Delta\text{position}^{(i)} \cdot \cos(\alpha_{wind}^{(i)}), \tag{A.27}$$

$$\Delta\text{position}_y^{(i)} = \Delta\text{position}^{(i)} \cdot \sin(\alpha_{wind}^{(i)}), \tag{A.28}$$

where $\alpha_{wind}^{(i)}$ is the azimuthal direction of the wind motion in the ith layer in radians. Next, a phase ramp matrix $\hat{\mathrm{P}}^{(i)}$ is constructed by creating a meshed grid with ramping x- and y-directions:

$$[\psi_x^{(i)}, \psi_y^{(i)}] = \text{meshgrid}\left(\left(-\frac{np}{2} : \frac{np}{2} - 1\right) \cdot \Delta\text{position}_x^{(i)}\,, \left(-\frac{np}{2} : \frac{np}{2} - 1\right) \cdot \Delta\text{position}_y^{(i)}\right), \tag{A.29}$$

where,

$$\hat{\mathrm{P}}^{(i)} = \psi_x^{(i)} + \psi_y^{(i)}. \tag{A.30}$$

The phase ramp matrix is then normalized and scaled to the magnitude of the pixel

speed. The frame number k (or sample number) is multiplied in as an integer number to increment the solution by one frame and directly calculate the phase ramp $\mathrm{P}_k^{(i)}$ at sample k for each layer:

$$\mathrm{P}_k^{(i)} = \left(\pi \cdot \Delta\mathrm{position}^{(i)} \cdot k\right) \cdot \frac{\hat{\mathrm{P}}^{(i)}}{\max(\hat{\mathrm{P}}^{(i)})}. \tag{A.31}$$

Finally, the total shifted phase screen ϕ_{total}^k at sample number k is obtained by summing the phase screens from all layers. This is expressed as:

$$\phi_{total}^k(x,y) \;=\; \sum_{i=1}^{n} \left(\mathrm{Re}\left(\mathcal{F}^{-1}\left[\sqrt{\Phi_\phi^{(i)}(f_x,f_y)} \cdot e^{i\theta^{(i)}(f_x,f_y)} \cdot e^{i\cdot \mathrm{P}_k^{(i)}} \right] \right) \cdot \frac{np}{\Delta x} \right), \tag{A.32}$$

where $\Phi_\phi^{(i)}(f_x, f_y)$ is the PSD for the i-th layer, $\mathcal{F}^{-1}$ represents the 2D inverse Fourier transform, $\theta^{(i)}(f_x, f_y)$ are the random phase angles, $e^{i\cdot \mathrm{P}^{(i)}}$ accounts for the wind-induced motion of each layer, and $\frac{np}{\Delta x}$ normalizes the power over the grid. By summing these contributions, this method captures the dynamic, multi-layered nature of atmospheric turbulence. As an example, Figure A.6 implements Equations A.25 through A.32 to simulate a three-layer model using typical atmospheric conditions measured at the summit of Maunakea, a well-used observation site [73, 178].

It is important to consider that the phase ramp will eventually cause the phase screen to wrap around the grid, returning the map to its original position. This will happen every multiple of $\Delta\mathrm{position} = np$, or when $k = L/v_{wind}\Delta t$. A multiple-layer simulation will repeat after the least common multiple of k for each layer i up to n layers:

$$k_{repeat} = \mathrm{lcm}\left(\frac{1}{v_{wind}^{(1)}}, \frac{1}{v_{wind}^{(2)}}, \frac{1}{v_{wind}^{(3)}}, ..., \frac{1}{v_{wind}^{(n)}} \right) \cdot \frac{L}{\Delta t}\ . \tag{A.33}$$

While having multiple layers moving in different directions at different speeds can help create more diverse and longer simulation before errors are repeated, this limitation should be considered if long simulations are required.

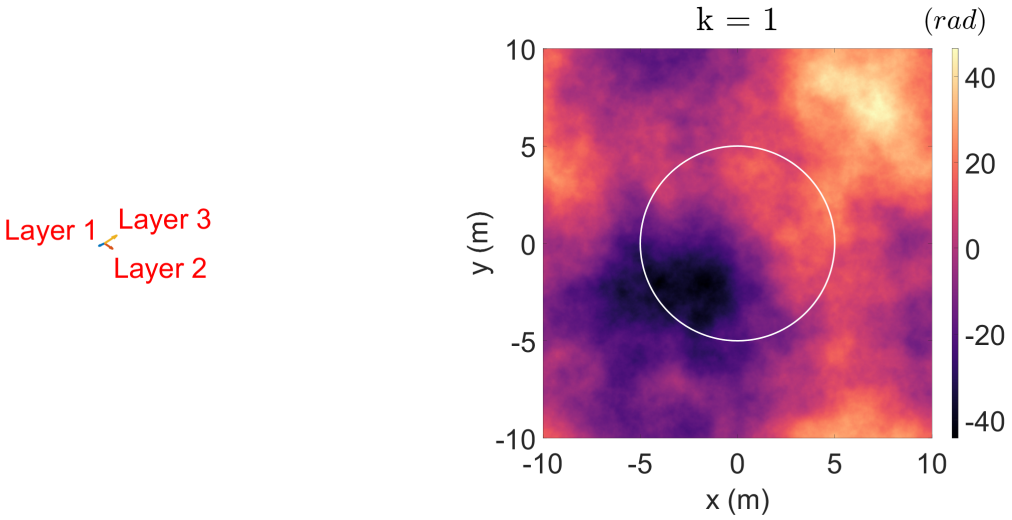

Figure A.6: Animation of a 1-second three-layer Kolmogorov atmosphere simulation over 20 frames at a sampling rate of $\Delta t = 0.05$ s (20 Hz), with arrows showing the direction and distance each layer moves between each sample k. The model is implemented using typical atmospheric conditions measured at the summit of Maunakea [73], such as $\mathrm{f}_{r_0} = [0.59, 0.21, 0.20]$, $v_{wind} = [5.67, 9.94, 14.87]$ m/s, and $\alpha_{wind} = [216.5, 312.8, 46.6] \cdot \frac{\pi}{180^\circ}$ radians. The other simulation parameters remain the same from the single phase screen generated in Figure A.5.

A.3.1 Validating the Atmospheric Turbulence Model

In this section, the methods used to validate the Kolmogorov phase screens generated in §A.3 are presented, ensuring that they accurately capture the stochastic nature of atmospheric turbulence. To assess the realism of the generated phase screens, the variance and standard deviation of the phase error across the aperture is calculated. These statistical metrics provide a quantitative characterization of the phase distortions, enabling comparison with theoretical models. The variance of the phase screen in units of rad^2 is calculated using the following expression:

$$\sigma_\phi^2 = \frac{1}{N_p} \sum_{i=1}^{N_p} (\phi_i - \mu)^2, \tag{A.34}$$

where μ is the mean phase over the aperture, defined as $\mu = \frac{1}{N_p} \sum_{i=1}^{N_p} \phi_i$. In this expression, ϕ_i represents the phase at each grid point, and N_p is the total number of grid points within the aperture. It is important to note that this computation is performed only within the aperture, excluding points outside its boundaries. This

variance quantifies the spread of phase fluctuations across the aperture. The root-mean-square (RMS) phase error, representing the standard deviation of the phase fluctuations, is then expressed as:

$$\sigma_\phi = \mathrm{RMS}_\phi = \sqrt{\sigma_\phi^2}\ . \tag{A.35}$$

The RMS phase error is a standard metric for evaluating the mean optical quality degradation due to turbulence, expressed in radians, but often provided in nanometers if describing optical surface quality of a lens or mirror at a certain wavelength or waveband.

While the theoretical formulation from the Zernike-Kolmogorov residual provide a robust estimate of the expected variance, randomly generated Kolmogorov phase screens will exhibit deviations due to the stochastic nature of their generation. Over many realizations, the mean variance should converge to the theoretical value; however, a substantial fraction of the total phase variance arises from the lowest-order Zernike modes (e.g., piston, tip, tilt, defocus). These modes tend to skew theoretical predictions higher than what is typically observed in practical applications.

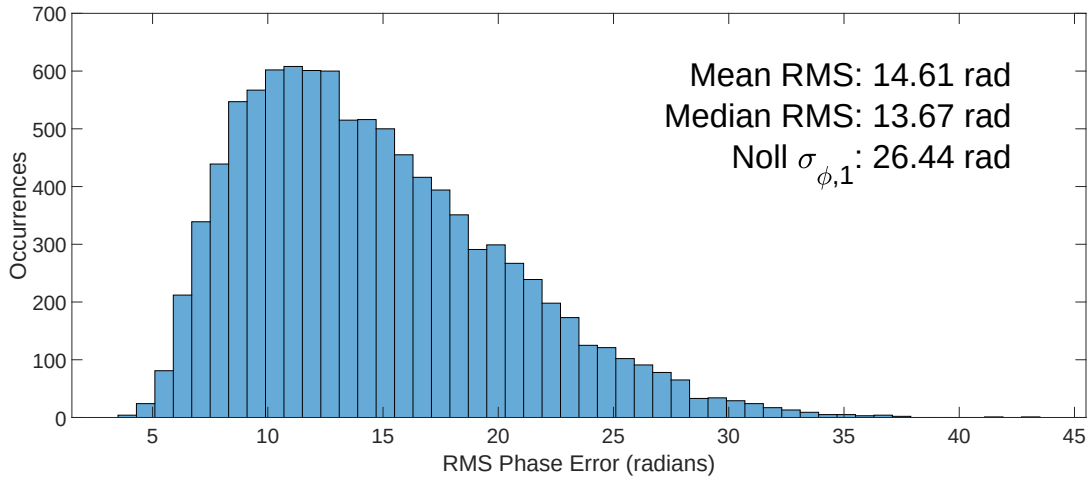

Figure A.7: Binned histogram of RMS phase error across a 10 m pupil for 10,000 randomly generated Kolmogorov phase screens with $r_0 = 20$ cm, after a least-squares fit subtraction of the first Zernike mode (piston). The theoretical RMS given by $\sigma_{\phi,1}$ in Equation 1.46 is nearly double the observed mean RMS, due to the remaining low-order contributions in the theoretical model, which occur infrequently.

To assess the agreement between the simulated phase screens in §A.3 and the-

oretical expectations from Equations 1.46, the RMS phase error was computed for a 10 m aperture with $r_0 = 20$ cm over 10,000 randomly generated piston-removed Kolmogorov phase screens. The results were compiled into a histogram, shown in Figure A.7.

By subtracting piston, tip, and tilt from each phase screen before computing the RMS across the aperture, a more direct comparison can be made with the expected Zernike-Kolmogorov residual phase variance, specifically $\sigma_{\phi,3}$. The corresponding histogram is shown in Figure A.8.

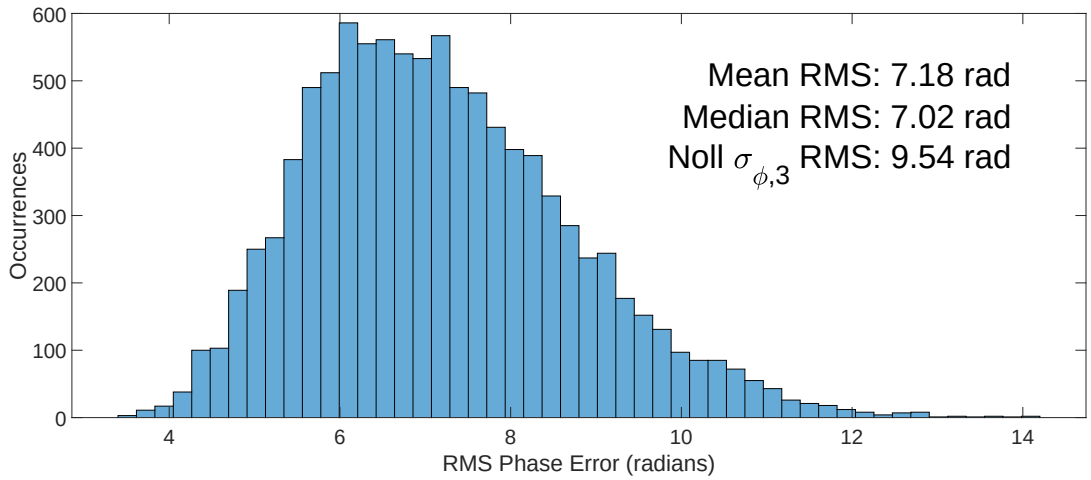

Figure A.8: Binned histogram of RMS phase error across a 10 m pupil for 10,000 randomly generated Kolmogorov phase screens with $r_0 = 20$ cm, after a least-squares fit subtraction of piston, tip, and tilt Zernike modes. The theoretical RMS given by $\sigma_{\phi,3}$ in Equation 1.46 aligns more closely with the observed mean.

To replicate specific turbulence conditions observed in historical data or experimental settings, the Fried parameter r_0 can be adjusted to achieve the desired mean RMS phase error while maintaining the Kolmogorov power spectral density (PSD) structure. Alternatively, the PSD can be tailored to represent distinct spatial frequency distributions, such as those associated with optical polishing errors, coating inconsistencies, or adaptive optics (AO) residuals arising from the finite spatial correction capability of a deformable mirror.

Bibliography

[1] M. C. Turnbull, W. A. Traub, K. W. Jucks, N. J. Woolf, M. R. Meyer, N. Gorlova, M. F. Skrutskie, and J. C. Wilson. Spectrum of a habitable world: Earthshine in the near-infrared. *The Astrophysical Journal*, 644(1):551–565, 2006.

[2] E. S. Douglas, J. R. Males, J. Clark, O. Guyon, J. Lumbres, W. Marlow, and K. L. Cahoy. Laser Guide Star for Large Segmented-aperture Space Telescopes. I. Implications for Terrestrial Exoplanet Detection and Observatory Stability. *The Astronomical Journal*, 157(1):36, January 2019. Publisher: The American Astronomical Society.

[3] Olivier Guyon. Limits of adaptive optics for high-contrast imaging. *The Astrophysical Journal*, 629(1):592, aug 2005.

[4] Michael Perryman. *The Exoplanet Handbook*. Cambridge University Press, 2nd edition, 2018.

[5] A. Lecavelier des Etangs and Jack J. Lissauer. The iau working definition of an exoplanet. *New Astronomy Reviews*, 94:101641, June 2022.

[6] Andrew Fraknoi, David Morrison, and Sidney Wolff. *Astronomy 1e*. OpenStax, 2016.

[7] A. Burrows, M. Marley, W. B. Hubbard, J. I. Lunine, T. Guillot, D. Saumon, R. Freedman, D. Sudarsky, and C. Sharp. A nongray theory of extrasolar giant planets and brown dwarfs. *The Astrophysical Journal*, 491(2):856–875, dec 1997.

[8] Philip S. Muirhead, Julie N. Skinner, Jacqueline Radigan, Amaury Triaud, Christopher Theissen, Daniella Bardalez Gagliuffi, Patrick Tamburo, Adam

Burgasser, Jacqueline Faherty, and Denise Stephens. Searching for exosatellites orbiting l and t dwarfs: Connecting planet formation to moon formation and finding new temperate worlds, 2019.

[9] Andrew Norton and Mariangela Bonavita. The formation of exoplanets. OpenLearn, The Open University, 2024. Adapted from the Open University course S384: Astrophysics of Stars and Exoplanets.

[10] Ravit Helled. On the mass of gas giant planets: Is saturn a failed gas giant? *Astronomy & Astrophysics*, 675:L8, 2023.

[11] S. H. Dole. Habitable planets for man. *Physical Science and Astronomy*, 35:58–72, 1964.

[12] S. S. Huang. *Astrophysics of Red Dwarfs and Planetary Habitability*. Cambridge University Press, Cambridge, UK, 2007.

[13] Ravi Kumar Kopparapu, Ramses Ramirez, James F. Kasting, Vincent Eymet, Tyler D. Robinson, Suvrath Mahadevan, Ryan C. Terrien, Shawn Domagal-Goldman, Victoria Meadows, and Rohit Deshpande. Habitable zones around main-sequence stars: New estimates. *The Astrophysical Journal*, 765(2):131, 2013.

[14] A. L. Shields, S. Ballard, and J. A. Johnson. The habitability of planets orbiting m-dwarf stars. *International Journal of Astrobiology*, 15(1):1–10, 2016.

[15] Mark J. Pecaut and Eric E. Mamajek. Intrinsic colors, temperatures, and bolometric corrections of pre-main-sequence stars. *The Astrophysical Journal Supplement Series*, 208(1):9, 2013.

[16] Z. Eker, V. Bakış, S. Bilir, F. Soydugan, I. Steer, E. Soydugan, H. Bakış, F. Aliçavuş, G. Aslan, and M. Alpsoy. Interrelated main-sequence mass-luminosity, mass-radius and mass-effective temperature relations. *Monthly Notices of the Royal Astronomical Society*, 479(4):5491–5511, 2018.

[17] J. F. Kasting, D. P. Whitmire, and R. T. Reynolds. Habitable zones around main sequence stars. *Icarus*, 101(1):108–128, 1993.

[18] Robert K. Tyson. *Principles of Adaptive Optics*. Academic Press, 1991.

[19] NASA Mission Pages. About the hubble space telescope. `https://www.nasa.gov/mission_pages/hubble/about`, April 2023.

[20] NASA Mission Pages. James webb space telescope. `https://www.nasa.gov/mission_pages/webb/main/index.html`, April 2023.

[21] Olivier Guyon, Brian Kern, Ruslan Belikov, Stuart Shaklan, Andreas Kuhnert, and Amir Giveon. Phase induced amplitude apodization (piaa) coronagraphy: Recent results and future prospects. In *Proceedings of the SPIE*, volume 7731, page 77313G, 2010.

[22] B. Gerard. *Exoplanet Imaging Speckle Subtraction: Current Limitations and a Path Forward*. University of Victoria, Victoria, BC Canada, 2020.

[23] Christian Marois, David Lafrenière, René Doyon, Bruce Macintosh, and Daniel Nadeau. Angular differential imaging: A powerful high-contrast imaging technique. *The Astrophysical Journal*, 641(1):556–564, April 2006.

[24] Katherine B. Follette. An introduction to high contrast differential imaging of exoplanets and disks. *The Astrophysical Journal*, 946(1):1–15, September 2023.

[25] Christian Marois, Bruce Macintosh, Travis Barman, B. Zuckerman, Inseok Song, Jennifer Patience, David Lafreniere, and Rene Doyon. Direct imaging of multiple planets orbiting the star HR 8799. *Science*, 322(5906):1348–1352, nov 2008.

[26] Michel Mayor and Didier Queloz. A jupiter-mass companion to a solar-type star. *Nature*, 378(6555):355–359, 1995.

[27] David Charbonneau, Timothy M. Brown, David W. Latham, and Michel Mayor. Detection of planetary transits across a sun-like star. *The Astrophysical Journal*, 529(1):L45–L48, January 2000.

[28] Gaia Collaboration, F. Arenou, C. Babusiaux, et al. Gaia data release 3: Stellar multiplicity, a teaser for the hidden treasure. *Astronomy & Astrophysics*, 674:A34, 2023.

[29] A. Sozzetti, S. Udry, S. Zucker, G. Torres, J. L. Beuzit, D. W. Latham, M. Mayor, T. Mazeh, D. Naef, C. Perrier, D. Queloz, and J.-P. Sivan. A

massive planet to the young disc star hd 81040. *Astronomy & Astrophysics*, 449:417–424, 2006.

[30] J.-P. Beaulieu, D. P. Bennett, P. Fouqué, A. Williams, M. Dominik, U. G. Jørgensen, D. Kubas, A. Cassan, C. Coutures, J. Greenhill, K. Hill, J. Menzies, P. D. Sackett, M. Albrow, S. Brillant, J. A. R. Caldwell, J. J. Calitz, K. H. Cook, E. Corrales, M. Desort, S. Dieters, D. Dominis, J. Donatowicz, M. Hoffman, S. Kane, J.-B. Marquette, R. Martin, P. Meintjes, K. Pollard, K. Sahu, C. Vinter, J. Wambsganss, K. Woller, K. Horne, I. Steele, D. M. Bramich, M. Burgdorf, C. Snodgrass, M. Bode, A. Udalski, M. K. Szymański, M. Kubiak, T. Wieckowski, G. Pietrzyński, I. Soszyński, O. Szewczyk, L. Wyrzykowski, B. Paczyński, F. Abe, I. A. Bond, T. R. Britton, A. C. Gilmore, J. B. Hearnshaw, Y. Itow, K. Kamiya, P. M. Kilmartin, A. V. Korpela, K. Masuda, Y. Matsubara, M. Motomura, Y. Muraki, S. Nakamura, C. Okada, K. Ohnishi, N. J. Rattenbury, T. Sako, S. Sato, M. Sasaki, T. Sekiguchi, D. J. Sullivan, P. J. Tristram, P. C. M. Yock, and T. Yoshioka. Discovery of a cool planet of 5.5 earth masses through gravitational microlensing. *Nature*, 439(7075):437–440, January 2006.

[31] Matthew J. Holman, Daniel C. Fabrycky, Darin Ragozzine, Eric B. Ford, Jason H. Steffen, William F. Welsh, Jack J. Lissauer, David W. Latham, Geoffrey W. Marcy, Lucianne M. Walkowicz, Natalie M. Batalha, Jon M. Jenkins, Jason F. Rowe, William D. Cochran, François Fressin, Guillermo Torres, Lars A. Buchhave, Dimitar D. Sasselov, William J. Borucki, David G. Koch, Gibor Basri, Timothy M. Brown, Douglas A. Caldwell, David Charbonneau, Edward W. Dunham, Thomas N. Gautier, John C. Geary, Ronald L. Gilliland, Michael R. Haas, Steve B. Howell, Ivan R. Linscott, Pavel Machalek, Sara Seager, Susan E. Thompson, Jeffrey Van Cleve, Joshua N. Winn, and Jerome A. Orosz. Kepler-9: A system of multiple planets transiting a sun-like star, confirmed by timing variations. *Science*, 330(6000):51–54, October 2010.

[32] Maxwell A. Millar-Blanchaer, James R. Graham, Laurent Pueyo, Paul Kalas, Rebekah I. Dawson, Jason Wang, Marshall D. Perrin, Dae-Sik Moon, Bruce Macintosh, S. Mark Ammons, Travis Barman, Andrew Cardwell, Christine H. Chen, Eugene Chiang, Jeffrey Chilcote, Tara Cotten, Robert J. De Rosa, Zachary H. Draper, Jennifer Dunn, Gaspard Duchêne, Thomas M. Esposito,

Michael P. Fitzgerald, Katherine B. Follette, Stephen J. Goodsell, Alexandra Z. Greenbaum, Markus Hartung, Pascale Hibon, Sasha Hinkley, Patrick Ingraham, Rebecca Jensen-Clem, Quinn Konopacky, James E. Larkin, Douglas Long, Jérôme Maire, Franck Marchis, Mark S. Marley, Christian Marois, Katie M. Morzinski, Eric L. Nielsen, David W. Palmer, Rebecca Oppenheimer, Lisa Poyneer, Abhijith Rajan, Fredrik T. Rantakyrö, Jean-Baptiste Ruffio, Naru Sadakuni, Leslie Saddlemyer, Adam C. Schneider, Anand Sivaramakrishnan, Remi Soummer, Sandrine Thomas, Gautam Vasisht, David Vega, J. Kent Wallace, Kimberly Ward-Duong, Sloane J. Wiktorowicz, and Schuyler G. Wolff. Beta pictoris' inner disk in polarized light and new orbital parameters for beta pictoris b. *The Astrophysical Journal*, 811(1):18, September 2015.

[33] Laura Alderson et al. Early release science of the exoplanet wasp-39b with jwst nirspec prism: Detection of atmospheric water and constraints on cloud properties. *Nature*, 614:664–669, 2023.

[34] NASA exoplanet archive, Apr 2024. `https://exoplanetarchive.ipac.caltech.edu/cgi-bin/TblView/nph-tblView?app=ExoTbls&config=PSCompPars`, Accessed on 30-04-2024.

[35] Leah Hustak (STScI) NASA, ESA. Illustration of transmission spectrum of an earth-like atmosphere. `https://webbtelescope.org/contents/media/images/01F8GF9XGA29AD3QWNPNKMPD1W`, 2021. Accessed: 2025-01-11.

[36] John H. Debes, Bin Ren, and Glenn Schneider. Pushing the limits of the coronagraphic occulters on hubble space telescope/space telescope imaging spectrograph. *Journal of Astronomical Telescopes, Instruments, and Systems*, 5(3):035003, 2019.

[37] Gemini Planet Imager Exoplanet Survey. Gpi. `http://planetimager.org/`, April 2023.

[38] Lawrence Livermore National Laboratory. Gemini planet imager, 2016. Accessed: 2025-03-03.

[39] European Southern Observatory. Sphere - spectro-polarimetric high-contrast exoplanet research. `https://www.eso.org/sci/facilities/paranal/instruments/sphere.html`, April 2023.

[40] J. L. Beuzit, A. Vigan, D. Mouillet, K. Dohlen, R. Gratton, A. Boccaletti, J. F. Sauvage, H. M. Schmid, M. Langlois, C. Petit, A. Baruffolo, M. Feldt, J. Milli, Z. Wahhaj, L. Abe, U. Anselmi, J. Antichi, R. Barette, J. Baudrand, P. Baudoz, A. Bazzon, P. Bernardi, P. Blanchard, R. Brast, P. Bruno, T. Buey, M. Carbillet, M. Carle, E. Cascone, F. Chapron, J. Charton, G. Chauvin, R. Claudi, A. Costille, V. De Caprio, J. de Boer, A. Delboulbé, S. Desidera, C. Dominik, M. Downing, O. Dupuis, C. Fabron, D. Fantinel, G. Farisato, P. Feautrier, E. Fedrigo, T. Fusco, P. Gigan, C. Ginski, J. Girard, E. Giro, D. Gisler, L. Gluck, C. Gry, T. Henning, N. Hubin, E. Hugot, S. Incorvaia, M. Jaquet, M. Kasper, E. Lagadec, A. M. Lagrange, H. Le Coroller, D. Le Mignant, B. Le Ruyet, G. Lessio, J. L. Lizon, M. Llored, L. Lundin, F. Madec, Y. Magnard, M. Marteaud, P. Martinez, D. Maurel, F. Ménard, D. Mesa, O. Möller-Nilsson, T. Moulin, C. Moutou, A. Origné, J. Parisot, A. Pavlov, D. Perret, J. Pragt, P. Puget, P. Rabou, J. Ramos, J. M. Reess, F. Rigal, S. Rochat, R. Roelfsema, G. Rousset, A. Roux, M. Saisse, B. Salasnich, E. Santambrogio, S. Scuderi, D. Segransan, A. Sevin, R. Siebenmorgen, C. Soenke, E. Stadler, M. Suarez, D. Tiphène, M. Turatto, S. Udry, F. Vakili, L. B. F. M. Waters, L. Weber, F. Wildi, G. Zins, and A. Zurlo. SPHERE: the exoplanet imager for the Very Large Telescope. , 631:A155, November 2019.

[41] PAUL PETER URONE and ROGER HINRICHS. *College physics for AP® courses 2E*. Openstax, 2 edition, 2022.

[42] A. Boccaletti, P.-O. Lagage, P. Baudoz, C. Beichman, P. Bouchet, C. Cavarroc, D. Dubreuil, Alistair Glasse, A. M. Glauser, D. C. Hines, C.-P. Lajoie, J. Lebreton, M. D. Perrin, L. Pueyo, J. M. Reess, G. H. Rieke, S. Ronayette, D. Rouan, R. Soummer, and G. S. Wright. The mid-infrared instrument for theijames webb space telescope/i, v: Predicted performance of the MIRI coronagraphs. *Publications of the Astronomical Society of the Pacific*, 127(953):633–645, jul 2015.

[43] Johnny P. Greco and Adam Burrows. The direct detectability of giant exoplanets in the optical. *The Astrophysical Journal*, 808(2):172, jul 2015.

[44] Nikku Madhusudhan and Adam Burrows. ANALYTIC MODELS FOR ALBEDOS PHASE CURVESAND POLARIZATION OF REFLECTED LIGHT FROM EXOPLANETS. *The Astrophysical Journal*, 747(1):25, feb 2012.

[45] Roderick De Cock, Timothy A. Livengood, Daphne M. Stam, Carey M. Lisse, Tilak Hewagama, and L. Drake Deming. Terrestrial planet optical phase curves. i. direct measurements of the earth. *The Astronomical Journal*, 163(1):5, dec 2021.

[46] Planet compare – nasa solar system exploration, Jan 2018.

[47] David S. Spiegel and Adam Burrows. SPECTRAL AND PHOTOMETRIC DIAGNOSTICS OF GIANT PLANET FORMATION SCENARIOS. *The Astrophysical Journal*, 745(2):174, jan 2012.

[48] Adam Burrows, W. B. Hubbard, J. I. Lunine, and James Liebert. The theory of brown dwarfs and extrasolar giant planets. *Reviews of Modern Physics*, 73(3):719–765, sep 2001.

[49] Thayne Currie, Beth Biller, Anne-Marie Lagrange, Christian Marois, Olivier Guyon, Eric Nielsen, Mickael Bonnefoy, and Robert De Rosa. Direct imaging and spectroscopy of extrasolar planets, 2022.

[50] OpenStax. *University Physics Volume 3*. OpenStax, 1st edition, 2020.

[51] Martin Harwit. *Astrophysical Concepts*. Springer, New York, 4th edition, 2006.

[52] NASA Goddard Space Flight Center. The sun: Facts and figures, n.d. Accessed: 2025-01-06.

[53] Dr. David R. Williams. Moon fact sheet, 2024. Accessed: 2025-03-05.

[54] NASA Exoplanet Archive. Stellar hosts table, 2023. Accessed: 2025-03-05.

[55] Christopher N. A. Willmer. The absolute magnitude of the sun in several filters. *The Astrophysical Journal Supplement Series*, 236(2):47, 2018.

[56] L. Colina, R. Bohlin, and F. Castelli. Absolute flux calibrated spectrum of vega. *The Astrophysical Journal*, 458:L1–L4, 1996. April 22, 1996.

[57] W. M. Keck Observatory. Hires (high resolution echelle spectrometer), 2020. Accessed: 2025-03-06.

[58] Space Telescope Science Institute. *JWST Near Infrared Spectrograph*, 2023. Accessed: 2025-03-06.

[59] L. Drissen, A.-P. Bernier, L. Rousseau-Nepton, A. Alarie, C. Robert, G. Joncas, S. Thibault, and F. Grandmont. SITELLE: a wide-field imaging Fourier transform spectrometer for the Canada-France-Hawaii Telescope. In Ian S. McLean, Suzanne K. Ramsay, and Hideki Takami, editors, *Ground-based and Airborne Instrumentation for Astronomy III*, volume 7735, page 77350B. International Society for Optics and Photonics, SPIE, 2010.

[60] Christian Marois, Olivier Lardière, William Thompson, Garima Singh, Adam Johnson, Tim Hardy, Joeleff Fitzsimmons, Benjamin Gerard, Suresh Sivanandam, Simon Thibault, Dmitry Savranksy, Colin Bradley, Rebecca Jensen-Clem, Mathieu Demers, Qiang Fu, Wolfgang Heidrich, and Mamadou N'Diaye. Deployment of focal plane wfs technologies on 8-m telescopes: from the subaru spiders pathfinder, to the facility-class gpi 2.0 cal2 system. volume 12185-70, 2022.

[61] National Astronomical Observatory of Japan. Mkid exoplanet camera (mec), 2025. Accessed: 2025-03-06.

[62] C.R. Kitchin. *Astrophysical Techniques*. CRC Press, Boca Raton, 7th edition, 2023.

[63] Steve B. Howell. *Handbook of CCD Astronomy*. Cambridge University Press, Cambridge, UK, 2nd edition, 2006. Based on work at the National Optical Astronomy Observatory and WIYN Observatory.

[64] Samuel W. Hasinoff. Photon, poisson noise. Technical report, Google Inc., 2012. Preprint.

[65] John W. Hardy. *Adaptive Optics for Astronomical Telescopes*. Oxford University Press, Oxford, 1998.

[66] Kyohoon Ahn, Olivier Guyon, Julien Lozi, and Alison Wong. Scexao: a testbed for developing high-contrast imaging technologies for elts. In *Techniques and Instrumentation for Detection of Exoplanets X*. SPIE, 2021. Conference Proceedings.

[67] Lindsey Payne, Robert T. Zellem, Marie Ygouf, and Bruce Macintosh. Absolute flux calibrations for the nancy grace roman space telescope coronagraph instrument. *arXiv*, July 2022.

[68] Joseph W. Goodman. *Introduction to Fourier Optics*. Roberts and Company Publishers, Greenwood Village, CO, 3rd edition, 2005.

[69] Sander Konijnenberg, Aurèle J.L. Adam, and H. Paul Urbach. *BSc Optics*. Delft University of Technology, 2017. Ch6.4, Ch6.6. Accessed: 2024-12-25.

[70] James W. Cooley, Peter A. W. Lewis, and Peter D. Welch. Historical notes on the fast fourier transform. *IEEE Transactions on Audio and Electroacoustics*, 15:76–79, 1967.

[71] Anna Bounchaleun. An elementary introduction to fast fourier transform algorithms. *Unpublished manuscript*, 1995. Accessed from: `https://www.math.cmu.edu/~bounchal/papers/fft.pdf`.

[72] Robert J Noll. Zernike polynomials and atmospheric turbulence. *Journal of the Optical Society of America*, 66(3):207–211, 1976.

[73] R. Dekany. Mauna kea ridge (mkr) turbulence models. Technical Note 503, Keck Adaptive Optics, November 2007. Original version: August 13, 2007; Revised Version 1.1.

[74] Geoffrey Ingram Taylor. The spectrum of turbulence. *Proceedings of the Royal Society of London. Series A-Mathematical and Physical Sciences*, 164(919):476–490, 1938.

[75] Olivier Guyon. Limits of adaptive optics for high-contrast imaging. *The Astrophysical Journal*, 629(1):592–614, 2005. Received 2005 February 23; accepted 2005 April 14.

[76] J. Mazoyer, P. Baudoz, R. Galicher, M. Mas, and G. Rousset. Estimation and correction of wavefront aberrations using the self-coherent camera: Laboratory results. *Astronomy & Astrophysics*, 557:A9, 2013.

[77] Andrew Romero-Wolf, Geoffrey Bryden, Sara Seager, N. Jeremy Kasdin, Jeff Booth, Matt Greenhouse, Doug Lisman, Bruce Macintosh, Stuart Shaklan, Melissa Vess, Steve Warwick, David Webb, John Ziemer, Andrew Gray, Michael Hughes, Greg Agnes, Jonathan W. Arenberg, S. Case Bradford, Michael Fong, Jennifer Gregory, Steve Matousek, Jason Rhodes, Phil Willems, Simone D'Amico, John Debesh, Shawn Domagal-Goldman, Sergi Hildebrandt, Renyu

Hua, Alina Kiessling, Nikole Lewis, Maxime Rizzo, Aki Roberg, Tyler Robinson, Leslie Rogers, Dmitry Savransky, and Chris Stark. Starshade rendezvous: Exoplanet sensitivity and observing strategy. *Proceedings of the National Academy of Sciences*, 122(10), 2025.

[78] Christian Marois, René Racine, René Doyon, David Lafrenière, and Daniel Nadeau. Differential imaging with a multicolor detector assembly: A new exoplanet finder concept. *The Astrophysical Journal*, 615(2):L61–L64, November 2004.

[79] William Thompson, Adam Johnson, Christian Marois, Olivier Lardière, and Tim Hardy. High-spectral resolution dark holes: Concept, results, and promise. In *Adaptive Optics for Extremely Large Telescopes 7*, 2023.

[80] Christian Marois, René Doyon, René Racine, and Daniel Nadeau. Efficient speckle noise attenuation in faint companion imaging. *Publications of the Astronomical Society of the Pacific*, 112(769):91–96, January 2000.

[81] Pierre Baudoz and Raphaël Galicher. Expected performance of a self-coherent camera. *Proceedings of the International Conference on Adaptive Optics for Extremely Large Telescopes*, pages 553–556, 2006.

[82] Raphaël Galicher, Pierre Baudoz, and Gérard Rousset. Wavefront error correction and earth-like planet detection by a self-coherent camera in space. *Astronomy & Astrophysics*, 488:L9–L12, 2008.

[83] Raphaël Galicher, Pierre Baudoz, Gérard Rousset, Julien Totems, and Marion Mas. Self-coherent camera as a focal plane wavefront sensor: simulations. *Astronomy & Astrophysics*, 509:A31, 2010.

[84] Benjamin L. Gerard, Christian Marois, and Raphaël Galicher. Fast coherent differential imaging on ground-based telescopes using the self-coherent camera. *Astronomical Journal*, 156(2):66, 2018.

[85] Steffen Mauch and Johann Reger. Real-time spot detection and ordering for a shack–hartmann wavefront sensor with a low-cost fpga. *IEEE Transactions on Instrumentation and Measurement*, 63(10):2379–2386, 2014.

[86] Roberto Ragazzoni. Pupil plane wavefront sensing with an oscillating prism. *Journal of Modern Optics*, 43(2):289–293, 1996.

[87] Anna Burvall, Elizabeth Daly, Stéphane R. Chamot, and Christopher Dainty. Linearity of the pyramid wavefront sensor. *Opt. Express*, 14(25):11925–11934, Dec 2006.

[88] Olivier Lardière, John Pazder, Jean-Pierre Véran, and Maaike van Kooten. Double-pyramid wavefront sensors: Tolerance relaxation and cheaper alternatives using achromatic double-roof prisms. In *Proceedings of the Adaptive Optics for Extremely Large Telescopes 5 (AO4ELT5)*, January 2017.

[89] Victoria Hutterer, Ronny Ramlau, and Iuliia Shatokhina. Real-time adaptive optics with pyramid wavefront sensors: Accurate wavefront reconstruction using iterative methods. *arXiv preprint arXiv:1809.10888*, October 2018.

[90] Iuliia Shatokhina, Victoria Hutterer, and Ronny Ramlau. Review on methods for wavefront reconstruction from pyramid wavefront sensor data. *Journal of Astronomical Telescopes, Instruments, and Systems*, 6(1):010901, 2020.

[91] William Thompson, Garima Singh, Christian Marois, Olivier Lardière, Qiang Fu, Wolfgang Heidrich, and Benjamin Gerard. Performance of the fast self coherent camera at the new-earth lab and simplified scc measurement algorithm. volume 12185-84, 2022.

[92] Raphaël Galicher and Johan Mazoyer. Imaging exoplanets with coronagraphic instruments. *Comptes Rendus. Physique*, 24(S2):1–45, 2023.

[93] Kate Jackson, Uriel Conod, Maaike A. van Kooten, Jean-Pierre Véran, Jennifer Dunn, Olivier Lardière, Tarun Kumar, Edward Chapin, and Jacob Taylor. Revolt: An on-sky adaptive optics technology research platform on a 1.2m telescope. In H. Friedman, J. Korkiakoski, J. Korkiakoski, and E. Pinna, editors, *Adaptive Optics Systems IX*, volume 13097, page 1309705. SPIE, 2024.

[94] John E. Krist. PROPER: an IDL optical propagation library. In *Proceedings of SPIE - The International Society for Optical Engineering*, volume 6675, Orlando, FL, USA, September 2007. SPIE. Paper 6675-36.

[95] Thorlabs, Inc. MEMS-Based Deformable Mirrors, 2025. Accessed: 2025-02-19.

[96] Boston Micromachines Corporation. Standard deformable mirrors, 2020. Accessed: 2025-02-19.

[97] ALPAO. Deformable mirrors, 2023. Accessed: 2025-02-19.

[98] Julien Lozi, Olivier Guyon, Sebastien Vievard, Vincent Deo, Michael Bottom, Yoshito Ono, Yusuke Minowa, Takashi Hattori, Yutaka Hayano, Miles Lucas, and Manon Lallement. AO3k at Subaru: First on-sky results of the facility extreme-AO. In Kathryn J. Jackson, Dirk Schmidt, and Elise Vernet, editors, *Adaptive Optics Systems IX*, volume 13097, page 1309703. International Society for Optics and Photonics (SPIE), 2024.

[99] Sam Potier, Justin Crepp, and Stanimir Letchev. Developing an error budget for the nonlinear curvature wavefront sensor. *arXiv preprint arXiv:2312.01465*, 2023. Accessed: 2025-04-07.

[100] Szymon Gladysz, Julian C. Christou, L. William Bradford, and Lewis C. Jr Roberts. Temporal variability and statistics of the strehl ratio in adaptive-optics images. *Publications of the Astronomical Society of the Pacific*, 120(872):1132–1141, 2008.

[101] Virendra N. Mahajan. Strehl ratio for primary aberrations: Some analytical results for circular and annular pupils. *Journal of the Optical Society of America*, 73(6):860–865, 1983. Received February 9, 1982.

[102] Benjamin L. Gerard and Christian Marois. Focal plane wavefront sensing with the fast tgv coronagraph. *Publications of the Astronomical Society of the Pacific*, 132:64401, 4 2020.

[103] Olivier Lardière, Christian Marois, Adam Johnson, William Thompson, Joeleff Fitzsimmons, Tim Hardy, Neal Kelly, Scott Macdonald, Garima Singh, Mamadou N'diaye, Qiang Fu, and Wolfgang Heidrich. Design, integration and tests of spiders: a subaru pathfinder instrument for detecting exoplanets & retrieving spectra. In *Adaptive Optics for Extremely Large Telescopes 7*, 2023.

[104] Subaru Telescope NAOJ. Faq for young astronomers: How does the subaru telescope observe astronomical objects? `https://subarutelescope.org/en/Kids/faq.html`, April 2023.

[105] William Thompson. *Lights in Motion: Observing Nearby Planets with Imaging, Wavefront Sensing, Orbital Detection, and Spectroscopy.* Phd dissertation,

University of Victoria, Victoria, British Columbia, Canada, April 2023. Supervisors: Christian Marois and Falk Herwig.

[106] Olivier Lardière, Christian Marois, William Thompson, Garima Singh, Adam Johnson, Joeleff Fitzsimmons, Tim Hardy, Mamadou N'Diaye, Wolfgang Heidrich, Qiang Fu, Denis Brousseau, and Simon Thibault. Optical design of spiders, a subaru pathfinder instrument for detecting exoplanets & retrieving spectra. volume 12185-156 of *Proc. SPIE*, 2022.

[107] Garima Singh, William Thompson, Olivier Lardière, Christian Marois, Mamadou N'Diaye, Adam Johnson, Jean-Pierre Véran, Glen Herriot, Benjamin Gerard, Qiang Fu, and Wolfgang Heidrich. Pupil-plane llowfs simulation and laboratory results from new-earth's high-contrast imaging testbed. volume 12185-192, 2022.

[108] WorkSafeBC. Occupational Health and Safety Regulation: Part 15 – Rigging, Amended by B.C. 312/2003, effective October 29, 2003. Accessed: 2025-04-30.

[109] American Society of Mechanical Engineers (ASME). *ASME B30.26-2015: Rigging Hardware*. ASME, New York, NY, 2015 edition, 2015. Approved by ANSI on August 6, 2015.

[110] Warren C. Young, Richard G. Budynas, and Ali M. Sadegh. *Roark's Formulas for Stress and Strain*. McGraw-Hill Education, New York, 8 edition, 2011.

[111] Athanasios A. Markou, Serenay Elmas, and Günther H. Filz. Revisiting stewart–gough platform applications: A kinematic pavilion. *Engineering Structures*, 249:113304, 2021.

[112] Tae-Young Lee and Jae-Kyung Shim. Algebraic elimination-based real-time forward kinematics of the 6-6 stewart platform with planar base and platform. In *Proceedings of the 2001 IEEE International Conference on Robotics and Automation (Cat. No. 01CH37164)*, volume 2, pages 1301–1306, Seoul, Korea, May 2001. IEEE.

[113] Andreas Müller. Manipulability and static stability of parallel manipulators. *Multibody System Dynamics*, 9(1):1–23, 2003.

[114] Thorlabs Inc. *Optical Chopper System, 120 VAC*, 5 2016. `https://www.thorlabs.com/thorproduct.cfm?partnumber=MC2000B`.

[115] Newport Corporation. *Phase Locked Optical Chopper*, 2014. https://www.newport.com/p/3502.

[116] Garima Singh, Frantz Martinache, Pierre Baudoz, Olivier Guyon, Taro Matsuo, Nemanja Jovanovic, and Christophe S. Clergeon. Lyot-based low order wavefront sensor for phase-mask coronagraphs: Principle, simulations and laboratory experiments. *Publications of the Astronomical Society of the Pacific*, 126:586–594, 2014.

[117] Olivier Lardière, Benjamin Gerard, William Thompson, Christian Marois, Jean-Pierre Véran, Celia Blain, Wolfgang Heidrich, and Qiang Fu. Optical design and preliminary results of new earth, first canadian high-contrast imaging laboratory test bench. page 282, 12 2020.

[118] Mamadou N'Diaye, Laurent Pueyo, and Rémi Soummer. Apodized pupil lyot coronagraphs for arbitrary apertures. iv. reduced inner working angle and increased robustness to low-order aberrations. *The Astrophysical Journal*, 799, 12 2014.

[119] Christian Marois, B. Gerard, O. Lardière, A. Anthony, C. Bradley, J. Dunn, Q. Fu, T. Hardy, W. Heidrich, G. Herriot, E. Nielsen, S. Sivanandam, D. Sivransky, S. Thibault, W. Thompson, and J.-P. Véran. Upgrading the gemini planet imager calibration unit with a photon counting focal plane wavefront sensor. 11448:1366–1376, 2020.

[120] Applied Motion Products. *TSM11Q-1RM - NEMA 11 StepSERVO™ Integrated Motor w/ Q Programming & Modbus RTU*, 6 2019. Rev. E.

[121] Applied Motion Products. *Applied Motion Products Step Motor Life & Reliability*. https://www.applied-motion.com/sites/default/files/Stepper%20Motor%20Life%20data-110817.pdf.

[122] Olivier Lardière, Benjamin L. Gerard, William Thompson, Christian Marois, Jean-Pierre Véran, Célia Blain, Wolfgang Heidrich, and Qiang Fu. Optical design and preliminary results of new earth, first canadian high-contrast imaging laboratory test bench. *Adaptive Optics Systems VII*, 2020.

[123] Overview of the subaru telescope. Accessed 2023.

[124] Ftpa2000-300 ft-nir process analyzer, abb.

[125] Mark A. Zumberge, Jonathan Berger, Matthew A. Dzieciuch, and Robert L. Parker. Resolving quadrature fringes in real time. *Applied Optics*, 43(4):771, 2004.

[126] Mark A Zumberge, Jonathan Berger, Robert L Parker, and Matthew Dzieciuch. Resolving quadrature fringes of interferometer signals in real time, 5 2007. US Patent: US7224463B1.

[127] Christopher R. Kitchin. *Optical astronomical spectroscopy*. Inst. of Physics Publ., 1995. Ch8.7 Fourier Transform Spectroscope (Michelson Interferometer).

[128] muqian wen and John Houlihan. *Application of the non-uniform fourier transform to non-uniformly sampled Fourier transform spectrometers*, 2023.

[129] Superk compact supercontinuum white light laser, nkt photonics, 5 2023.

[130] C-red 2: Very high speed ultra low dark scientific ingaas infrared camera, first light, 10 2023.

[131] Christian Marois, Olivier Lardière, Joeleff Fitzsimmons, Mathieu Demers, Adam B. Johnson, Saugata Dutt, Patrick Nkwari, Benjamin Gerard, Jennifer Dunn, Duan Li, Qiang Fu, Denis Brousseau, Suresh Sivanandam, William Thompson, Christopher Mann, Garima Singh, Marc-André Boucher, Tim Hardy, Krzysztof Caputa, Simon Thibault, Dmitry Savransky, Wolfgang Heidrich, Maaike van Kooten, Jean-Pierre Véran, Rebecca Jensen-Clem, Darryl Gamroth, Colin Bradley, Sanjana Rawat, Öykü S. Galvan, Glen Herriot, and Jean-Thomas Landry. CAL2: Project update of the NRC Canada facility-class focal plane wavefront sensor for the Gemini Planet Imager 2 upgrade. In *Proceedings of SPIE*, volume 13097, pages 13097–07, Bellingham, WA, 2024. SPIE. Presented at the SPIE Astronomical Telescopes + Instrumentation 2024 conference, Yokohama, Japan.

[132] Edward L. Chapin, Jennifer Dunn, Dan Kerley, Lianne Mueller, Malcolm Smith, and Jonathan Stocks. HEART: automated build and test infrastructure for real-time controller development. In *Proceedings of SPIE - Software and Cyberinfrastructure for Astronomy VIII*, volume 13101, page 131013H. SPIE,

2024. Presented at SPIE Astronomical Telescopes + Instrumentation, Yokohama, Japan, 25 July 2024.

[133] Nye Lubricants, Inc. NyeBar® – Barrier Films. https://www.nyelubricants.com/nyebar. Accessed: 2025-05-16.

[134] Socomore. Aeroglaze Z306 – Absorptive Polyurethane Coating. https://www.socomore.com/en/aeroglaze-z306-quart.html. Accessed: 2025-05-16.

[135] Nicola Baccilieri and Giorgio Savini. A review of absorptive materials for mid and far-infrared instrumentation. In *Far Infrared Space Interferometer Critical Assessment – 3rd Workshop: Bringing Far Infrared Interferometry Into Vision*, December 2015. Poster presentation.

[136] Fomblin ut18 grease (100 gram). https://www.timeconnectioninc.com/products/fomblin-ut18-grease-100-gram-1. Accessed: 2025-05-20.

[137] Armstrong a-12 adhesive 4oz kit. https://www.silmid.com/adhesives/epoxy-adhesives/armstrong-a-12-adhesive-4oz-kit/. Accessed: 2025-05-20.

[138] U.S. Government Accountability Office. *James Webb Space Telescope: Opportunity Nears to Provide Additional Assurance That Project Can Meet New Cost and Schedule Commitments*. March 2019. https://www.gao.gov/products/gao-19-189, Accessed on 2024-03-08.

[139] *Financial Statements*. September 2024. https://www.keckobservatory.org/about/library/, Accessed on 2024-03-08.

[140] A. H. Greenaway. Satellite borne laser for adaptive optics reference. In *Proc. Space Astronomical Telescopes and Instruments*, volume 1494. International Society for Optics and Photonics (SPIE), 1991.

[141] W. Alan Navar Marlow, A. Carlton, H. Yoon, J. Clark, C. Haughwout, K. Cahoy, J. Males, L. Close, and K. Morzinski. Laser guidestar satellite for ground-based adaptive optics imaging of geosynchronous satellites. In *Advanced Maui Optical and Space Surveillance Technologies Conference*, page 99, 2016.

[142] William Thompson and Christian Marois. Extremely bright orbital guide beacons for extremely large telescopes. Adaptive Optics for Extremely Large Telescopes 6 (AO4ELT6), 2019.

[143] Eliad Peretz, Christine Hamilton, John C Mather, Lucas Pabarcius, Kevin Hall, Adam Michaels, Robert Pritchett, Wayne Yu, Peter Wizinowich, and Eric Golliher. Orcas–orbiting configurable artificial star mission architecture. In *UV/Optical/IR Space Telescopes and Instruments: Innovative Technologies and Concepts X*, volume 11819, pages 26–40. SPIE, 2021.

[144] Adam B. Johnson, Christian Marois, William Thompson, Kate Jackson, Jean-Pierre Véran, Maaike A. van Kooten, Olivier Lardière, Darryl Gamroth, and Colin Bradley. An optical feasibility study for starlite: Superluminous tomographic atmospheric reconstruction with laser-beacons for imaging terrestrial exoplanets. volume 13097-161, 2024.

[145] Cal Poly SLO. Cubesat design specification. `https://www3.nasa.gov/sites/default/files/atoms/files/cubesatdesignspecificationrev14_12022-02-09.pdf`, Accessed on 2024-03-08.

[146] NASA. Pioneers solicitation. `https://nspires.nasaprs.com/external/viewrepositorydocument/cmdocumentid=747257/solicitationId=%7B0E11C629-2FB1-CF8B-15AA-744BB8CC5D86%7D/viewSolicitationDocument=1/D.16%20Pioneers%20Amend%2054%20Fire%20delay.pdf`, Accessed on 2024-03-08.

[147] Bill Nelson. 2022 NASA strategic plan. 2022.

[148] Read "pathways to discovery in astronomy and astrophysics for the 2020s" at NAP.edu. `https://nap.nationalacademies.org/read/26141/chapter/1`, Accessed on 2024-03-08.

[149] Eric Mamajek and Karl Stapelfeldt. NASA exoplanet exploration program (ExEP) mission star list for the habitable worlds observatory (2023).

[150] Canada-France-Hawaii Telescope (CFHT). ESPaDOnS Processed Data, 2009. "`https://www.cfht.hawaii.edu/Instruments/Spectroscopy/Espadons/CLASSICAL`, Accessed on 2024-03-08, Principal Investigator: Gregg Wade, Run ID: 09BC15.

[151] TESS orbit design – TESS | spaceflight101, 2024. https://spaceflight101.com/tess/tess-orbit-design/, Accessed on 2024-03-08.

[152] SpaceX. Smallsat rideshare program, 2024. https://www.spacex.com/rideshare/, Accessed on 2024-03-08.

[153] ArianeSpace. Ariane 6: Access to space for all applications under the best conditions!, 2024. https://www.arianespace.com/vehicle/ariane-6/, Accessed on 2024-03-08.

[154] Katherine Bair, John Reed, Marcus Nichols, and George Budris. Ula vulcan centaur – next generation multi manifesting for low-cost access to space, 2024. https://www.ulalaunch.com/docs/default-source/rideshare/ascend-2021-vulcan-centaur---next-gen-multi-manifesting-for-low-cost-access-pdf, Accessed on 2024-03-08.

[155] ExoLaunch. Ariane 6: Access to space for all applications under the best conditions!, 2024. https://www.arianespace.com/vehicle/ariane-6/, Accessed on 2024-03-08.

[156] Maverick Space Systems. Hardware: Seperation systems, 2024. https://www.maverickspace.com/hardware/, Accessed on 2024-03-08.

[157] ArianeGroup. Rit 10 evo, 2024. https://www.ariane.group/en/equipment-and-services/satellites-and-spacecraft/rit-10-evo/, Accessed on 2024-03-08.

[158] Nammo Space. Svt01 cold gas thruster, 2024. https://www.nammo.com/product/cold-gas-thruster/, Accessed on 2024-03-08.

[159] Danny Baird. Record-breaking satellite advances nasa's exploration of high-altitude gps. nasa, 2019.

[160] Satlab. SRS-3 s-band transceiver, 2024. https://satlab.com/products/srs-3/, Accessed on 2024-03-08.

[161] Anywaves. S-band TT&c antenna | anywaves, space antenna makers, 2024. https://anywaves.com/products/s-band-ttc-antenna/, Accessed on 2024-03-08.

[162] Scott H. Schaire. Near earth network (NEN) users' guide, 2020. https://ntrs.nasa.gov/citations/20205005784, Accessed on 2024-03-08.

[163] SkyfoxLabs. Active multiband GNSS patch antenna for microsatellites - pipatch-max | satsearch, 2024. https://satsearch.co/products/skyfox-labs-pipatch-max-active-multiband-gnss-patch-antenna-module, Accessed on 2024-03-08.

[164] Record-breaking satellite advances NASA's exploration of high-altitude GPS - NASA, 2019. https://www.nasa.gov/missions/mms/record-breaking-satellite-advances-nasas-exploration-of-high-altitude-gps/, Accessed on 2024-03-08.

[165] DMSA-3U Deployable Multifunction Solar Array. Product page. Accessed on: 2024-05-27. https://www.cubesat.market/dmsa-3u-deployable-multifunction-solar-array.

[166] BA01 Battery Array. Product page. Accessed on: 2024-05-27. https://www.cubesat.market/ba01-battery-array.

[167] CubeSat EPS - STARBUCK-nano | AAC clyde space, 2024. https://www.aac-clyde.space/what-we-do/space-products-components/pcdu/cubesat-eps-starbuck-nano, Accessed on 2024-03-08.

[168] NASA. Mission radiation environment modeling and analysis: Avionics trade study for gcd rad-neuro project. Ames Research Center, Technical Memorandum Document ID 20220011775, August 1, 2022.

[169] NASA. Cubesat design specification. https://www.nasa.gov/wp-content/uploads/2018/01/cubesatdesignspecificationrev14_12022-02-09.pdf, Accessed on 2024-03-08.

[170] Michael Garcia. Astrophysics sub-orbital 'pioneers' 2020 ROSES solicitation. 2020.

[171] Cornell SmallSat Mission Design School. https://smds.cornell.edu/, Accessed on 2024-04-30.

[172] Wesley A. Traub and Ben R. Oppenheimer. Direct imaging of exoplanets. In *Exoplanets*, pages 111–156. University of Arizona Press, Tucson, AZ, 2009.

[173] E. S. Douglas, J. R. Males, J. Clark, O. Guyon, J. Lumbres, W. Marlow, and K. L. Cahoy. Laser guide star for large segmented-aperture space telescopes. i. implications for terrestrial exoplanet detection and observatory stability. *The Astronomical Journal*, 157(1):36, jan 2019.

[174] Habitable Worlds Observatory. Home. Available online at, n.d. `https://habitableworldsobservatory.org/home`.

[175] Keck Observatory. `https://www.keckobservatory.org/keck-observatory/`, 2024. Accessed: 2024-05-24.

[176] About subaru telescope, 2024. Accessed: 2024-06-09.

[177] Gemini Observatory. About Gemini. `https://www.gemini.edu/about`, 2024. Accessed: 2024-05-24.

[178] Maunakea observatories. `https://www.maunakeaobservatories.org/`. Accessed on: 2024-06-03.

[179] C. et al Marois. Imaging and characterization of rocky earth-size habitable zone planets in the solar neighbor- hood with tm. Presented at the Spirit of Lyot 2019, Tokyo, Japan, October 21-25, 2019, private comms, 2019.

[180] David L. Fried. Statistics of a geometric representation of wavefront distortion. *JOSA*, 55(11):1427–1435, 1965.

[181] Frederick G. Smith, editor. *The Infrared & Electro-Optical Systems Handbook Volume 2: Atmospheric Propagation of Radiation*. SPIE Press, 1993.

[182] Alain Fuchs, Michel Tallon, and Jean Vernin. Focusing on a turbulent layer: Principle of the 'generalized scidar'. *Publications of the Astronomical Society of the Pacific*, 110:86–91, January 1998.

[183] Rodolphe Conan. Mean-square residual error of a wavefront after propagation through atmospheric turbulence and after correction with zernike polynomials. *JOSA A*, 17(10):1793–1803, 2008.

[184] Frank L. Pedrotti, Leno S. Pedrotti, and Leno M. Pedrotti. *Introduction to Optics*. Cambridge University Press, 2017.

[185] Max Born and Emil Wolf. *Principles of Optics: Electromagnetic Theory of Propagation, Interference and Diffraction of Light*. Cambridge University Press, 2013.

[186] Francis A. Jenkins and Harvey E. White. *Fundamentals of Optics*. McGraw-Hill, 2001.

[187] Charles Savage. *Principles of Lasers*. Springer, 2009.

[188] François (Ed.) Roddier. *Adaptive Optics in Astronomy*. Cambridge University Press, 1999.

[189] Boston Micromachines Corporation. `https://bostonmicromachines.com/`. Accessed on: 2024-05-30.

[190] ALPAO. `https://www.alpao.com/`. Accessed on: 2024-05-30.

[191] William H. Press, Saul A. Teukolsky, William T. Vetterling, and Brian P. Flannery. *Numerical Recipes: The Art of Scientific Computing*. Cambridge University Press, 2007.

[192] S. Mark Ammons, Lisa Poyneer, Donald T. Gavel, Renate Kupke, Claire E. Max, and Luke Johnson. Evidence that wind prediction with multiple guide stars reduces tomographic errors and expands MOAO field of regard. In Brent L. Ellerbroek, Enrico Marchetti, and Jean-Pierre Véran, editors, *Adaptive Optics Systems III*, volume 8447, page 84471U. International Society for Optics and Photonics, SPIE, 2012.

[193] Yoshito H. Ono, Masayuki Akiyama, Shin Oya, Olivier Lardiére, David R. Andersen, Carlos Correia, Kate Jackson, and Colin Bradley. Multi time-step wavefront reconstruction for tomographic adaptive-optics systems. *J. Opt. Soc. Am. A*, 33(4):726–740, Apr 2016.

[194] B. D. O. Anderson and J. B. Moore. Kalman filtering: Whence, what and whither? *Control and Dynamic Systems*, 23:215–235, 1986.

[195] Thierry Fusco, Jean-Marc Conan, Vincent Michau, Gerard Rousset, and Laurent M. Mugnier. Isoplanatic angle and optimal guide star separation for multiconjugate adaptive optics. In Peter L. Wizinowich, editor, *Adaptive Optical*

Systems Technology, volume 4007, pages 1044 – 1055. International Society for Optics and Photonics, SPIE, 2000.

[196] Richard M. Myers, Mark Milman, and Christoph U. Keller. Tomographic reconstruction for wide field adaptive optics systems: Fourier domain analysis and fundamental limitations. *Journal of the Optical Society of America A*, 37(3):C167–C178, 2020.

[197] Bernadett Stadler and Ronny Ramlau. Performance of an iterative wavelet reconstructor for the multi-conjugate adaptive optics relay of eso's elt, 2022.

[198] Ronny Ramlau and Bernadett Stadler. On some analytic properties of the atmospheric tomography operator: Non-uniqueness and reconstructability issues, 2024.

[199] Matthias Beckmann. Lecture notes on computerized tomography, 2023.

[200] Maria Pina Limongelli and Valter Carvelli. Damage localization in a glass fiber reinforced composite plate via the surface interpolation method. *Journal of Physics: Conference Series*, 628, 07 2015.

[201] Simon Hubmer and Ronny Ramlau. A frame decomposition of the atmospheric tomography operator. *Inverse Problems*, 36(9):094001, August 2020.

[202] David J. C. MacKay. Bayesian Interpolation. *Neural Computation*, 4(3):415–447, 05 1992.

[203] Luc Gilles, Lianqi Wang, and Brent L. Ellerbroek. Minimum variance split tomography for laser guide star adaptive optics. *European Journal of Control*, 17(3):327–334, 2011.

[204] Alexander B. Walter, Neelay Fruitwala, Sarah Steiger, and Benjamin A. Mazin. The mkid exoplanet camera for subaru scexao. *arXiv preprint*, arXiv:2010.12620, October 2020.

[205] S. Cova, M. Ghioni, A. Lacaita, C. Samori, and F. Zappa. Avalanche photodiodes and quenching circuits for single-photon detection. *Appl. Opt.*, 35(12):1956–1976, Apr 1996.

[206] Chandra Natarajan, Michael Tanner, and Robert Hadfield. Superconducting nanowire single-photon detectors: physics and applications. *Superconductor Science and Technology*, 25, 04 2012.

[207] O. Gravrand, J. Rothman, C. Cervera, N. Baier, C. Lobre, J.-P. Zanatta, O. Boulade, V. Moreau, and B. Fieque. Hgcdte detectors for space and science imaging: General issues and latest achievements. *Journal of Electronic Materials*, 45(9):4532–4541, 2016.

[208] Bernard J. Rauscher, Ori D. Fox, Pierre Ferruit, Robert J. Hill, Augustyn Waczynski, Yiting Wen, Wei Xia-Serafino, Brent Ido, David Alexander, Clifford K. Brambora, Rebecca Derro, Chuck Engler, Ginn Lee, John Nieznanski, Peter Wallis, and James York. Detectors for the James Webb Space Telescope near-infrared spectrograph I: Readout mode, noise model, and calibration considerations. *Publications of the Astronomical Society of the Pacific*, 119(857):768–786, July 2007.

[209] Bei Zhang, Tianyu Xiao, and Jinzuomu Zhong. A simple determination approach for zero padding of fft method in focal spot calculation. *Optics Communications*, 440:133–137, 2019. Department of Automation Science and Electrical Engineering, Beihang University, Beijing 100191, China.